Universitat de Barcelona

Facultat de Química

Departament de Química Física

Programa de doctorat de Química Teòrica i Computacional

Quantum dynamics of physicochemical processes in superfluid ^{4}He nanodroplets

Memòria presentada per optar al grau de doctor per la Universitat de Barcelona

Arnau Vilà Casanovas

Juliol de 2015

Directors:

Prof. Dr. Miguel González Pérez
Catedràtic del Departament de Química Física
Facultat de Química, Universitat de Barcelona

Prof. Dr. Ricardo Mayol Sánchez
Professor titular del Departament d'Estructura i Constituents de la Matèria
Facultat de Física, Universitat de Barcelona

Voldria agrair l'ajuda, de tota aquella gent que ha estat al meu costat i ha ajudat d'alguna marea o altre a que aquesta tesi hagi sigut possible:

- Primerament, voldria agrair els meus directors de tesi Miguel González i Ricardo Mayol pel seu suport i mestratge durant aquests quatre anys. En especial al Miguel, amb qui he compartit una pila d'hores al despatx conversant tant sobre temes científics (relacionats o no amb la tesi) com sobre aspectes de la vida més personals. Sens dubte, d'ell me n'emporto un gran aprenentatge científic i com a persona que em serà de gran ajuda per a la vida.

- Als meus pares i germanes que han hagut (i sabut) suportar-me tant en els bons moments intentant explicar-los la meva recerca com en els moments amb més estrès i angoixa en què sempre han estat amb mi per recolzar-me.

- Als companys del màster i la facultat amb els quals hem compartit aquesta aventura. La seva companyia ha sigut molt agraïda. En especial, al Melchor pels seus coneixements del "mundillo" de la recerca; a l'Oriol, sempre disposat a ajudar i fer favors; i al Gian amb qui he compartit grans estones i aventures.

- A la gentussa de Barcelona (Marc, Gerard, Javier, Chema, Gian...) per fer del dia a dia d'aquests quatre anys hagi sigut bastant increïble. En especial al Gerard, que ha hagut de suportar hores i hores de "rollos" sobre ciència, la tesi i sobre la universitat.

- Als meus amics, per donar-me sempre suport i interessar-se pel que estava fent. Especialment voldria agrair a l'Oriol Forts, per la seva ajuda amb l'anglès i edició de textos i a en Gerard Corominas, per l'ajuda en l'edició d'imatges i la confecció de la portada.

- Finalment, vull agrair al meu tiet, en Joaquím Fradera i al meu amic Aleix Forts. Ells van ser probablement les persones que van despertar el meu interès per la ciència. El primer pels seus regals en forma de llibre sobre temes científico-filosòfics i el segon per les moltíssimes hores de conversa sobre ciència quan érem dos marrecs (i encara).

The development of the present Ph.D. thesis has been possible thanks to the financial support provided by:

- Predoctoral research grants:

University of Barcelona grant (APIF) (2010-2011)

Catalonian Autonomous Government grant (2012-2015)

-Research projects:

The main support to the research developed here has been provided by

National projects

Spanish Ministry of Science and Innovation, ref. CTQ2011-27857-C02-01.

Spanish Ministry of Science and Innovation, ref. FIS2011-28617-C02-01.

and some support has been provided by the

Autonomous Government projects

Catalonian Autonomous Government, refs. 2009SGR 17. 2014SGR 25 and XRQTC

Contents

Preface

The study of physical processes taking place in superfluid helium nanodroplets (T=0.37 K) has become an active area of research in physics during the last 20 years. These investigations range from fundamental physics aspects to some spectroscopic applications. The former ones focus on obtaining a deeper understanding of liquid helium, because of its quantum liquid nature and the superfluidity phenomenon. The latter studies refer to possibility of carrying out atomic and molecular high resolution experiments in helium nanodroplets taking advantage of the exceptional properties of this fluid. In addition, many applications of superfluid helium nanodroplets have appeared very recently in the chemical context as, e.g., the synthesis of novel chemical species as metallic nanoclusters or nanowires. Thus, nowadays this field of research can be considered as a frontier topic in which both the physical and chemical communities share their efforts.

From a purely chemical perspective, a significant number of reactions have been experimentally investigated inside these nanoreactors, but only a few of these studies were focused on the reaction dynamics. Most of them merely use helium nanodroplets as very low temperature matrices, but without trying to elucidate the influence of this peculiar liquid to the reaction mechanism.

The present thesis is probably the first attempt to explore the reaction dynamics inside superfluid helium nanodroplets from a theoretical perspective. This aim is considered to be quite relevant because at present it is not possible to experimentally determine the detailed mechanism of a process taking place inside these nanodroplets.

The complexity of the problem motivates the union of the efforts coming from the physical and chemical communities (and also from theoreticians and experimentalists of both groups). The former is necessary in order to have a good description of superfluid liquid helium and the latter because of their knowledge of quantum reaction dynamics in gas phase. Besides, it is worth noting that this thesis is the first contribution of our research group into

this field and the dynamics of most processes reported has been investigated here for the first time.

The present thesis is organized in eleven chapters. The first ones introduce both the topic of liquid helium and its nanodroplets (Chapter 1) and the theoretical methods developed for the study of superfluid liquid helium (Chapter 2). The following chapters can be grouped into three main areas as: structure, energy and spectroscopy of oxygen atom-doped helium nanodroplets (Chapter 3); photodissociation dynamics of homonuclear diatomic molecules inside helium nanodroplets (Chapters 4-7); and the capture process of neon atoms (Chapter 8) and synthesis reaction of its van der Waals dimer (Ne_2) (Chapter 9).

With the only exception of Chapter 3, the chapters with original results are dedicated to investigate the quantum dynamics of the processes indicated above, using the theoretical approach developed in Chapter 4 (or a related one) and taking into account nanodroplets of different sizes. Basically, it is the first time that the dynamics of these processes has been studied theoretically. The contents of the thesis are described in more detail below.

An historical introduction of the discovery of liquid helium and its fascinating superfluid character is given in Chapter 1, together with a short review on the development of helium nanodroplets and the related previous investigations.

Chapter 2 presents a brief description of the theoretical methods employed to describe superfluid liquid helium, focusing mainly in the method used in the present thesis, i.e., the density functional theory.

The first chapter including original results is Chapter 3, which includes a theoretical investigation of the structure, energy and spectroscopy of helium nanodroplets doped with atomic oxygen in its three lower electronic states. This is the only chapter focused on the stationary states (statics), i.e., that does not consist in real-time dynamical simulation of processes.

Chapter 4 is the first one related with the study of the photodissociation of homonuclear molecules inside helium nanodroplets. The hybrid theoretical method developed is presented and applied to the photodissociation of Cl_2.

The natural continuation of the previous chapter is exposed in Chapter 5, where the relaxation process of the excited helium nanodroplets arising from the Cl_2 photodissociation is examined.

To complete the analysis of the photodissociation of Cl_2, Chapter 6 is dedicated to obtain a deeper insight into the (confinement) quantum resonances that lead to the rich structures (oscillations) found in the velocity distribution of the Cl fragments.

Chapter 7 ends the part of the thesis focused on the study of the photodissociation dynamics inside helium nanodroplets. The theoretical method presented in Chapter 4 is applied to explore the photodissociation of two additional halogen molecules (Br_2 and I_2). Moreover, a systematic model study on the effect of the mass of the atoms forming the diatomic molecule in the photodissociation process is also carried out, taking the Cl_2 case as the reference.

The pickup (or capture process) of a Ne atom by a helium nanodroplet is investigated in Chapter 8.

The last original results obtained during this thesis are presented in Chapter 9, where the synthesis reaction of a van der Waals complex inside helium nanodroplets (Ne_2) has been studied. The theoretical approach used here in a sense corresponds to an extension of those employed in the study of the photodissociation of diatomics and capture of Ne atoms.

To complete the thesis, the main conclusions obtained are collected in Chapter 10, while a summary of the thesis in Catalan is given in Chapter 11.

From the work developed in the present thesis two papers have already been published:

-Vilà, A; González, M.; Mayol, R. Photodissociation Dynamics of Homonuclear Diatomic Molecules in Helium Nanodroplets. The Case of $Cl_2@(^4He)_N$. *J. Chem. Theory Comput.* **2015**, *11*, 899-906.

- Vilà, A; González, M.; Mayol, R.; Paniagua, M. Theoretical Approach to the Structure, Energy and Electronic Spectroscopy of $O@(^4He)_N$ Nanodroplets. *RSC Adv.* **2014**, *4*, 44972-44979.

Moreover, three more papers have been already submitted (corresponding with the studies of the Chapters 5, 6 and 8) and three additional papers will be submitted for publication in the following months.

1. Introduction

1.1 Liquid helium

Two stables isotopes of helium are present in nature: ^{3}He and ^{4}He. Their relative abundance[1] in number $\left(n_{^3He}/n_{^4He}\right)$ is about $1.38 \cdot 10^{-6}$. Due to the difference in the number of neutrons, ^{3}He has spin ½ and it is a fermion, while ^{4}He has spin 0 and is a boson. Thus, they obey different quantum statistics and this fact has a crucial relevance, determining many of the characteristics of the liquid phase of these isotopes.

Only two electrons surround the nucleus, with a electronic configuration $1s^2$. Thus, this consists of a closed-shell electronic structure, which gives them a chemical inert character. Furthermore, since helium has only two electrons, they are close to the nucleus and, hence, it is very difficult to perturb them, which results in a very low polarizability. At the end, these facts result in a very weak van der Waals type He-He interaction (instantaneous dipole-instantaneous dipole interaction), with a potential well of around 10 K. Another consequence of the closed-shell electronic structure of helium is a zero electronic orbital angular momentum, and so, an isotropic distribution of the electronic cloud. This leads to a non-directional He-He potential (i.e., only depending on the distance between the two atoms) or, in other words, there is only one electronic state for the He_2 dimer correlating with the ground state of the atoms. For short distances, a high repulsion is present due to the overlap of the electronic clouds.

The He-He potential energy curve can be fitted to a Lennard-Jones potential with parameters $\epsilon = 10.22\ K$ and $\sigma = 2.556$ Å.

$$V(r) = 4\epsilon\left[\left(\frac{\sigma}{r}\right)^{12} - \left(\frac{\sigma}{r}\right)^{6}\right] \tag{1.1}$$

Moreover, a very popular and more accurate potential is the so-called Aziz potential[2]. Despite this, the Lennard-Jones form is the one selected in the present work as it is accurate

enough and has a simpler mathematical expression[i]. More recently, Cybulski et al.[3] reported an accurate *ab-initio* He-He potential. These potential energy curves are represented in Figure1.1.

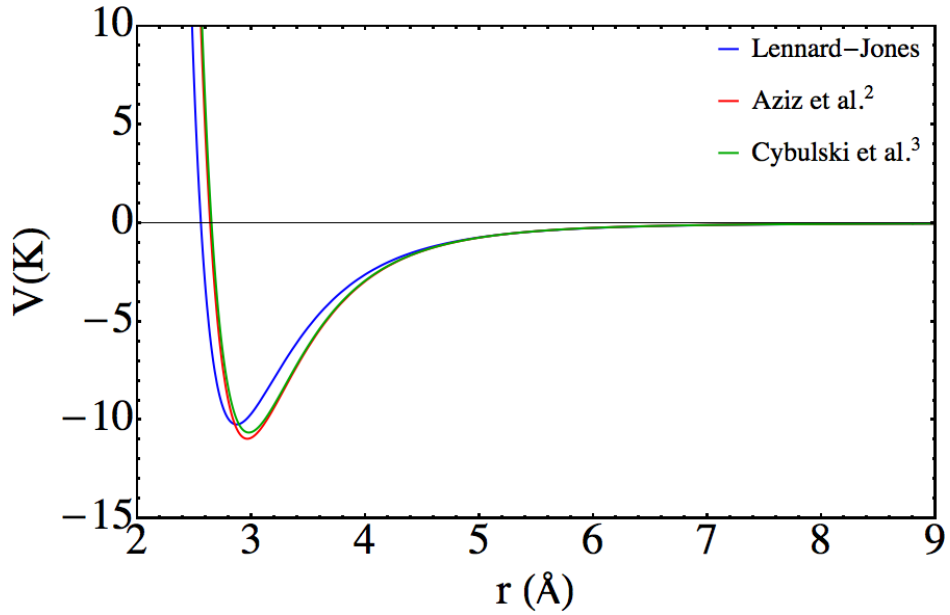

Figure 1.1. Potential energy curves for the He-He interaction.

In the present work we have studied the dynamics of physic-chemical processes involving ^{4}He superfluid nanodroplets. Therefore, some important properties of the liquid helium-4 will be reviewed here.

The phase diagram of ^{4}He has a critical temperature of 5.2 K and therefore helium-4 will remain in gas phase at higher temperatures, regardless of the applied pressure[4]. Also, it has no triple point, in which the three phases (solid, liquid and gas) would coexist. At atmospheric pressure (1 atm) the liquid-gas equilibrium temperature is 4.21 K. Lowering temperature (close to zero Kelvin) helium remains liquid, unless the pressure is substantially increased (25-30 bar). ^{4}He is the only chemical element with this property, which is purely a quantum phenomenon that results from the combined effect of its light atomic mass and the low attractive interaction between helium atoms.

Solidification takes place when temperature is low enough that the interaction between the atoms overcomes their kinetic energy, and so fixes their position into concrete sites. The mean kinetic energy is reduced with temperature until a minimum amount imposed by the Heisenberg uncertainty principle (position and its conjugate momentum cannot be perfectly

[i] It can be Fourier transformed analytically.

defined at the same time). This is known as zero point energy (ZPE) or zero point motion (ZPM) and can be estimated by the *particle in a box* model. Thus, the ZPE is inversely proportional to the mass and to the square of the dimension of the box, whose size can be estimated as the atomic separation corresponding to the minimum of the interaction potential. Hence, the very low mass of ^{4}He involves high kinetic energies, which gives a positive value of total energy. Therefore, solidification does not take place.

Another important feature is the change of phase taking place at 2.18 K (at atmospheric pressure), from normal liquid (helium I) to superfluid liquid (helium II). This second phase has surprising properties, such as zero viscosity below certain velocity flow (superfluidity), thermal conductivity approaching to infinity, or a new thermal waves called second sound. These special properties of helium-II makes it a particularly important quantum liquid ("a many-particle system in whose behaviour not only the effects of quantum mechanics, but also those of quantum statistics, are important", as given by A. J. Leggett in his book entitled *Quantum Liquids*[5].

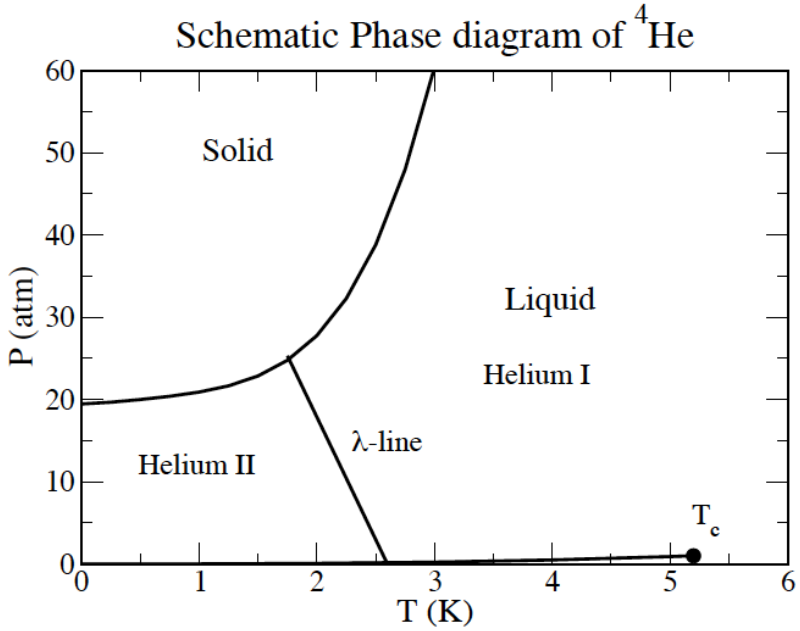

Figure 1.1. Phase diagram (P,T) of ^{4}He at low temperatures. This figure has been taken from Reference 6.

Finally, to conclude this subsection it is worth mentioning that liquid helium is completely transparent to photons below 20 eV [7]. This fact is really important for spectroscopic considerations, which correspond to one of the main applications of helium nanodroplets.

1.2 History of the superfluidity

Helium was not directly discovered on Earth, but it was found from the analysis of the Sun spectrum during an eclipse in 1868[8]. That is the reason for its name, which comes from the Greek term *helios.* In 1908 Kammerlingh Onnes liquefied helium for the first time[9] and, afterwards, he tried to solidify it. Then, a non-typical behavior of the density with temperature was found, and in 1923 Dana and Onnes measured the latent heat and found a discontinuity at around 2.2 K, whose shape resembled the Greek letter lambda[10]. That was the reason for naming the corresponding temperature as *lambda-point* T_λ.

In 1927 Keesom and co-workers wrote a paper entitled "Two Different Liquid States of Helium" where they concluded the existence of a phase change in liquid ^{4}He (*lambda transition*)[11]. The two liquid phases were named helium-I (above T_λ) and helium-II (below T_λ), and their behavior was very different. It was not until 1937 when Allen and Misener[12] at the Royal Society Laboratories in Cambridge and, independently, Kapitza[13] at the Soviet Academy of Sciences, discovered the frictionless flow of helium-II below the lambda point (the papers were published in *Nature* the 8 of January of 1938)[14]. Both experiments aimed to measure the viscosity by flowing He through channels, instead of by oscillating cylinders as it was previously done by Misener in 1935. This property was since then called *superfluidity* and hence it is very often related to the absence of viscosity. Nevertheless, superfluidity includes many other curious effects, such as "free" rotation (Andronikashvili experiment), formation of quantized vortices or fountain effect.

After this discovery many theorists began to develop different models in order to explain these amazing properties. Few months after the discovery of superfluidity was published, London suggested that this phenomenon should be related with the Bose-Einstein statistics, and more concretely with the formation of a Bose-Einstein Condensate [15,16]. Also, he pointed out that it might have a strong connection with superconductivity, whose discovery was made many years before, interpreting this latter phenomenon as the superfluidity of an electron gas in a metal. One month later, Tisza proposed the *two fluid model*[17], in which the existence of a mixture of two fluids (a condensate and a normal part) flowing under different dynamics was assumed.

Landau made an enormous progress in the theoretical understanding of liquid helium[18,19,20]. In 1941 he quantized the hydrodynamics of fluids and concluded that the weak

excited states of fluids can be considered as *elementary excitations*. He divided them into two main groups depending on its momentum: phonons which correspond to low momenta excitations (sound quanta) and rotons for higher momenta (a sort of elementary vortices), with a linear dispersion relation for the former and quadratic one for the latter. Within his approach, a new interpretation of the *two fluid model* was possible, identifying the superfluid component with the ground state of liquid helium and the normal component with the elementary excitations. The parameters related to these elementary excitations were chosen phenomenologically. Hence, Landau never related the superfluidity to the presence of a Bose-Einstein condensate, which ended up being completely wrong.

One of the milestones of Landau's theory was the explanation given for the flow without viscosity. Noting that viscosity consists in energy and momentum transfer between the liquid and the walls of capillary, he imposed the balance of these physical quantities taking into account the dispersion relation, i.e., $\varepsilon(p)$ of the liquid helium-II and obtained relative velocity limiting value for this process to take place. This is the so-called *Landau's critical (limiting) velocity*, which is given by[21,22]:

$$v_c = Min_p \frac{\varepsilon(p)}{p} \tag{1.2}$$

For the case of bulk liquid helium-II this has a value of about 58 m/s. In fact, this relationship determines that an ideal non-interacting condensed gas of bosons will never be superfluid in the sense of absence of friction. The quadratic dispersion relation for low momentum excitations gives a zero value for this Landau's critical velocity. This is a very important fact, since it forbids the possibility of an explanation of this phenomenon only in terms of the presence of a macroscopic wave function.

In 1947 Bogoliubov theoretically proved[23] that in a degenerate non-ideal (low-interacting) boson gas there is a Bose Einstein condensation. Furthermore, he shown that there are not individual particle excitations at low energy but only collective modes. In this case (dispersion relationship), superfluidity can arise. Afterwards, in 1951 Penrose[24] generalized the concept of BEC as the "off-diagonal long range order" (ODLRO). A further definition was given by this author together with Onsager in 1956[25], which is still used and allows the condensate fraction to be significantly less than one. Nowadays, it is known that

liquid ^{4}He at (almost) zero Kelvin is superfluid but only around 10% of the liquid is condensed.

1.3 Helium nanodroplets

Helium nanodroplets are aggregates of He atoms, ranging from few hundreds to around 10^7 atoms, having nanometric dimensions. When Kamerling Onnes was initially trying to liquefy helium from a gas expansion he already realized the formation of droplets, but he did not pay much attention[26] to this fact. Droplets began to be studied in order to analyse the evolution of the liquid properties when decreasing the size of the system (finite-size effects for quantum systems[7]). This was achieved in Karlsruhe (firstly reported by Becker at 1961[27]) and the investigation continued in the 1970s and 1980s. In the late 1980s and early 1990s the ability of helium droplets to pickup almost any chemical species (atomic or molecular) was discovered, which generated the attraction of the chemistry community. This was discovered by the Toennies' group in Göttingen, using electron impact mass-spectrometry as detection[28,29] technique. An important feature of this experimental method is the possibility to obtain droplets doped with only a single impurity, by tuning the experimental conditions in a suitable way. In 1992 Scoles and coworkers combined the pickup technique with spectroscopic interrogation by laser induced evaporation and were able to investigate the infrared spectroscopy of SF_6. Afterwards, in 1994 Toennies and Vilesov showed for the first time the rovibrational spectrum of this molecule, embedded in helium droplets, with a very high resolution. This spectrum corresponded with the expected one for this specie freely rotating (at vacuum), suggesting the superfluid character of the helium droplets. This and other experiments motivated the interest of both physics and chemistry communities, which have many relevant questions to be asked and answered.

The experimental techniques employed to generate helium droplets are based on free jet supersonic expansions, mostly of very pure helium gas but in a few cases carrying out expansions of the liquid[30]. Nowadays, helium droplets from several hundreds to 10^4 atoms are produced by expanding gas at high pressures (20-100 bar) and temperatures of about 5-20 K through a tiny nozzle of several microns of diameter or a narrow orifice. After this expansion, that as a good approximation can be considered as adiabatic, the temperature decreases rapidly and atoms begin to be collected forming clusters. Afterward, the clusters merge

forming big aggregates (10^6-10^7). Then, at the vacuum chamber, evaporative cooling takes place until the droplets arrive at the mentioned steady-state temperature (0.37 K) and the usual sizes (10^3-10^4 helium atoms). Depending on the experimental conditions, different mean values for the droplet size can be obtained, the width of the size distribution (FWMH) being comparable to the mean value. A schematic representation of the typical experimental setup is given in Figure 1.2.

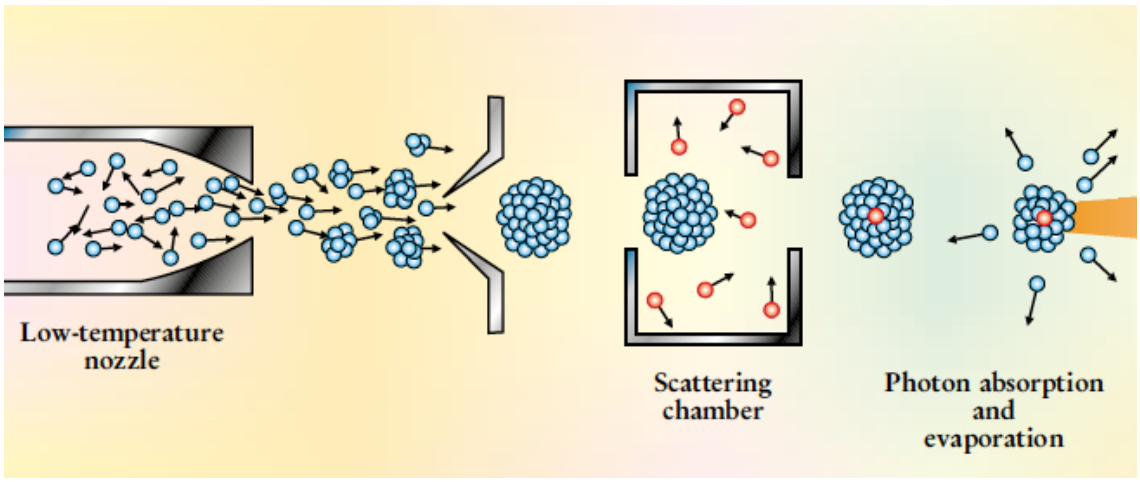

Figure 1.2. Schematic representation of the helium droplet experimental production. Illustration taken from Reference 26.

Another important feature is that the usual temperatures achieved in the droplets are 0.37 K and 0.15 K for droplets of ^{4}He and ^{3}He, respectively. Therefore bosonic droplets are at the superfluid phase while the fermionic ones are in the normal phase. Hence, they constitute very low temperature matrices (i.e., cryogenic matrices). These properties make these systems very interesting from a very wide range of perspectives. In this sense, their study has become an important "meeting point" where theoretical and experimental physicists and chemists can work together.

From the energy point of view it is worth noting that these are saturating systems: when increasing the size, the density and binding energy per particle take an asymptotic value corresponding to the bulk one. Focusing on the extreme cases, the He_2 dimer, which was detected experimentally by diffraction from a transmission grating[31] and has a binding energy of 1.1 $(+0.3/-0.2)\cdot 10^{-3}$ K (and internuclear distance of 52±4 Å !), while the bulk value is 7.2 K. The ground state droplets are spherical and, hence, a liquid drop model can be applied to estimate the energy per helium atom as a function of the number of atoms of the droplet. The corresponding equation will appear afterwards in the present thesis and will not be exposed

here. However, it has been determined both theoretical[32,33] and experimentally[33,34] that the droplet surface has a rather large size. Its thickness, which is defined by the distance where the density falls from 90% to 10% of bulk value, is around 6 Å. Therefore, large clusters have regions with bulk character. Furthermore, some calculations showed that in this region the condensate fraction is close to the unit.

To conclude with the properties of helium nanodroplets we should note that the finite-size of them implies the existence of a discrete excitation spectra rather than continuum one. Regarding the excitation modes of a helium nanodroplet, two kinds of them can be distinguished[34]. First we have the compressional modes (phonons) that resemble to those the helium bulk, but in this case they are discrete, and rotons, which points out the superfluid character of the droplets. Besides, there are multipolar surface modes (ripplons), in general of low energy (below the threshold energy to evaporate an atom) so that they are long-lived.

Regarding the doped helium droplets, it should be noted that not all the atomic or molecular impurities are placed at the centrum of the droplet. For very strong interacting dopants, such as, e.g., cations, they induce a snowball-like structure in the surrounding helium. This is like a solid phase in the sense that in the solvation shells helium atoms are almost in fixed positions. For weaker interactions the main impurities are often located at the centrum but, e.g., alkali atoms get stuck at the droplet surface, at the so-called *dimple*.

The location of the impurity is the result of an energy balance between the interaction energy and the surface energy of the generated atomic or molecular cavity inside the droplet. A remarkably good estimation of this phenomenon was done by Ancilotto et. al.[35] They defined an adimensional parameter (λ_A), whose value determines the position of the dopant, that depends on the helium surface tension (σ) and saturation density (ρ), the distance (r_{min}) and depth (ε) of the interaction potential.

$$\lambda_A = \frac{\rho \varepsilon r_{min}}{2^{1/6}\sigma} \tag{1.3}$$

If λ_A takes a value greater than 1.9 the impurity is expected to be fully solvated (preference for the solvated state), while if it is smaller the surface state is favourable. For values really close to this number, it is not clear what happens and more accurate calculations or experiments must be done in order to elucidate what situation is preferred. This is the case

of alkaline earth[36] atoms. In addition, when more than one impurities are present different structures can be present (cluster-like or foam-like[37]).

Although there are several motivations for the study of helium nanodroplets, they are not decoupled to each other. A reasonable classification can be done, depending on the main aim of the investigation. Below, we will briefly review them, beginning from the oldest (and more fundamental) perspective, continuing from an applied and finishing with the point of view the present thesis resides on.

Liquid helium has fascinating properties that come from its *quantum liquid* nature, as it has been mentioned above. They mainly arise from the quantum statistics, which allows the system to have a "macroscopic" number of atoms in the same quantum state. Therefore, to deepen more into these extraordinary properties it is natural to try to study what happens with these features when decreasing the size of the system, i.e., checking to what extent this consists in a macroscopic phenomenon. Therefore, one of the viewpoints for the study of helium droplets could be considered *fundamental physics*. In this sense, many investigations on pure and isotopic mixtures (^{4}He-^{3}He) droplets have been reported trying to elucidate the role played by the statistics.

From this perspective doping droplets with atoms or molecules is very interesting because these chemical species can act as probes, in order to extract information on the droplets properties. One of the key experiments in this context was the microscopic Andronikashvili experiment carried out by Grebenev, Toennies and Vilesov in 1998[38]. They proved the (rotational) superfluidity of helium clusters from the vibrorotational spectrum of the OCS dopant. Thus, preparing pure and mixed ^{3}He/^{4}He droplets, progressively increasing the amount of the latter. For the pure ^{4}He droplets, sharped and well-resolved lines were obtained, while in the case of pure ^{3}He droplets a broad spectrum was found. For the mixtures they found a monotonic transition between these two situations. This was interpreted in terms of the free rotation of OCS when solved in superfluid ^{4}He. A number of around 60 ^{4}He atoms was estimated from the onset of the superfluid solvation of this molecule. Hence, spectroscopy of dopants can provide rich information on helium as a solvent.

Another important characteristics of superfluid helium nanodroplets, whose discovery implied the presence of a dopant, is the existence of a critical (or limit) velocity in these systems[39] (Landau's velocity). To arrive to this conclusion dynamical phenomena involving

impurities were investigated. Also within this fundamental viewpoint many studies have been performed on the droplet excitation spectra, vortex nucleation, etc[30,34].

Besides their fundamental interest, helium nanodroplets have become an active area of research as an ideal cryogenic matrix for the study of a wide variety of phenomena related with atoms and molecules (low temperature chemistry[40]). This fact has attracted the interest of the chemical community because they share the interesting properties of both gas phase and matrix-isolation techiques[30]. Low temperature chemistry has an especial interest for several reasons and in different contexts, e.g., in Astrochemistry.

Quantum effects are enhanced when reducing the temperature. A simple justification of this fact comes from the de Broglie wavelength ($\lambda = h/p$). Thus, since the mean momentum (or kinetic energy) of the particles is related with the temperature, the wavelength increases, getting values comparable with the size of the particles. When this situation is reached, quantum effects become more important[4].

On the other hand, at low temperatures a reduced number of quantum states are populated in a significant way. This is very important for the spectroscopy of atoms and molecules, because it reduces the number of transitions, which simplifies the spectrum analysis. Furthermore, the superfluidity and the very low chemical reactivity of helium (i.e., very low interaction with the dopant species) also help in obtaining high-resolution spectroscopy, since the broadening of the spectrum coming from matrix effects is minimized and the system is chemically stable (no reactions are produced), respectively. These extraordinary matrix properties were firstly reported by Scoles et. al.[41] in the context of the absorption spectrum of SF_6. In rotational spectroscopy the molecular symmetry is maintained and there is just a change in the rotational constants due to the effect of this particular solvent. Therefore, this technique allows the determination of the rotational behavior of large molecules that would not be possible or very difficult in gas phase or solid matrices. Regarding vibrational spectroscopy, the perturbations are often weak so the results can be directly compared with the theoretical results for the fully isolated species.

Other matrix applications[4,26,30] involve the synthesis of a very wide range of chemical species, from small metastable molecules or radicals to metal clusters[42] or nanowires[43]. Helium nanodroplets easily stabilizes the dopant by releasing the excess kinetic energy coming from the pickup process by evaporation. Moreover, since the impurities generally are

located at the centrum of the droplet, this makes easier the (binary) encounters of the dopants close to the centrum. Furthermore, the excess energy resulting from the synthetic process is released to the droplet, stabilizing the obtained products.

The studies mentioned in the last paragraph can be regarded as different applications of the helium droplets "technology" for different purposes related to the chemical synthesis. However, from a more fundamental chemical perspective, i.e. from the *reaction dynamics* viewpoint little has been done up to now. As far as we know, there are only three experimental studies on the photodissociation of alkyl iodides[44,45,46], a theoretical study of the photodissociation of Cl_2[47] (hybrid method quantum wavepacket / path integral centroid molecular dynamics) and an hybrid path integral molecular dynamics / bosonic path integral Monte Carlo[48] has been recently proposed. The main features of *gas phase reaction dynamics* is well established and nowadays, progressively more attention is being devoted to the study of the reaction dynamics in liquid phase in order to deepen into the microscopic reaction mechanism and dynamic properties in a more common situation in a chemical laboratory.

Keeping this in mind, the study of the chemical reactivity in helium nanodroplets from a fundamental viewpoint provides clues to better understand the reaction chemical dynamics both at a very low temperature and in a quantum liquid fluid. Furthermore, reaction dynamics could also provide some more information of this fascinating liquid. The aim of the present thesis is to push a little bit forward the understanding of these processes at a theoretical level, taking also into account the dynamics of other related and important physico-chemical processes.

1.4 References

[1] Physics/nist.gov/PhyRefData/Handbook/Tables/heliumtable1.htm.

[2] Aziz, R. A.; McCourt, F. R. W.; Wong, C. C. K. *Mol. Phys*., **1987**, 61, 1487.

[3] Cybulski, S. M.; Toczylowski, R. R. *J. Chem. Phys*., **1999**, 111, 10520.

[4] Yang, S.; Ellis, A. M. *Chem. Soc. Rev.*, **2013**, *42*, 472.

[5] A. J. Leggett. *Quantum Liquids*, Oxford Graduate Texts, **2006**.

[6] J. Navarro. *Density Functional Theory of Liquid Helium*. Lectures given at the Jyväskylä Summer School, Finland, **August 2003**.

[7] Choi, M. Y.; Douberly, T. M.; Falconer, T. M.; Lewis, W. K.; Lindsay, C. M.; Merrit, J. M.; Stiles, P. L.; Miller, R. E. *Int. Rev. Phys. Chem.*, **2006**, 25, 15.

[8] Keesom, W. H. Helium, *Elsevier*, **1942**.

[9] Kamerlingh Onnes, H. *Commun. Phys. Lab. Univ. Leiden*, **1908**, 105, 744.

[10] Donnelly, R. Physics Today, **July 1995**.

[11] Wolfke, M.; Keesom, W. H. *Proc. Amst.*, **1927**, 31, 81.

[12] Allen, J. F.; Misener, A. D. *Nature*, **1938**, 141, 75.

[13] Kapitza, P. *Nature*, **1938**, 141, 74.

[14] Balibar, S. *J. Low. Temp. Phys.* **2007**, 146, 441.

[15] London, F. *Nature*, **1938**, 141, 643.

[16] London, F. *Phys. Rev.*, **1938**, 54, 947.

[17] Tisza, L. *Nature,* **1938**, 141, 913.

[18] Landau, L. D. *Phys. Rev.*, **1941**, 60, 356.

[19] Landau, L. D. *J. Phys. USSR*, **1941**, 5, 71.

[20] Landau, L. D. *J. Phys. USSR*, **1947**, 11, 91.

[21] Khalatnikov, I. M. *An Introduction to the Theory of Superfluidity*. Advanced Books Classics, **1965**.

[22] Tilley, D. R.; Tilley, J. *Superfluidity and Superconductivity*. Institute of Physics Publishing, **1974**.

[23] Bogoliubov, N. N, *J. Phys. USSR*, **1947**, 11, 23.

[24] Penrose, O. *Phil. Mag*., **1951**, 42, 1373.

[25] Penrose, O.; Onsager, L. *Phys. Rev*., **1956**, 104, 576.

[26] Toennies, J. P.; Vilesov, A.; Whaley, K. B. *Physics Today*, **February 2011**, 31.

[27] Becker, E. W. *Zeitschrift für Physik D*, **1986**, 3, 101.

[28] Scheidemann, A.; Toennies, J. P.; Northby, J. A. *Phys. Rev. Lett*., **1990**, 64, 1899.

[29] Scheidemann, A.; Schilling, B.; Toennies, J. P.; Northby, J. A. *Physica B*, **1990**, 165, 135.

[30] Toennies, J. P.; Vilesov, A. *Angew. Chem. Int. Ed*., **2004**, 43, 2622.

[31] Grissenti R. E.; Schöllkopf, W.; Toennies, J. P.; Hegerfeldt, G. C.; Köhller, T.; Stoll, M. *Phys. Rev. Lett*., **2000**, 85, 2284.

[32] Barranco, M.; Hernandez, E. S. *Phys Rev. B*, **1994**, 49, 12078.

[33] Harms, J.; Toennies, J. P.; Dalfovo, F. *Phys. Rev. B*, **1998**, 58, 3341.

[34] Barranco, M.; Guardiola, R.; Hernández, S.; Mayol, R.; Navarro, J.; Pi, M. *J. Low. Temp. Phys.*, **2006**, 142, 1.

[35] Ancilotto F.; Lerner, P. B.; Cole, M.W. *J. Low. Phys.*, **1995**, 101, 1123.

[36] Hernando, A.; Mayol, R.; Pi, M.; Barranco, M.; Ancilotto, F.; Buenerman, O.; Stienkemeier, F. *J. Phys. Chem. A*, **2007**, 111, 7303.

[37] Eloranta, J. *J. Low Temp. Phys.*, **2011**, 162, 718.

[38] Grebenev, S.; Toennies, J. P.; Vilesov, A. *Science*, **1998**, 279, 2083.

[39] Brauer, N. B.; Smolarek, S.; Loginov, E.; Mateo, D.; Hernando, A.; Pi, M.; Barranco, M.; Buma, W. J.; Drabbels, M. *Phys. Rev. Lett*., **2013**, 111, 153002.

[40] Krasnokutski, S. A.; Huisken, F. *J. Phys. Chem. A*, **2011**, 115, 7120.

[41] Goyal, S; Schutt, D. L; Scoles, G. *Phys. Rev. Lett.,* **1992**, 69, 933.

[42] Yang, S.; Ellis, A. M.; Spence, D.; Feng, C.; Boatwright, A.; Latimer, E.; Binns, C. *Nanoscale*, **2013**, *5*, 11545.

[43] Latimer, E.; Spence, D.; Feng, C.; Boatwright, A.; Ellis, A. M.; Yang, S. *Nano Lett.*, **2014**, *14*, 2902.

[44] Braun, A.; Drabbels, M. *J. Chem. Phys.,* **2007**, *127*, 114303.

[45] Braun, A.; Drabbels, M. *J. Chem. Phys.,* **2007**, *127*, 114304.

[46] Braun, A.; Drabbels, M. *J. Chem. Phys.,* **2007**, *127*, 114305.

[47] Takayanagi, T.; Shiga, M. *Chem. Phys. Let.*, **2003**, *372*, 90.

[48] Walewski, L.; Forbert, H.; Marx, D. *Comp. Phys. Comm*., **2014**, 85, 3, 884.

2. Theoretical Methods

2.1 Theoretical approaches to liquid helium

Since the discovery of superfluidity[1,2] several theoretical approaches have been proposed in order to understand this complex phenomenon[3,4]. As it has been mentioned in the introduction chapter, the two isotopes of helium (^{3}He and ^{4}He) obey different quantum statistics. So, despite both liquids have a superfluid phase, its nature is completely different: bosonic (macroscopic quantum occupation of the same single-particle state) vs. fermionic pairing (Cooper pairs). Since this thesis is focused on the study of ^{4}He nanodroplets, only the methods applied to bosons will be briefly reviewed here.

Helium-II is a quantum liquid and so this is the mainstone for understanding its behaviour. Therefore, classical theories as conventional molecular dynamics are not able to describe correctly this liquid, and the application of quantum mechanics treatments is unavoidable. In fact, this is the main feature to account for when dealing with liquid helium.

The study of this topic from a theoretical point of view has been carried out within a wide range of approximations, although the way the nature of helium is modelled is always the same (treating the atoms as single particles without internal structure). Helium atoms have a closed-shell electronic structure (zero electronic angular momentum) formed by just two electrons, which turn out into a very low polarizability and a very low chemical activity. This makes very plausible to consider each helium atom as a rigid sphere, without internal structure[5]. Noting that we want to study the liquid phase at very low temperatures, this kind of modelling is supported by looking at the different energy scales involved (about five orders of magnitude) between the van der Waals induced dipole induced-dipole induced dispersion interaction between two helium atoms and the electronic transition to the first excited state of helium. Thus, in all the theoretical approaches helium atoms are considered simply as particles interacting with each other via an interaction potential.

Regarding the different theoretical methodologies used for the study of the superfluid liquid helium, they can be approximately divided in two main groups: microscopic and phenomenological theories. While the former methods aim to obtain the full wave function (at zero temperature) or the density matrix (at finite temperature) of the system, the latter ones just deal with the one-body density of the system (*Density Functional Theory*, DFT). The studies presented in this thesis have been performed by means of a DFT level of theory and, because of this, only a brief description of the most important microscopic schemes is present here for the sake of completeness.

The use of microscopic theories implies to deal with a huge amount of degrees of freedom, since they deal with the wave function, which depends on the coordinates of all the particles. For a 3-dimensional problem regarding N helium-4 atoms, 3N degrees of freedom must be taken into account. So that, in order to make the calculation feasible, Monte Carlo algorithms are used to calculate the multidimensional integrals implied. The microscopic theories can be roughly classified in two groups: *Variational Monte Carlo* (VMC) and *Quantum Monte Carlo* (QMC)[5] methods.

In the framework of the variational approach, an ansatz form of the wave function (normally a Jastrow-Feenberg expression and modifications of it) is proposed in terms of some parameters. Then a variational principle is employed in order to determine the best values for these parameters. A modification of this method is the *Hipernetted Chain Euler-Lagrange* (HNC-EL)[5] method. On the other hand, in the QMC theories, instead of making use of an ansatz, the wave function is obtained by direct integration of the Schrödinger equation. Depending on the way this fundamental equation is presented different approaches within the QMC scheme appear. The starting point for the *Diffusion Monte Carlo* (DMC) method is the time dependent Schrödinger equation, written in terms of an imaginary time, which highly resembles a diffusion equation. It can be shown that, provided the trial initial wave function overlaps somewhat with the real ground state wave function of the system, the propagation of this initial guess to the infinite time limit leads to the exact ground state of the system. The *Green's Function Monte Carlo* method (GFMC)[6] is close to DMC but, instead of expressing the equation as a differential equation, it is converted into an integral equation whose kernel or Green's function is sampled exactly. This procedure avoids the systematic errors arising from to the finite time step used in DMC[7].

The only theoretical approach able to describe liquid helium at finite temperatures is the so-called *Path Integral Monte Carlo* (PIMC) method, which allows computing thermal averages of the observables of the system. Nevertheless, as it works based on the thermal density matrix it is difficult to extract information about the pure states of the system. This method derives from the path integral formulation of the quantum mechanics proposed by Feynman. For a detailed description of the microscopic theories describing both liquid helium I and II see Reference 5.

2.2 Density Functional Theory (DFT) and Time Dependent DFT (TDDFT)

Despite microscopic theories provide, to some extent, the "exact" solution to the complex many-body problem resulting from the superfluid liquid helium, their extremely large computational requirement favoured the development of phenomenological DFT approaches to facilitate the theoretical description of this physical problem. The finite size of the droplet makes the computational cost rapidly increase when so it does the number of helium atoms forming the droplet, since each one contributes with three more coordinates to the wave function. This fact reduces the size of the nanodroplets that microscopic techniques allow to calculate to few hundreds helium atoms. Furthermore, with the microscopic approaches it is not possible to perform real time dynamical simulations of processes.

Regarding phenomenological theories, DFT methods deal with the one-body density (only 3 degrees of freedom!) and belong to the so-called *mean field* theories, i.e. theoretical schemes that replace the many-body problem into an effective one-body problem.

The main aim of the present thesis is the study of the dynamics of chemical and physical processes involving helium droplets and atoms or molecules (dopants). To do so, real-time dynamical simulations are needed and, up to now, this is only possible making use of a Time Dependent DFT (TDDFT) approach. It is worth noting here that for many purposes there is no need of the full wave function of the system, but just information about the observables that depend on the one or two body density matrices[8], as is the case of the energy.

Working with a DFT approach highly reduces the number of degrees of freedom needed to account for many observables, and this procedure has been extensively used to

study problems related with the quantum many-body theory, such as, e.g., atoms, molecules or liquid helium. Density functional theoretical treatments are based on the fact that the one-body density can be used as a fundamental variable in quantum mechanics, as proved by the Hohenberg-Khon and Runge-Gross theorems. Unfortunately, these theorems do not provide any recipe for the calculation of the density.

2.2.1 Density Functional Theory (DFT)

The Density Functional Theory is based on the Hohenberg-Khon theorem[9]. In some sense it shows that all the information of the system is contained in the one-body density. From the Schrödinger equation it is clear that, given a potential energy operator, the wave function (and so the density) are completely determined for a non-degenerate ground state. In this theorem it is proved that this map between these three physical objects is invertible. Hence, as a corollary, any observable of the system can be written as a functional of the density, at least in a formal sense. In particular, the most important observable is the energy, i.e., we can write $E[\rho]$[i]. However, this theorem does not provide a recipe for the exact form of this functional energy of the density. For the superfluid liquid helium many phenomenological energy functionals have been proposed and a brief report of them will be presented in section 2.3.

Given a particular energy density functional, the DFT approach works as follows. In order to obtain the one-body density of the ground state of the system one has to find the density function that minimizes the energy value. If any constrain is present, it must be introduced using the Lagrange multipliers method. For the investigations of the present thesis the number of helium atoms (N) forming the droplet must be constant[ii]. Thus, the well-known Euler-Lagrange equation reads as:

$$\frac{\delta(E[\rho] - \mu_{He}N)}{\delta\rho(\boldsymbol{r})} = 0 \tag{2.1}$$

Up to now, the μ_{He} term is simply a Lagrange multiplier, but in the following discussion it will be shown that it corresponds to the chemical potential of liquid helium.

[i] In the present section, since all variables concern liquid helium, we will omit the specification of this fact. So that, $\rho(\boldsymbol{r})$ stands for $\rho_{He}(\boldsymbol{R}_{He})$.

[ii] For the case of the static calculations, which corresponds to the situation considered in this section (DFT). In the dynamic simulations (TDDFT context) helium atoms can be evaporated from the droplet.

The number of particles can also be taken as a functional of the density $\left(N = \int d\boldsymbol{r}\, \rho(\boldsymbol{r})\right)$. Thus, its functional derivative[iii] is $\frac{\delta N}{\delta \rho(\boldsymbol{r})} = 1$ and therefore from the Eq. 2.1 we obtain $\frac{\delta E[\rho]}{\delta \rho(\boldsymbol{r})} = \mu_{He}$. Now we can determine the expression of the chemical potential and prove that this coincides with the Lagrange multiplier μ_{He}. The chemical potential is defined as the partial derivative of the energy respects the particle number. So that, during the following discussion the variations of the energy and density will only be due to the change of the number of particles, i.e., the external potential is kept fixed. The previously mentioned identification is straightforward calculating the chemical potential from its definition:

$$\begin{aligned} \frac{\partial E}{\partial N} &= \lim_{\epsilon \to 0} \frac{E[N+\epsilon] - E[N]}{\epsilon} = \lim_{\epsilon \to 0} \frac{\delta E}{\epsilon} = \lim_{\epsilon \to 0} \frac{1}{\epsilon} \int d\boldsymbol{r} \frac{\delta E[\rho]}{\delta \rho(\boldsymbol{r})} \delta \rho(\boldsymbol{r}) \\ &= \lim_{\epsilon \to 0} \frac{1}{\epsilon} \mu_{He} \int d\boldsymbol{r} (\rho_{N+\epsilon}(\boldsymbol{r}) - \rho_N(\boldsymbol{r})) = \lim_{\epsilon \to 0} \frac{\epsilon}{\epsilon} \mu_{He} = \mu_{He} \end{aligned} \tag{2.2}$$

All the energy functionals for liquid helium have the following general form in which the first term accounts for the kinetic energy and the second includes the potential and correlation energies:

$$E[\rho_{He}] = \frac{\hbar^2}{2m_{He}} \int d\boldsymbol{r} \left(\boldsymbol{\nabla}\sqrt{\rho}\right)^2 + \int d\boldsymbol{r}\ \mathcal{E}_c[\rho] \tag{2.3}$$

From the functional derivative of the energy one obtains the Schrödinger-like equation, whose solution gives the ground state one-body density.

$$\left[-\frac{\hbar^2}{2m_{He}} \boldsymbol{\nabla^2} + \int d\boldsymbol{r} \frac{\delta \mathcal{E}_c}{\delta \rho(\boldsymbol{r})}\right] \sqrt{\rho(\boldsymbol{r})} = \mu_{He} \sqrt{\rho(\boldsymbol{r})} \tag{2.4}$$

The second term of the bracket acts as an effective potential and depends on the density functional selected for the study. The higher quality of the functional (more physics contained in it) the more accurate will be the solution, i.e., the one-body density.

[iii] Given a functional $F[\rho] = \int d\boldsymbol{r}\, f(\boldsymbol{r}, \rho(\boldsymbol{r}), \boldsymbol{\nabla}\rho(\boldsymbol{r}))$ its functional derivative reads as:

$$\frac{\delta F[\rho]}{\delta \rho(\boldsymbol{r})} = \frac{\partial f}{\partial \rho} - \boldsymbol{\nabla} \frac{\partial f}{\partial \boldsymbol{\nabla}\rho}$$

2.2.2 Time Dependent Density Functional Theory (TDDFT)

The time dependent density functional theory (TDDFT) is supported by the Runge-Gross theorem[10]. In their seminal paper it is showed the existence of an invertible map between the one-body density at any time $\rho(\boldsymbol{r},t)$ and the time-dependent external potential $V_{ext}(\boldsymbol{r},t)$, provided the latter can be expanded in Taylor series around a given time[iv].

Runge and Gross reported three different schemes with their corresponding equations, whose solutions is the density: a set of hidrodynamical equations, a stationary action principle and an effective single-particle Schrödinger-like equation. That is, three different ways to provide methods of determining the density. The operational procedure for the study of the real time dynamics of liquid helium is generally introduced by means of an action principle. Thus, firstly, let us introduce the action integral or Dirac action by:

$$\mathcal{A}[\phi] = \int dt \left\langle \phi(t) \middle| i\hbar \frac{\partial}{\partial t} - \widehat{H}(t) \middle| \phi(t) \right\rangle \tag{2.5}$$

In this equation $|\phi(t)\rangle$ stands for the quantum many-body ket vector and $\widehat{H}(t)$ is (in general) the time-dependent Hamiltonian of the system. This action allows the formulation of Quantum Mechanics in terms of a least action principle, since its minimization $\delta\mathcal{A}[\phi] = 0$ leads to the Schrödinger equation. Introducing in the first term of the Eq. 2.5 the resolution of the identity in the position basis set, i.e., $\int d\boldsymbol{R}|\boldsymbol{R}\rangle\langle\boldsymbol{R}|$, where $\boldsymbol{R}$ represents the coordinates of all the particles of the system, i.e., $\boldsymbol{R} = \{\boldsymbol{r}_1 \cdots \boldsymbol{r}_N\}$, and identifying the energy expected value by $\langle E\rangle[t]$, one obtains:

$$\begin{aligned} \mathcal{A}[\phi] &= \int dt \left\{ \left\langle \phi(t) \middle| \int d\boldsymbol{R}|\boldsymbol{R}\rangle\langle\boldsymbol{R}|\, i\hbar \frac{\partial}{\partial t} \middle| \phi(t) \right\rangle - \left\langle \phi(t) \middle| \widehat{H}(t) \middle| \phi(t) \right\rangle \right\} \\ &= \int dt \left\{ \int d\boldsymbol{R}\, \phi^*(\boldsymbol{R},t) i\hbar \frac{\partial}{\partial t} \phi(\boldsymbol{R},t) - \left\langle \phi(t) \middle| \widehat{H}(t) \middle| \phi(t) \right\rangle \right\} = \\ &= \left\{ \int dt \int d\boldsymbol{R}\, \phi^*(\boldsymbol{R},t) i\hbar \frac{\partial}{\partial t} \phi(\boldsymbol{R},t) - \langle E\rangle[t] \right\} \end{aligned} \tag{2.6}$$

The third theorem of that seminal paper asserts the possibility of formally writing the action integral defined by Eq. 2.5 as a density functional $\mathcal{A} = \mathcal{A}[\rho(\boldsymbol{r},t)]$. However, in the

[iv] Nevertheless, it is important noting that the density formally determines the external potential just up to an additive function of time. This, in turn, fixes the wave function excepting a complex phase. Mathematically, if the wave function obtained from the exact density functional is $\tilde{\phi}[\rho(t)]$, then the wave function solution of the Schrödinger equation is related to this by $\phi(t) = \tilde{\phi}[\rho(t)]e^{-i\alpha(t)}$, where $\alpha(t)$ is an arbitrary time-dependent function.

context of the TDDFT method applied to the study of liquid helium this action is not written in terms of the density but of an effective complex wave function $\Psi(\boldsymbol{r},t)$, which is assumed to be related with the one-body density by the following relation:

$$|\Psi(\boldsymbol{r},t)|^2 \equiv \rho(\boldsymbol{r},t) \tag{2.7}$$

The postulated action is inspired in the last row of Eq. 2.6, replacing the mean value of the energy by the corresponding phenomenological energy functional, $E[\Psi(\boldsymbol{r},t)]$, and the wave function by the effective complex wave function. This has the following the typical form:

$$\mathcal{A}[\Psi(\boldsymbol{r},t)] = \int dt \left\{ \Psi^*(\boldsymbol{r},t) i\hbar \frac{\partial}{\partial t} \Psi(\boldsymbol{r},t) - E[\Psi(\boldsymbol{r},t)] \right\} \tag{2.8}$$

Then, the equation of motion for $\Psi(\boldsymbol{r},t)$ is obtained by minimization of this action, and the resulting to the time dependent Schrödinger-like equation is the analogous equation of Eq. 2.4:

$$i\hbar \frac{\partial}{\partial t} \Psi(\boldsymbol{r},t) = \left[-\frac{\hbar^2}{2m_{He}} \boldsymbol{\nabla^2} + \int d\boldsymbol{r} \frac{\delta \mathcal{E}_c}{\delta \Psi^*} \right] \Psi(\boldsymbol{r},t) \tag{2.9}$$

During the last discussion the functional has been expressed in terms of $\Psi(\boldsymbol{r},t)$, which is not the "recipe" given by the theorem, but is equivalent to the energy functionals of the density, provided by Eq. 2.7. However, the first term of the action integral is not equivalent, and so, it does not generate an action functional of the density, because of the time dependence of this effective wave function. To shed more light on this fact, the following discussion, which is related to the fourth theorem presented by Runge and Gross, provides a reasonable interpretation of all of this. This theorem reads as follow:

The exact time-dependent density of the system can be computed from:

$$\rho(\boldsymbol{r},t) = \sum_j \varphi_j^*(\boldsymbol{r},t) \varphi_j(\boldsymbol{r},t) \tag{2.10}$$

where the single-particle orbitals $\varphi(\boldsymbol{r},t)$ *fulfill the time-dependent Schrödinger equation*

$$i\hbar \frac{\partial}{\partial t} \varphi_j(\boldsymbol{r},t) = \left[-\frac{\hbar^2}{2m} \boldsymbol{\nabla^2} + V_{eff}[\boldsymbol{r},t;\rho(\boldsymbol{r},t)] \right] \varphi_j(\boldsymbol{r},t) \tag{2.11}$$

with an effective one-particle potential given by

$$V_{eff}[\boldsymbol{r},t;\rho(\boldsymbol{r},t)] = V_{ext}(\boldsymbol{r},t) + \int d\boldsymbol{r}'\,\rho(\boldsymbol{r}',t)V_{int}(\boldsymbol{r},\boldsymbol{r}') + \frac{\delta\mathcal{E}_c}{\delta\rho}(\boldsymbol{r},t) \tag{2.12}$$

Hence, provided that the density has the desired mathematical behavior (v-representable), this scheme resembles the Khon-Sham approach for the time independent problem and, for liquid helium the density must account for the bosonic nature of the constituents.

When the time-independent situation is considered[v], the system is in its ground state (zero-temperature approach) and this corresponds to the situation in which all the particles occupy the lowest energy single-particle wave function ($\varphi_0(\boldsymbol{r},t)$). Thus, in this context the density takes the form:

$$\rho(\boldsymbol{r},t=0) = N|\varphi_0(\boldsymbol{r},t=0)|^2 \tag{2.13}$$

So that, this single-particle function is essentially the same as the complex effective wave function at the initial time, with the exception of a global phase (which plays no role) and the $\frac{1}{\sqrt{N}}$ factor. Then, we can identify:

$$\Psi(\boldsymbol{r},t=0) = \frac{1}{\sqrt{N}}\varphi_0(\boldsymbol{r},t=0)e^{i\theta} \tag{2.14}$$

In this way, the equivalence at the initial time has been shown. When considering the dynamics, from inspection of Eq. 2.9 and Eq. 2.11 the correspondence can be inferred, since both wave functions (the macroscopic effective and the single-particle ones) evolve following the same equation[vi]. Thus, we have a temporal evolution under an effective potential that depends on the one-body density. For liquid helium the form of this potential comes from a phenomenological energy functional, which has some external parameters fitted in order to reproduce some experimental properties of helium.

[v] In the problems investigated in the present thesis this corresponds to the initial time situations, in which the droplet is assumed to be in its ground state. Then, when different physical objects or situations are included, the Hamiltonian changes, and so the time dependent dynamics begins.

[vi] In the context of this thesis, the external time dependent potential $V_{ext}(\boldsymbol{r},t)$ comes from the presence of an impurity. This is the only difference between the Eqs. 2.9 and 2.11 and arises because the former was written for pure helium, i.e., without the presence of impurities.

This is the common way to apply DFT in a Bose system. The representation of the whole system making use of only one effective wave function, of course, would have nonsense for a system of fermions, where the Pauli principle limits to only two particles the population of each orbital (for spin ½). Therefore, this approach can be somehow understood in terms of having a full condensate. As mentioned in the introduction this is not really the case for liquid helium, where only about 10% in bulk is in the condensate fraction. Nevertheless, despite this approximation, there is compensation due to the accuracy in the election of the functionals, which incorporates the physics of the system in a satisfactory way.

2.3 Density Functionals for liquid ^{4}He

Here, a brief review of the historical evolution of the energy functionals for the liquid Helium-II is presented for the sake of completeness. It is important to keep in mind that this is a phenomenological approach. The experimental properties of bulk He are taken as input in order to build up the functional, and then this is extended to deal with non-uniform systems[5,11] (films, droplets, etc…). Another important fact is that ^{4}He droplets are at a temperature of 0.37 K, which is really close to zero. This makes very plausible to study ^{4}He droplets using a zero-temperature DFT (ground state), although some finite-temperature functionals have been also developed in the literature[12]. Properties at finite temperatures near zero Kelvin are well described, as a first approximation, in terms of low energy excited states of non-interacting quasi-particles.

The general expression for the energy functional of liquid helium can be expressed as:

$$E[\rho_{He}] = \frac{\hbar^2}{2m_{He}} \int d\boldsymbol{r} \left(\boldsymbol{\nabla}\sqrt{\rho}\right)^2 + \int d\boldsymbol{r}\ \mathcal{E}_c[\rho] \qquad (2.15)$$

The first term corresponds to the kinetic energy functional for a non-interaction system of bosons at zero temperature and it is referred sometimes as "quantum pressure"[13]. The $\mathcal{E}_c[\rho]$ term stands for the potential and exchange-correlation energy density.

The different functionals proposed share this kinetic term, so that they only differ in the form of the second term, which is the one that contains the physics of this strongly correlated liquid system. The first DFT approach to the study of liquid helium was made by Stringari and Treiner at 1987[13], who adapted a Skyrme-like functional coming from nuclear

physics to the present system. This consists in a zero-range functional, since the energy density only depends on the local density, and the exchange-correlation term is given by:

$$\mathcal{E}_c[\rho] = \frac{1}{2} b\rho^2(\boldsymbol{r}) + \frac{1}{2} c\rho^{2+\gamma}(\boldsymbol{r}) + d|\nabla\rho(\boldsymbol{r})|^2 \tag{2.16}$$

The parameter b accounts for the attractive atomic interaction (b <0) since weights the quadratic term. The c is involved in the repulsion at short distances (c >0) because has importance when densities are high (the particle densityρ is always less than one (in $Å^{-3}$)). Finally, d represents the repulsion energy due tot the interphase liquid-vapor, since this is only important in regions where the density changes in a substantial way.

More accurate energy functionals are the so-called finite-range functionals. These functions accounts for the atom-atom interaction in a better way, which consist in van der Waals interactions. Thus, the corresponding asymptotic behavior r^{-6} is introduced by a Lennard-Jones potential, while for the short range of atom-atom distances the strong repulsion is screened in a different ways, depending on the functional.

The first non-local energy density functional was proposed by Dupont-Roc et al. in 1990 and it is called Orsay-Paris (OP) functional[14]. The quadratic term in the density of Eq. 2.16 is replaced by a two-body potential energy, containing a Lennard-Jones interaction (the definition of $V_l(|\boldsymbol{r}-\boldsymbol{r}'|)$, depending on the functional and is given in Eq. 2.1).

$$V_l(r) = \begin{cases} 4\epsilon\left[\left(\frac{\sigma}{r}\right)^{12} - \left(\frac{\sigma}{r}\right)^{6}\right] & r \geq h_0 \\ \begin{cases} V_0 r^4 & Orsay-Paris \\ 0 & Orsay-Trento \end{cases} & r \leq h_o \end{cases} \tag{2.17}$$

with the values of ϵ = 10.22 K, σ = 2.556 Å and h_0 depending on the functional. Another important feature is that the term with the power of γ is not the local density but the coarse-grained density ($\bar{\rho}_{\boldsymbol{r}}$), which the density averaged on a sphere of the atomic size. This is defined by:

$$\bar{\rho}_{\boldsymbol{r}} \equiv \int d\boldsymbol{r}'\, \Pi_{h_l}(|\boldsymbol{r}-\boldsymbol{r}'|)\rho(\boldsymbol{r}') \qquad \Pi_{h_l} \equiv \begin{cases} \frac{3}{4\pi h_l^3} & |r| \leq h_l \\ 0 & |r| > h_l \end{cases} \tag{2.18}$$

Thus, the potential plus exchange-correlation energy density of the OP functional has the following form:

$$\mathcal{E}_c[\rho] = \frac{1}{2}\rho(\boldsymbol{r}) \int d\boldsymbol{r}' V_l(|\boldsymbol{r}-\boldsymbol{r}'|)\rho(\boldsymbol{r}') + \frac{c}{2}\rho^2(\boldsymbol{r})\bar{\rho}_{\boldsymbol{r}}(\boldsymbol{r})^{\gamma} \tag{2.19}$$

The most widely used energy functional for the study of liquid helium was proposed in 1995 by Dalfovo et al. and is called Orsay-Trento (OT)[15]. The main difference with respect to the OP functional is the addition of two new terms to better account for the properties at the atomic scale. The first one is a non-local term, depending on the gradients of the density, which helps to obtain a better description of the static response function in a wide range of wave vectors and its pressure dependence. The second one vanishes for the ground state calculations and it will be considered afterwards. According to this functional the effective potential and the potential and exchange-correlation energy density are given by:

$$\begin{aligned}\mathcal{E}_c[\rho] = \frac{1}{2}\,\rho(\boldsymbol{r}) \int d\boldsymbol{r}'\, V_l(|\boldsymbol{r}-\boldsymbol{r}'|)\rho(\boldsymbol{r}') + \frac{c_2}{2}\rho(\boldsymbol{r})(\bar{\rho}_{\boldsymbol{r}})^{\mathbf{2}} + \frac{c_3}{3}\rho(\boldsymbol{r})(\bar{\rho}_{\boldsymbol{r}}(\boldsymbol{r}))^{\mathbf{3}} \\ -\frac{1}{4m_{He}}\alpha_s \int d\boldsymbol{r}'\, F(|\boldsymbol{r}-\boldsymbol{r}'|)\left(1-\frac{\ddot{\rho}(\boldsymbol{r})}{\rho_{os}}\right)\boldsymbol{\nabla}\rho(\boldsymbol{r})\boldsymbol{\nabla}\rho(\boldsymbol{r}')\left(1-\frac{\ddot{\rho}(\boldsymbol{r}')}{\rho_{os}}\right)\end{aligned} \tag{2.20}$$

where another coarse-grained density (exponential weighted) is defined by:

$$\begin{aligned}\ddot{\rho}(\boldsymbol{r}) &= \int d\boldsymbol{r}'\, F(|\boldsymbol{r}-\boldsymbol{r}'|)\rho(\boldsymbol{r}') \\ F(r) &= \frac{l^3}{\pi^{\frac{3}{2}}} exp\left(-\frac{r^2}{l^2}\right)\end{aligned} \tag{2.21}$$

The values of the parameters are obtained from a fitting procedure addressed to reproduce some measured properties of liquid helium (bulk). Although there are a few parameters labelled with the same letter their value is not the same for all the functionals. Since the energy density functional used through the present thesis is the OT, here we just give the values for its corresponding parameters. Some parameters are determined from the fitting of some properties of the bulk liquid helium such as the compressibility, the energy per atom and the saturation density ($c_2 = -2.41186 \cdot 10^4\ K\ \text{Å}^6$ and $c_3 = 1.85850 \cdot 10^6\ K\ \text{Å}^9$). The two terms where the coarse-grained density $\bar{\rho}_{\boldsymbol{r}}$ enters are chosen to account for the short-range correlations (atomic scale). The parameters $l = 1\ \text{Å}$, $\alpha_s = 54.31\ \text{Å}^3 K^{-1}$, $\rho_{os} = 0.04\ \text{Å}$, have been selected to reproduce the static response function. The factors $\left(1-\frac{\ddot{\rho}(\boldsymbol{r})}{\rho_{os}}\right)$ are introduced to obtain a pressure dependence of the static response function closed to the one predicted by DMC calculations. This last term in the summation represent a non-local correction to the kinetic energy

The energy density corresponding to the OT density functional described above (Eq. 2.20) lacks the second new term compared with the OP, which helps to properly describe well the phonon-roton part of the excitation curve in bulk. As it has been mentioned above, this term is not present in a calculation of the ground state, and depends on local variations of the velocity field. Citing the authors "the idea is to model the backflow effects, which are important at small wavelengths, by a non-local kinetic energy term"[15]. With the inclusion of this term the accuracy of this DFT approach is rather good.

The introduction of this velocity dependent term requires a slight change of paradigm in the DFT approach, as now the energy is no longer a density functional $E[\rho]$ but also a velocity functional $E[\rho, \boldsymbol{v}]$. This functional is immersed in the typical DFT approach used for liquid helium described above, in which the dynamical physical object is the effective complex wave function $\Psi(\boldsymbol{r}, t)$. This can be rewritten in terms of two real functions as:

$$\Psi(\boldsymbol{r}, t) \equiv \sqrt{\rho(\boldsymbol{r}, t)} e^{\frac{i}{\hbar} S(\boldsymbol{r}, t)} \tag{2.22}$$

Then, the velocity field defined in the OT functional is given following the usual prescription, but with a macroscopic and hydrodynamic interpretation by:

$$\boldsymbol{v}(\boldsymbol{r}, t) \equiv \frac{1}{m_{He}} \boldsymbol{\nabla} S(\boldsymbol{r}, t) \tag{2.23}$$

Finally, the new (backflow) term consists in a velocity dependent effective potential, which depends on local variations of the velocity field, as has the following expression:

$$E_{Backflow}[\rho, \boldsymbol{v}] = -\frac{m_{He}}{4} \int d\boldsymbol{r} \int d\boldsymbol{r}' \, V_j(|\boldsymbol{r} - \boldsymbol{r}'|) \rho(\boldsymbol{r}) \rho(\boldsymbol{r}') \big(\boldsymbol{v}(\boldsymbol{r}) - \boldsymbol{v}(\boldsymbol{r}')\big)^2 \tag{2.24}$$

With the inclusion of this term the Orsay-Trento energy density functional is fully described. In the studies carried out in the present thesis, however, not all the terms of the OT functional have been included in the calculations for computational reasons. Thus, the terms depending on the density gradients and the velocity require a huge computational effort compared with the gain achieved in the accuracy of the liquid description. Moreover, since the main objective of this thesis is to "catch the essential of the physics" involved in the dynamical process studied, we consider that this is a good scientific strategy. On the other hand, it is not clear to what extent this (full) functional can be used in practice for real time dynamics of processes involving the presence of impurities, because it implies the generation

of high oscillations in the helium density which, in turns, complicates even more the computational cost[vii].

[vii] This situation demands very dense spatial Cartesian grids. Additional comments of this fact will be given in the following chapters.

2.4 References

[1] Allen, J. F.; Misener, A. D. *Nature*, **1938**, 141, 75.

[2] Kapitza, P. *Nature*, **1938**, 141, 74.

[3] Donnelly, R. *Physics Today*, **July 1995**.

[4] Tilley, D. R.; Tilley, J. *Superfluidity and Superconductivity*. Institute of Physics Publishing, **1974**.

[5] Krotscheck, E.; Navarro, J. *Microscopic Approaches to Quantum Liquids in Confined Geometries. Series on Advances in Quantum Many-Body Theory-Vol.4*, Ed. World Scientific, **2002**.

[6] Ceperley, D.M.; Kalos, M. H. *Monte Carlo Methods in Statistical Physics*, Ed. Springer, **1979**.

[7] Ceperley, D. M.; Alder, B. *Science*, **1986**, 231, 555.

[8] Navarro, J. *Density Functional Theory of Liquid Helium*. Lectures given at the Jyväskylä Summer School, Finland, **August 2003**.

[9] Hohenberg, P.; Khon, W. *Phys Rev. B*, **1964**, 136, 864.

[10] Runge, E.; Gross, E. K. U. *Phys. Rev. Lett*., **1984**, 52, 997.

[11] Barranco, M.; Guardiola, R.; Hernández, S.; Mayol, R.; Navarro, J.; Pi, M. *J. Low. Temp. Phys.*, **2006**, 142, 1.

[12] Biben, T.; Frenkel, D. *J. Phys. Condens. Matter*, **2002**, 14, 9077.

[13] Stringari, S.; Treiner, J. *Phys Rev. B*., **1987**, 36, 8369.

[14] Dupont-Roc, J.; Himbert, M.; Pabloff, N.; Treiner, J. *J. Low Temp. Phys.,* **1990**, 81, 31.

[15] Dalfovo, F.; Lastri, A.; Pricaupenko, L.; Stringari, S.; Treiner, J. *Phys. Rev. B*, **1995**, *52*, 1193.

3. Theoretical approach to the structure, energy and electronic spectroscopy of O@(^{4}He)$_N$ doped nanodroplets

3.1 Introduction

In the last two decades the study of helium nanodroplets, (^{4}He)$_N$, has become an important field of research, due to their fundamental physico-chemical properties and to the applications that they provide, such as acting as an excellent matrix, where high resolution spectroscopy[1] and chemical reactions can be investigated[2,3]. Moreover, superfluid helium droplets have been used recently in the synthesis of clusters, nanoparticles and nanowires[4,5,6].

A theoretical study on ultracold helium nanodroplets doped with atomic oxygen has been conducted in the present work. We studied the solvation of this impurity in both the electronic ground state, O(^{3}P), and the first two electronic excited states, O(^{1}D) and O(^{1}S). In addition of the chemical relevance of this atom in different electronic states, this study also corresponds to the first required stage toward the theoretical investigation of helium nanodroplets doped with an O_2 molecule, if we are interested, e.g., in fragmentation processes induced by photodissociation.

In this context, the knowledge of the diatomic OHe excited states plays a fundamental role, because the electronic ground state of the oxygen atom is not the only one involved in O_2 photodissociation. We have also studied the spectroscopy of the O(^{1}D$\leftarrow{}^1$S) electronic transition (emission) in the (^{4}He)$_N$ matrix considering different nanodroplet sizes, since this provides data that could be compared with the experiments.

The chapter is structured as follows: in Section 3.2 we describe the theoretical methods used to investigate the OHe excited states potential energy curves, the OHe

anisotropic potentials, the O@^4He_N nanodroplet calculations, and the O(^{1}D←^{1}S) spectroscopy. The main results of the different type of calculations are shown in Section 3.3, and the summary and conclusions are given in Section 3.4.

3.2 Theoretical methods

3.2.1 *Ab initio* calculations and fitting of the O-He potential energy curves

While in the case of the O(^{3}P)-He ground state potential energy curves ($^3\Sigma$ and $^3\Pi$ curves) there are experimental curves available (which were derived from molecular beam experiments results),[7] this is not the case for the O(^{1}D)-He and O(^{1}S)-He excited diatomic potential energy curves ($^1\Sigma$, $^1\Pi$ and $^1\Delta$ curves and $^1\Sigma$ curve, respectively). Due to this, the excited potential energy curves have been calculated here using the correlation consistent polarized valence quintuple-zeta basis set of Dunning[8], augmented with diffuse functions and including bond centered uncontracted functions consisting of *3s* and *3p* (exponents 0.9, 0.3, 0.1), *2d* and *2f* (exponents 0.6, 0.2), and *1g* (exponent 0.3) functions, which are placed in the middle of the van der Waals bond (aug-cc-pV5Z+b basis set).

The *ab initio* electronic structure calculations of the O-He potentials have been performed with the MOLPRO suite of programs[9]. As initial method, a full valence state-averaged complete active space MCSCF (Multi Configurational Self Consistent Field) calculation[10,11] (SA-CASSCF method) has been considered. The molecular orbitals (MOs) correlating with the *2s* and *2p* oxygen atom atomic orbitals have been used to determine the valence space, since this allows to describe in a satisfactory way the ground (^{3}P) and two lowest excited (^{1}D and ^{1}S) electronic states of this atom. All MOs have been optimized maintaining the *1s* oxygen atom orbital doubly occupied. The calculations were performed in the C_{2v} abelian point subgroup of the $C_{\infty v}$ symmetry group. The SA-CASSCF wave function was optimized with respect to nine electronic states in C_{2v} (three $^1A_1$, one $^1B_1$, one $^1B_2$, one $^1A_2$, one $^3B_1$, one $^3B_2$ and one $^3A_2$), which correspond to the $^3\Sigma^-$, $^3\Pi$, $^1\Sigma^+$, $^1\Pi$, $^1\Delta$ and $^1\Sigma^+$ electronic states of O(^{3}P,^{1}D,^{1}S)-He.

Using the SA-CASSCF orbitals previously obtained, internally contracted multi-reference configuration interaction (icMRCI) calculations have been performed,[12,13] taking into account the single and double excitations with respect to all the SA-CASSCF

configurations (reference functions). A total of three $^1A_1$, one $^1B_1$, one $^1B_2$, one $^1A_2$, one $^3B_1$, one $^3B_2$ and one $^3A_2$ electronic states were calculated. With this state selection, the icMRCI calculations involve a number of contracted (uncontracted) configurations of the order of 1.8×10^6 (36.8×10^6) for the $^1A_1$ states, 0.84×10^6 (36.7×10^6) for the $^1B_1$, $^1B_2$, and $^1A_2$ states and 1.0×10^6 (6.4×10^6) for the $^3B_1$, $^3B_2$ and $^3A_2$ states respectively. Furthermore, a multi-reference Davidson correction technique[14] (icMRCI+Q method) was applied to the final energies, in order to approximately account for higher order electronic correlation effects. The basis set superposition error (BSSE) was also taken into account in the calculations.

Table 3.1 shows that there is a good agreement between the icMRCI+Q+BSSE and experimental[15] energies for the ^{3}P, ^{1}D and ^{1}S electronic states of oxygen. Moreover, all the O-He dissociation curves studied upon dissociation lead to the ground electronic state of the helium atom, He(^{1}S), with the first excited states of helium having substantially higher energies.

Table 3.1. Energy levels of the oxygen atom (eV).

Term	Experimental[a]	ic-MRCI	ic-MRCI+Q
^{3}P	0.000	0.000	0.000
^{1}D	1.9673	1.9484	1.9522
^{1}S	4.1896	4.1677	4.1914

[a] Experimental values from Ref. 15. Zero of energy taken in the ground term.

The excited potential energy curves have been fitted to the following analytical expression[16]:

$$V(r) = c_1\frac{1}{r} + \sum_{i=2}^{N} c_i e^{-(i-1)r} r^{i-1} \qquad (3.1)$$

where the parameters selected (N=27) were found using a weighted least squares minimization algorithm. This was done in order to prioritize the quality of the fitting in the well and long-range regions, which are the most important zones in the calculation of the nanodroplet structure.

3.2.2 Calculation of the O(^{1}D,^{1}S)-He(^{1}S) interaction potentials

To determine the structure and other properties of the nanodroplets, we have to take into account that we are dealing with many particle systems. Thus, the exact many body

potential (or potential energy surface (PES)) is computationally unaffordable in practice, due to the high number of particles involved (even though nearly all atoms considered have a small number of electrons). This is the reason why we have employed a pairwise potential approach which, on the other hand, is considered to be a reasonable choice in this context.

However, for atoms with non-zero electronic orbital angular momentum the electronic densities are not isotropic, and this leads to different kinds of overlapping for the electronic densities of the two atoms involved in the bonding (depending on their relative orientation). This fact is reflected in the calculation of the eigenvalues of the O-He system, which are characterized by the projection of the total electronic orbital angular momentum onto the diatomic molecular axis, with its corresponding quantum number Λ arising from the axial symmetry of the system[17] (each diatomic eigenvalue corresponds to one type of interaction).

Hence, when building up the global interaction potential, we have to bear in mind that it is not possible to have the same kind of interaction with all the helium atoms considered. These facts will be revealed in a more clear way after the determination of the anisotropic potential for the interaction between O(^{3}P, ^{1}D) and He(^{1}S).

The potentials are calculated in terms of the eigenvalues of the diatomic system, using a perturbative scheme[18,19]. This procedure is only feasible for systems in which the positions of the matrix atoms are known, as in the case of the study of impurities in crystalline environments. Nevertheless, we have also used here these ideas, which are spread in the literature in the context of electronic spectroscopy calculations in clusters,[20,21,22,23,24,25] in order to estimate the anisotropic potentials.

For the calculation of the nanodroplets it is not possible to follow exactly this procedure, because this interaction is what actually determines their structure. On the other hand, in the spectroscopic study the evaluation of these potentials has been carried out on the basis of the Franck-Condon principle. Thus, the positions of the helium atoms do not change during the ^{1}D$\leftarrow{}^1$S electronic transition of the oxygen, i.e., they are already known. The main aspects of this procedure are exposed in Section 3.2.3.

We consider an oxygen atom perturbed by the presence of a helium atom. In the case of many helium atoms it is straightforward to extend this theoretical approach considering a pairwise potential approximation. Concretely, we define our system in terms of the oxygen atom valence electronic degrees of freedom[24], because the inner electrons are not expected to

be influenced by the perturbation in a significant way. We define the degenerate basis set of the unperturbed system as $|lm_l\rangle$[26], where $l = 2$ and $m_l = 0, \pm1, \pm2$. The perturbation of the system arises from the $V_{He-O}(\boldsymbol{R}_{He}, \boldsymbol{r}_O)$ potential, where $\boldsymbol{R}_{He}$ refers to the coordinate of the helium atom and $\boldsymbol{r}_O$ refers to the coordinates of the oxygen valence electronic degrees of freedom.

In the context of the perturbation theory for degenerate states, the first order eigenvalues are found diagonalizing the interaction matrix, whose elements are given by:

$$\langle lm_i | V_{He-O} | lm_j \rangle \tag{3.2}$$

Now, a Legendre polynomials expansion of the potential allows us to separate the radial and angular dependences:

$$V_{He-O}(\boldsymbol{R}_{He}, \boldsymbol{r}_O) = \sum_{\mu=0}^{\infty} V_\mu(R_{He}) P_\mu(\boldsymbol{R}_{He} \cdot \boldsymbol{r}_O) \tag{3.3}$$

For the sake of simplicity the reference frame origin has been taken in the oxygen nucleus. This is the reason why the coefficients in this expansion only depend on the modulus of the $\boldsymbol{R}_{He}$ vector. Moreover, the addition theorem allows us to express each Legendre polynomial as a product of spherical harmonics.

$$P_\mu(\boldsymbol{r}_O \cdot \boldsymbol{R}_{He}) = \frac{4\pi}{2\mu + 1} \sum_{m_\mu=-\mu}^{\mu} Y^*_{\mu m_\mu}(\theta_{He}, \varphi_{He}) Y_{\mu m_\mu}(\theta_O, \varphi_O) \tag{3.4}$$

Considering Eq. 3.3 and Eq. 3.4 together and substituting the resulting expression for $V_{He\text{-}O}$ in Eq. 3.2 we obtain:

$$\langle lm_i | V_{He-O} | lm_j \rangle$$

$$= \langle lm_i | \sum_{\mu=0}^{\infty} V_\mu(R_{He}) \frac{4\pi}{2\mu + 1} \sum_{m_\mu=-\mu}^{\mu} Y^*_{\mu m_\mu}(\theta_{He}, \varphi_{He}) Y_{\mu m_\mu}(\theta_O, \varphi_O) | lm_j \rangle$$

$$= \sum_{\mu=0}^{\infty} \frac{4\pi}{2\mu + 1} V_\mu(R_{He}) Y^*_{\mu m_\mu}(\theta_{He}, \varphi_{He}) \sum_{m_\mu=-\mu}^{\mu} \langle lm_i | \mu m_\mu | lm_j \rangle \tag{3.5}$$

For the P state (l=1) the summation over μ is nonzero only for 0 and 2, while for the D state (l=2) this occurs for 0, 2 and 4, due to the properties of the spherical harmonics.

To get the anisotropic potentials, we arbitrarily select one of the m degenerated levels and evaluate the expectation value of the perturbation energy for this orbital. The selected value will only affect the orientation of the axis (the $m = 0$ orbital was selected here).

In order to describe these interactions in terms of the O-He diatomic potentials previously calculated using *ab initio* methods (i.e., the $V_\Lambda(r)$ terms), well-known relationships between them and the radial potentials $V_\mu(r)$ are used[27]:

P state: $$V_0 = \frac{1}{3}(V_\Sigma + 2V_\Pi) \quad , \qquad V_2 = \frac{5}{3}(V_\Sigma - 2V_\Pi)$$

D state: $$V_0 = \frac{1}{5}(V_\Sigma + 2V_\Pi + 2V_\Delta) \ , \quad V_2 = (V_\Sigma + V_\Pi - 2V_\Delta)$$

$$V_4 = \frac{9}{5}(V_\Sigma - V_\Pi) + \frac{3}{5}(V_\Delta - V_\Pi) \tag{3.6}$$

Then, finally we arrive to the following expressions for the anisotropic potentials:

$$\langle 10|V_{He-O}|10\rangle \equiv V_{He-O(\,^3P)} = V_\Sigma cos^2\theta + V_\Pi sin^2\theta$$

$$\langle 20|V_{He-O}|20\rangle \equiv V_{He-O(\,^1D)}$$

$$= \frac{1}{4}(3V_\Delta + V_\Sigma - 6(V_\Delta - 2V_\Pi + V_\Sigma)cos^2\theta + 3(V_\Delta - 4V_\Pi + 3V_\Sigma)cos^4\theta) \tag{3.7}$$

3.2.3 Structure and energy of O@(^{4}He)$_N$ doped nanodroplets

Helium nanodroplets doped with oxygen, either in the ground state (^{3}P) or in the first two excited states (^{1}D and ^{1}S), have been calculated within the framework of the Density Functional Theory (DFT). This kind of methodology allows us to deal with nanodroplets from few hundreds up to thousands of atoms, with a good compromise between accuracy and computational cost. The phenomenological functional used here is the Orsay-Trento (OT)[28] one with some modifications[29]. The details of these type of calculations are described elsewhere[30] and here we only review its main features.

Due to the He/O mass ratio, we have treated the impurity as an external potential placed at the origin of the coordinate system. The energy of the system has the following expression:

$$E[\rho] = \frac{\hbar^2}{2m_{He}} \int d\boldsymbol{R}_{He} \left(\boldsymbol{\nabla}\sqrt{\rho}\right)^2 + \int d\boldsymbol{R}_{He}\ \mathcal{E}_c[\rho] + \int d\boldsymbol{R}_{He}\, V_{He-O}(\boldsymbol{R}_{He})\, \rho(\boldsymbol{R}_{He}) \qquad (3.8)$$

Where $\rho(\boldsymbol{R}_{He})$ is the ^{4}He density and $\mathcal{E}_c[\rho]$ is the energy density of the liquid helium, which takes into account the potential and the strong correlation energies between the helium atoms in the superfluid state. Minimizing the energy with respect to $(\boldsymbol{R}_{He})$, under the restriction of keeping the number of helium atoms constant, we obtain a Schrödinger-like equation that describes this system:

$$\left[-\frac{\hbar^2}{2m_{He}}\boldsymbol{\nabla^2} + V_{O-He}(\boldsymbol{R}_{He}) + V_{He}(\boldsymbol{R}_{He})\right]\sqrt{\rho(\boldsymbol{R}_{He})} = \mu_{He}\sqrt{\rho(\boldsymbol{R}_{He})} \qquad (3.9)$$

where $V_{O-He}(\boldsymbol{R}_{He})$ is the potential energy arising from the interaction between the helium and the impurity and $V_{He}(\boldsymbol{R}_{He})$ is an effective potential that comes out from the functional derivative of the energy density (i.e., $V_{He}(\boldsymbol{R}_{He}) = \frac{\boldsymbol{\delta}\mathcal{E}_c[\rho]}{\boldsymbol{\delta}\rho}$**).**

3.2.4 O(1D←1S) emission spectrum in ^{4}He$_N$

The atomic emission spectrum corresponding to the O(^{1}D←^{1}S) electronic transition in helium nanodroplets has been studied. Here, we have used the semiclassical Franck-Condon principle as described in Ref. 31 with some adaptations[32,33]. The intensity of emission (absorption) in a condensed phase transition between two electronic states S and D[34], with vibro-rotationals levels *m* and *n* respectively is given by:

$$I_{DS}(\omega) \propto Av_n \sum_m \left| \int \Psi^*_{Sm}(\boldsymbol{Q}) M_{DS} \Psi_{Dn}(\boldsymbol{Q}) d\boldsymbol{Q} \right|^2 \delta(E_{Dn} - E_{Sm} - \hbar\omega) \qquad (3.10)$$

where S and D are the labels for the electronic states of high and low energy, and E_{Dn} and E_{Sm} are the vibro-rotational eigenvalues related to the PES of the D and S states, respectively. $\boldsymbol{Q}$ takes into account the nuclear coordinates of all atoms of the system and the term Av_n refers to the thermal average over all starting vibro-rotational states. M_{DS} is the transition dipole momentum, which can be approximated to be independent of the atomic positions. The next approximation consists in the replacement of the vibro-rotational eigenvalues E_{Sm} and

E_{Dn} by the local electronic energies at the turning points (i.e., by the potential of these electronic states $V_S(\boldsymbol{Q})$ and $V_D(\boldsymbol{Q})$, respectively). The justification of this is based on the huge number of degrees of freedom that these condensed media systems have[33]. After these reasonable simplifications equation (10) becomes:

$$I_{DS}(\omega) \propto \int d\boldsymbol{Q}\, |\Psi_D(\boldsymbol{Q})|^2\ \delta(V_D(\boldsymbol{Q}) - V_S(\boldsymbol{Q}) - \hbar\omega) \tag{3.11}$$

The above expression has been evaluated using a DFT atom-like sampling simulation, which is an idea inspired by the work of Nakatsukasa et al[35], which was already applied in the spectroscopy in helium nanodroplets context[32,36]. This is based on the generation of different nanodroplet configurations by sampling the positions of the helium atoms, which are treated as a hard spheres, using the helium density obtained in the DFT calculation as the probability density function. Importance sampling techniques[37] have been used to implement this procedure. The diameter of the hard spheres that represent the helium atoms is not fixed but depends on the density, to take into account the variations in the atomic volume[32]. The correlations between the atomic positions are considered by accepting only those configurations for which there is no overlap between the hard spheres. Thus, the position of an atom is dependent on the position of the others.

To determine the electronic spectrum it is necessary to know the many-body (or global) interaction potentials O(^{1}S,^{1}D)-He(^{1}S)$_N$, which we have called $V_S(\boldsymbol{Q})$ and $V_D(\boldsymbol{Q})$, respectively. The O(^{1}S)-He(^{1}S)$_N$ global potential is simply obtained by considering a pair potential approximation, while the global potential concerning O(^{1}D) is obtained perturbatively following the ideas already mentioned in Section 3.2.2 (summing the contribution of each helium atom (Eq. 3.5) to the global perturbation matrix). Thus, for each configuration of the nanodroplet, the interaction matrix has to be diagonalized to find the contribution of each component to the global spectrum:

$$\langle \psi_i | V_{He-O} | \psi_j \rangle = \sum_{n=1}^{N} \sum_{\mu=0}^{\infty} \frac{4\pi}{2\mu+1} V_\mu(r_n) Y^*_{\mu m_\mu}(\theta_n, \varphi_n) \sum_{m_\mu=-\mu}^{\mu} \langle lm_i | \mu m_\mu | lm_j \rangle \tag{3.12}$$

This matrix is real and symmetric, since the basis functions used are real. This allows us to use the Jacobi's method to carry out the diagonalization.

These matrix elements expressed in Cartesian coordinates can be found in the Appendix. Finally, since the transition to the five components of the D state have the same probability, the global spectrum will be given directly by the sum of all these contributions. This leads to a single transition energy for each nanodroplet configuration. To obtain the spectrum from the large number of nanodroplet configurations explored, we have performed a histogram analysis by dividing the transition energies space into small bins and counting for each bin the number of times we have a configuration with the transition energy placed in the energy interval of the bin. Thus, we have the following equation:

$$I_{DS}(\omega) = \frac{1}{n_c}\sum_{m_l}\sum_{i}^{n_c}\delta\left(V_D^{m_l}\{i\} - V_S\{i\} - \hbar\omega\right) \tag{3.13}$$

3.3 Results and discussion

3.3.1 O@(^{4}He)$_N$ doped nanodroplets

Due to the lack of experimental potential energy curves for the first two excited atomic states (^{1}D and ^{1}S), they have been calculated using the *ab initio* icMRCI method, as described in Section 3.2 (Fig. 3.1). This is a complicated task since it concerns excited states keeping the van der Waals nature of the bond. A total number of 74 points have been calculated for each excited state, with internuclear distances spaced by 0.1 au from to 4.1 au to 10.0 au and by 1.0 au from 10 au to 24 au.

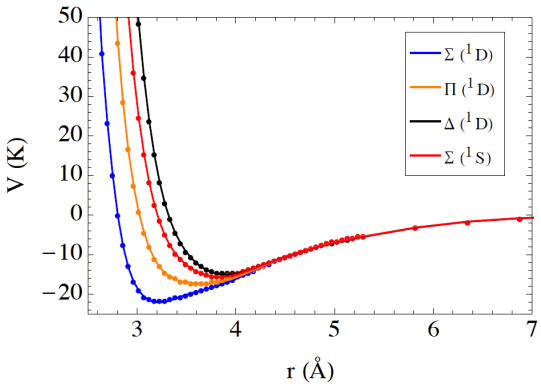

Fig. 3.1. *Ab initio* points obtained for the interaction potentials between O(^{1}D,^{1}S) and He(^{1}S) and fitted curves. Please, note that these potential energy curves have been placed together (same asymptotic dissociation limit) to make more evident the essentially identical long range dependence of the potentials. The three lowest energy curves dissociate into O(^{1}D) + He (blue, orange and red) while the highest energy curve dissociates into O(^{1}S) + He (black). These dissociation products are placed 2.24 eV above the former ones.

The spectroscopic parameters (equilibrium distance and dissociation energy) of the potential energy curves are listed in Table 3.2, including the experimental values for the ground state[7]. The optimal parameters of the fitting, according to the Aguado-Paniagua function (Eq. 3.1), are collected in the Appendix (Table A3.1.). It can be seen that the depth of the well decreases when the projection of the electronic orbital angular momentum quantum number Λ increases from zero to two, while the equilibrium distance increases with Λ.

Table 3.2. Spectroscopic constants of the O(^{3}P, ^{1}D,^{1}S)-He(^{1}S) potential energy curves.[a]

dissociation	state	R_e (Å)	D_e (K)
O(^{3}P)-He(^{1}S)	$^3\Pi$	3.11	34.2
	$^3\Sigma$	3.52	15.1
O(^{1}D)-He(^{1}S)	$^1\Sigma$	3.00	33.9
	$^1\Pi$	3.60	17.4
	$^1\Delta$	3.70	13.9
O(^{1}S)-He(^{1}S)	$^1\Sigma$	3.81	15.5

[a] Those for the electronic ground state of oxygen were obtained from the experiments of ref. 6, while the excited ones were obtained here from the *ab initio* calculations.

In the DFT calculations the position of the impurity was optimized without any kind of restriction and, at the end of the optimization process, it was found that the oxygen atom was always placed in the centre of the nanodroplet. This result is consistent with the model proposed by Ancilotto based on energy balances[38].

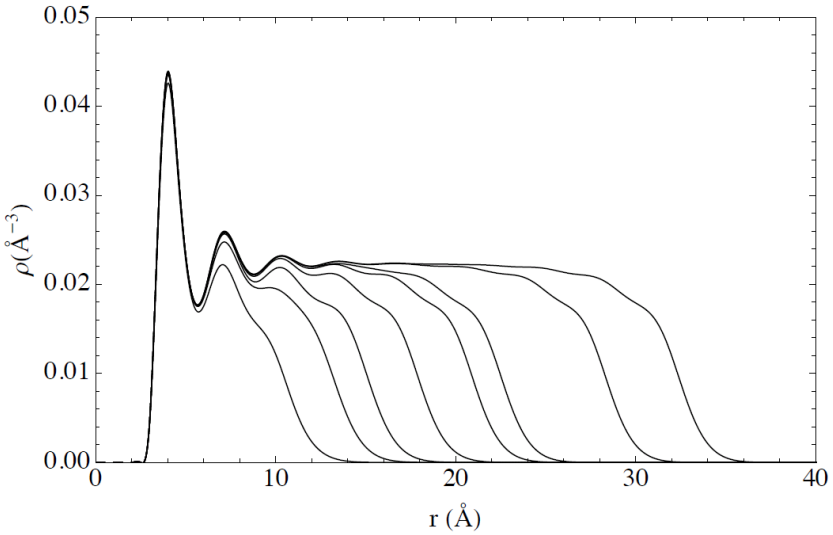

Fig. 3.2. Radial density profiles of the O(^{1}S)@^{4}He$_N$ nanodroplets. The values of N are 100, 200, 300, 500, 800, 1000, 2000 and 3000.

In Fig. 3.2 are shown the radial density profiles of O(^{1}S)@(^{4}He)$_N$ nanodroplets for different values of N, ranging from 100 to 3000. The shape of the solvation profiles are similar, independently of the nanodroplet size, although this tendency cannot be followed until the case of few atoms nanodroplets for obvious reasons. The first solvation layer is located at a distance of ~4 Å from the centre of the nanodroplet and the number of atoms involved in this layer is independent of the nanodroplet size. This is important because it is precisely this helium layer that provides the superfluid environment to the impurity. Moreover, the second solvation layer, which exhibits a lower intensity peak, is located at a distance of ~7 Å. Some other structures (less significant solvation layers) are also observed at larger distances for the nanodroplets of larger sizes.

The xz plane density surfaces of the *N*=100 nanodroplets doped with O(^{3}P) and O(^{1}D) and are represented in Figures 3.3a and 3.3b, respectively. The anisotropy of the potential is manifested, resulting in a non-isotropic helium density near the impurity. For the ^{3}P electronic state doped nanodroplets the first solvation layer has a most dense region in the xy plane, where the potential corresponds to the $^3\Pi$ diatomic potential energy curve. This curve is more attractive than the $^3\Sigma$ one, which mainly acts in the z axis (cf. Eq. 3.7). For the ^{1}D electronic state such an important anisotropy is not observed, due to the resulting combination of the $^1\Delta$, $^1\Pi$ and $^1\Sigma$ diatomic curves (cf. Eq. 3.7).

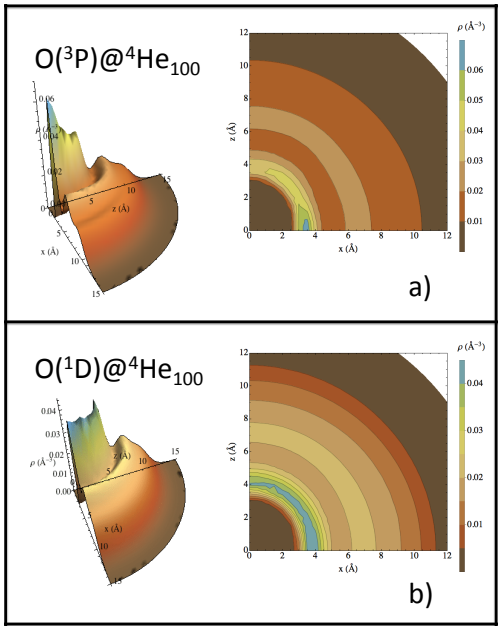

Fig. 3.3. Three-dimensional (left) and two-dimensional (right) representations of the helium density in the xz plane for the helium nanodroplet with N=100 and two electronic states of the oxygen atom: (a) O(^{3}P)@^{4}He$_{100}$; (b) O(^{1}D)@^{4}He$_{100}$.

The O(^{1}D←^{1}S) emission spectrum corresponds to the well known greenline of atomic oxygen,[39] and it has been investigated in many contexts such as, e.g., in the study of the Venus atmosphere [39]. Its importance lies in the metastability of the ^{1}S state, whose de-excitation to the ^{3}P ground state is forbidden by electronic spin, while de-excitation into the ^{1}D excited state is forbidden by electronic orbital angular momentum. In order to obtain a smooth spectrum, we calculated over half a million sampled configurations for each nanodroplet.

In Figure 3.4a the spectra for different nanodroplet sizes are reported. It comes out that the dependence of the spectrum on the nanodroplet size is not very strong, which reflects the fact that only the first solvation layer of helium atoms influences the spectrum in a significant way, as expected. Furthermore, as the number of atoms per nanodroplet increases the spectrum broadens, since the variety of distributions increases. This is valid up to a value of approximately N = 100, from which the spectrum does not change with the size of the nanodroplet, since the distance between the impurity and the outer helium atoms is so large that the interaction is negligible. Another remarkable fact is that the spectra are blue shifted relative to that in the gas phase, which points out that the most intense stabilizing interaction with helium occurs for the ^{1}D state (see Figure 3.1).

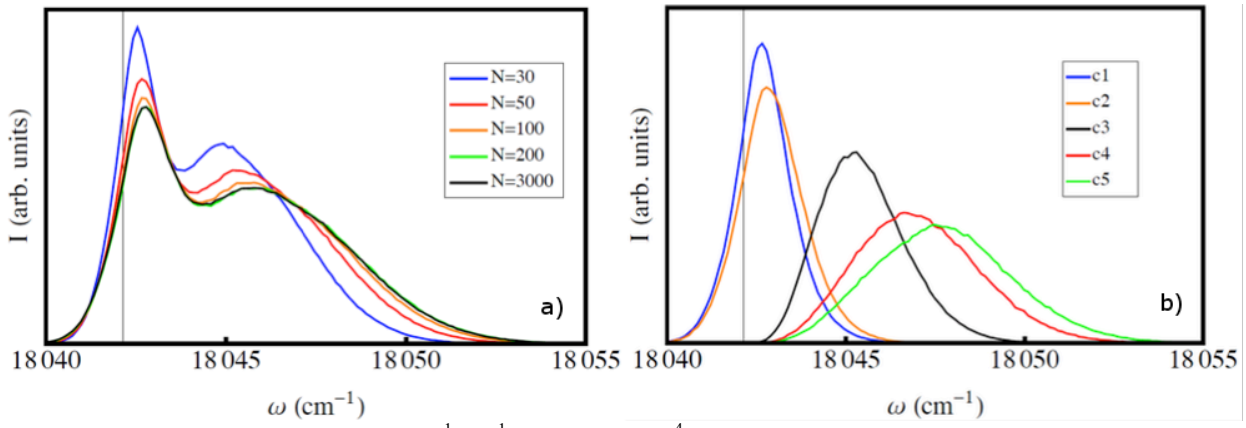

Fig. 3.4. (a) Emission spectra of the O(^{1}D←^{1}S) transition in ^{4}He nanodroplets of different size. The vertical line indicates the transition wavenumber in gas phase. (b) The five components that contribute to the emission spectrum of the O(^{1}D←^{1}S) transition in a ^{4}He$_{100}$ nanodroplet.

The decomposition of the spectrum into the different components corresponding to the five eigenvalues of the interaction matrix (Eq. 3.2) is shown in Figure 3.4b. The breaking of the spherical symmetry caused by the atom sampling induces the splitting of these components. The analysis of the changes occurring in the case of the ^{1}D state while descending the symmetry until the linear arrangement, corresponding to the point group $D_{\infty h}$

and whose eigenstates are already known (i.e., $^1\Sigma$, $^1\Pi$ and $^1\Delta$ states), allows us to interpret the spectrum shape. Obviously, no one of the configurations generated belongs exactly to any particular point group, but it can be close to one of them.

If the configurations were completely isotropic the point group of system would be the K_h one. Starting from this group, the first descend in symmetry corresponds to the O_h octahedral group, followed by T_d tetrahedral group. In these lasts groups the irreducible representation D of the K_h point group splits into the E and F irreducible representations, which are doubly and triply degenerated, respectively. Therefore, the majority of configurations (which may have small deviations from spherical symmetry) will generate grouping schemes of the type "2 + 3", corresponding to the grouping of the components c1 + c2 and c3 + c4 + c5 (see Fig 3.4b). The c3 component is less overlapped with the others two, and this happens due to the splitting of the F components into the Σ and Π (doubly degenerate) ones, when keeping on descending in symmetry.

To conclude the analysis of the spectrum, the frequency shift with respect to the gas phase transition (vertical straight line in Fig. 3.4) has been interpreted. This shift is a manifestation of the different interactions of the oxygen ^{1}D states generated in each configuration with respect to what happens for the O(^{1}S) state. Furthermore, the $^1\Sigma$ and $^1\Pi$ states (arising from O(^{1}D)), which contribute to the c3, c4 and c5 components, have stronger interactions with the helium atom than the $^1\Delta$ state, thus leading to a greater energy blue shift.

3.4 Summary and conclusions

The theoretical study of superfluid helium nanodroplets doped with atomic oxygen has been performed for the ground (^{3}P) and the two first excited states (^{1}D and ^{1}S) of the oxygen atom. To do this, we have used a DFT based treatment of helium, the *ab initio* icMRCI O-He excited potential energy curves derived here, and the experimental ground potential energy curve. There were no very large differences when comparing the properties resulting from these electronic states, which is consistent with the similar polarizabilities of the oxygen atom in these states. The main feature found in these systems, probably, corresponds to the

appearance of anisotropy, due to the open shell nature of the P and D states, which is especially evident for the former case.

The spectroscopic study reflects the well-known behaviour of 4-helium nanodroplets as excellent high resolution spectroscopy matrices, since the frequency shift observed relative to the gas phase is really small. On the other hand, here we have just considered the broadening induced by the helium environment, generating an ensemble with large number of nanodroplet configurations, in order to account for the mobility of helium atoms inside the nanodroplet. We expect this kind of broadening to be the most important one and it has been found to be about 10 cm^{-1}.

The study of these systems corresponds to the first step in the study of the reaction dynamics of simple chemical systems in helium nanodroplets. In this context, the reactions of molecular species containing oxygen atoms are especially interesting, due to their importance in many atmospheric and space processes.

3.5 Appendix

Here we show the expressions of the interaction matrix elements. The basis used corresponds to the real spherical harmonics. These expressions have already been published in the literature, but we have reviewed them here since there are some typographical errors in both the first publication[22] and the subsequent correction[24].

$$V_{11} = V_0 - \frac{1}{7}\left[1 - 3\frac{z^2}{r^2}\right]V_2 + \left[\frac{3}{28} - \frac{15}{14}\frac{z^2}{r^2} + \frac{5}{4}\frac{z^4}{r^4}\right]V_4$$

$$V_{22} = V_0 + \frac{1}{7}\left[1 - 3\frac{z^2}{r^2}\right]V_2 + \left[\frac{1}{56} - \frac{5}{28}\frac{z^2}{r^2} - \frac{5}{24}\frac{(-x^4+6x^2y^2-y^4-z^4)}{r^4}\right]V_4$$

$$V_{33} = V_0 + \frac{1}{7}\left[1 - 3\frac{z^2}{r^2}\right]V_2 + \left[\frac{1}{56} - \frac{5}{28}\frac{z^2}{r^2} + \frac{5}{24}\frac{(-x^4+6x^2y^2-y^4+z^4)}{r^4}\right]V_4$$

$$V_{44} = V_0 - \frac{1}{14}\left[1 + 3\frac{(x^2-y^2-z^2)}{r^2}\right]V_2 - \left[\frac{1}{14} - \frac{5}{42}\frac{(x^2-y^2+6z^2)}{r^2} + \frac{5}{6}\frac{z^2(x^2-y^2+z^2)}{r^4}\right]V_4$$

$$V_{55} = V_0 - \frac{1}{14}\left[1 - 3\frac{(x^2-y^2+z^2)}{r^2}\right]V_2 - \left[\frac{1}{14} + \frac{5}{42}\frac{(x^2-y^2-6z^2)}{r^2} - \frac{5}{6}\frac{z^2(x^2-y^2-z^2)}{r^4}\right]V_4$$

$$V_{12} = \frac{-x^2+y^2}{\sqrt{3}r^2}\left[\frac{3}{7}V_2 + \left(\frac{5}{28} - \frac{5}{4}\frac{z^2}{r^2}\right)V_4\right]$$

$$V_{13} = \frac{xy}{\sqrt{3}r^2}\left[-\frac{6}{7}V_2 - \left(\frac{5}{14} - \frac{5}{2}\frac{z^2}{r^2}\right)V_4\right]$$

$$V_{14} = \frac{yz}{\sqrt{3}r^2}\left[\frac{3}{7}V_2 - \left(\frac{15}{14} - \frac{5}{2}\frac{z^2}{r^2}\right)V_4\right]$$

$$V_{15} = \frac{xz}{\sqrt{3}r^2}\left[\frac{3}{7}V_2 - \left(\frac{15}{14} - \frac{5}{2}\frac{z^2}{r^2}\right)V_4\right]$$

$$V_{23} = \frac{5}{6}\frac{x\,y\,(x^2-y^2)}{r^4}V_4$$

$$V_{24} = \frac{yz}{r^2}\left[-\frac{3}{7}V_2 - \left(\frac{5}{28} - \frac{15x^2-5y^2+5z^2}{12\,r^2}\right)V_4\right]$$

$$V_{25} = \frac{xz}{r^2}\left[\frac{3}{7}V_2 + \left(\frac{5}{28} + \frac{5x^2-15y^2-5z^2}{12\,r^2}\right)V_4\right]$$

$$V_{34} = \frac{xz}{r^2}\left[\frac{3}{7}V_2 + \left(\frac{5}{28} + \frac{-5x^2 + 15y^2 - 5z^2}{12\,r^2}\right)V_4\right]$$

$$V_{35} = \frac{yz}{r^2}\left[\frac{3}{7}V_2 + \left(\frac{5}{28} + \frac{15x^2 - 5y^2 - 5z^2}{12\,r^2}\right)V_4\right]$$

$$V_{45} = \frac{xy}{r^2}\left[\frac{3}{7}V_2 - \left(\frac{5}{21} - \frac{5z^2}{3\,r^2}\right)V_4\right]$$

Table A3.1: Parameters of the fitting (c_i coefficients) for the O(^{1}D, ^{1}S)-He(^{1}S) potential energy curves according to Eq. 3.1. All parameters are in atomic units.

	O(^{1}D)+He(^{1}S)			O(^{1}S)+He(^{1}S)
	$^1\Sigma$	$^1\Pi$	$^1\Delta$	$^1\Sigma$
C_1	1.56573371762050E+01	1.57140416676055E+01	1.61787314213319E+01	1.57188110262194E+01
C_2	-1.75743221952477E-01	-1.76308717586338E-01	-1.81177718941059E-01	-1.76936207553317E-01
C_3	-4.36755987788300E+01	-4.37936993668278E+01	-4.50023541481152E+01	-4.31570499234773E+01
C_4	6.26769453543773E+03	6.30504851719866E+03	6.53044497366572E+03	6.09921768108209E+03
C_5	-8.23565970719959E+05	-8.27590688777757E+05	-8.55274369004700E+05	-7.82548123831272E+05
C_6	7.10991816775153E+07	7.14252302137883E+07	7.37628194945625E+07	6.61258663863852E+07
C_7	-3.88954205800374E+09	-3.90676089261729E+09	-4.03268032936840E+09	-3.56468315357775E+09
C_8	1.25535346656858E+11	1.26082164873116E+11	1.30098575494295E+11	1.16356389046445E+11
C_9	-1.73669185171286E+12	-1.74456599763813E+12	-1.80015532514246E+12	-1.90390045458663E+12
C_{10}	-2.21250941613814E+13	-2.21925259820200E+13	-2.28402236126105E+13	3.29196667822296E+11
C_{11}	1.08312468994951E+15	1.08704607587877E+15	1.11936741805840E+15	3.31984561828086E+14
C_{12}	-4.85337647664313E+15	-4.87184397779273E+15	-5.00901855388915E+15	6.51728883256457E+15
C_{13}	-2.77258620252325E+17	-2.78281123696166E+17	-2.86697534169114E+17	-3.52021023262454E+17
C_{14}	2.60593986627724E+18	2.61826549819710E+18	2.70072632368539E+18	3.64162965554917E+18
C_{15}	5.58217673085917E+19	5.59518481595069E+19	5.74844816535358E+19	2.38928912669336E+19
C_{16}	-1.05130472736066E+21	-1.05502734795609E+21	-1.08594338480129E+21	-6.17483981793850E+20
C_{17}	7.79834935220323E+21	7.83559155740029E+21	8.08911267235945E+21	-2.47782229914783E+21
C_{18}	-3.34105815137547E+22	-3.34182839510815E+22	-3.44299358853572E+22	2.21089931326431E+23
C_{19}	-1.49241006841360E+24	-1.49935398559069E+24	-1.54592998507797E+24	-3.09729156764500E+24
C_{20}	9.65265464251326E+24	9.65572106558530E+24	9.94435177181880E+24	7.59718575338439E+24
C_{21}	2.15553177907418E+26	2.16507372188400E+26	2.22766448876706E+26	-4.12268268979515E+26
C_{22}	1.18580263219039E+28	1.18993801233724E+28	1.22462453120852E+28	2.39463688692670E+28
C_{23}	-3.28586742867138E+29	-3.29739958177349E+29	-3.39561805101968E+29	-3.76392168960089E+29
C_{24}	1.23798965328232E+30	1.24396279693138E+30	1.28519351289401E+30	1.20388371521338E+30
C_{25}	2.85161329828626E+31	2.86197218060332E+31	2.95023674039125E+31	3.19511222097695E+31
C_{26}	-2.91959839731158E+32	-2.93560333153385E+32	-3.03874523552216E+32	-4.18750801795299E+32
C_{27}	7.64453530022366E+32	7.71234240178240E+32	8.04021095147756E+32	1.67051583104849E+33

3.6 References

[1] Toennies, P.; Vilesov, A. *Angew. Chem. Int. Ed*., **2004**, 43, 2622.

[2] Krasnokutski, S. A.; Huisken, F. *J. Phys. Chem. A*., **2011**, 115, 7120.

[3] Lugovoj, E.; Toennies, P.; Vilesov, A. *J. Chem. Phys*., **2000**, 112, 8217.

[4] Yang, S.; Ellis, A. M.; Spence, D.; Feng, C.; Boatwright, A.; Latimera, E.; Binnsb, C. *Nanoscale* **2013**, 5, 11545.

[5] Spence, D.; Latimer, E.; Feng, C.; Boatwright, A.; Ellis, A. M.; Yang, S. *Phys. Chem. Chem. Phys.,* **2014**, 16, 6903.

[6] Latimer, E.; Spence, D.; Feng, C.; Boatwright, A.; Ellis, A. M.; Yang, S. *Nano Lett.,* **2014**, 14, 2902.

[7] Aquilanti, V.; Candori, R.; Pirani, F. *J. Chem. Phys.*, **1988**, 89, 6157.

[8] Dunning, Jr., T. H. *J. Chem. Phys.*, **1989**, 90, 1007.

[9] MOLPRO, a package of *ab initio* programs designed by H.-J. Werner and P. J. Knowles, version **2009**.

[10] Werner, H.-J.; Knowles, P. J. *J. Chem. Phys.*, **1985**, 82, 5053.

[11] Werner, H.-J.; Knowles, P. J. *Chem. Phys. Lett.*, **1985**, 115, 259.

[12] Werner, H.-J.; Knowles, P. J. Knowles, *J. Chem. Phys.*, **1988**, 89, 5803.

[13] Werner, H.-J.; Knowles, P. J. *Chem. Phys. Lett.*, **1988**, 145, 514.

[14] Davidson, E.R. *J. Comput. Phys.*, **1975**, 17, 87.

[15] *NIST Chemistry Webbook*, NIST Standard Reference Database No. 69, edited by P.J. Linstrom and W. G. Mallard (National Institute of Standards and Technology, Gaithersburg, MD, **2009**).

[16] Aguado, A.; Paniagua, M. *J. Chem. Phys.*, **1992**, 96**,** 1265.

[17] Landau, L. D.; Lifschitz, M. Quantum Mechanics, *Pergamon*, **1965**.

[18] Lawrence, W. G.; Apkarian, V. A. *J. Chem. Phys*., **1994**, 101, 1820.

[19] These authors use the name *many body potential* to refer to that but we think it's better to keep this name to refer to the actual many body potential, which is the PES that would be obtained from an *ab initio* calculation considering all the electrons of all the atoms of the whole system.

[20] Baylis, W. E. *J. Phys. B.* **1977**, 10, 308.

[21] Balling, L. C.; Wright, J. J. *J. Chem. Phys*. **1983**, 79, 2941.

[22] Danilychev, A. V.; Apkarian, V. A. *J. Chem. Phys*., **1994**, 100, 5556.

[23] Boatz, J. A.; Fajardo, M. E. *J. Chem. Phys*., **1994**, 101, 3472.

[24] Li, Z.; Apkarian, V. A.; Harding, L. B. *J. Chem. Phys*., **1997**, 106, 942.

[25] Nakayama, A.; Yamashita, K. *J.Chem.Phys*., **2000**, 114, 780.

[26] Really, we have chosen the real spherical harmonic as the unperturbed valence electron basis set, which consist in linear combinations of the $|lm\rangle$. To simplify the discourse we omitted this detail.

[27] Aquilanti, V.; Grossi, G. *J. Chem. Phys*. **1980**, 73, 1165.

[28] Dalfovo, F.; Lastri, A.; Pricaupenko, L.; Stringari, S.; Treiner, J. *Phys. Rev. B*, **1995**, 52, 1193.

[29] Barranco, M.; Pi, M.; Gaticia, S. M.; Hernández, E. S.; Navarro, J. *Phys. Rev. B,* **2008**, 78, 8997.

[30] Hernando, A.; Mayol, R.; Pi, M.; Barranco, M.; Ancilotto, F.; Bünermann, O.; Stienkemeier, F. *J. Phys. Chem. A,* **2007**, 111, 7303.

[31] Lax, M. *J. Chem. Phys*., **1952**, 20, 1752.

[32] Hernando, A.; Barranco, M.; Mayol, R.; Pi, M.; Ancilotto, F.; Bünermann, O.; Stienkemeier, F. *J. Low. Phys.,* **2010**, 158, 105.

[33] Cheng, C.; Walley, K. B. *J. Chem. Phys*., **1996**, 104, 3155.

[34] In this case the electronic state corresponds to the oxygen atom since helium atoms are always in their ground state 1S.

[35] Nakatsukasa, T.; Yabana, K.; Bertsch, G. F. *Phys. Rev. A,* **2002**, 65, 032512.

[36] Bünermann, O.; Dvorak, M.; Stienkemeier, F.; Hernando, A.; Mayol, R.; Pi, M.; Barranco, M.; Ancilotto, F. *Phys. Rev. B,* **2009**, 79, 214511.

[37] Salvat, F.; Fernández, J. M.; Senpau, J. *Penelope-2008: A Code System for Monte Carlo Simulation of Coupled Electron- Photon Transport* (OECD Nuclear Energy Agency, Issy-les-Moulineaux, France, **2009**)
http://www.nea.fr/html/dbprog/peneloperef.html.

[38] Ancilotto, F.; Lerner, P. B.; Cole, M.W. *J. Low. Phys.,* **1995**, 101, 1123.

[39] Slanger, T. G.; Cosby, P. C.; Huestis, D. L.; Vida, T. A. *Science,* **2001**, 291, 463.

4. Photodissociation dynamics of homonuclear diatomic molecules in helium nanodroplets. The case of $Cl_2@(^4He)_N$

4.1 Introduction

The study of helium nanodroplets has become an active area of research since the first experiments, which were performed in the early nineties of the last century.[1,2,3] Apart from its fundamental interest, being a quantum liquid system of intermediate size (between bulk liquid and molecular clusters), these droplets have attracted the interest of many investigators for the applications they provide acting as a matrix, due to its facility to pick up almost any chemical specie. The inert chemical character of helium together with the superfluidity[4] of these nanoscopic systems make them very useful to carry out high resolution spectroscopy studies[5] of chemical species embedded in these nanodroplets. A lot of work has been done in this context, both from the experimental and theoretical perspectives, providing information not only about the embedded species but also about the solvation structure and other properties of these nanoscopic systems.

On the other hand, a wide variety of chemical processes has been investigated experimentally.[6,7,8] Moreover, from the perspective of the chemical synthesis, the encounter of reactants is facilitated by the ability of helium droplets to be doped with the majority of chemical species and by the tendency of most dopants to be placed in the center of the droplet. The evaporation of some ^4He atoms allows the excess of energy to be dissipated, stabilizing complexes that would not be stable in gas phase. In this context many efforts have been made to investigate, e.g., reactions of inorganic clusters,[9] synthesis of metallic nanoclusters,[10] nanowires,[11] entrance channel van der Waals complexes (X-HF, X=Cl, Br, I)[12] and polymers.[13] Nevertheless, these studies were focused on the synthesis of novel chemical

species, rather than in the investigation of the reaction dynamics in the quantum fluid. To date, little effort has been devoted to this topic.[14] Thus, to the best of our knowledge, only a set of experimental reaction dynamics studies has been reported so far (photodissociation of alkyl iodides in helium nanodroplets).[8,15,16] From a theoretical point of view, only a single study has been reported in the literature on this field,[17] considering the same system investigated here, but using a very different methodology and taking into account strongly different physical conditions (non-superfluid helium nanodroplets (T = 4 K) containing up to 200 ^{4}He atoms), where significant quantum effects were found.

Here, we present a theoretical study of a prototypic and relatively simple reaction, corresponding to the adiabatic photodissociation of a homonuclear diatomic molecule embedded in superfluid helium nanodroplets (T = 0.37 K), i.e., X_2(ground state)@$(^4He)_{N}$ + hν → X_2(excited state)@$(^4He)_N$ → 2 X + $(^4He)_{N'}$ + (N-N') ^{4}He, where the last term simply refers to the total number of vaporized He atoms (maximum N value of 500). In order to do this we have coupled one of the main methods used to describe relatively large systems of bosonic liquid helium and a usual procedure in gas phase quantum reaction dynamics. More concretely, a hybrid approach using the density functional theory (DFT) for the description of the superfluid ^{4}He system[18] and a quantum wave packet dynamics[19] for the description of the X_2 molecule has been proposed. The DFT method allows us to deal with nanodroplets of big sizes, from a hundred to thousands of helium atoms, depending on the system and the process considered, obtaining a good compromise between accuracy and computational cost. These nanodroplet sizes are in a rather good correspondence with the ones employed in the experiments and so the simulations take into account the fully solvated nature of the X_2 dopant during the photodissociation process. As a particular example, we have studied the interesting case of the $Cl_2\left(X^1\Sigma_g^+\right) + h\upsilon \rightarrow Cl_2(B^3\Pi_u(0_u^+)) \rightarrow Cl(^2P_{3/2}) + Cl(^2P_{1/2})$ photodissociation process ($\lambda \approx 400$ nm (3.10 eV)) in helium nanodroplets of different sizes (cf. potential energy curves of Cl_2 [20] in Figure 4.1).

The type of process considered here is a good starting point for the theoretical investigation of the reaction dynamics in helium nanodroplets as, in addition of its interest, it is less complex than a bimolecular process. Besides, from the experimental point of view, we expect this process to be not so much complicated to be studied and have well controlled reaction conditions and chemical and physical properties measurements. In contrast to this, in the case of bimolecular reactions, which involve two pick-up steps, the conditions would not

be so well defined. On the other hand, the symmetry of the $X_2@^4He_N$ systems reduces the computational cost. Thus, it will be seen that only the X-X relative coordinate wave packet is needed to describe the evolution of the diatomic molecule along the dissociation axis (cf. Section 4.2).

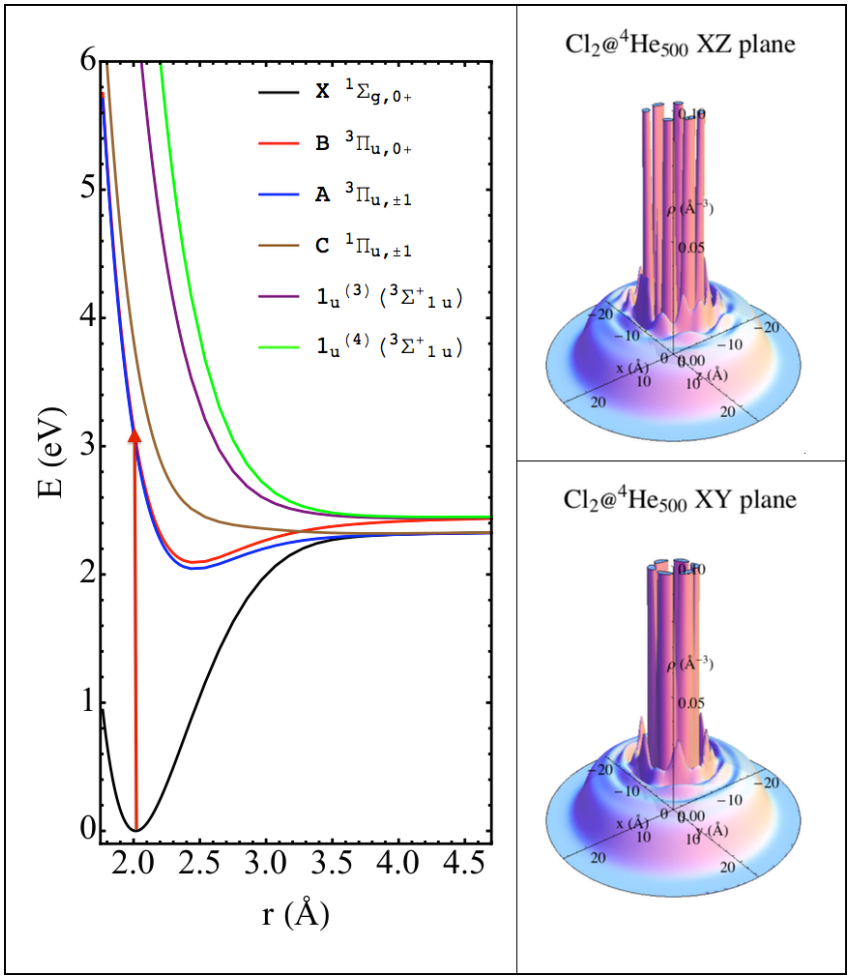

Figure 4.1. Left panel: ground (X) and five lowest excited (A, B, C, $1_u^{(3)}$ and $1_u^{(4)}$) potential energy curves of Cl_2, including relativistic corrections, where the arrow shows the B ← X electronic transition (data taken from Ref. 20). The vibrational energy of the initial state of Cl_2(X, v=0) is 0.035 eV. The two Cl_2 dissociation limits shown correspond to $Cl(^2P_{3/2})$ + $Cl(^2P_{3/2})$ (ground state atoms) and $Cl(^2P_{3/2})$ + $Cl(^2P_{1/2})$ (ground and excited atoms, respectively). Right panel: helium density for Cl_2(X, v=0)@$(^4He)_{500}$ in the xz and xy planes (the molecule is found in the center of the nanodroplet and along the z axis).

4.2 Theoretical methods

There are several steps implied in the experimental study of the photodissociation of a homonuclear diatomic molecule X_2 embedded in helium nanodroplets. The first one consists in the production of nanodroplets by supersonic expansion of He gas through a nozzle. Once the nanodroplets are generated, the next step is the picking up of the molecule and the following relaxation mediated by evaporation of some helium atoms. After that, for a given doped nanodroplet, $X_2@(^4He)_N$, a suitable laser photon (hν) induces the electronic transition of X_2 from the ground electronic state to a selected excited state, which leads to the dissociation of the two X atoms and the evaporation of several He atoms, i.e., 2 X + $(^4He)_{N'}$ + (N-N') ^4He. Finally, the resulting helium nanodroplet, $(^4He)_{N'}$, suffers a relaxation process in which it loses the excess of energy by evaporation of some additional helium atoms.

In the present work, we have focused on the dynamics of the photodissociation step employing a full quantum mechanical treatment. The helium description is based on the DFT, using the so called Orsay-Trento functional[18] (T = 0 K) to account for the properties of the helium superfluid, with a modification that allows to describe the formation of solid-like structures (snowballs), when the interaction between the impurity and the helium is strong.[21] The backflow and kinetic correlation terms of this functional have been neglected for computational reasons, as usual.[22,23] The consequence of not including the backflow term is the increasing of the Landau's critical velocity for the bulk liquid ^4He.[22] The description of the diatomic molecule is based on the relative coordinate (Cl-Cl distance in this case) wave function, owing to the symmetry of the system. In the first study of this type of processes in superfluid helium nanodroplets we do not have considered the X_2 rotational degree of freedom (of course, the very low temperature of the nanodroplets (around 0.37 K) makes the j=0 rotational state to be, essentially, the only populated one in the diatomic electronic ground state). Moreover, the rotational motion of the Cl_2 free molecule is very slow compared to the time scale of photodissociation. Thus, the rotational period of Cl_2 (j = 1) is about 68 and 103 ps for the X and B states, respectively ($\tau_{rot} \approx h/2B_e$, where B_e is the rotational constant).

The potential energy surfaces (PESs) describing the interaction potential between the helium atom and the selected molecule in the ground and excited electronic states (He-Cl_2(X) and He-Cl_2(B) PESs, respectively) have been taken from Ref. 24. The structure and energetics

of the nanodroplets, in general, depends in an important way on the electronic state of the atomic or molecular embedded species (see, e.g., Ref. 25).

As starting point for the reaction dynamics study, we have determined the structure and energy of the system in the ground state, $Cl_2(X)@(^4He)_N$. We have treated the molecule as an external potential[25] (with internal structure (vibration)) for the helium nanodroplet, and the center of mass (CM) degree of freedom of the molecule has been treated classically, because of its large effective mass ($2m_{Cl}$) compared to the helium atom mass. Concerning the relative coordinate, it has been described by its corresponding wave function $\varphi_{Cl_2}(r)$ and the vibrationally adiabatic approximation (see, e.g., Ref. 26) has been used. This simplification is sound since the energy perturbation made by the helium solvation on the diatomic molecule is much smaller than the diatomic potential energy, which results in the decoupling of the vibrational degree of freedom. So that, we selected the v=0 vibrational wave function of the free (gas phase) molecule to describe the embedded molecule.

Therefore, to determine the ground state of the system (static part of the calculation) we have to optimize the ^{4}He density, taking into account the interaction potential arising from the $Cl_2\left(X^1\Sigma_g^+, v=0, j=0\right)$ molecule. The pseudo-Schrödinger equation to be solved that provides this ground state is found by performing a minimization of the energy functional (Eq. 4.3), varying the helium density while keeping the number of helium atoms in the droplet constant.

This yields the following expression:

$$\left[-\frac{\hbar^2}{2m_{He}}\boldsymbol{\nabla^2} + \int dr\, V_{He-Cl_2(X)}(r, \boldsymbol{R}_{He})\left|\varphi_{Cl_2(X,v=0)}(r)\right|^2 + \frac{\delta\mathcal{E}_c[\rho_{He}]}{\delta\rho_{He}}\right]\sqrt{\rho(\boldsymbol{R}_{He})} =$$

$$= \mu_{He}\sqrt{\rho(\boldsymbol{R}_{He})} \qquad (4.1)$$

where μ_{He} stands for the chemical potential of helium and $\frac{\delta\mathcal{E}_c[\rho_{He}]}{\delta\rho_{He}}$ is the functional derivative of the helium energy functional. This equation has been solved by means of the imaginary time step propagation method. From these calculations it was obtained that the Cl_2 molecule in the electronic ground state is always found in the center of the nanodroplet, independently of the nanodroplet size. This will simplify the subsequent photodissociation dynamics study because, due to the symmetry of the problem, the CM of the molecule will remain unchanged.

The dynamical process begins with the B ← X electronic transition of Cl_2. We have assumed the Franck-Condon principle (sudden vertical electronic excitation process) and because of this both the Cl_2 vibrational wave function and helium density are kept frozen during the electronic transition. This leads to the $[Cl_2(B)@(^4He)_N]^*$ nanodroplet which has a significant excess of energy with respect to that in the equilibrium configuration $(Cl_2(B)@(^4He)_N)$. Once the B ← X excitation occurs, the $Cl_2(B)$ energy is 11094 K (199 K correspond to kinetic energy), and the $Cl_2(B)$-$(^4He)_N$ interaction energy is, e.g., equal to -388.7 K (N = 100) and -421.5 K (N = 500). Furthermore, electronic adiabaticity is also considered for $Cl_2(B)$ based on the weak coupling of the B state with the other electronic states of the molecule. The framework used to describe this real time evolution is based on the time dependent DFT (TDDFT) approach, as we have already mentioned. To obtain the governing equations of motion the least action principle is used. The quantum action of the system depends on two functions and is defined as

$$\mathcal{A}\left[\Psi_{He}, \varphi_{Cl_2}\right] = \int dt \left\{ E\left[\Psi_{He}, \varphi_{Cl_2}\right] - i\hbar \int d\boldsymbol{R}_{He}\, \Psi^*_{\boldsymbol{He}}(\boldsymbol{R}_{He}) \frac{\partial}{\partial t} \Psi_{He}(\boldsymbol{R}_{He}) - i\hbar \int dr\, \varphi^*_{Cl_2}(r) \frac{\partial}{\partial \mathrm{t}} \varphi_{Cl_2}(r) \right\} \quad (4.2)$$

with

$$E\left[\Psi_{He}, \varphi_{Cl_2}\right] = \frac{\hbar^2}{2m_{He}} \int d\boldsymbol{R}_{He}\, |\boldsymbol{\nabla}\Psi_{He}|^2 + \int d\boldsymbol{R}_{He}\; \mathcal{E}_c[\rho_{He}] + \int d\boldsymbol{R}_{He} \int dr\, V_{He-Cl_2(B)}(r, \boldsymbol{R}_{He})\, \rho_{He}(\boldsymbol{R}_{He}) \left|\varphi_{Cl_2}(r)\right|^2 - \frac{\hbar^2}{m_{Cl_2}} \int dr\, \varphi^*_{Cl_2}(r) \frac{\partial^2}{\partial r^2} \varphi_{Cl_2}(r) + \int dr\, V_{Cl_2(B)}(r) \left|\varphi_{Cl_2}(r)\right|^2 \quad (4.3)$$

where $\rho_{He}(\boldsymbol{R}_{He})$ and $\mathcal{E}_c[\rho_{He}]$ are the density and the sum of the correlation and potential energy densities of liquid ^{4}He, respectively. This last term accounts for the potential and the strong correlation energies between the helium atoms in the superfluid state. Here, the functional dependence is defined in terms of the ^{4}He effective complex wave function $\Psi_{He}(\boldsymbol{R}_{He}, t) \equiv \sqrt{\rho_{He}(\boldsymbol{R}_{He}, t)}$ and the diatomic wave packet $\varphi_{Cl_2}(r, t)$. Considering variations with respect to these two functions, two coupled Schrödinger-like time dependent dynamical equations are obtained for the helium and chlorine molecule, respectively:

$$i\hbar\frac{\partial}{\partial t}\Psi_{He}(\boldsymbol{R}_{He}) = \\ = \left[-\frac{\hbar^2}{2m_{He}}\boldsymbol{\nabla^2} + \int dr\, V_{He-Cl_2(B)}(r,\boldsymbol{R}_{He})\left|\varphi_{Cl_2}(r)\right|^2 + \frac{\delta\mathcal{E}_c[\rho_{He}]}{\delta\rho_{He}}\right]\Psi_{He}(\boldsymbol{R}_{He}) \tag{4.4a}$$

$$i\hbar\frac{\partial}{\partial t}\varphi_{Cl_2}(r) = \\ = \left[-\frac{\hbar^2}{m_{Cl_2}}\frac{\partial^2}{\partial r^2} + \int d\boldsymbol{R}_{He}V_{He-Cl_2(B)}(r,\boldsymbol{R}_{He})\rho_{He}(\boldsymbol{R}_{He}) + V_{Cl_2(B)}(r)\right]\varphi_{Cl_2}(r) \tag{4.4.b}$$

These equations have been solved numerically by discretization of the space in a grid of points for each degree of freedom. The diatomic molecule has been placed along the z axis and the grid for the relative coordinate is spaced by 0.0174 Å. For the helium part we have worked with Cartesian coordinates, using a spatial separation of 0.35 Å for the x and y axis and 0.09 Å for the z axis. The numerical integrator used is a fourth order Adams predictor-corrector method,[27] initiated by a Runge-Kutta method of fourth order[28] (time step = 1.5 10^{-5} ps). The evaluation of the derivatives for the kinetic energy terms has been carried out in momentum space, performing a Fourier transform using the FFTW package of Ref. 29. This strategy is useful not only from the point of view of the computational cost but also because it allows to check the quality of the derivatives.

To finish with the computational details, it is worth noting that quartic negative imaginary potentials (NIPs) have been employed in order to avoid artificial reflections of the molecular and helium wave functions at the grid edges,[30]

$$V_{\mathrm{NIP}} = -i\,A\frac{5}{2}\left(\frac{d-d_{\mathrm{NIP}}}{L}\right)^4 \tag{4.5}$$

for $d > d_{\mathrm{NIP}}$, where the absorption strength (A) is equal to 5171.4 and 3315.0 K Å^{-4} for the molecule and helium, respectively, and the length (L) and location (d_{NIP}) of the NIPs are indicated below. The molecular NIP has been placed in the z axis at a distance of 12.0 Å with respect to the nanodroplet surface and has a length of 1.1 Å. The NIPs for helium have been located in the z axis at a distance of 12.0 Å with respect to the surface (length of 3.3 Å), while in the x and y axis they have been placed at 6.0 Å (length of 3.3 Å).

The final photofragment (Cl) velocity distribution has been obtained from the Cl_2 wave function, expressed in momentum representation, before applying the molecular NIP.

Moreover, a flux analysis has been performed to check the quality of the propagation, using the continuity equation ($\frac{\partial}{\partial t}\rho_{Cl_2} + \frac{\partial}{\partial r} j_{Cl_2} = 0$).

4.3 Results and discussion

We have studied theoretically the photodissociation dynamics of Cl_2 in helium nanodroplets of different sizes: $Cl_2(X)@(^4He)_N + h\nu \rightarrow [Cl_2(B)@(^4He)_N]^* \rightarrow Cl(^2P_{3/2}) + Cl(^2P_{1/2}) + (^4He)_{N'} + (N\text{-}N')\ ^4He$, with N = 50, 100, 200, 300 and 500. Although the smaller experimental nanodroplets are formed with around 500 helium atoms, the analysis of the results achieved for the selected systems can show the main features and patterns of the properties related to the nanodroplet size.

The microscopic mechanism of the investigated process can be elucidated quite well from Figures 4.2 and 4.3 and the two movies included in the Appendix, which correspond to the $[Cl_2(B)@(^4He)_{500}]^*$ case, although the general trends described here also apply to the other nanodroplets, unless otherwise indicated. The time evolution of the Cl_2 wave packet (relative coordinate, r, probability density) takes place along the z axis and is shown in Figure 4.2 together with the effective potential that governs the dynamics of this degree of freedom, i.e., the sum of the Cl_2 potential energy (B state) and the Cl_2-helium interaction potential (which depends on time due to the evolution of the nanodroplet density).

Strong oscillations are produced in the wave packet due to the collision with the first solvation shell (cf. Figure 4.2 and movie 4.1 (t = 0.24 ps)), and its shape changes when it becomes close to the nanodroplet surface. Thus, with the exception of what happens for the smaller droplets (N = 50 and 100), the most intense peak changes from the "head" (higher r) to the "tail" (smaller r) region of the wave packet (cf. Figure 4.2 and movie 4.1 (t = 0.94 and 1.20 ps, respectively)). This phenomenon is due to the opening of the cavity (which has been generated inside the nanodroplet by the Cl dissociating atoms) to the exterior of the nanodroplet and the non-equilibrated force balance experienced by each Cl atom when they reach the surface, due to the anisotropy of the surrounding helium density. Another important feature is the confinement provided by the helium environment, which avoids the spatial spreading of the wave packet with time, and differing from what occurs in gas phase translational dynamics.

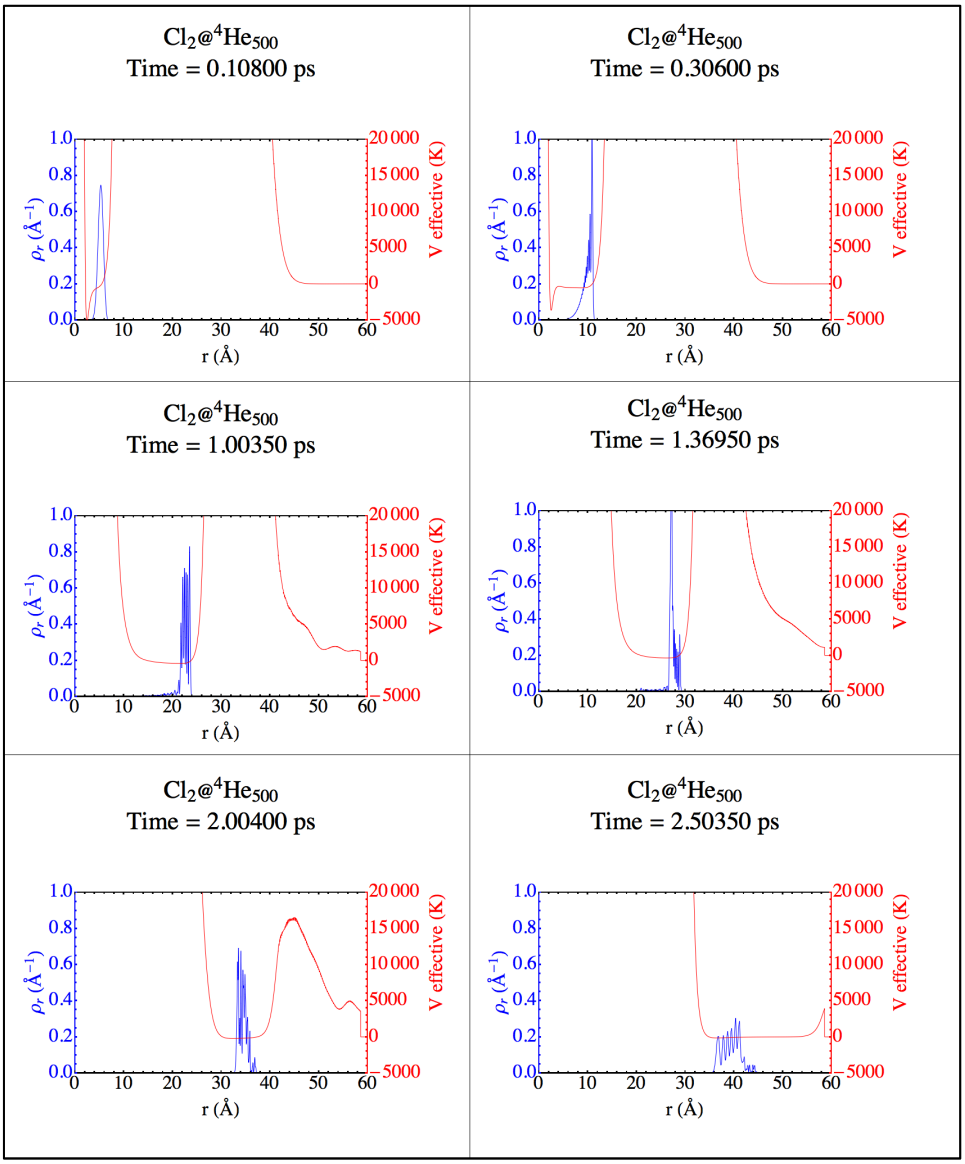

Figure 4.2. Snapshots showing the time evolution of the squared modulus of the relative coordinate wave packet (blue) and effective potential (red), during nearly all the $[Cl_2(B)@(^4He)_{500}]^*$ photodissociation process. See also movie 1 (Appendix).

The time evolution of the helium density (xz plane) is represented in Figure 4.3 and in movie 4.2. At the beginning of the process strong distortions are produced in the density, mainly in the vicinity of the z axis. Supersonic shock waves are formed as a consequence of the collision of the wave packet with the first solvation shell. These waves travel at very high velocities (around 4500 m/s) and, when they collide with the nanodroplet surface, some helium density escapes (evaporation process). It can also be observed how the complicated interference pattern motivates the generation of waves travelling in perpendicular direction to the molecular dissociation axis (z axis) and the destruction of the snowball structures. This is

facilitated by the freed space between the two Cl atoms, when they separate from each other, that becomes available for helium.

Our results point out that, as a result of the energy transfer between the $Cl_2(B)$ molecule and the helium droplet, a direct escape process is taking place. From the beginning to the end of the photodisociation, it involves the evaporation of some atoms (3 to 10 He atoms from N=50 to 500, respectively; see below) with a rich energy content, rather than the evaporation of the whole nanodroplet. This is consistent with what has been found in the experiments of Ref. 8 on the photodissociation of alkyl iodides (R-I → R + I, R = CH_3, CF_3, and C_2H_5; λ = 266 nm (4.66 eV)) in helium nanodroplets.

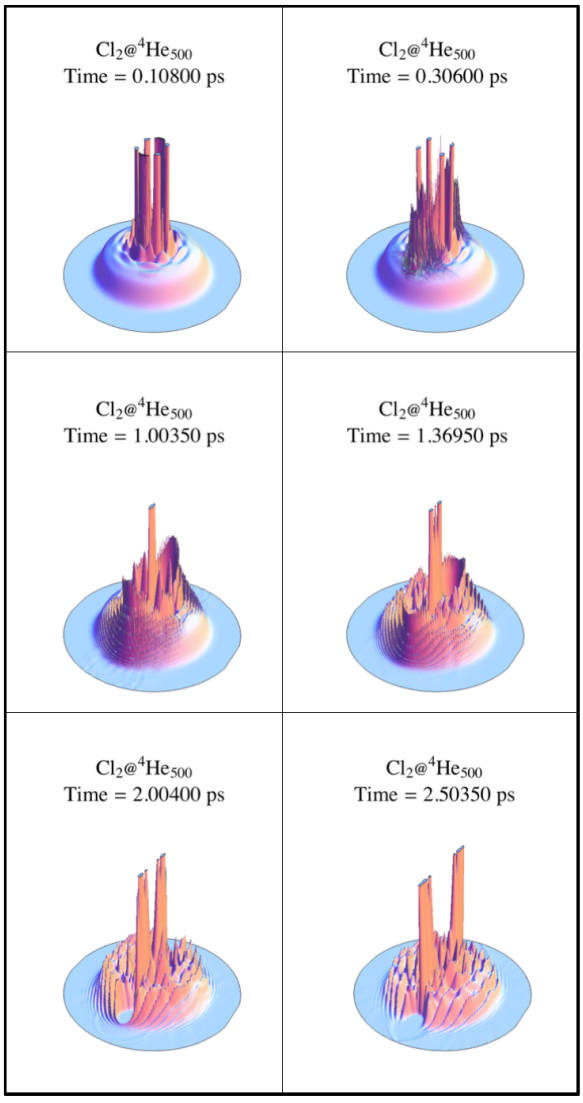

Figure 4.3. Snapshots showing the time evolution of the helium density (xz plane), during nearly all the $[Cl_2(B)@(^4He)_{500}]^*$ photodissociation process. See also movie 4.2.

In Figure 4.4 the evolution of the expectation value of the Cl-Cl relative velocity with time is represented together with the evolution of the expectation value of the $Cl_2(B)$ energy (kinetic and Cl-Cl interaction energy). The photodissociation process takes place on the picosecond time scale. Thus, in order to reach a Cl-Cl separation of 20 Å, which is one order of magnitude above the initial Cl_2 distance, the $[Cl_2(B)@(^4He)_N]^*$ systems require a similar amount of time (0.8-0.9 ps); while the time required for the Cl dissociating atoms to reach the nanodroplet surface increases with the size (0.85, 1.14, 1.63, 2.01, and 2.57 ps for N = 50, 100, 200, 300, and 500, respectively). This last time has been arbitrarily defined as that one needed by the expected value of the Cl-Cl distance to be equal to the initial length of the droplet along the z axis, which is taken as twice the corresponding radius (R = 11.0, 13.0, 15.7, 17.5, and 20 Å, respectively).

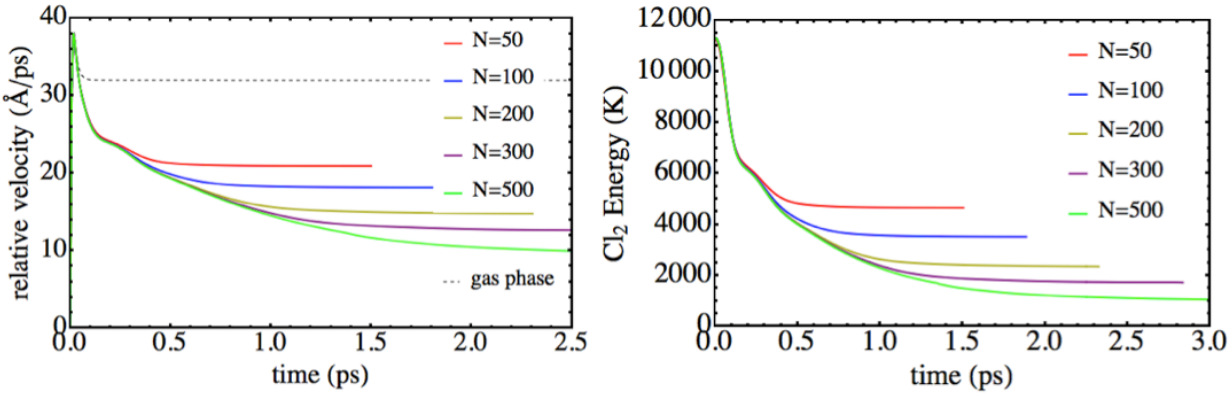

Figure 4.4. Time evolution of the expectation value of the relative velocity (left) and Cl_2 energy (right) with time for different $[Cl_2(B)@(^4He)_N]^*$ nanodroplet sizes. The gas phase result is also included in the former case (dashed black line).

The initial acceleration and deceleration found are governed by the $Cl_2(B)$ potential energy curve and it is very similar to what happens in the photodissociation evolution in gas phase (cf. Figure 4.4). This fact points out that, at the beginning (below ≈ 0.035 ps), the process of bond breaking is not appreciably influenced by solvation, due to the high energy difference between the chemical and van der Waals interactions. At somewhat larger times, however, the relative velocity in gas phase becomes constant while that in the droplet decays, indicating that the molecule is exchanging energy with the helium. This happens because the velocities involved (1000-3500 m/s) are clearly above (orders of magnitude) the Landau's critical velocity for superfluid (bulk) helium (≈58 m/s (0.58 Å/ps))[31,32] which, on the other hand, has also been observed in helium nanodroplets (N ≈ 1000 and above).[33]

Comparison of the profiles of the relative velocity (or Cl_2 energy) curves for the different nanodroplet sizes investigated (cf. Figure 4.4), suggests that the mechanism of energy exchange is the same for all them, as they are very similar to each other. Under these circumstances the helium behaviour is similar to that of a conventional liquid (i.e., the fluid viscosity is different from zero) and here this will be more evident when analysing the expectation value of the Cl-Cl relative velocity *vs*. the expectation value of the Cl-Cl distance. Furthermore, in Figure 4.4 is also seen that the energy of the dopant is monotonically decreasing, avoiding the possibility of a mechanism in which the solvent and the molecule are exchanging energy back and forth. Finally, we can infer that the fastest energy exchange takes place during the collision with the first solvation shell, which is when the first supersonic waves are produced.

The Cl atomic photofragment velocity distributions are shown in Figure 4.5. The oscillating shape and presence of an important number of peaks in the distributions can be interpreted from the time evolution of the squared modulus of the relative coordinate wave packet expressed in the momentum representation. Thus, a little after (≈ 0.1 ps) the B ← X electronic transition, a clear oscillating pattern with a significant number of peaks is produced and, although the contributions of the different momentum values change with time, this behavior is maintained until the final of the photodissociation process, being reflected in the final velocity distribution. These oscillating structures are present for all the nanodroplets and they probably result from quantum resonances (confinement resonances) arising from the interaction of the $Cl_2(B)$ wave packet with the helium solvent. Although resonances are one of the most striking phenomena in physics and chemistry and resonance analysis is a very interesting topic in reaction dynamics, it is out of the scope of the present chapter. In fact, this is a very specific and complex analysis,[19,34] even for systems of a small number of degrees of freedom,[35] which is interesting by itself, that will be the subject of the chapter 6.

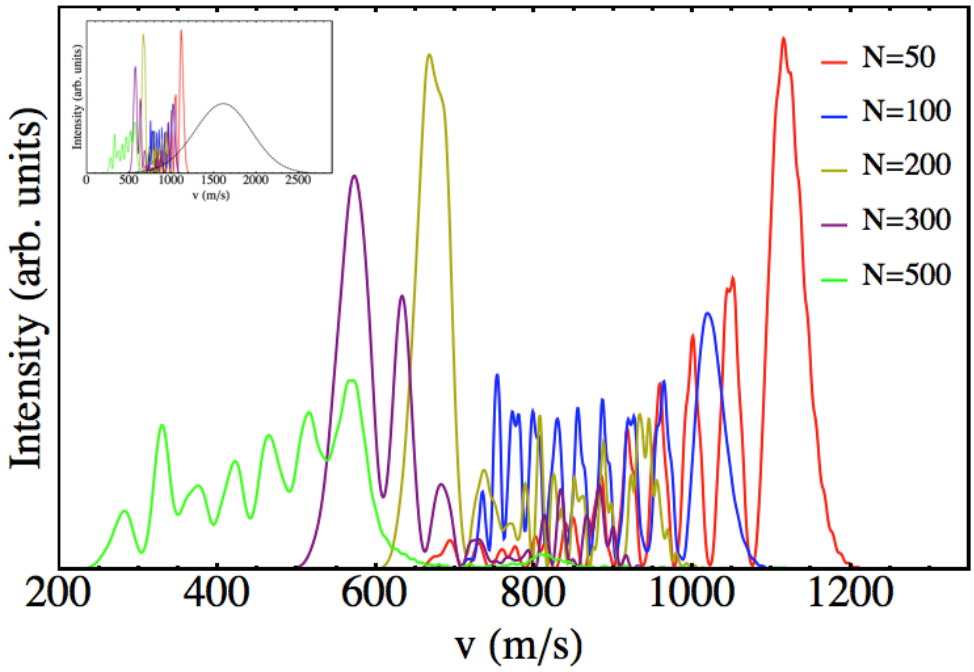

Figure 4.5. Velocity distributions of the Cl photofragment for different $[Cl_2(B)@(^4He)_N]^*$ nanodroplet sizes. The gas phase result (black line) is also given in the small figure.

The mean (expectation) values of the Cl velocity distributions are collected in Figure 4.6a. A quantitative agreement is found when these data are fitted to a $N^{1/3}$ dependence (cf. Figure 4.7a), suggesting that the mean velocity of the fragments decreases in a proportional manner with the path length of the nanodroplet. With the help of Figure A4.1 we have verified that his behavior occurs in all cases (and Figure A4.2 shows the time evolution of the Cl-Cl distance mean value)[i]. Thus, we can see that the mean value of the Cl-Cl relative velocity, $\langle v_r \rangle$, depends almost linearly on the mean value of Cl-Cl relative distance, $\langle r \rangle$, for the two $\langle r \rangle$ zones which are defined by the ~2.6-5.1 Å and ~6.4-24.5 Å intervals (the higher limit for the second zone is defined by the N = 500 case). The same relation, of course, also applies for the mean value of the Cl velocity ($\langle v_{Cl} \rangle = \langle v_r \rangle/2$) *vs*. the mean value of the Cl z-axis coordinate ($\langle z_{Cl} \rangle = \langle r \rangle/2$; Cl atom moving along the positive z-semiaxis).

[i] Figures A4.1 and A4.2 are included in the Appendix.

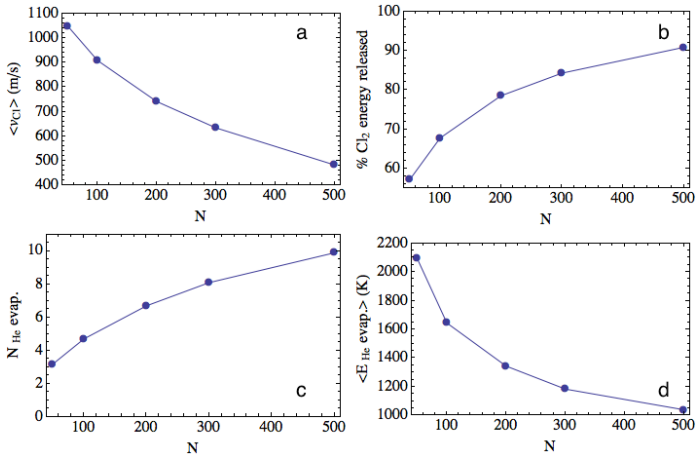

Figure 4.6. Mean value of the Cl escape velocity (a), percentage of the Cl_2 energy released to the droplet (b), number of ^{4}He evaporated atoms (c), and mean energy per evaporated ^{4}He atom (d), for different $[Cl_2(B)@(^4He)_N]^*$ nanodroplet sizes (N = 50, 100, 200, 300 and 500).

For each zone, we can write $\langle v_{Cl} \rangle \approx a_0 - a_1 \langle z_{Cl} \rangle$, where a_0 and a_1 are (positive) constants that depend on the zone. Now, if we derive with respect to time and multiply by the atomic mass of Cl (m_{Cl}) both sides of the previous $\langle v_{Cl} \rangle$ expression, we obtain the quantum mechanics analogue of a well know equation describing the force of friction (z component), F_f, acting on a body which is moving, at a given velocity, inside a conventional fluid:

$$\langle F_f \rangle \approx -b \langle v_{Cl} \rangle \tag{4.6}$$

where $b \equiv m_{Cl}\, a_1$. Hence, for these mean quantities the behavior of the $(^4He)_N$ nanodroplets, at the (large) energies involved in the $Cl_2(B)$ photodissociation, resembles that of a conventional liquid.

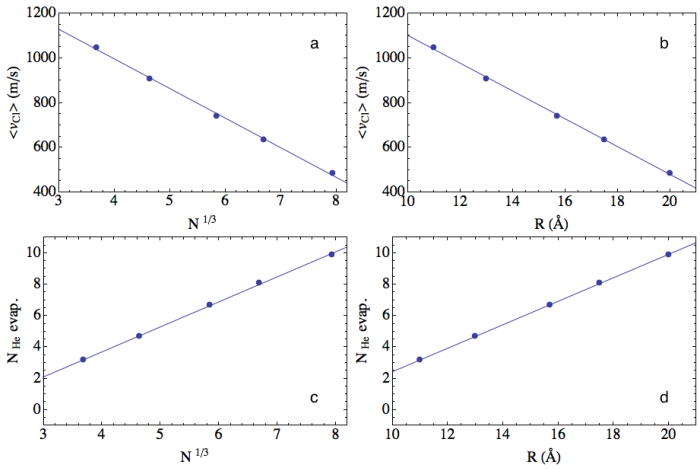

Figure 4.7. Mean value of the Cl escape velocity as a function of $N^{1/3}$ (a) and R (b), and number of ^{4}He evaporated atoms as a function of $N^{1/3}$ (c) and R (d), for different $[Cl_2(B)@(^4He)_N]^*$ nanodroplet sizes (N = 50, 100, 200, 300 and 500).

In Figure 4.6b the percentage of energy released from $Cl_2(B)$ to the helium solvent is shown. The large values obtained (57%, 84% and 91% of the diatomic energy is released to helium for droplets of 50, 300, and 500 He atoms, respectively) point out that the energy exchange mechanism is very efficient. The number of helium atoms evaporated, $N_{He\ evap}$, as a function of the nanodroplet size is collected in Figure 4.6c. This number increases with the droplet size in a smooth way ($N_{He\ evap}$ = 3, 8, and 10 for N = 50, 300, and 500, respectively) and follows a $N^{1/3}$ law in a quantitative way (Figure 4.7c).

To understand this dependence we have considered the following expression $N_{He\ evap} = k(R - R_{cavity})$, where k and R_{cavity} (cavity radius) are constants. This cavity, which is similar to a sphere, corresponds to the volume placed inside the droplet and centered in the Cl_2 molecule in which no helium atoms are found. The term $R - R_{cavity}$ corresponds to the distance travelled by each Cl atom through the helium nanodroplet. By doing this fitting ($N_{He\ evap}\ vs.\ R$) we obtained that R_{cavity} is about 4.8 Å, a value that compares quite well with the initial radius of the cavity along the z axis (≈4.6 Å) and shows the plausibility of our hypothesis. Finally, in Figure 4.6d the mean energy per evaporated ^{4}He atom is shown, which exhibits a moderate decrease with N (the value for N = 500 is nearly half of that obtained for N = 50).

4.4 Summary and conclusions

We have developed a quantum mechanical approach based on a hybrid theoretical method to describe the photodissociation dynamics of a homonuclear diatomic molecule embedded in ^{4}He superfluid nanodroplets (T = 0.37 K). In this way, the time evolution of helium is described within the TDDFT framework, while the time dependent wave packet quantum dynamics is used for the diatomic molecule. Using this hybrid strategy we have studied the interesting case of the Cl_2 photodissociation dynamics, induced by the B ← X electronic transition, for $Cl_2(v{=}0,X)@(^4He)_N$ doped nanodroplets, with N ranging from 50 up to 500. These droplets correspond to the initial configuration for the dynamics and the process takes place on the picosecond time scale. The time required for the Cl dissociating atoms to reach the nanodroplet surface increases with the size (0.85-2.57 ps).

At the large velocities involved, which clearly exceed the Landau's critical velocity, an efficient energy exchange mechanism has been found (e.g., 57% and 91% of the $Cl_2(B)$ energy is released to the helium for N = 50 and 500, respectively), and the energy exchange mechanism is independent of the size of the nanodroplet. Furthermore, simple linear expressions between the average Cl final velocity and the (small) number of evaporated He atoms with respect to the radius of the nanodroplet have been reported, together with the existence of confinement resonances leading to very well defined sharp structures (strongly oscillating peaks) in the Cl final velocity distribution.

We hope that the present theoretical study will encourage the experimentalists to investigate the reaction dynamics of this and related photodissociation processes.

4.5 Appendix

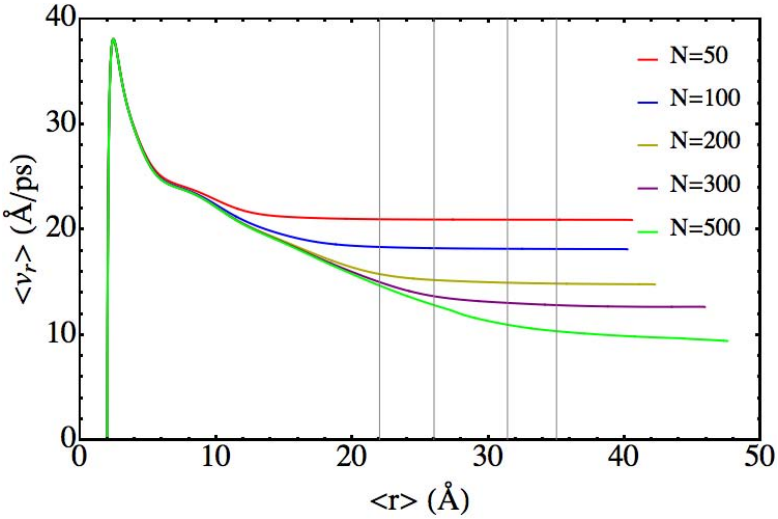

Figure A4.1. Expected value of the Cl-Cl relative velocity as a function of the expected value of the Cl-Cl distance for different $[Cl_2(B)@(^4He)_N]$*.nanodroplet sizes. The vertical lines indicate the diameters of the $Cl_2(X)@(^4He)_N$ nanodroplets.

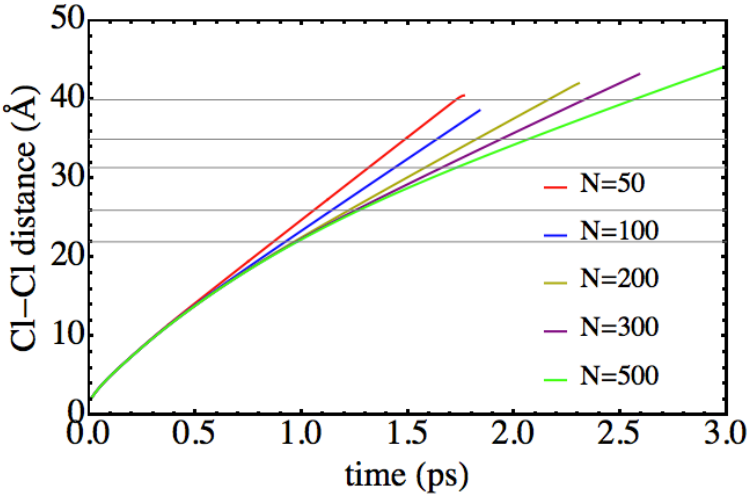

Figure A4.2. Time evolution of the Cl-Cl distance expectation value for different $[Cl_2(B)@(^4He)_N]$*.nanodroplet sizes. The parallel lines indicate the diameters of the $Cl_2(X)@(^4He)_N$ nanodroplets.

Movie 4.1. Time evolution of the squared modulus of the relative coordinate wavepacket (red) and effective potential (blue), during part of the photodissociation process, for the $[Cl_2(B)@(^4He)_{500}]$* nanodroplet.

Movie 4.2. Time evolution of the helium density, during part of the photodissociation process, for the $[Cl_2(B)@(^4He)_{500}]$* nanodroplet.

4.6 References

[1] Buchenau, H; Knuth, E.L; Northby, J; Toennies, J. P; Winkler, C. *J. Chem. Phys.* **1990**, *92*, 6875.

[2] Hartmann, M; Mielke, F; Toennies, J. P; Vilesov, F; Benedek, G. *Phys. Rev. Lett.* **1996**, *76*, 4560.

[3] Goyal, S; Schutt, D. L; Scoles, G. *Phys. Rev. Lett.* **1992**, *69*, 933.

[4] Hartmann, M; Miller, R. E; Toennies, J. P; Vilesov. *Science*. **1996**, *272*, 1631.

[5] Toennies, J. P.; Vilesov, A. *Angew. Chem. Int. Ed*., **2004**, *43*, 2622.

[6] Krasnokutski, S. A.; Huisken, F. *J. Phys. Chem. A*., **2011**, *115*, 7120.

[7] Lugovoj, E.; Toennies, P. J.; Vilesov, A. *J. Chem. Phys*., **2000**, *112*, 8217.

[8] Braun, A.; Drabbels, M. **2007**, *127*, 114303.

[9] Müller, S; Krapf, S.; Koslowski, Th.; Mudrich, M.; Stienkemeier, F. *Phys. Rev. Lett.* **2009**, *102*, 183401.

[10] Yang, S.; Ellis, A. M.; Spence, D.; Feng, C.; Boatwright, A.; Latimer, E.; Binns, C. *Nanoscale*. **2013**, *5*, 11545.

[11] Latimer, E.; Spence, D.; Feng, C.; Boatwright, A.; Ellis, A. M.; Yang, S. *Nano Lett.* **2014**, *14*, 2902.

[12] Merritt, J. M.; Küpper, J.; Miller, R. E. *Phys. Chem. Chem. Phys.* **2005**, *7*, 67.

[13] Douberly, G. E.; Miller, R. E. *J. Phys. Chem. B*, **2003**, *107*, 4500.

[14] Yang, S.; Ellis, A. M. *Chem. Soc. Rev.* **2013**, *42*, 472.

[15] Braun, A.; Drabbels, M. *J. Chem. Phys.* **2007**, *127*, 114304.

[16] Braun, A.; Drabbels, M. *J. Chem. Phys.* **2007**, *127*, 114305.

[17] Takayanagi, T.; Shiga, M. *Chem. Phys. Let.* **2003**, *372*, 90.

[18] Dalfovo, F.; Lastri, A.; Pricaupenko, L.; Stringari, S.; Treiner, J. *Phys. Rev. B*, **1995**, *52*, 1193.

[19] Tannor, D. J. *Introduction to Quantum Mechanics. A Time Dependent Perspective*; University Science Books: Sausalito, **2007**.

[20] Asano, Y.; Yabushita, S. *J. Phys. Chem. A* **2001**, *105*, 9873.

[21] Ancilotto, F.; Barranco, M.; Caupin, F.; Mayol, R.; Pi, M. *Phys. Rev. B*. **2005**, *72*, 214522.

[22] Mateo, D.; Hernando, A.; Barranco, M.; Loginov, E.; Drabbels, M.; Pi, M. *Phys. Chem. Chem. Phys.* **2013**, *15*, 18388.

[23] Mateo, D.; Gonzalez, F.; Eloranta, J. *J. Phys. Chem. A*, **2014**, DOI: 10.1021/jp5057286.

[24] Williams, J.; Rohrbacher, A.; Seong, J.; Marianayagam, N.; Janda, K. C.; Burcl, R.; Szcześniak, M. M.; Chałasiński, G.; Cybulski, S. M.; Halberstadt, N. *J. Chem. Phys.* **1999**, *111*, 997.

[25] Vilà, A; González, M.; Mayol, R.; Paniagua, M. *RSC Adv.* **2014**, *4*, 44972.

[26] Paesani, F.; Gianturco, F. A. *J. Chem. Phys.* **2002**, *116*, 10170.

[27] Ralston, A.; *Numerical Integration Methods for the Solution of Ordinary Differential Equations. In Mathematical Methods for Digital Computers*, John Wiley & Sons: New York, **1960**.

[28] Thompson R. J. *Commun. ACM*. **1970**, *13*, 739.

[29] Frigo, M.; Johnson, S. G. IEE Proceedings **2005**, *93*, 216.

[30] Vibók A.; Balint-Kurti G. G. *J. Phys. Chem.* **1992**, *96*, 8712.

[31] Tilley, D. R.; Tilley, J. *Condensates and Excitations. Superfluidity and Superconductivity*, Institut of Physics Publishing, **1990**.

[32] Annet, J. F. *Superfluid Helium-4. Superconductivity, Superfluids and Condensates*, Oxford University Press, **2004**.

[33] Brauer, N. B.; Smolarek, S.; Loginov, E.; Mateo, D.; Hernando, A.; Pi, M.; Barranco, M.; Buma, W. J.; Drabbels, M. *Phys. Rev. Lett.* **2013**, *111*, 153002.

[34] Moiseyev, N. *Non-Hermitian Quantum Mechanics*; Cambridge University Press, **2011**.

[35] Gamallo, P.; Huarte-Larrañaga, F.; González, M. *J. Phys. Chem. A* **2013**, *117*, 5393.

5. Relaxation dynamics of helium nanodroplets after photodissociation of a dopant homonuclear diatomic molecule. The case of $Cl_2@(^4He)_N$

5.1 Introduction

The nanometric length-scale of superfluid helium nanodroplets (T = 0.37 K), ^4He_N, makes these systems very interesting because they are in the midpoint between small molecular clusters and bulk liquid and so, they help in elucidating the properties of quantum fluids and how they emerge due to the increasing of the system size. The use of doping impurities inside ^4He_N allows considering two types of studies. Thus, sometimes they are used as a probe, in order to obtain a better understanding of the droplet system, while in other cases the interest is focused in the impurity itself and the helium nanodroplets are the matrix where the study of the properties of these chemical species is performed. This last kind of studies includes, e.g., spectroscopy[1] and chemical synthesis of different products, ranging from small metastable molecules up to metallic clusters such as nanoparticles[2] and nanowires.[3]

From a theoretical standpoint many efforts have been made during the last two decades involving the study of the structure, energetics and spectroscopy of doped ^4He_N.[4] Moreover, the study of the real-time dynamics of processes occurring in (atomic) doped helium nanodroplets has become an intensive area of research during the last few years.[5] Nowadays, the theoretical study of these processes is only affordable within the time dependent density functional theory (TDDFT) framework; and from these investigations exciting properties of ^4He_N have been revealed, such as, e.g., the existence of the critical Landau velocity in helium nanodroplets.[6]

Recently, we presented a theoretical approach to describe the photodissociation quantum dynamics of homonuclear molecules embedded in superfluid 4-helium

nanodroplets.[7] It corresponds to a hybrid quantum mechanical time-dependent method that combines TDDFT (helium density) and wavefunction (diatomic molecule wavepacket) dynamics. Despite the relative simplicity of this type of processes, the investigation pointed out the presence of remarkable features of the reaction dynamics in this quantum solvent.

The problem under consideration here can be interpreted as a chemical reaction taking place in a system with a large number of atoms:

$$X_2(\text{ground state})@(^4He)_N + h\nu \rightarrow [X_2(\text{excited state})@(^4He)_N]^* \quad (5.1)$$

$$[X_2(\text{excited state})@(^4He)_N]^* \rightarrow X + X^* + [(^4He)_{N'}]^* + (N\text{-}N')\ ^4He \quad (5.2)$$

$$[(^4He)_{N'}]^* \rightarrow (^4He)_{N''} + (N'\text{-}N'')\ ^4He \quad (5.3)$$

where the (N-N') ^{4}He and (N'-N") ^{4}He terms only denote the total number of vaporized ^{4}He atoms in the photodissociation of the X_2 diatomic molecule and relaxation of the nanodroplet, respectively (maximum $N = 500$). Moreover, the symbol "*" indicates that the corresponding species are in an excited state (electronic excited state in the case of X_2 and one of the X atoms and, simply, distorted geometry in the case of the nanodroplet).

The excitation and photodissociation processes (steps (5.1) and (5.2)) have been considered by us in a previous contribution[7] and, in order to complete the investigation of the whole process (i.e., steps (5.1)-(5.3)), here we present the study of the final step. This corresponds to the nanodroplet relaxation which takes place once the X and X* photofragments have left the droplet. To do this, we have employed the same quantum dynamics theoretical approach (TDDFT) as in Ref. 7 and, as far as we know, this is the first time that the dynamics of this type of relaxation process has been examined.

As it will be seen, this process is mediated by the evaporation of helium atoms but it is, of course, different from the evaporative cooling process that takes place when the droplets have been just formed, from the aggregation of many atoms, and decrease their energy and temperature until they reach the thermodynamic equilibrium.[8,9] Moreover, the relaxation process investigated also differs from the process known as "quantum evaporation", which corresponds to the evaporation of surface helium atoms due to the collision with atoms, rotons or phonons.[10]

The chapter is organized as follows: Section 5.2 presents a brief description of the theoretical methods employed; Section 5.3 reports the main results obtained and the corresponding analysis and interpretation of results and, finally, the summary and conclusions are given in Section 5.4.

5.2 Theoretical methods

The description of the superfluid liquid 4-helium adopted in this study is based on a TDDFT approach, using the phenomenological Orsay-Trento functional,[11] where, as usual,[5,7] for computational reasons we have neglected in the functional the non-local contributions to the correlation energies and the backflow term. A detailed description of this procedure can be found in our previous contribution on the $X_2@(^4He)_N$ photodissociation process[7] and here we just give a brief explanation.

Within the TDDFT framework, the equation of motion is obtained by minimizing the quantum action, varying the complex effective wave function of helium, which is defined by $\Psi_{He}(\boldsymbol{R}_{He}, t) \equiv \sqrt{\rho_{He}(\boldsymbol{R}_{He,}t)}$, where $\rho_{\mathrm{He}}(R_{\mathrm{He}},t)$ is the helium density at the time t for the nanodroplet (x,y,z) point specified by the position vector R_{He}. This treatment leads to the following Schrödinger-like equation:

$$i\hbar\frac{\partial}{\partial t}\Psi_{\mathrm{He}}(\boldsymbol{R}_{He}) = \left[-\frac{\hbar^2}{2m_{He}}\boldsymbol{\nabla^2} + \frac{\delta\mathcal{E}_c[\rho_{He}]}{\delta\rho_{He}}\right]\Psi_{He}(\boldsymbol{R}_{He}) \qquad (5.4)$$

This non-linear equation has been solved discretizing the space in a Cartesian coordinate grid of points, whose size has been optimized for each droplet (N = 50, 100, 200, 300 and 500). The grid spacing used is the same employed for describing the photodissociation process,[7] i.e., 0.09 Å for the z-axis (Cl-Cl molecular axis) and 0.35 Å for the x and y axes.

The numerical integration of Eq. 5.4 has been carried out by means of a fourth order Adams predictor-corrector-modificator method,[12] initiated by a fourth order Runge-Kutta method,[13] using a time step of 3.5 10^{-4} ps (23.3 times larger than the time step used in the photodissociation process),[7] while the evaluation of the derivatives for the kinetic energy terms has been performed in momentum space (Fourier transform using the FFTW package[14]). Furthermore, in order to avoid non-physical reflections of the effective wave

function of helium in the limits of the grid, quartic negative imaginary potentials (NIPs)[15] have been applied in these regions. More details on the theoretical methods used can be found in Ref. 7.

5.3 Results and discussion

As already indicated above (cf. Eqs. 5.1-5.3), there are two steps strongly related to the photodissociation process of Cl_2 embedded in helium nanodroplets. Even though the separation of steps 5.2 and 5.3 is useful for the (intuitive) understanding of the global process (photodissociation of the diatomic molecule and relaxation of the droplet), they are really not so clearly separated, and this point should be clarified in order to define the beginning of the process of interest in this work.

From a purely energetic point of view, we could consider that the relaxation process begins when the first helium atom evaporates from the droplet, releasing some energy (kinetic) with it. However, this would lead to widely different initial conditions for the relaxation process, depending on the initial size of the droplet. This is because after a very short time from the $Cl_2\left(X^1\Sigma_g^+\right) + h\upsilon \rightarrow Cl_2(B^3\Pi_u(0_u^+))$ electronic transition, energy is being transferred from the molecule to the helium and shortly after the helium evaporation begins. With this criterion there would be initial conditions of the systems for which the impurities would be still inside the droplet (big droplet sizes), while in other cases the resulting atomic photofragments would be about to leave the helium environment (small droplet sizes).

Taking into account this fact, we have considered that the relaxation process begins when the chlorine atoms have left the droplet and are far enough, so that there is practically no interaction between the droplet and them. More concretely, we have defined the starting point of the relaxation process as the time for which the norm of the diatomic wavepacket in the system is less than $\approx 5.0\ 10^{-5}$. This approximately corresponds to a ratio between the helium-Cl_2 interaction energy and the helium energy of less than or equal to 1 part in 1000. This choice has some consequences as, for example, that the more excited nanodroplets at the beginning of the relaxation process are the smaller ones, even though they have received less energy from Cl_2.[7] The values of several relevant properties at the relaxation initial time definition are reported in Table 5.1, and from now on to label each nanodroplet we have kept

its initial number of ^{4}He atoms (i.e.; the number before the Cl_2 electronic transition; N_0 = 50, 100, 200, 300 and 500).

The main properties (extensive variables) obtained in the TDDFT calculations showing the temporal evolution of the helium nanodroplets relaxation are the energy (E) and the number of ^{4}He atoms (N). In Figure 5.1 is shown how E and N evolve with time and it can be seen that the main energy (and ^{4}He atoms) release takes place during the first ≈5 ps. Using these plots an estimation of the time scale of the relaxation process can be inferred, taking into account the asymptotic character of the two variables with time. The time-scale obtained is of the order of several hundred of picoseconds, and the concrete values of the relaxation times are somewhat dependent on the nanodroplets considered. Some additional useful information is provided in Figure A5.1 (*E vs t*; 0-10 ps) and Figure A5.2 (% of ^{4}He atoms in the nanodroplets *vs* time; 0-150 ps) of Appendix.

Table 5.1. Values of some properties at the relaxation initial time.

N_0	**50**	**100**	**200**	**300**	**500**
Elapsed time from B←X transition (ps)	3.65	3.36	3.43	4.30	7.08
Cl_2 wave packet norm	$5.0\ 10^{-5}$	$4.6\ 10^{-5}$	$5.0\ 10^{-5}$	$4.9\ 10^{-5}$	$4.1\ 10^{-5}$
N_i [a]	43.48	91.78	190.22	287.89	480.96
Interaction energy (K) [b]	$4.9\ 10^{-4}$	$6.2\ 10^{-2}$	$6.0\ 10^{-2}$	$8.6\ 10^{-2}$	$7.7\ 10^{-2}$
Helium energy (K)	179.01	150.08	-60.33	-565.69	-1844.47
e (K) [c]	4.12	1.64	-0.32	-1.96	-3.84
Interaction energy/Helium energy ($^o/_{oo}$)	$2.7\ 10^{-6}$ (0.00)	$4.1\ 10^{-4}$ (0.41)	$-9.9\ 10^{-4}$ (-0.99)	$-1.5\ 10^{-4}$ (-0.15)	$-4.2\ 10^{-5}$ (-0.04)

[a] Initial number of He atoms.
[b] Cl_2-helium interaction energy.
[c] Energy per ^{4}He atom.

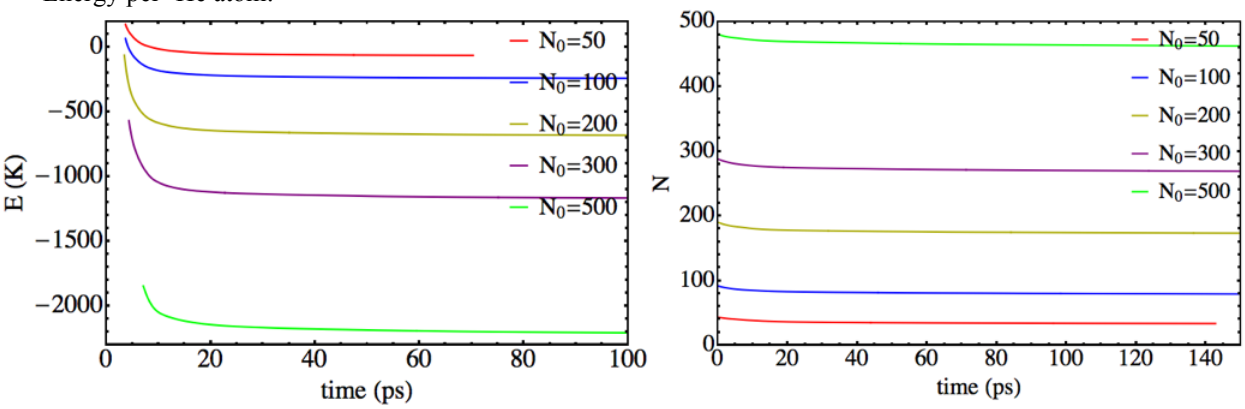

Figure 5.1. Time evolution of the energy (left) and number of ^{4}He atoms (right) for nanodroplets of different sizes.

However, *E* and *N* are extensive physical magnitudes and due to this they are not the most suitable properties to follow the relaxation process. In order to achieve a better characterization of the relaxation process, the intensive magnitude "energy per ^{4}He atom" ($e \equiv E/N$) has been considered for all the excited nanodroplets (cf. Figure 5.2) and compared to the ground state corresponding values (e_{gs}). This has been done by calculating a wide set of pure helium nanodroplets in the ground state (ranging from 25 to 10000 ^{4}He atoms), using the same DFT functional approximation employed in the TDDFT study and fitting the e_{gs} values to the well-known liquid drop model,[16]

$$e_{gs}(N) \equiv \frac{E_{gs}(N)}{N} = a_v + a_s N^{-\frac{1}{3}} + a_c N^{-\frac{2}{3}} + a_d N^{-1} \qquad (5.5)$$

where a_v, a_s, a_c, and a_d correspond to the volume energy, surface energy, curvature energy, and correction parameters, respectively (a_v=-7.156 K, a_s=17.47 K, a_c=4.027 K and a_d=-26.33 K, while $a_d N^{-1}$ is a correction factor which allows to include small droplets in the fitting). In order to better compare the relaxation process for the different droplets, we define the excitation energy per ^{4}He atom as $\Delta e(N,t) \equiv e(N,t) - e_{gs}(N)$, which is also an intensive property. This property defines the asymptotic limit in which the relaxation process will be fully accomplished, i.e., $\lim_{t \to relax.\ time} \Delta e(N,t) = 0$.

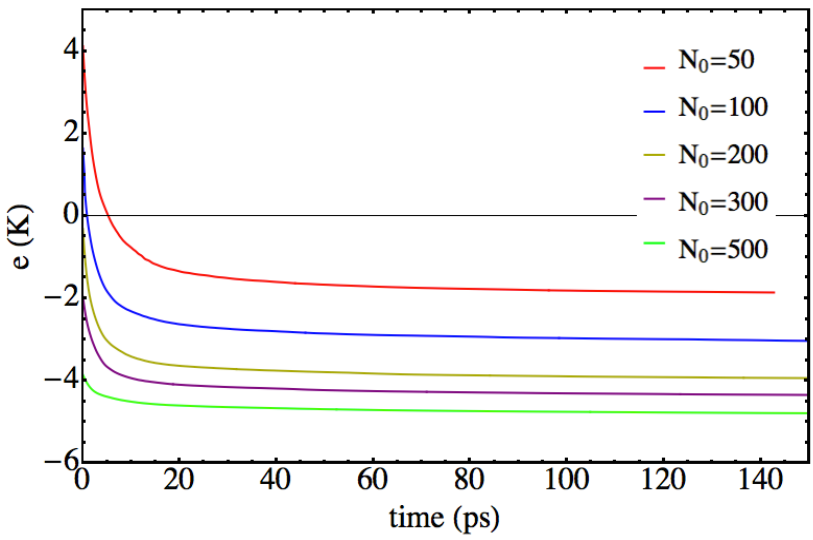

Figure 5.2. Time evolution of the energy per ^{4}He atom for different nanodroplets.

The excitation energy per ^{4}He atom decreases with time as it is shown in Figure 5.3. Besides, *Δe* decreases when increasing the nanodroplet size. As already mentioned, this occurs because the main energy exchange taking place between the Cl_2 molecule and the

droplet is produced when the chlorine atoms collide with the first solvation shell (which is common for all the droplets), and the time needed to complete the photodissociation process increases with the size. Hence, big nanodroplets have more time to release energy, even though energy exchange is still present during the translational motion of the Cl atoms inside the droplet.

The de-excitation (relaxation) curves fit well to a simple inverse law with respect to time, and two dynamic regimes are evident (the high and low excitation energy per ^{4}He atom regions) linked by a transition zone (Figure 5.3). Furthermore, the related $1/\Delta e$ *vs* t dependence is plotted in Figure 5.4 and it is observed that also in this case all curves follow the same pattern. The fits shown in this figure correspond to the low excitation regime and it comes out that the slopes of the straight lines increase with the droplet size until they reach an, essentially, limit value for the biggest droplets considered here (i.e., N_0 = 200, 300 and 500). These facts suggest that for this regime the dissipation energy time evolution depends on the size but with a threshold or reference value from which this dependency almost disappears. A somewhat similar though more complex behaviour is found for the high excitation region (cf. Figure A5.3 in Appendix).

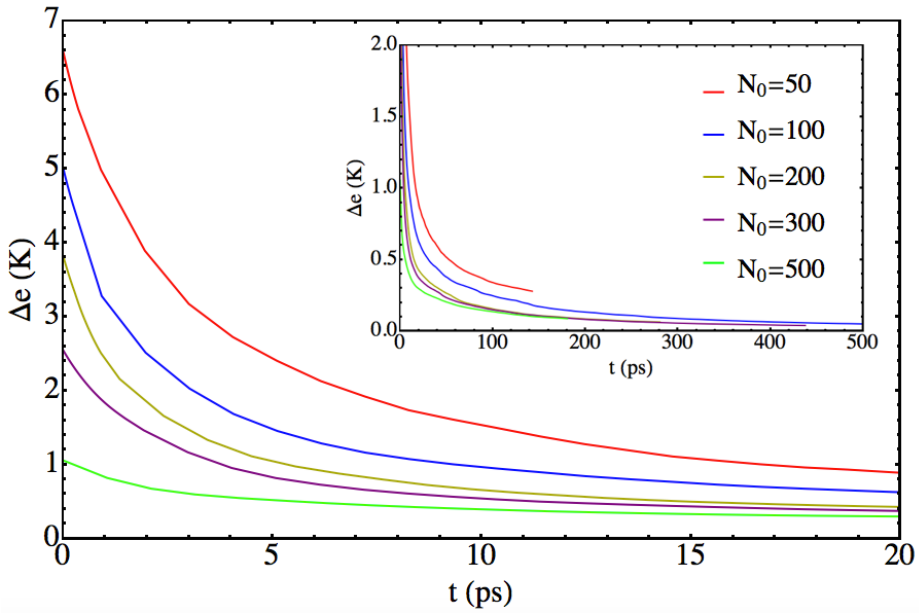

Figure 5.3. Time evolution of the excitation energy per ^{4}He atom for different nanodroplets.

Regarding the dynamics of the relaxation mechanism of the nanodroplets, the analysis of the time evolution of the helium density (Figure 5.5) shows that it is common to all of

them. This is consistent with the similarity we have also found for other properties of the nanodroplets.

Thus, at the beginning of the relaxation process intense oscillations are evident in the helium density, that are particularly important along the z axis (axis along which the photodissociation of the Cl_2 molecule has previously occurred), specially at low times. The magnitude of the oscillations gradually decreases with time, becoming essentially coincident first the helium densities along the x and y axis (which were already rather similar at the beginning of the relaxation). Besides, the helium density along the z axis, the most initially disturbed density, is becoming progressively more similar to the density along the x and y axis and, finally, all them become essentially coincident.

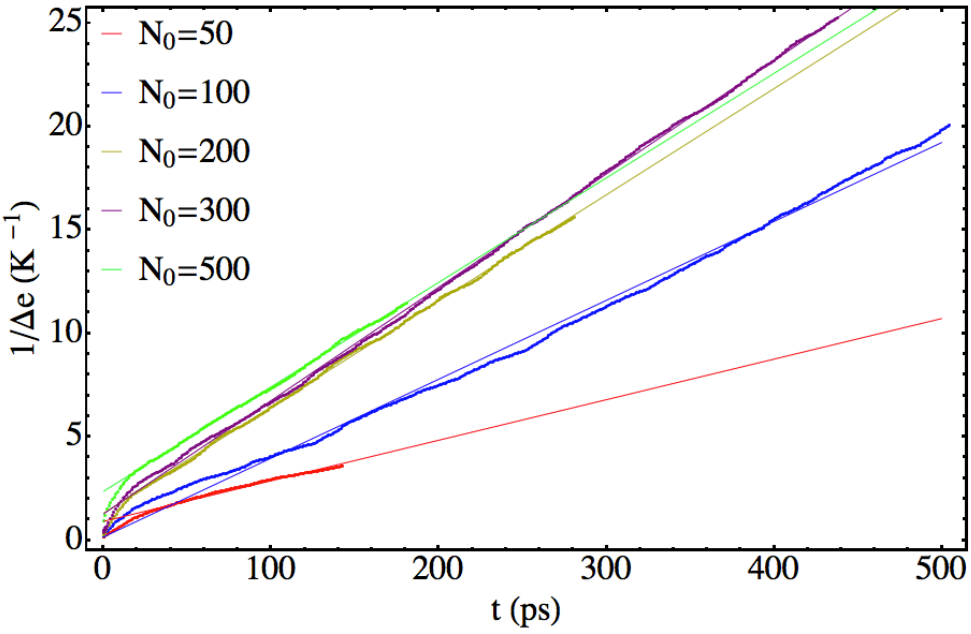

Figure 5.4. Time evolution of the inverse of the excitation energy per ^{4}He atom for different nanodroplets.

In Figure 5.5 the radial density of helium (i.e., the density along the z axis) and the density in the xy and xz planes are presented, for the relaxing helium nanodroplet with N_0=500 and considering small (t=3.0 ps) and large (t=518.7 ps) relaxation times. Analogous plots but for N_0=100 have been reported in Figure A5.4 of the Appendix. Moreover, in Movies 5.1-5.3 (N_0=100) and Movies 5.4-5.6 (N_0=500) of the Appendix the time evolution of these densities are shown, taking into consideration time intervals that correspond to low, intermediate and high relaxation times.

On the other hand, to obtain a deeper insight into the relaxation process, we propose a (very) simple model where we have assumed that the change of energy per ^{4}He atom of the nanodroplet per evaporated ^{4}He atom $\left(\frac{de}{dN}\right)$ is proportional to the intensive excitation Δe; i.e., we consider that this is the only driving force governing the amount of energy carried by an evaporated ^{4}He atom. Of course, this may be considered as a rough approximation, since we neglect both the size and shape effects, but the slight dependency of the shape of the excitation time evolution with the nanodroplet size supports the main idea of this model. From this approach we expect to be able to account for all the nanodroplets studied, regardless of their size, since this would show the characteristics of the common part of all the droplets, i.e., the liquid helium.

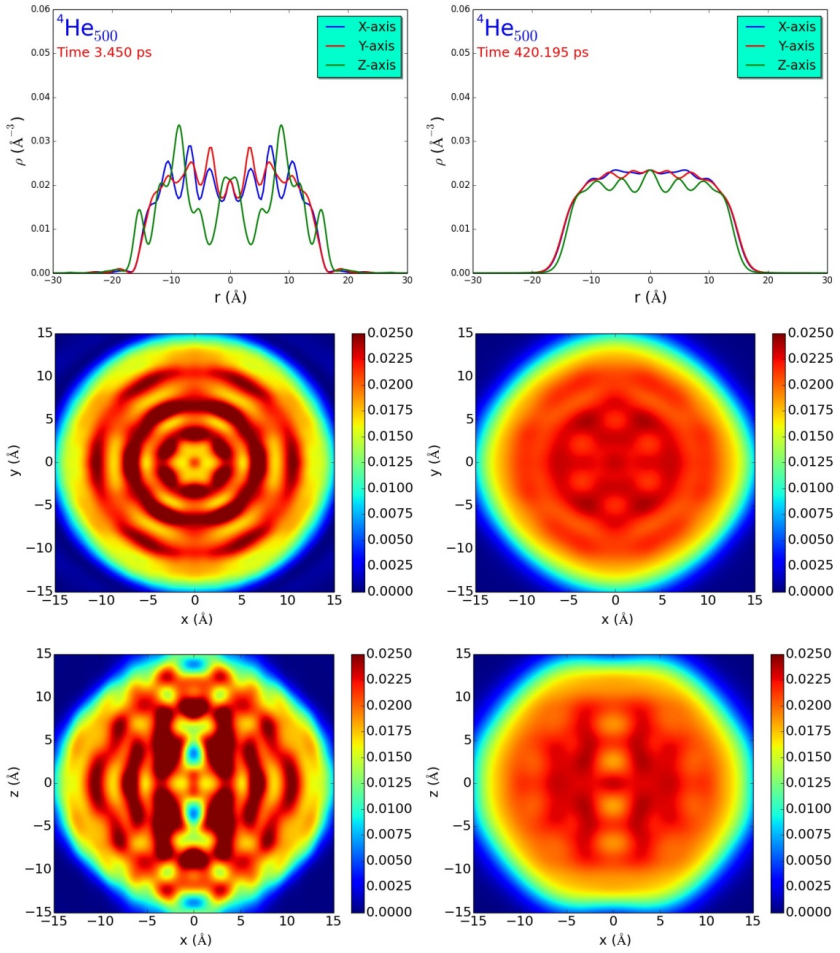

Figure 5.5. Helium density (radial (i.e., along the z axis), xy plane and xz plane densities) for the relaxing helium nanodroplet with N_0=500 at t=3.0 ps (left) and t=518.7 ps (right).

From the calculation of the $\frac{de}{dN}$ derivative and the representation of these data versus the Δe excitation per ^{4}He atom (Figure 5.6), it follows that the $\frac{de}{dN}$ *vs* Δe plots almost follow a straight line for the low excitation regime, which points out the common nature of all of them (i.e., the superfluid liquid helium). This tendency does not take place for the high excitation regime, where a more complex dependency of $\frac{de}{dN}$ is evident. Therefore, although the simple model proposed here does not account for all the physics of the relaxation process, we infer that the excitation energy per ^{4}He atom of the nanodroplet is the main driving force that dictates the de-excitation energy per ^{4}He atom of the nanodroplet obtained by the evaporation of one helium atom.

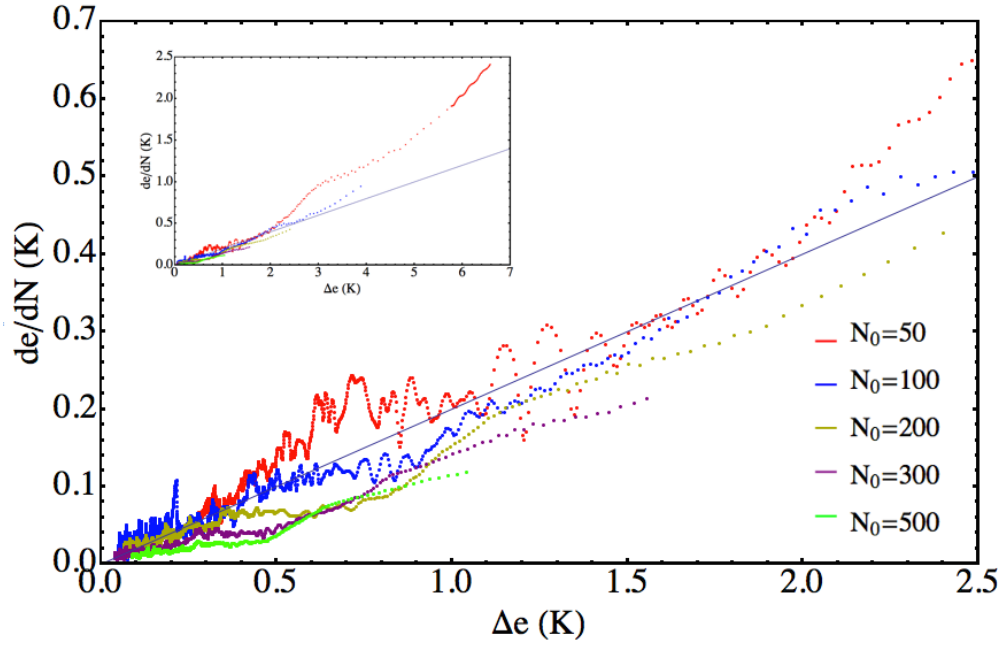

Figure 5.6. Derivative of the energy per ^{4}He atom with respect to the number of helium atoms versus the excitation energy per ^{4}He atom, for different nanodroplets.

On the other hand, we have also explored the suitability of describing the relaxation kinetics as a unimolecular fragmentation process, i.e., as a unimolecular chemical reaction of a very large molecule (the whole nanodroplet). In this context, we have fitted the obtained TDDFT data to the well known Rice-Ramsperger-Kassel (RRK) statistical kinetics model for unimolecular reactions.[17]

In short, this model describes the molecular internal degrees of freedom as a set of coupled harmonic oscillators, and the molecular decomposition (fragmentation) is supposed to occur when a certain amount of energy is placed in one of them. Thus, for a given excess of

energy of the system, $\mathcal{E}$ (see below), the fragmentation rate constant, $k(\mathcal{E})$, is determined by calculating the probability to have an energy above a threshold value, $\mathcal{E}_0$, in a given oscillator (i.e., in the bond to be broken). The parameters of the model are the number of oscillators, s, the characteristic harmonic vibrational frequency of the oscillators, υ, and the threshold energy $\mathcal{E}_0$ required for the fragmentation (evaporation of a helium atom in the present case), and the classical RRK rate constant has the following expression:[17]

$$k(\mathcal{E}) = \upsilon\left(1 - \frac{\mathcal{E}_0}{\mathcal{E}}\right)^{s-1} \tag{5.6}$$

The rate constant $k(\varepsilon)$ has been evaluated for each single atom vaporization process that happens during the relaxation process of each selected nanodroplet (Figure 5.7). Besides, since we have employed a continuous theoretical method (TDDFT) to describe the nanodroplets dynamics, in order to apply the RRK model to the present problem, we have performed a numerical integration to obtain the (mean) values of the properties (k, ε) associated to each atomic evaporation.

For each nanodroplet, we have fixed the $\mathcal{E}_0$ value to the average binding energy per ^{4}He atom of the set of ground state nanodroplets ranging from N=N_i to N=N_f, i.e.,

$$\mathcal{E}_0 = \frac{1}{(N_f - N_i)} \int_{N_i}^{N_f} \mathrm{e}_{gs}(N) N dN \tag{5.7}$$

where the subscripts f and i stands for final and initial number of atoms of the relaxing nanodroplet, respectively. It has been checked that variations in the $\mathcal{E}_0$ value do not lead to significant changes in the profiles of the curves in Figure 5.7, but only to small variations in the υ parameter (in the fitting procedure to obtain the optimal υ and s parameters of Eq. 5.6). Following the same idea, the $\mathcal{E}$ value of this model has been calculated as the mean value of the excitation energy obtained for each atomic evaporation (where the "i" symbol in Eq. 5.8 refers to an arbitrary single atom vaporization and not to the initial situation of the system):

$$\mathcal{E} = \int_{N_i}^{N_i - 1} \Big(E(N,t) - N e_{gs}(N)\Big)\, dN \tag{5.8}$$

The obtained points for the rate constants (TDDFT calculations) and the RRK fitting parameters (υ, s) are collected in Figure 5.7 and Table 5.2, respectively. The agreement

between the quantum dynamics TDDFT results and this fitting is quite good for all the droplets studied and the determined values of the RRK parameters are reasonable.

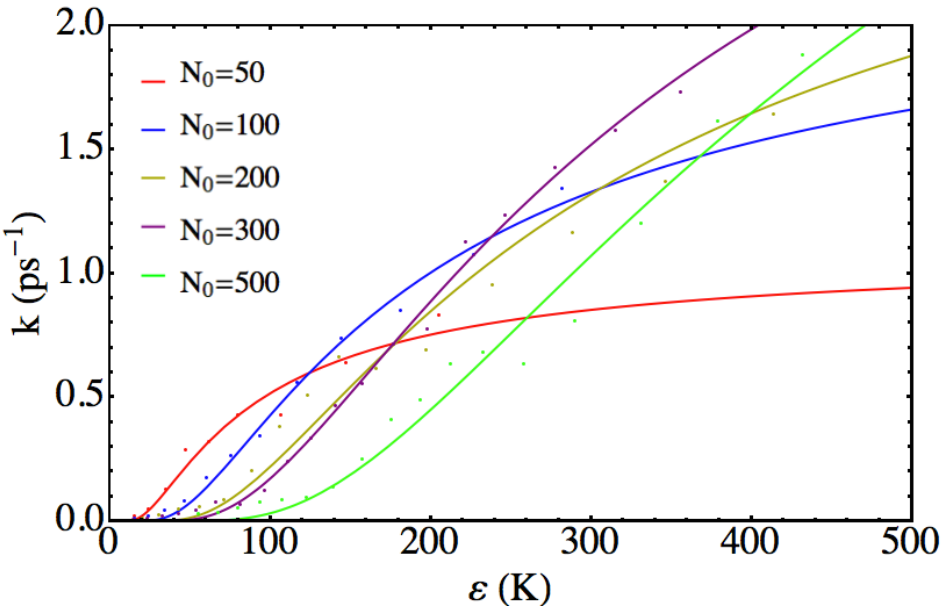

Figure 5.7. Rate constant for ^{4}He atoms evaporation versus the excitation mean energy for different nanodroplets. The curves correspond to the fitting according to the RRK rate constant expression (eq 6; see text).

Table 5.2. Optimal parameters for the RRK statistical unimolecular chemical kinetics model.

N_0	50	100	200	300	500
υ (ps^{-1})	1.09	2.32	3.18	4.41	5.95
s^{-1}	31.8	50.7	64.0	70.7	104.1
ε_0(K)	2.33	3.28	4.09	4.48	4.90

Finally, we have also investigated a large number of average intensive properties in order to determine possible correlations between them. We have found rather clear correlations in two cases: in the percentage of ^{4}He atoms evaporated in the relaxation process of the nanodroplets and in the increment of the mean energy per ^{4}He atom in the nanodroplet corresponding to the evaporation of one ^{4}He atom, i.e., $\frac{e_f - e_i}{N_f - N_i}$. More concretely, it has been found that these properties follow a linear dependence with respect to the initial excitation energy per ^{4}He atom of the nanodroplets (Figure 5.8). This also reinforces our assumption that Δe is the most important property guiding this relaxation process.

The number of evaporated ^{4}He atoms ranges from 10 (N_0=50) to 19 (N_0=500), and in Figure 5.8 is shown that the percentage of ^{4}He atoms evaporated during the relaxation

depends in a significant way on the nanodroplet size: 23.0, 15.1, 9.4, 7.3, and 3.9% for N_0=50, 100, 200, 300, and 500, respectively (where, of course, the percentages are given with respect to the corresponding N_i values; cf. Table 5.1). This results from the fact that the smaller the droplet size the higher the excited character of the droplet at the initial relaxation time, as indicated at the beginning of this section.

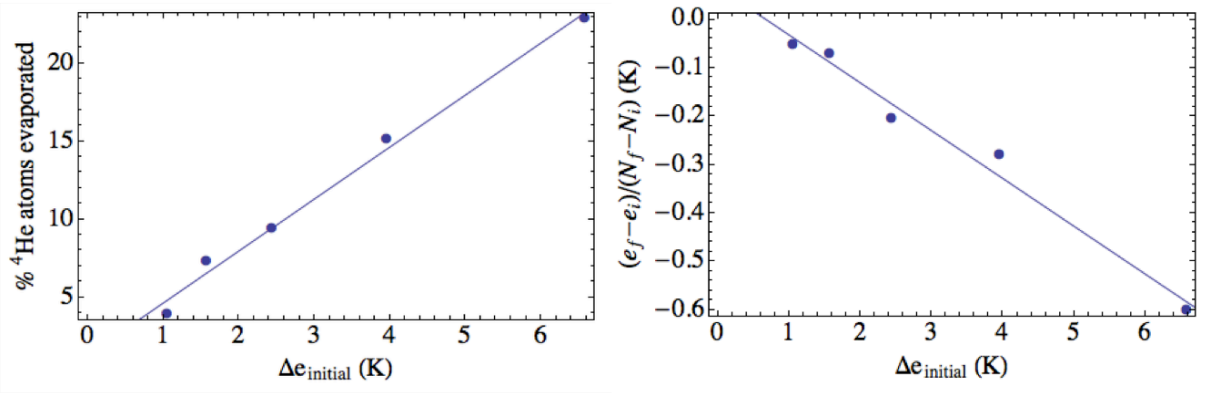

Figure 5.8. Percentage of ^{4}He atoms evaporated (left) and ratio between the change in the energy per ^{4}He atom in the nanodroplet and the number of ^{4}He atoms evaporated (right) for the relaxation processes investigated, and in both cases as a function of the initial excitation energy per ^{4}He atom.

5.4 Summary and conclusions

The dynamics of superfluid helium nanodroplets, ^4He_N, relaxation process (N=50, 100, 200, 300 and 500) that take place after the photodissociation of a Cl_2 embedded molecule [arising from the $Cl_2\left(X^1\Sigma_g^+\right) + h\upsilon \rightarrow Cl_2(B^3\Pi_u(0_u^+))$ electronic transition] has been studied at the time-dependent DFT theoretical level, extending a previous investigation which was focused on the photodissociation step. To the best of our knowledge, this is the first time that the dynamics of this type of process has been investigated.

The relaxation mechanism is common for all nanodroplets and it occurs in the timescale of several hundred picoseconds. Moreover, a simple dependence (Δe vs t inverse law) has been found for the evolution of the excitation energy per ^{4}He atom of the nanodroplet with time. This applies in two regimes, the high and low excitation energy per ^{4}He atom regions, even though a somewhat more complex behavior is evident for the former case.

The results have been rationalized by means of two simple models. The first one consists in a phenomenological approach, where it is proposed that the energy released by the

evaporation of a ^{4}He atom is, simply, proportional to the excitation energy per ^{4}He atom of the droplet. Despite its simplicity, the accuracy for this model is accurate enough for low excitation energies and points out the common aspects of different droplets, since the parameters of the fit are unique for all of them. The second model corresponds to the well-known RRK statistical kinetic model for unimolecular reactions, from which a quite satisfactory agreement has been also obtained.

We hope that this study will encourage further research on this little-known and interesting research topic involving superfluid nanodroplets of helium-4.

5.5 Appendix

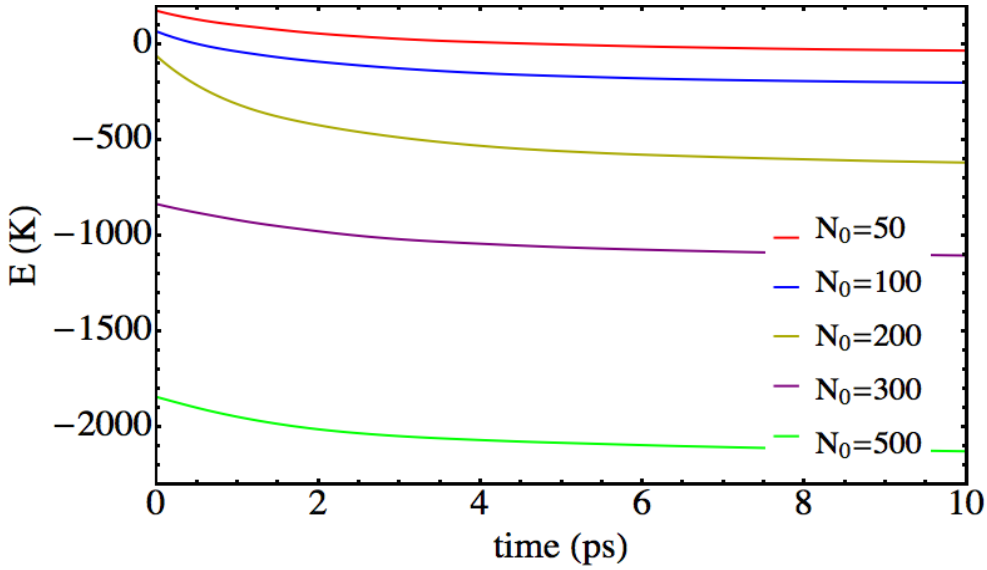

Figure A5.1. Time evolution of the energy of the nanodroplets in the time interval 0-10 ps, for nanodroplets of different sizes.

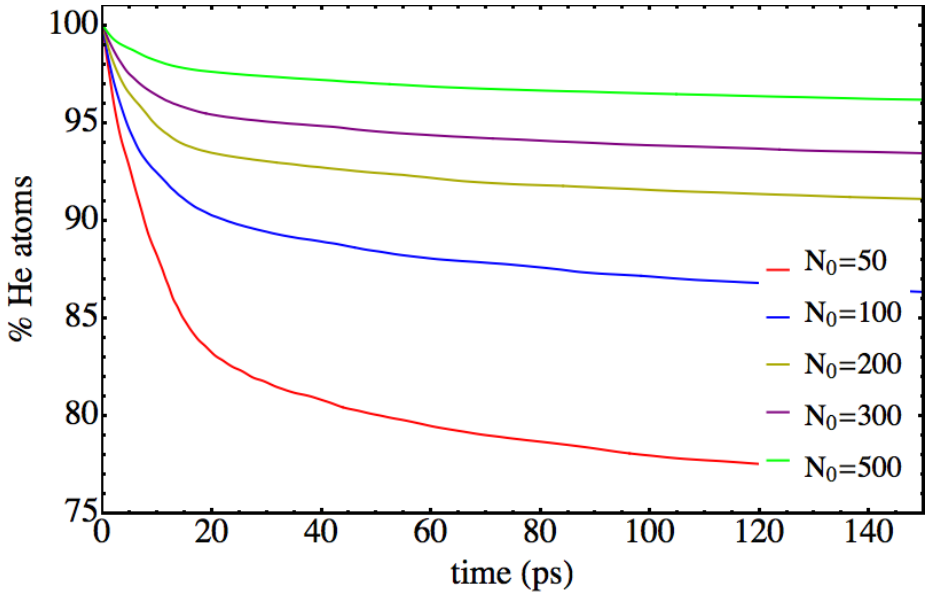

Figure A5.2. Time evolution of the percentage of ^{4}He atoms in the nanodroplets in the time interval 0-150 ps, for nanodroplets of different sizes

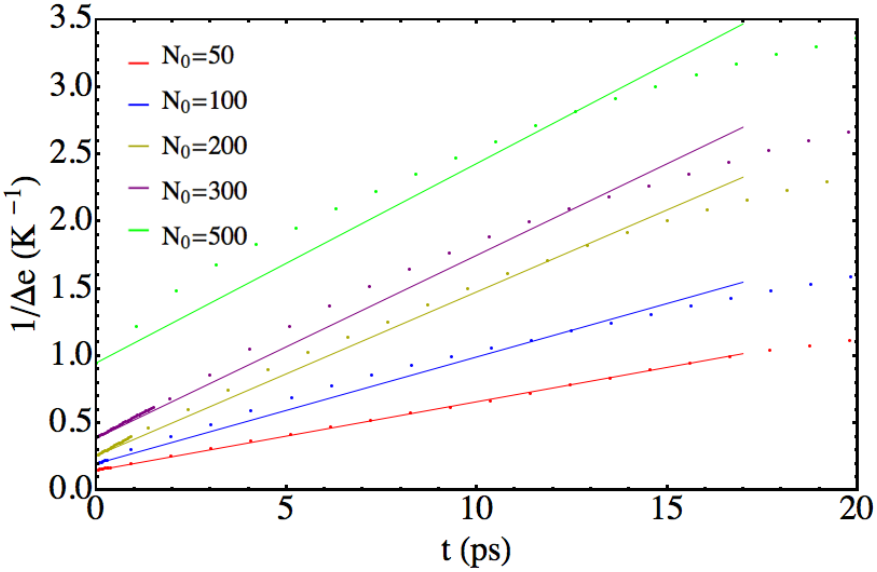

Figure A5.3. Time evolution of the inverse of the excitation energy per ^{4}He atom for different nanodroplets in the high excitation regime.

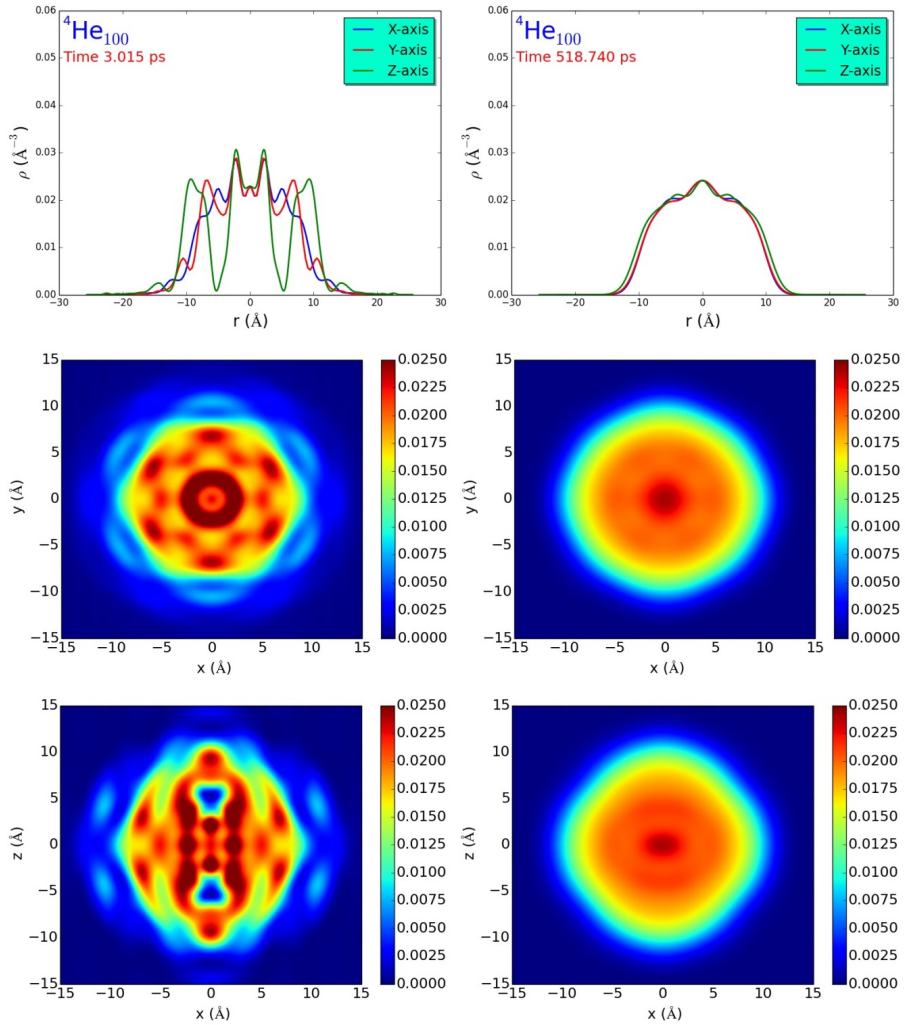

Figure A5.4. Helium density (radial (i.e., along the z axis), xy plane and xz plane densities) for the relaxing helium nanodroplet with N_0=100 at t=3.0 ps (left) and t=518.7 ps (right).

Movie 5.1. Time evolution of the helium density (radial (i.e., along the z axis), xy plane and xz plane densities) for the relaxing helium nanodroplet with N_0=100 within the 0.4-23 ps time interval. For the xz plane the density is given in both 2D and 3D representations (in the last case the colours code does not apply and the density value is proportional to the height of the plot).

Movie 5.2. The same as movie 1 but for the 100-123 ps time interval.

Movie 5.3. The same as movie 1 but for the 550-570 ps time interval.

Movie 5.4. Time evolution of the helium density for the relaxing helium nanodroplet with N_0=500 within the 0.5-22 ps time interval. For the xz plane the density is given in both 2D and 3D representations (in the last case the colours code does not apply and the density value is proportional to the height of the plot).

Movie 5.5. The same as movie 5.4 but for the 100-120 ps time interval.

Movie 5.6. The same as movie 5.4 but for the 493-517 ps time interval.

5.6 References

1. Toennies, J. P.; Vilesov, A. *Angew. Chem. Int. Ed*. **2004**, *43*, 2622.

2. Yang, S.; Ellis, A. M.; Spence, D.; Feng, C.; Boatwright, A.; Latimer, E.; Binns, C. *Nanoscale*. **2013**, *5*, 11545.

3. Latimer, E.; Spence, D.; Feng, C.; Boatwright, A.; Ellis, A. M.; Yang, S. *Nano Lett.* **2014**, *14*, 2902.

4. Barranco, M.; Guardiola, R.; Hernández, S.; Mayol, R.; Navarro, J.; Pi, M. *J. Low Temp. Phys*. **2006**, *142*, 112.

5. Mateo, D.; Hernando, A.; Barranco, M.; Loginov, E.; Drabbels, M.; Pi, M. *Phys. Chem. Chem. Phys.* **2013**, *15*, 18388.

6. Brauer, N. B.; Smolarek, S.; Loginov, E.; Mateo, D.; Hernando, A.; Pi, M.; Barranco, M.; Bruma, W. J.; Drabbels, M. *Phys. Rev. Lett*., **2013**, *111*, 153002.

7. Vilà, A; González, M.; Mayol, R. *J. Chem. Theory Comput.* **2015**, *11*, 899.

[8]. Brink, D. M.; Stringari, S. *Z. Phys. D*, **1990**, *15*, 257.

9. Lehmann, K. K.; Dokter, A. M. *Phys. Rev. Lett*., **2004**, *92*, 173401.

10. Dalfovo, F.; Guilleumas, M.; Lastri, A.; Pitaevskii, L.; Stringari, S. *J. Phys.: Condens. Matter* , **1997**, *9*, L369.

11. Dalfovo, F.; Lastri, A.; Pricaupenko, L.; Stringari, S.; Treiner, J. *Phys. Rev. B*, **1995**, *52*, 1193.

12. Ralston, A.; *Numerical Integration Methods for the Solution of Ordinary Differential Equations. In Mathematical Methods for Digital Computers*, John Wiley & Sons, **1960**.

13. Thompson R. J. *Commun. ACM*. **1970**, *13*, 739.

14. Frigo, M.; Johnson, S. G. *IEE Proceedings,* **2005**, *93*, 216.

15. Vibók A.; Balint-Kurti G. G. *J. Phys. Chem.* **1992**, *96*, 8712.

16. Bohr, A.; Mottelson, B. *Nuclear Structure,* Benjamin: New York, **1975**.

17. Steinfeld, J. I.; Francisco, J. S.; Hase, W. L. *Chemical Kinetics and Dynamics*, Prentice Hall: Englewood Cliffs, **1998**.

6. Quantum resonances in the photodissociation of $Cl_2(B)$ in superfluid helium nanodroplets $(^4He)_N$

6.1 Introduction

From a physical perspective, the study of the properties (structure, energy and dynamics) of superfluid helium nanodroplets (T=0.37 K), $(^4He)_N$, is a well established and active research area. [1,2] These systems can act as a low temperature liquid matrix which allow to carry out high resolution spectroscopic studies of embedded atomic or molecular species (thanks to the chemically inert character of helium and the superfluid behavior of helium-4 below a critical temperature; T=2.17 K). Furthermore, these nanodroplets are also of great interest since they correspond to intermediate size quantum fluid systems, lying between the bulk liquid and molecular clusters.

From a chemical point of view, although the research activity developed up to now on the chemical reactivity in helium nanodroplets has been important (see, e.g., Refs. 3, 4, and the references cited therein), its intensity is not comparable to the effort carried out in the context of the studies of physical type. Recently, however, it appears that the chemical interest on these low temperature fluid systems has increased significantly; and this probably occurs thanks to the new possibilities offered by them in the chemical synthesis of novel chemical species. In fact, they allow to synthesize species that would not be stable in gas phase as, for instance, some metallic nanoclusters[5] and nanowires.[6]

On the other hand, little effort has been addressed up to date to explore the reaction dynamics in the $(^4He)_N$ quantum fluid. Thus, as far as we know, only a set of reaction dynamics experiments (photodissociation of alkyl iodides in $(^4He)_N$) has been reported so far.[7,8,9] On the theoretical side, in addition to our recent paper[4] and the present work on the title system, only a reaction dynamics contribution has been found in the literature;[10] which is

centered in the same problem examined here, but considering both a very different approach and strongly diverse physical conditions (non-superfluid helium nanodroplets at T=4 K with up to 200 ^{4}He atoms).

The present study extends and complements our recent investigation on the photodissociation of homonuclear diatomic molecules in superfluid helium nanodroplets (T=0.37 K), where the theoretical method proposed by us was applied for the first time to the photodissociation of a Cl_2 excited embedded molecule (B←X electronic transition): $Cl_2(X)@(^4He)_N + h\nu \rightarrow [Cl_2(B)@(^4He)_N]^* \rightarrow Cl(^2P_{3/2}) + Cl(^2P_{1/2}) + [(^4He)_{N'}]^* + (N\text{-}N')\ ^4He$, $\lambda \approx 400$ nm (3.10 eV),[11] where the term (N-N') ^{4}He merely shows the total number of vaporized He atoms with N maximum=500 (Figure 6.1).

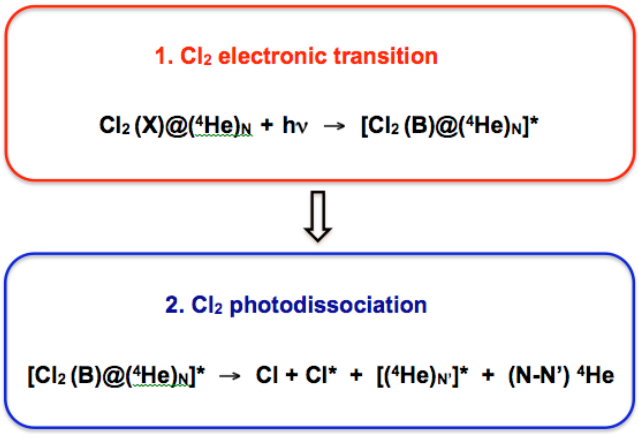

Figure 6.1. Schematic representation of the two steps involved in the study of the photodissociation of an embedded Cl_2 molecule in a helium nanodroplet: electronic excitation of Cl_2 from the ground (X) to the excited (B) electronic state followed by the photodissociation of $Cl_2(B)$. Some ^{4}He atoms of the nanodroplet are vaporized in step 2.

More concretely, here we have analyzed in detail the (confinement) quantum resonances which are present in this reactive system, and arise from the interaction between $Cl_2(B)$ and the helium solvent. The resonance effects are clearly evident in the final Cl atomic photofragment velocity distributions, which show strongly oscillating patterns with a significant number of well defined peaks for all the nanodroplets (N=50, 100, 200, 300 and 500). Even though resonances are one of the most interesting phenomena in chemical physics[12] and, of course, in reaction dynamics,[13,14] they were not the main focus of our previous work,[4] because of its very specific character and often complex analysis[12,13,14] (even for small systems).[15]

This chapter is organized as follows: in section 6.2 the theoretical methods used are briefly described, section 6.3 is dedicated to the description and analysis of the main results obtained and, finally, the summary and conclusions are given in section 6.4. Additional useful data can be found in the Appendix.

6.2 Theoretical methods

An exhaustive description of the theoretical framework used to study the photodissociation dynamics of $Cl_2(B)$ in helium nanodroplets can be found in Ref. 4. However, here we briefly summarize the main features, for the sake of completeness.

The hybrid theoretical scheme proposed in our previous work,[4] where the time dependent density functional theory (TDDFT)[16] and the quantum wave packet dynamics[17] methods have been used to describe the evolution of the helium nanodroplet and the relative coordinate of the homonuclear diatomic molecule, respectively, has also been used here. So, we have coupled one of the key procedures employed to describe rather large systems of bosonic liquid helium (from a hundred to thousands of ^{4}He atoms) and a common method used in gas phase reaction quantum dynamics, allowing in this way to compare the theoretical results with the experimental data, when available.

We have neglected the rotational degree of freedom of the molecule as a first approximation to this problem. Nevertheless, this assumption is well justified considering the conditions of nanodroplet and the rotational constants of the chlorine molecule.[4] Within this theoretical approach the two coupled equations of motion governing the evolution of the helium effective complex wave function, defined as $\Psi_{He}(t, \boldsymbol{R}_{He}) \equiv \sqrt{\rho_{He}(t, \boldsymbol{R}_{He})}$, and the relative coordinate wave function (wave packet (WP)), $\varphi_{Cl_2}(r)$, are respectively the following:

$$i\hbar \frac{\partial}{\partial t}\Psi_{He}(\boldsymbol{R}_{He}) =$$

$$= \left[-\frac{\hbar^2}{2m_{He}}\boldsymbol{\nabla^2} + \int dr\, V_{He-Cl_2(B)}(r, \boldsymbol{R}_{He}) \left|\varphi_{Cl_2}(r)\right|^2 + \frac{\delta \mathcal{E}_c[\rho_{He}]}{\delta \rho_{He}}\right] \Psi_{He}(\boldsymbol{R}_{He}) \quad (6.1)$$

$$i\hbar\frac{\partial}{\partial t}\varphi_{Cl_2}(r) =$$

$$= \left[-\frac{\hbar^2}{m_{Cl_2}}\frac{\partial^2}{\partial r^2} + \int d\boldsymbol{R}_{He} V_{He-Cl_2(B)}(r, \boldsymbol{R}_{He})\rho_{He}(\boldsymbol{R}_{He}) + V_{Cl_2(B)}(r)\right]\varphi_{Cl_2}(r) \quad (6.2)$$

where $\rho_{He}(\boldsymbol{R}_{He})$ and $\mathcal{E}_c[\rho_{He}]$ are the density and the sum of the correlation and potential energy densities of liquid ^{4}He, respectively, and the Orsay-Trento phenomenological functional (T=0 K)[16] is used to describe the superfluid helium, which is introduced via the term $\frac{\delta\mathcal{E}_c[\rho_{He}]}{\delta\rho_{He}}$.

These equations have been solved numerically by discretization of the space in a grid of points for each degree of freedom, using standard methods. Furthermore, negative imaginary potentials (NIPs) have been used so as to avoid artificial reflections of the Cl_2 and helium wave functions at the grid limits (cf. Ref. 4). The final atomic (Cl) velocity distribution arising from the photodissociation has been determined from the asymptotic (Cl + Cl*) Cl_2 relative coordinate wave function, described in momentum representation, before applying the molecular NIP.

6.3 Results and discussion

6.3.1 Early times of the photodissociation process and resonances

We have recently studied the dynamics of the photodissociation process $Cl_2(X)@(^4He)_N + h\nu \rightarrow [Cl_2(B)@(^4He)_N]^* \rightarrow Cl(^2P_{3/2}) + Cl(^2P_{1/2}) + (^4He)_{N'} + (N\text{-}N')\ ^4He$ (Figure 6.1), which takes place on the picosecond time scale (0.85, 1.14, 1.63, 2.01, and 2.57 ps for N = 50, 100, 200, 300, and 500, respectively);[4] and in the present chapter we focus our attention on the quantum resonances which occur in this reaction which, as indicated before, were described but not analyzed in our previous contribution because of its complexity. For the time interval of main interest here there is no vaporization of He atoms from the nanodroplet (this process begins, e.g., around 0.56 and 0.70 ps for N=50 and 500, respectively).

The excitation of the embedded Cl_2 molecule from the ground to the B excited state leads to the formation of what can be considered as a metastable (quasibound) state. In fact, differing from what happens in gas phase, here the Cl_2 excited molecule is surrounded and

temporarily confined by the helium nanodroplet and due to this it takes a substantially larger amount of time to produce the photodissociation of $Cl_2(B)$ into $Cl(^2P_{3/2}) + Cl(^2P_{1/2})$.

Thus, the "time delay" observed, which has been defined as the time required for the WP(r) to reach a <r> expected value equal to the initial diameter of the nanodroplet (i.e., the photodissociation time definition)[4] minus the time required for the WP(r) in the gas phase to reach the same <r> value, takes the following values: 0.23, 0.39, 0.71, 0.98 and 1.38 ps for N = 50, 100, 200, 300 and 500, respectively.

The interaction of the molecule with the helium environment leads to quantum interferences which are evident in the Cl_2 wave packet as described and analyzed below (movies 5.1 and 5.2). This leads to a rich structure (oscillations) in the Cl_2 wave function, which is initially (early times) much more evident in the Cl_2 wave packet in momentum representation, and that also becomes evident for the main observable of this system (final velocity distribution of the Cl atoms).

In spite of its large conceptual interest the quantum confinement has been the object of little attention.[18,19] The existence of confinement resonances was proposed theoretically in a different context (fullerenes that contain endohedral atoms or molecules) in the year 2000, but they remained so elusive experimentally that during many years they were serious doubts about their real existence. They were observed for the first time in 2010 in the photoionization spectrum of endohedral Xe in C_{60}^+.[18,20]

The main reaction observable here is the velocity distribution of the chlorine photofragments and its dependence on the nanodroplet size. The results obtained for the different droplet sizes are reported in Figure 6.2. It can be seen that strong oscillations, resulting from the quantum resonances, are present for all the droplets considered, but not for the photodissociation in the gas phase. This clearly points out that the oscillations are caused by the interaction of the chlorine molecule with the helium environment.

Figures 6.3(left) and 6.3(right) show the time evolution of the (squared modulus) molecular wave packet in coordinate, WP(r), and momentum, WP(p), representations (case N=500), respectively, within the 0.08-0.20 ps interval. Oscillations are found in both representations (although they are much more evident in the second case) but we will focus our attention in the momentum one, since it is directly related to the reaction observable investigated. Additional information on the molecular wave packet time evolution in the

momentum space can be seen in the Appendix for the nanodroplets with *N*=300 and 500 (movies 6.1 and 6.2, respectively). This temporal evolution is in strong contrast to what happens for the free (gas phase) photodissociation of $Cl_2(B)$ (Figure A6.1), as expected.

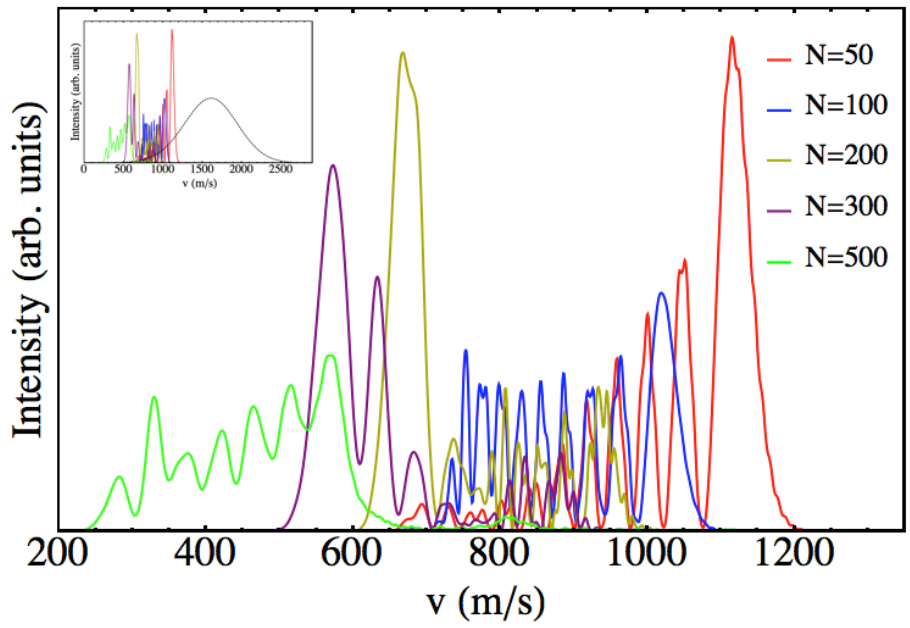

Figure 6.2. Velocity distribution of the Cl photofragments produced during the photodissociation of Cl_2 inside nanodroplet of different sizes. The resonance phenomenon is present and the gas phase result is also included (dashed black line).

Figures 6.3(left) and 6.3(right) show the time evolution of the (squared modulus) molecular wave packet in coordinate, WP(r), and momentum, WP(p), representations (case *N*=500), respectively, within the 0.08-0.20 ps interval. Oscillations are found in both representations (although they are much more evident in the second case) but we will focus our attention in the momentum one, since it is directly related to the reaction observable investigated. Additional information on the molecular wave packet time evolution in both coordinate and momentum representations can be seen in the ESI for the nanodroplets with and *N*=500 (movies 6.1 and 6.2, respectively). This temporal evolution is in strong contrast to what happens for the free (gas phase) photodissociation of $Cl_2(B)$ (Figure 6.A.1), as expected.

Schematically, the full process can be divided in three steps: the initial collision of the Cl atoms with the walls of the cavity (initial volume placed in the droplet and centered in the Cl_2 molecule where no He atoms are found), the translation of the Cl atoms through the droplet, and their arrival to the droplet surface and subsequent leaving. Of course, these parts

are not completely decoupled, but the separation is useful because of their different contributions to the final WP(p) profile.

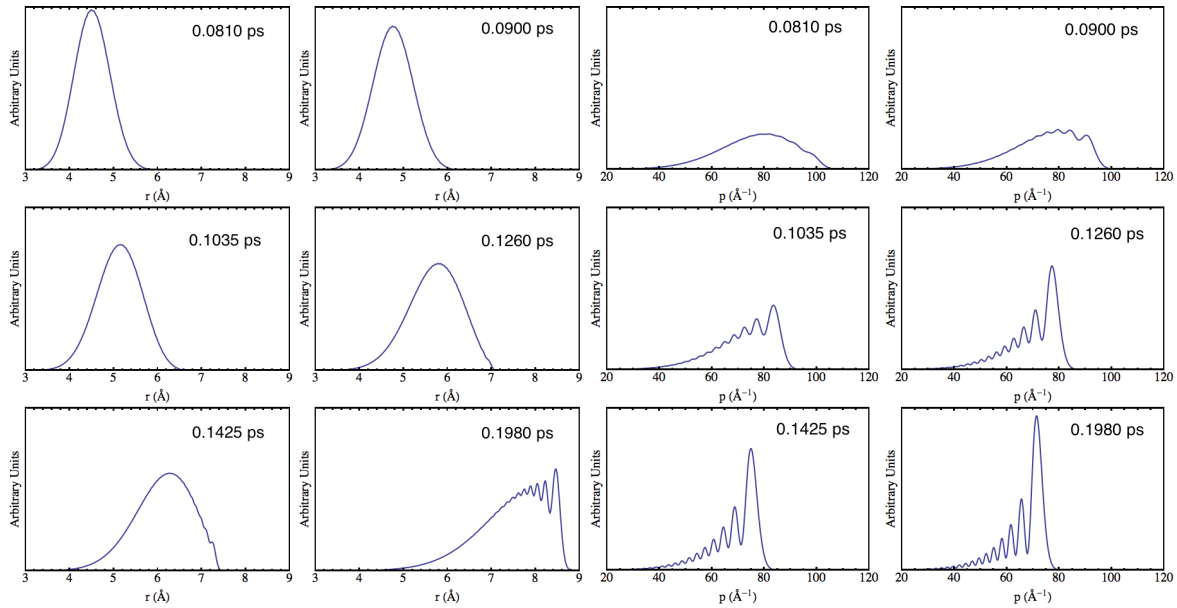

Figure 6.3. (left) Snapshots of the evolution of the Cl_2 relative coordinate wave packet (squared modulus) for the nanodroplet of 500 ^{4}He atoms. (right) The same as left but for the wave packet in momentum representation.

At the beginning (t = 0.014-0.015 ps) the momentum space wave packet moves towards high momenta and then goes back with no important modification of its gaussian shape (cf. movies 6.1 and 6.2). In the coordinate representation, this part of the evolution mostly corresponds to the travelling of WP(r) through the Cl_2 B-state electronic well; i.e., it mainly relates to the breaking of the diatomics chemical bond. From the perspective of the quantum resonance phenomenon, this part does not contribute to any peculiarity.

The appearance of structures (oscillations) in the squared modulus of the momentum wave packet begins around t = 0.08 ps (Figure 6.3(right) and movie 6.2). The high momentum components are being decelerated towards lower momentum values, leading to a decrease of the WP(p) width. At a time about 0.1 ps the first well defined oscillating pattern is already formed.

Then, it can be observed that from a time around 0.2 ps the low-momenta components of the WP(p) begin to jiggle, and then goes towards higher values. This process approximately ends around t = 0.5 ps, and makes WP(p) compressed into an specific range of momenta (p~40-65 A^{-1}; cf. movies 6.1 and 6.2). From the movie corresponding to the same

time period but in position representation (movie 6.1), it can be seen that this process correlates with the "filling" of the electronic potential well.

That is to say, some helium density begins to occupy the space placed between the two chlorine atoms, in this way making the global potential experienced by the chlorine atoms less attractive. The contribution of the electronic potential well of $Cl_2(B)$ to the global (or effective) potential is fully destroyed at around t = 0.46 ps (cf. movie 6.1). So that, the evolution observed in the low-momenta components of WP(p) is a consequence of the helium pushing of the remaining part of the WP(r) placed in the $Cl_2(B)$ electronic well. From this situation the helium environment confines from both sides each Cl atom along the Cl-Cl molecular (photodissociation) axis.

At larger times the passage of the Cl atoms through the nanodroplet takes place, which implies different time values, depending on the nanodroplet size (~ 1.5 and 2.1 ps for N = 300 and 500, respectively). During this time interval the WP(p) evolves gradually toward lower momenta, although the friction force exerted by the helium fluid makes no substantial change in the shape of WP(p) in a considerable part of this interval. Concerning the wave packet WP(r), it progresses in a dynamical effective potential well which depends on time, due to the changes of the helium density. This process is similar to that of a "particle evolving in a moving box" (cf. movie 6.1).

If instead of small or moderately large nanodroplets the solvent was superfluid bulk liquid or bigger droplets, we would expect that, at a given time, the mean value of the velocity of each Cl atom would reach the Landau's critical velocity (≈58 m/s (0.58 Å/ps) in superfluid (bulk) helium[21,22] and it has been also observed in nanodroplets[23] with $N \geq 1000$). Then, the moving effective potential well and WP(r) would be fully adapted to each other, and would lead to a WP(p) centered at the corresponding momentum of that critical velocity.

Finally, a substantial variation in the shape of WP(p) takes place when the dissociating atoms reach the nanodroplet surface,[4] due to the change in the shape of the effective potential well produced by the large anisotropy of the helium around the chlorine impurity. In Figure 6.4 we have plotted the effective potential wells for the nanodroplets with N=300 and 500 and the WP(p)'s (square modulus) corresponding to the same times (WP(p)'s are given in more detail in Figure A6.2). This graphic clearly shows the contribution of the nanodroplet surface to the quantum resonance phenomenon since, although the depth of the effective potential

well is always different, its shape changes when the dissociating atoms reach the nanodroplet surface. These potential wells present two high walls with a zone in between where the WP(r) is placed.

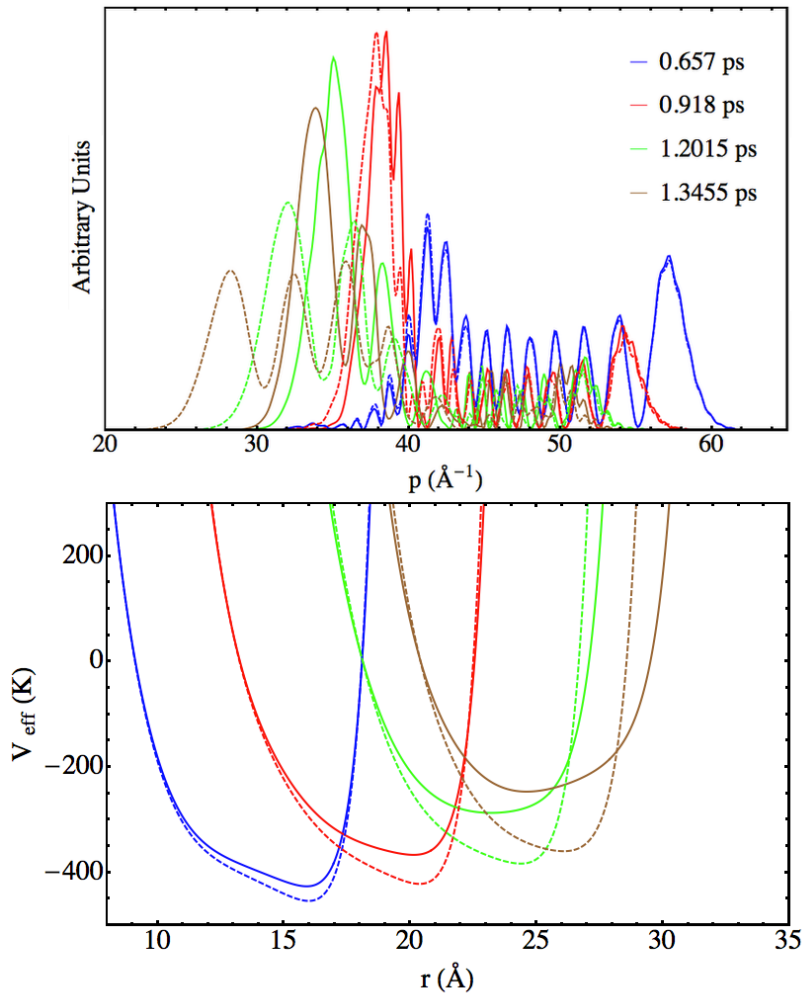

Figure 6.4. Cl_2 wave packet in momentum representation (squared modulus) (up) and effective potential (down) at some time values for which the Cl atoms are travelling inside the nanodroplet Two nanodroplet sizes are considered: N=300 (dashed line) and N=500 (solid line).

During the atomic trip through the nanodroplet, the slope of the effective potential well is pointing towards the direction of the motion, i.e., to large values of the relative coordinate. This profile arises from the fact that in the direction of motion (increasing r) the helium is compressed (increasing its density), this causing both a deeper potential well and a larger slope in the potential wall profile. In contrast, in the opposite direction (decreasing r) the helium is filling the empty space left by the atomic impurity (lower helium densities).

The shape of the effective potential well reverses when the atomic cavity is opened to the exterior of the nanodroplet. This slightly modifies the momentum space wave packet by shifting it to lower momenta, because the dissociating atoms are being attracted by the nanodroplet. Once the atoms are well outside the nanodroplet, the shape of WP(p) almost does not change while WP(r) spreads with time, which is consistent with the evolution of a (nearly) free particle (see also Fig. A6.1).

The former qualitative description of the process accounts for all the nanodroplet sizes considered. The main differences between them arise from the time needed by the atoms to leave the droplet, i.e., in the elapsing time of the penultimate step described above. The formation of the first oscillations in the squared modulus of WP(p) (Figure 6.3(right) and movie 6.2), which is due to the atomic collision with the first helium solvation layer is almost quantitatively coincident for all cases (Figure 6.5); the differences are larger for N=50 since the molecule is never fully solvated.

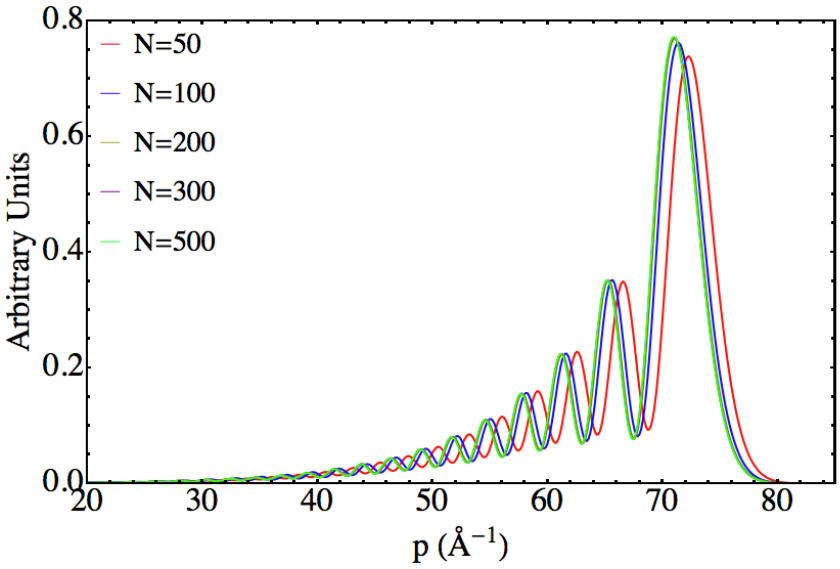

Figure 6.5. Cl_2 wave packets in momentum representation (squared modulus) at t=0.198 ps for different nanodroplet sizes (N).

In spite of the differences in the nanodroplet surface curvatures, we consider that the last contribution to the resonances (i.e., that involving the surface) is also almost the same for all the nanodroplets examined. The dynamical step that influences the shape of the resonances and varies with the nanodroplet size probably results from the trip of the atomic impurities through the nanodroplets, which leads to the main differences observed in the final Cl velocity distributions of the nanodroplets.

6.3.2 Understanding the birth of resonances

Here we will obtain a deeper insight into the origin of the oscillations in the momentum wave packet including the analysis on the energy fluxes involved. The initial oscillations are produced in the 0.08-0.20 ps time interval, where the pattern is well defined. The mechanism of formation of oscillations can be inferred from Figure 6.6 and also from the movies 6.1 and 6.2 (Appendix). Thus, at each time the largest component of WP(p) (p_{max}) is released the corresponding probability density is redistributed, in different ratios, among the lower p values at very specific distances with respect to the $p_{\max}$. This gradually leads to the formation of peaks, since the relative separations from p_{max} to the other peaks is always constant. If this were not like this a structured pattern would not be observed.

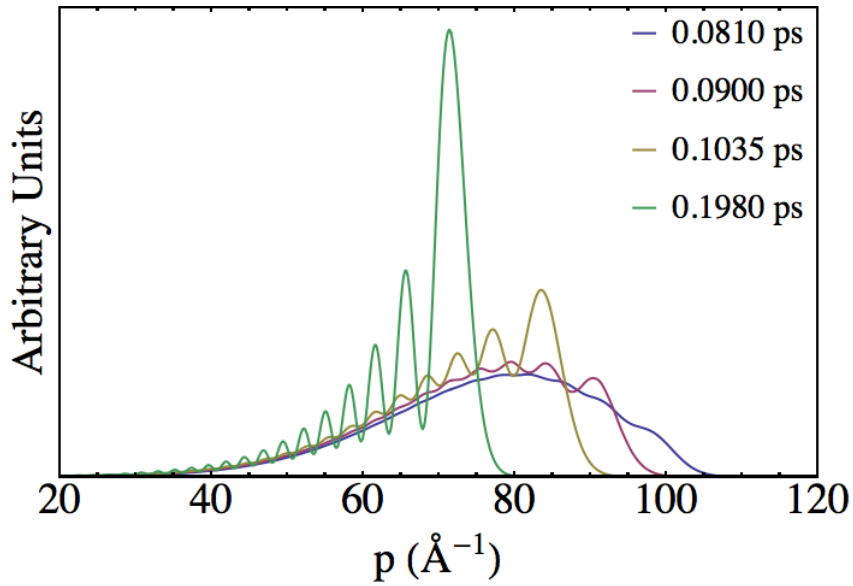

Figure 6.6. Snapshots of the evolution of the Cl_2 wave packet in momentum representation (squared modulus) showing the birth of the resonances for the nanodroplet of 500 ^{4}He atoms.

From a quantitative analysis of the resulting peaks in the probability density of WP(p) at t= 0.198 ps, we have determined that their positions follow a square root dependency on the order of each peak, beginning at the peak corresponding to the greatest momentum value and moving toward the peaks with lower momentum values. Hereafter, we will characterize each peak by the label Δn, which values are increasing natural numbers beginning by Δn = 1 (the meaning of this election will be clear in the following discussion); and a suitable representation for the peak analysis is collected in Figure 6.7, where the momentum of each peak is plotted as a function of $\Delta n^{1/2}$, obtaining a linear dependence.

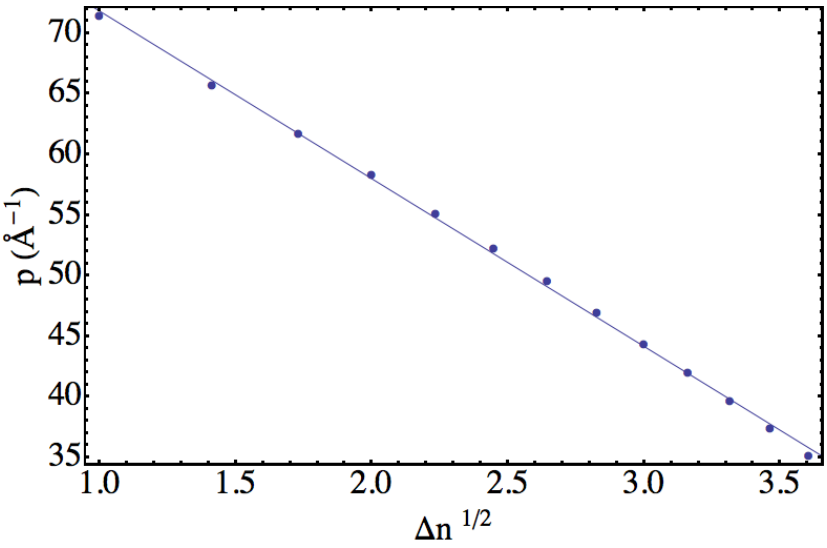

Figure 6.7. Position of the peaks for the Cl_2 wave packet in momentum representation (squared modulus) at t=0.198 ps as a function of $\Delta n^{1/2}$, which accounts for the number of level transitions of a harmonic quantum oscillator.

This type of dependence (which is also evident for other times in the time period of interest) suggests that the mechanism to reduce the kinetic energy of the diatomic embedded molecule involves the transition of some sort of harmonic oscillator, since the transitions are characterized by $\Delta E_{oscillator} = h\nu(n_f - n_i) \equiv h\nu\Delta n$. Therefore, associating a momentum value to the energy transferred, according to $p = \Delta E_{oscillator}^{1/2} \propto \Delta n^{1/2}$, then each transition causes in WP(p) a change of momentum from p_{max} to p_{max} minus a quantity which is proportional to $\Delta n^{1/2}$.

To deepen into the resonance phenomenon, it is also interesting to pay attention to the energy exchanges that occur between the chlorine atoms and the helium nanodroplet, during the formation of oscillations in WP(p), at the initial times of the photodissociation process. The modifications produced in the different energies involved with respect to their values at t = 0 (Table A6.1) and the associated time derivatives (rates of the energy changes) are plotted in Figure 6.8 for the nanodroplet with N = 500 and the 0.00-0.30 ps time interval and are analyzed below. Although these results correspond to N=500, it should be noted that, at the early times of the photodissociation, the same type of behavior is found for all the nanodroplets (cf. Figure A6.4).

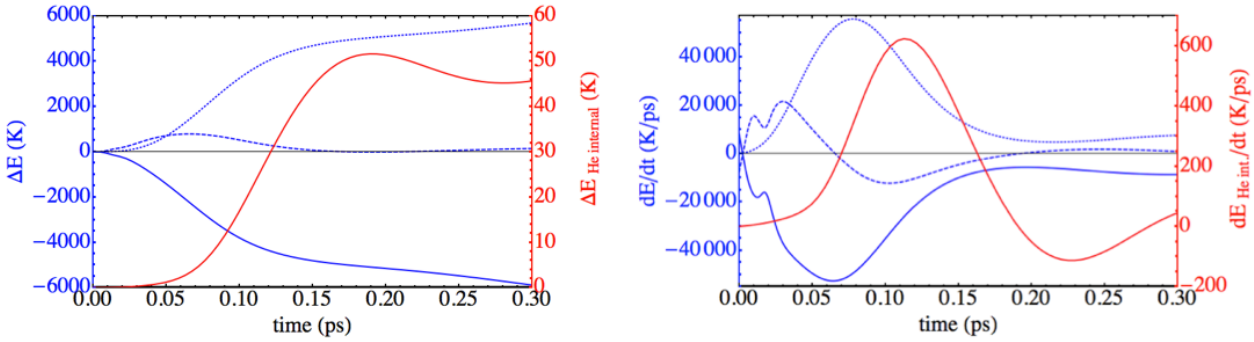

Figure 6.8. Time evolution of Cl_2 kinetic+potential energy (solid blue line), Cl_2-helium interaction energy (dashed blue line), helium internal kinetic energy (dotted blue line), and helium internal potential+correlation energy (red) for the initial time period of the photodissociation (left). Evolution of the time derivatives of the former quantities, i.e., their rates of change (right). The values reported are for $N = 100$, but at the early times of the photodissociation the results are almost coincident for all nanodroplets.

Initially, there is an energy release from Cl_2 to the Cl_2-helium interaction energy with monotonic rates of variation, with the exception of what happens at the very initial times (t = 0.01-0.03 ps) when small peaks are present. The rate of increase of the helium kinetic energy overcomes that of the interaction energy quite soon (t = 0.034 ps), and the energy loss of the Cl atoms and kinetic energy gain of helium continue being accelerated until t = 0.064 ps and 0.078 ps, respectively (they are slightly out of phase since one is the cause of the other and both are linked by the Cl_2-helium interaction; cf. Figure 6.8 (right)). The Cl_2-helium interaction energy increases with time, passes through a maximum value (t = 0.066 ps) and then decreases, reaching an almost constant value in the 0.16-0.24 ps time interval. Roughly speaking, the mean distance between the chlorine atoms and the cavity walls suffers a decrease and a subsequent increase. Finally, the helium (internal) potential + correlation energy begins to increase considerably around t = 0.066 ps, although it implies a much less amount of energy than in the other cases (cf. the different energy scales in Figure 6.8).

Hence, we can conclude that the most intense energy exchanges among the different energies involved occur at the beginning of the photodissociation (≈ 0.00 and 0.20 ps). Moreover, the energy changes which are more evident occur in the Cl_2 energy (kinetic + potential) and in the kinetic energy of helium (Figure 6.8 (left)), and the significant decrease observed in the former mostly corresponds with the important increase taking place in the latter.

Regarding the resonances, it is worth noting here that the maximum increase (ΔE) in the Cl_2-helium interaction energy occurs at a time (0.066 ps) which is similar, although

smaller, to that for which the structures are observed for the first time in the WP(p) probability density. Though, a much stronger correlation is found between the maximum rate of production of helium kinetic energy (t = 0.078 ps; cf. Figure 6.8 (down)) and the onset of structures in WP(p) which occur almost at the same time. So that, when the rather well separated atoms (cf. Figure A6.3) and the wall of the helium cavity begin to separate and during this push between each other is when resonances are produced. Thus, the fact that the resonances seem to be the consequence of transitions of a harmonic oscillator can be related with the interaction energy. Nevertheless, the physical meaning of this is unclear.

The (confinement) quantum resonances found in the present theoretical study probably correspond to a rather general phenomenon in the photodissociation of molecules in superfluid helium nanodroplets, as suggested by the present study and further work (in progress) involving other diatomic molecules. Furthermore, it is worth noting here that oscillations in the Cl velocity distribution were also reported in ref. 10, but using a very different theoretical method and considering strongly different physical conditions (non-superfluid helium nanodroplets at T=4 K with N up to 200 ^{4}He atoms).

6.3.3 Feasibility of the experimental detection of the resonances

Regarding the experimental detection of the confinement resonances found, it is worth mentioning the significant advances achieved in recent years in the experimental techniques of chemical reactions dynamics and, in particular, in those addressed to characterize scattering resonances.[24,25,26,27] Accordingly, on the basis of the energy resolution needed, there should be no significant difficulties to resolve the peaks of the Cl final velocity distributions (separation between peaks of ≈46 and 56 m/s for N =300 and 500, respectively; or, alternatively, ≈0.38 and 0.57 meV).[24]

The larger obstacles in order to detect the oscillations in the velocity distributions would probably arise from the technical difficulties involved in the production of doped superfluid helium nanodroplets in well defined conditions (number of atoms ^{4}He and molecular vibro-rotational state). Thus, e.g., the presence of nanodroplets of different sizes, obviously, will tend to blur the oscillating structure of the individual distributions. Of course, the study of photodissociation processes in ^{4}He nanodroplets is, in principle, less complicated that the study of bimolecular reactions in the same solvent, which involves two pick-up steps and, probably, leads to less well defined conditions as in the former experiments.

It should be noted that, due to the particularly careful experimental conditions required to produce nanodroplets with N = 500, the case with N = 1000 (a droplet size more easily achievable experimentally) could also be considered in the experiments. In fact, preliminary theoretical results show that for nanodroplets with N = 1000 an oscillating structure is also observed in the Cl velocity distribution.

6.4 Summary and conclusions

This work extends and complements our recent investigation on the photodissociation of homonuclear diatomic molecules in superfluid helium nanodroplets (T=0.37 K).[4] In Ref. 4 a hybrid theoretical method was developed and applied for the first time to investigate the photodissociation of a Cl_2 embedded molecule via the B←X electronic excitation ($Cl_2(X)@(^4He)_{N+}$ $h\nu \rightarrow [Cl_2(B)@(^4He)_N]^* \rightarrow Cl(^2P_{3/2}) + Cl(^2P_{1/2}) + [(^4He)_{N'}]^* + (N\text{-}N')\ ^4He$, with N = 50-500). This method allowed us to consider helium nanodroplets with sizes which can be compared with those achieved in the experiments, thus making easier the (highly desirable) interaction between theory and experiment.

More concretely, here we have focused our efforts in the theoretical study of the dynamics of the process leading to the formation of (confinement) quantum resonances in the photodissociation of Cl_2 (B←X) embedded in $(^4He)_N$. The existence of these resonances was reported but not analyzed in our previous contribution because they were not the main target and also due to their specific character and complexity. As far as we know, this is the first time that this rather new type of resonances, experimentally confirmed in 2010, is described in the reaction dynamics context.

The excitation of the embedded Cl_2 to the B excited state produces what can be considered as a quasibound state. Contrary to what happens in gas phase, here the excited molecule is surrounded and provisionally confined by the helium nanodroplet and therefore a considerably larger amount of time is required to obtain the product fragments ($Cl(^2P_{3/2})$ + $Cl(^2P_{1/2})$).

From the examination of the time evolution of the $Cl_2(B)$ wave packet (probability density in momentum and space representations) at the early times of the photodissociation (0.00-0.20 ps), it comes out that the interaction of $Cl_2(B)$ with the ^4He environment generates

quantum interferences. The rich structure (oscillations) produced in the Cl_2 wave function (which in the early times is much more evident in the momentum representation) is the responsible of the strong oscillations which are evident in the main observable of the system (final velocity distribution of the Cl atoms).

These oscillations are evident for all the nanodroplets, but not for the photodissociation in gas phase, which also clearly shows that they are caused by the interaction of $Cl_2(B)$ with the helium environment. Moreover, a deeper insight has been obtained paying attention to the birth of the resonances (origin and development of the oscillations in the probability density of the momentum representation wave packet) and to the energy fluxes involved.

The existence of quantum resonances is probably one of the most fascinating phenomena in chemical physics and probably corresponds to a quite general behaviour for the kind of systems examined. We hope that this work will encourage the experimentalists to carry out photodissociation dynamics studies on these highly interesting and challenging doped helium-4 nanodroplet systems.

6.5 Appendix

a

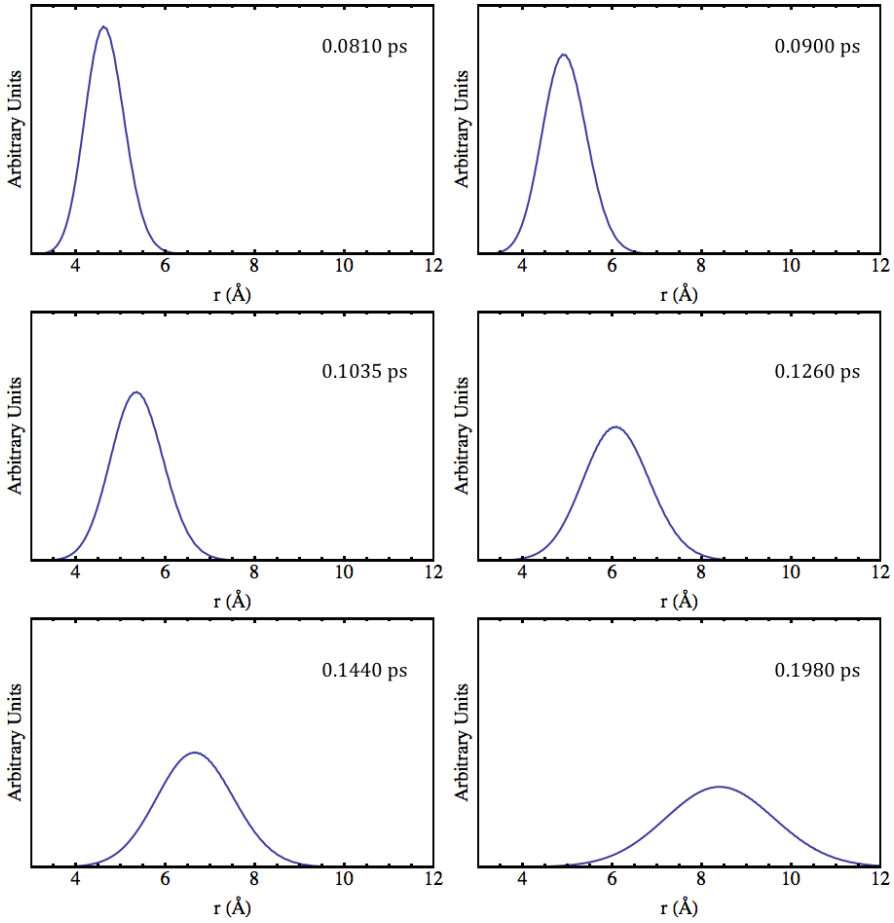

b

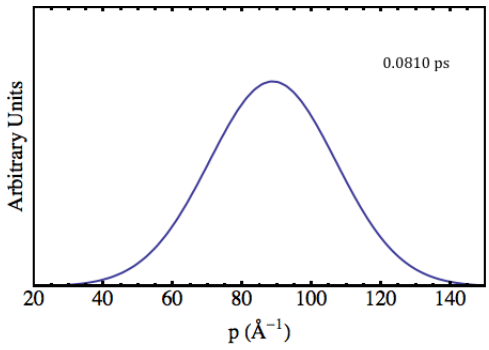

Figure A6.1. (a) Snapshots of the of the $Cl_2(B)$ relative coordinate wave packet (squared modulus) in gas phase. (b) The same as in (a) but for the wave packet in momentum representation; in this case the results for the other times are coincident with that for the smallest one (t=0.0810 ps).

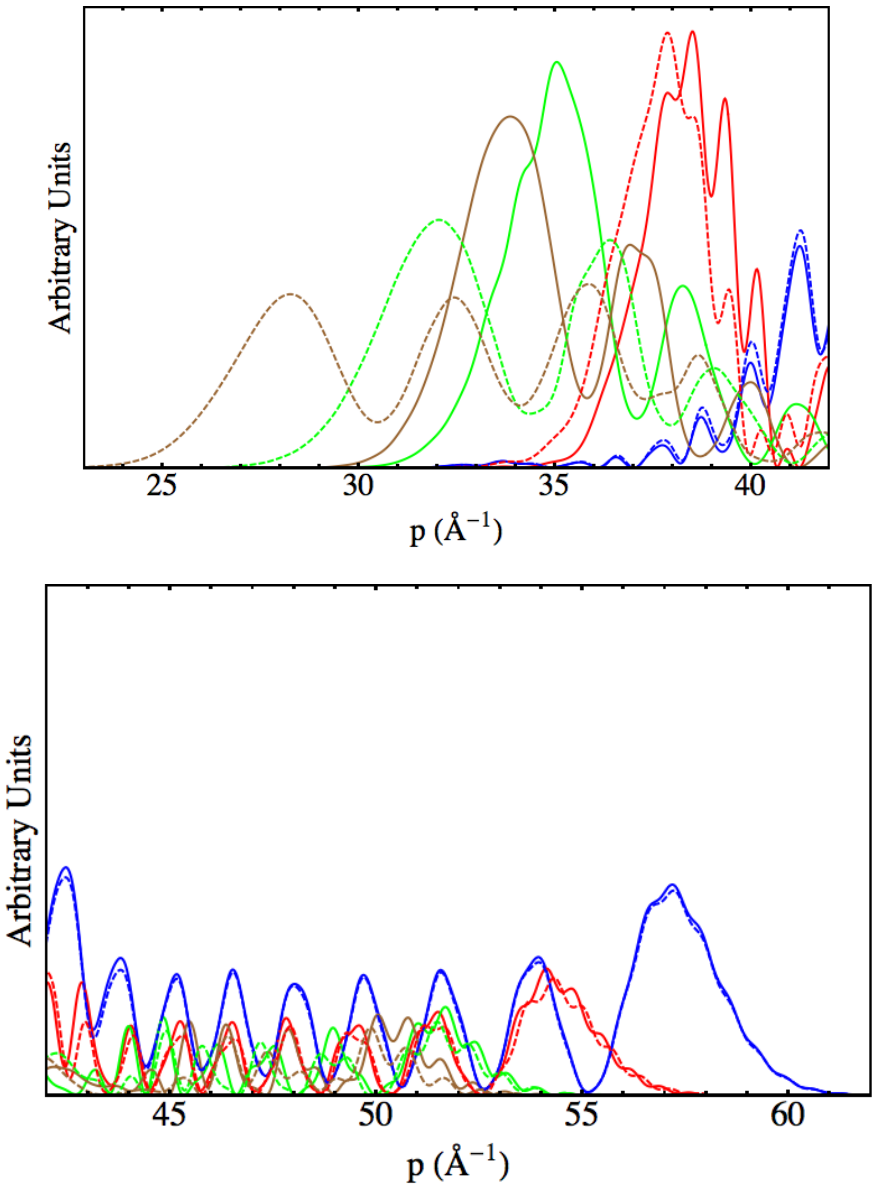

Figure A6.2. $Cl_2(B)$ wave packet in momentum representation (squared modulus), given in more detail than in Figure 4 (up), at some time values for which the Cl atoms are travelling inside the nanodroplet [t(ps) = 0.657 (blue), 0.918 (red), and 1.202 (green)] and when they are relatively close to the nanodroplet surface [t(ps) = 1.346 (brown)]. Low-intermediate p values (up) and intermediate-high p values (down). Two nanodroplet sizes are considered: N=300 (dashed line) and N=500 (continuous line).

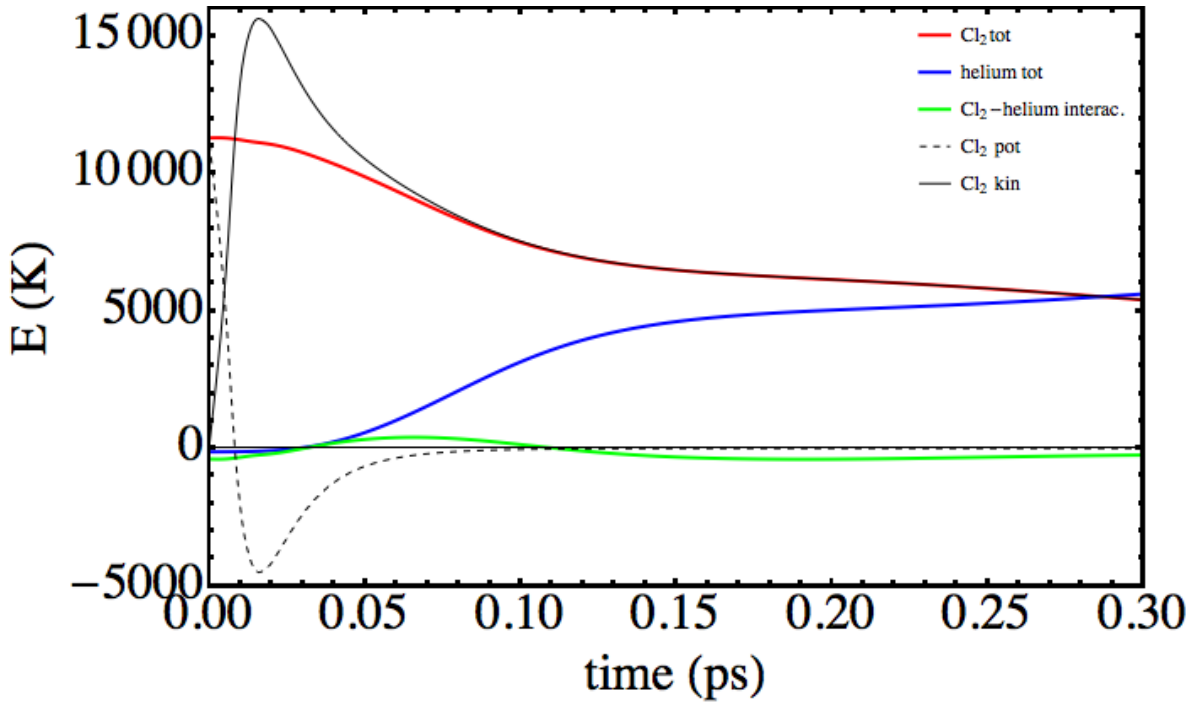

Figure A6.3. Time evolution of the energies involved in the process: $Cl_2(B)$ total energy (Cl-Cl potential + kinetic), solid red line; helium total energy (helium potential+correlation + kinetic), solid blue line; $Cl_2(B)$-helium interaction, solid green line; $Cl_2(B)$ potential energy, dotted black line; $Cl_2(B)$ kinetic energy, solid black line. The values reported are for N = 100, but at the early times of the photodissociation the same trends are found for all nanodroplets.

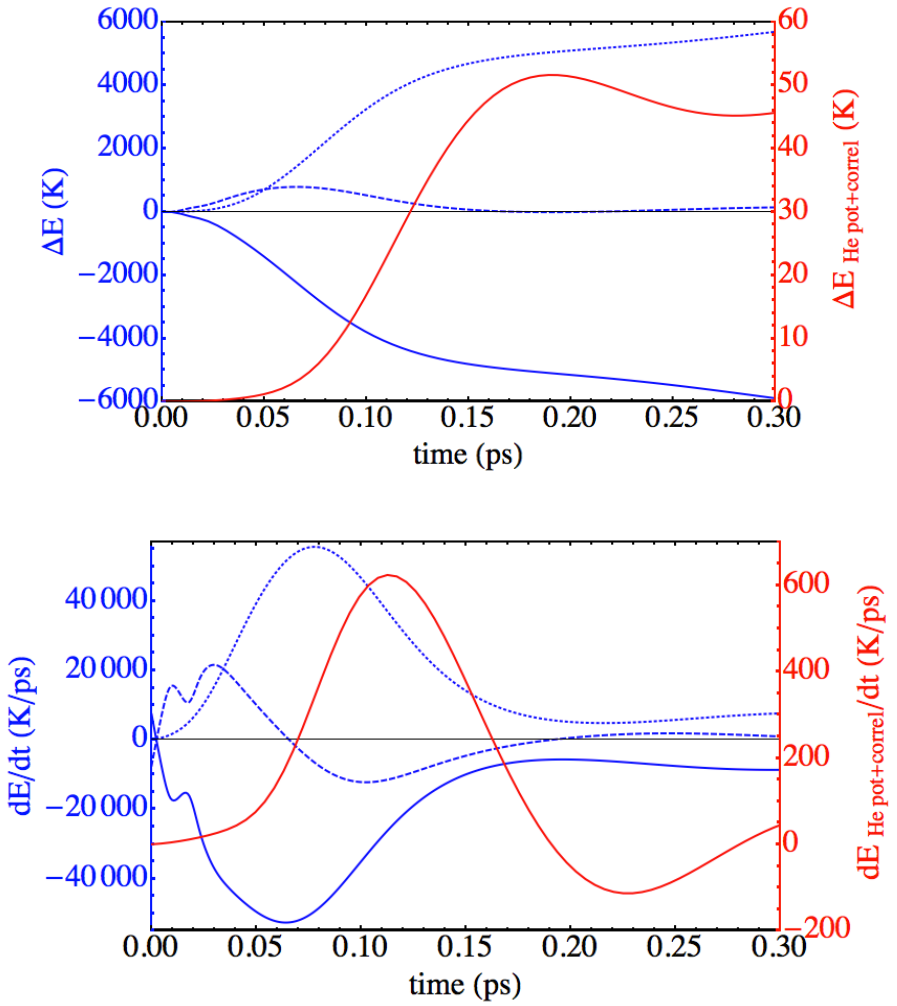

Figure A6.4. Time evolution of the change of $Cl_2(B)$ kinetic+potential energy (solid blue line), $Cl_2(B)$-helium interaction energy (dashed blue line), helium internal kinetic energy (dotted blue line), and helium internal potential+correlation energy (red) for the initial time period of the photodissociation (up). Evolution of the time derivatives of the former quantities, i.e., their rates of change (down). The values reported are for $N = 100$.

Movie 6.1. Time evolution of the $Cl_2(B)$ wave packet (squared modulus) in coordinate representation (blue) and effective potential (red), during part of the photodissociation process (0.0-3.0 ps time interval), for the $[Cl_2(B)@(^4He)_{500}]^*$ nanodroplet. In this case the time required for <r> to be equal to the diameter of the nanodroplet is ≈ 2.6 ps.

Movie 6.2. Time evolution of the $Cl_2(B)$ wave packet (squared modulus) in momentum representation (blue), during part of the photodissociation process (0.0-3.0 ps time interval), for the $[Cl_2(B)@(^4He)_{500}]^*$ nanodroplet.

6.6 References

[1] Toennies, J. P.; Vilesov, A. *Angew. Chem. Int. Ed*. **2004**, *43*, 2622.

[2] Barranco, M.; Guardiola, R.; Hernández, S.; Mayol, R.; Navarro, J.; Pi, M. *J. Low Temp. Phys.* **2006**, 142, 1.

[3] Yang, S.; Ellis, A. M. *Chem. Soc. Rev.* **2013**, *42*, 472.

[4] Vilà, A.; González, M.; Mayol, R. *J. Chem. Theory Comput.* **2015**, *11*, 899.

[5] Yang, S.; Ellis, A. M.; Spence, D.; Feng, C.; Boatwright, A.; Latimer, E.; Binns, C. *Nanoscale.* **2013**, *5*, 11545.

[6] Latimer, E.; Spence, D.; Feng, C.; Boatwright, A.; Ellis, A. M.; Yang, S. *Nano Lett.* **2014**, 14, 2902.

[7] Braun, A.; Drabbels, M. *J. Chem. Phys.* **2007***, 127*, 114303.

[8] Braun, A.; Drabbels, M. *J. Chem. Phys.* **2007***, 127*, 114304.

[9] Braun, A.; Drabbels, M. *J. Chem. Phys.* **2007***, 127*, 114305.

[10] Takayanagi, T.; Shiga, M. *Chem. Phys. Let.* **2003**, *372*, 90.

[11] Asano, Y.; Yabushita, S. *J. Phys. Chem. A* **2001**, *105*, 9873.

[12] Moiseyev, N. *Non-Hermitian Quantum Mechanics*, Cambridge University Press, **2011**.

[13] Liu, K. *Adv. Chem. Phys.* **2012**, *149*, 1.

[14] Skodje, R. T. *Adv. Quantum Chem.* **2012**, *63*, 119.

[15] Gamallo, P.; Huarte-Larrañaga, F.; González, M. *J. Phys. Chem. A,* **2013**, 117, 5393.

[16] Dalfovo, F.; Lastri, A.; Pricaupenko, L.; Stringari, S.; Treiner, J. *Phys. Rev. B*, **1995**, *52*, 1193.

[17] Tannor, D. J. *Introduction to Quantum Mechanics. A Time Dependent Perspective*, University Science Books, Sausalito, **2007**.

[18] Connerade, J. P. From Pauli's Birthday to 'Confinement Resonances' – a Potted History of Quantum Confinement. *J. Phys. Conf. Ser.* **2013**, *438*, 012001.

[19] Dolmatov, V. K. *Adv. Quantum Chem.* **2009**, *58*, 13.

[20] Kilkoyne, A. L. D.; Aguilar, A.; Muller, A.; Schippers, S.; Cisneros, C.; Alma'Washi, G.; Aryal, N. B.; Baral, K. K.; Esteves, D. A.; Thomas, C. M.; Phaneuf, R. A. *Phys. Rev. Lett.* **2010**, 105, 213001.

[21] Tilley, D. R.; Tilley, J. *Condensates and Excitations. Superfluidity and Superconductivity*, Institut of Physics Publishing, **1990**.

[22] Annet, J. F. *Superfluid Helium-4. Superconductivity, Superfluids and Condensates*, Oxford University Press, **2004**.

[23] Brauer, N. B.; Smolarek, S.; Loginov, E.; Mateo, D.; Hernando, A.; Pi, M.; Barranco, M.; Buma, W. J.; Drabbels, M. *Phys. Rev. Lett.,* **2013**, *111*, 153002.

[24] Ashfold, M. N. R.; Nahler, N. H.; Orr-Ewing, A. J.; Vieuxmaire, O. P. J.; Toomes, R. L.; Kitsopoulos, T. N.; Anton Garcia, I.; Chestakov, D. A.; Wuc, S.-M.; Parker, D. H. *Phys. Chem. Chem. Phys.* **2006**, *8*, 26.

[25] Henson, A. B.; Gersten, S.; Shagam, Y.; Narevicius, J.; Narevicius, E. *Science,* **2012**, *338*, 234.

[26] Naulin, C.; Costes, M. *Int. Rev. Phys. Chem.m* **2014**, *33*, 427.

[27] Ashfold, M. N. R.; Parker, D. H. *Phys. Chem. Chem. Phys.* **2014**, *16*, 381. Editorial of the Imaging Molecular Dynamics themed collection (31 articles).

7. Photodissociation dynamics: Other halogens and mass effects

7.1 Introduction

This chapter consists in the natural extension of Chapter 4 (photodissociation dynamics of Cl_2 inside helium nanodroplets), where two more investigations regarding photodissociation dynamics are presented. The first study corresponds to the photodissociation of the Br_2 and I_2 halogen molecules, while the second one aims to elucidate the role played by the mass of the atoms in the mechanism of photodissociation dynamics of homonuclear diatomic molecules inside helium nanodroplets.

At the time of the presentation of this thesis these studies are still in progress. However, since we have already obtained several interesting results and only a few calculations are still running, we have decided to include these results here.

In Chapter 4 it was presented a theoretical hybrid approach to study at a quantum level the photodissociation dynamics of homonuclear diatomic molecules inside helium nanodroplets. As a first application of this method the Cl_2 molecule was selected for several reasons (e.g., relevance in chemistry, the electronic adiabaticity of its dynamics or the possibility of an experimental study, etc.). The global process can be indicated as follows:

$$X_2(\text{ground state})@(^4He)_{N} + h\nu \rightarrow X_2(\text{excited state})@(^4He)_{N} \rightarrow 2\,X + (^4He)_{N'} + (N\text{-}N')\ ^4He$$

,where (N-N') ^{4}He only refer to the total number of helium atoms evaporated from the nanodroplet.

Regarding the first part of the present chapter, the main goal of this study is to analyse the different dynamical behaviours that occur when changing the halogen molecule. The lower potential energy curves of these molecules (X and B states) have very similar profiles, but differentiate in the excess of energy coming from the B←X electronic transition. Furthermore,

the different masses and interactions with helium of these halogen molecules might also influence the process.

Moreover, it is worth noting that as the atomic number increases the approximation of electronic adiabaticity becomes less accurate. However, the investigation carried out here corresponds to the first stage for a more complete study including non-adiabatic couplings.

The election of the Br_2 and I_2 molecules resides in order to achieve softer photodissociation conditions, i.e., low-moderate values of the excess of energy, so that (droplet induced) recombination is also a possible process. In this context, the investigation of F_2 would lead to a high kinetic energy content that would increase significantly the computational effort needed for the study (higher kinetic energy implies larger momentum grids) and thus, it is not a good candidate. On the other hand, we have determined that I_2 almost completely recombines for the nanodroplets with N=100 ^{4}He atoms, what suggests not to consider heavier halogens.

The second part of this chapter involves the study of the photodissociation dynamics of hypothetic homonuclear diatomic molecules inside helium nanodroplets, considering the potential energy curves of Cl_2 already used in Chapter 4. The aim of this investigation is to understand the role played by the mass of the photofragments in this phenomenon. This was motived by some experimental results obtained by the Drabbels' group[1], who found a strong correlation between the amount of energy released from the molecule to the nanodroplet and the mass of the fragments. To do so, they studied different photodissociations with similar excess of energy but different masses of the photofragments, keeping fixed the droplets sizes.

To model this situation we have examined the photodissociation of fictitious isotopes variants of the Cl_2 molecules, since the photodissociation process of Cl_2 is well-known (Chapter 4). This means that bot the initial ground state vibrational wave packet and the potential energy curves involves in the dynamics are identical to those of Chapter 4. Proceeding in this way we can attribute the differences found in the dynamical simulations only to the mass corresponding to each specific case analyzed.

7.2 Theoretical Methods

The theoretical methods used in the present chapter are the ones presented in Chapter 4 in the study of the Cl_2 photodissociation. Therefore, here we will only briefly review the main

features of this approach and we address the reader to the Chapter 4 (and Ref. 2) for further details.

To study the photodissociation dynamics of Br_2 and I_2 the initial time situation, i.e., the ground state doped nanodroplet (X_2(v=0)@^4He_N) has to be calculated. The $Br_2(X^1\Sigma_g^+)$-He(^{2}S) and $I_2(X^1\Sigma_g^+)$-He(^{2}S) potential energy surfaces needed for these calculations have been obtained from References 3 and 4, respectively.

Regarding the study of the mass effects on the dynamics of the photodissociation, the initial wave packet $\varphi_{X_2}(v = 0, j = 0)$, which suddenly evolves through the Cl_2(B) state electronic potential energy curve (Franck-Condon principle) has not been modified, in order to keep the potential energy of the hypothetic molecule equal for all the cases. This potential energy will be progressively converter into kinetic energy as time evolves (progressively larger X-X distance). We have selected nanodroplets formed by 300 ^{4}He atoms, which represents a compromise between the computational cost and dealing with a minimum size. This ensures a part of the mechanism consisting in each atom travelling through the droplet in its own helium cavity. If a small droplet had been selected, for instance N=100, the dynamics would only result in the collision of the fragment atoms with the solvation shell (cavity) and then the atomic impurities would be leaving the droplet surface.

The method used is based on a hybrid scheme in which the mean field Time Dependent Density Functional Theory (TDDFT) is employed to describe the superfluid liquid helium, and the standard wave packet quantum dynamics is considered for the molecule. The phenomenological energy functional selected is the so-called Orsay-Trento (T = 0 K)[5], but neglecting the non-local corrections of the kinetic energy and the backflow terms, for computational reasons. The evolution of the nanodroplet and the molecule are coupled (see Eqs. 7.1 and 7.2). Furthermore, due to the symmetry of the problem and the zero angular momentum assumption, only one degree of freedom is needed to describe the diatomic molecule consisting in the relative position (r), which corresponds to the distance between the two atoms. The equations of motion read as:

$$i\hbar\frac{\partial}{\partial t}\Psi_{He}(\boldsymbol{R}_{He}) = \left[-\frac{\hbar^2}{2m_{He}}\boldsymbol{\nabla^2} + \int dr\, V_{He-X_2(B)}(r, \boldsymbol{R}_{He})\left|\varphi_{X_2}(r)\right|^2 + \frac{\delta\mathcal{E}_c[\rho_{He}]}{\delta\rho_{He}}\right]\Psi_{He}(\boldsymbol{R}_{He}) \tag{7.1}$$

$$i\hbar\frac{\partial}{\partial t}\varphi_{X_2}(r) = \left[-\frac{\hbar^2}{m_X}\frac{\partial^2}{\partial r^2} + \int d\boldsymbol{R}_{He} V_{He-X_2(B)}(r,\boldsymbol{R}_{He})\rho_{He}(\boldsymbol{R}_{He}) + V_{X_2(B)}(r)\right]\varphi_{X_2}(r) \quad (7.2)$$

Eq. 7.1 governs the evolution of the effective complex wave function of helium, defined by $\Psi_{He}(\boldsymbol{R}_{He},t) \equiv \sqrt{\rho_{He}(\boldsymbol{R}_{He},t)}$, and Eq. 7.2 accounts for the relative coordinate molecular wave packet φ_{X_2}. In the first investigation X=Br and I, while for the second study (mass effects) the potentials are the ones of chlorine (X=Cl) but the mass (m_X) adopts different values. The selected potentials for the Br_2(B) and I_2(B) - He systems are obtained from the references 6 and 7 , respectively. For the Br-Br (B) and I-I (B) potential energy curves we have employed a composite scheme from the references 8, 9, 10, 11 and 12, 13, respectively.

7.3 Photodissociation dynamics of Br_2 and I_2

Here we present the photodissociation dynamics of Br_2 and I_2 via the B←X electronic transition. These potential energy curves are similar for all of these species, and so it is the electronic excitation implied. The main difference of these curves is the excess of (kinetic) energy obtained from the transition to the B excited state (assuming the Franck-Condon principle). These quantities show a clear monotonic tendency: the higher atomic number the lower excess of energy. The obtained dissociation probabilities are collected in Table 7.1. For heavier halogens the result of the B←X transition is no longer expected to be the rupture of the X-X chemical bond; instead of this recombination process should be clearly the main result. Some of the calculations have still not finished at present date. These corresponds to the *N*=300 and 1000 droplets in the study of the Br_2.

Many of the observed features of these processes are analogous to the case of Cl_2. Hence, here we just mention them without further explanations, and we will mainly focus on the new different phenomena observed in the present study. Now we focus into the case or Br_2, which have been extensively studied, and at the end of this section a short discussion about I_2 dynamics will be reported, since we have just made a brief study of I_2, because the photodissociation probability is very small.

Table 7.1. Photodissociation probability for Br_2 and I_2 at different initial conditions

Case	Dissociation probability	$\langle v_{escape} \rangle$[a] (m/s)
Br_2 gas phase	0.88	380
$Br_2@^4He_{100}$	0.83	197
$Br_2@^4He_{200}$	0.83	152
$Br_2@^4He_{300}$	-	-
$Br_2@^4He_{500}$	0.15	59
$Br_2@^4He_{1000}$	0.00	-
I_2 gas phase	0.43	214
$I_2@^4He_{100}$ 2-body PES	0.11	144
$I_2@^4He_{100}$ 3-body PES	0.00	-

[a]Notice that the mean value of the velocity is not obtained from the whole wave function, but just from the leaving fraction.

The photodissociation of Br_2 inside helium nanodroplets has been studied for nanodroplets of N=100, 200, 300, 500 and 1000. Also, in order to determine the effect of the helium droplet to this process, the gas phase photodissociation has also been calculated within the same approximations (electronic adiabatic dynamics and rotational degree of freedom neglected).

The dynamical evolution of the process can be easily pictured by inspecting the animations collected in the Appendix and Figure 7.1. At the left side of the movies is collected time evolutions regarding the molecule; concretely, the squared modulus of the wave packet in both the position $\left|\varphi_{X_2}(r)\right|^2$ (relative coordinate; top panel) and conjugate momentum $\left|\varphi_{X_2}(p_r)\right|^2$ (bottom panel) representations. The images shown at right side correspond the helium density at the *xz-plane* in a 2D representation with colour scale (top) and in a 3D plot (bottom).

Focusing on the wave packet in position representation, for the initial times all the cases almost follow the same tendency in what respects to the temporal evolution. So that, we will begin commenting the general trends and afterwards we will point out the singularities of each case.

At the initial times the wave packet is essentially evolving through the excited electronic (B state) potential (the interaction with helium is negligible), which causes a highly oscillatory pattern in its tail. This behaviour is also observed for the gas phase case, and it is related with the fraction of the wave packet that can be considered bonded. This fact can be rationalized by means of considering an ensemble of classical particles with a position

distribution given by the squared modulus of the wave packet. Thus, the fraction of distribution whose potential energy takes negative values is in a bound state and no dissociation is expected for them.

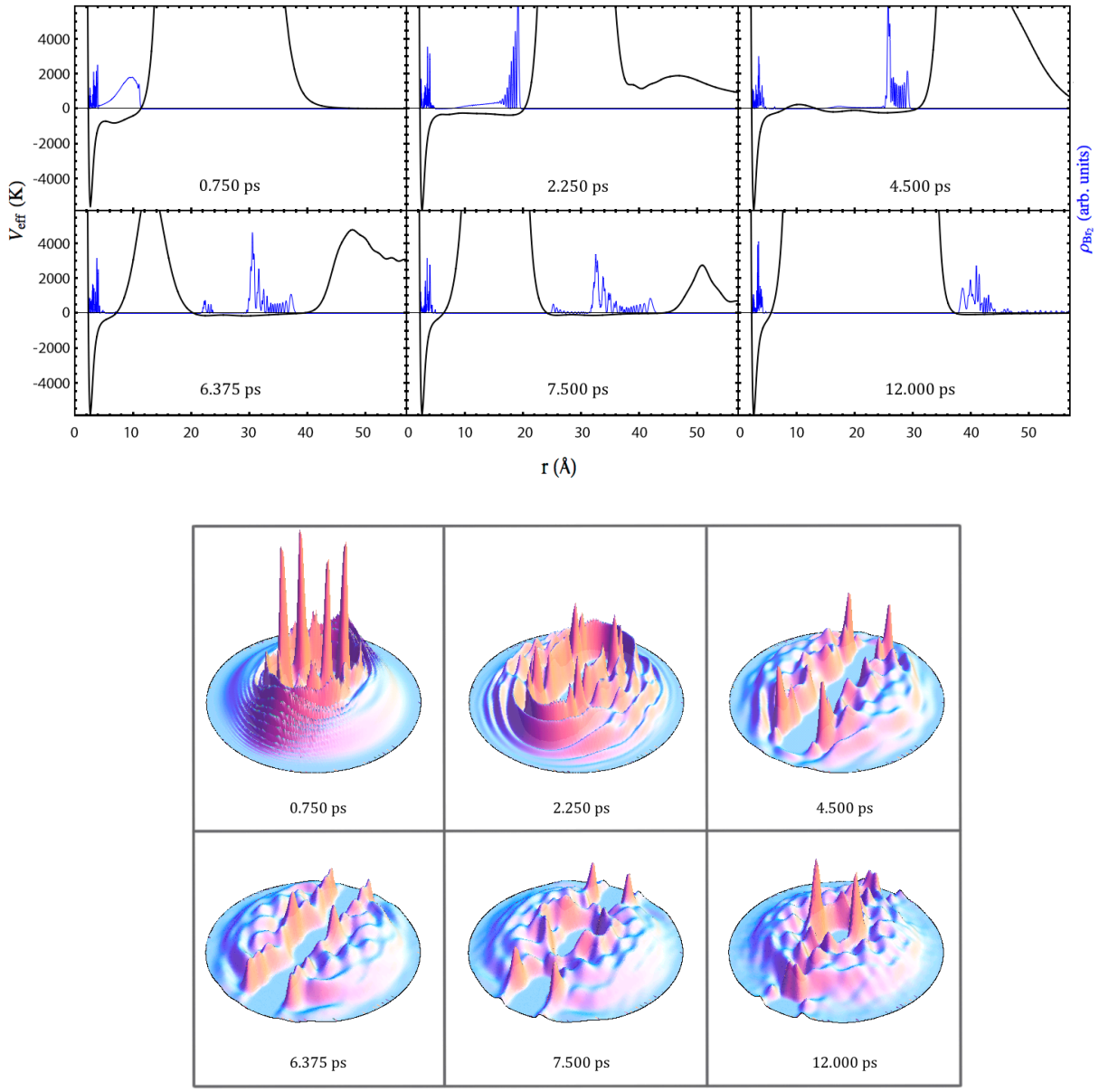

Figure 7.1. Snapshots of the time evolution of the relative coordinate wave packet of Br_2 and the effective potential (a) and the helium density in the xz-plane (b), for selected representative times.

The remaining part of the wave packet evolves maintaining the initial Gaussian shape until the Br atoms reach the walls of the helium cavity. Then, this shape is no longer maintained and oscillations appear in the front of the wave packet. This behaviour is very close

to the one observed for the case of chlorine, which has been described with a lot of detail in Chapter 6.

After this initial period of time, the evolution of the Br_2 wave packet results from the superposition of two dynamics: the bound (vibrational relaxation) and the quasi-bound parts. At the time of around 4 ps, the wave packet is fragmented in two parts. This is mediated by liquid helium, which tries to close the big hole generated in the droplet by the Br_2 photodissociation. Despite it cannot be seen in the animations in terms of the helium density, this is clearly evident from the top left movie taking into consideration the effective potential exerted by the helium. When the effective potential (sum of all potentials affecting Br_2) takes positive values the wave packet is divided in two fragments. This fact does not happen for the gas phase case.

Then, these two parts become compacted in a more narrow shape. At this time (around 8 ps), the remaining part of the wave packet is fully surrounded by helium, i.e. it is re-solvated and the other fragment leaves the droplet. Afterwards, the vibrational relaxation of the remaining part of the wave packet would take place, but we stopped the calculation before for computational reasons (it takes a lot of time to vibrationally relax the wave packet) and because this kind of study is out of the scope of the present work. This process implies the existence of strong oscillations of the molecular cavity (surface modes).

Although all the cases follow similar general trends, each nanodroplet size leads to some specific behaviour. For the smallest droplets (N=100 and 200), the broad character of the Br_2 wave packet combined with their small sizes induces the formation of a hole crossing the whole droplet. Besides, for N=100 case, the hole is never closed while for N=200 a dynamical opening-closing pattern is found.

For N=500 an interesting phenomenon is observed. The leaving part of the bromine wave function reaches the droplet surface at very low (mean) velocity. Then, a small part of this wave packet leaves the nanodroplet surface carrying the corresponding kinetic energy. The other fraction remains placed at the surface for a rather long time, and then it comes back to the droplet centre. Indeed, this consists in a “frontier case” for the recombination process. For the N=1000 case, a full recombination process takes place.

To conclude this qualitative part it is important mentioning that one of the main features obtained from these calculations is the time scale of the photodissociation process. Since the phenomenology is very rich the time scale depends in a significant way on the case considered.

Nevertheless, for the smallest droplets cases, where recombination is not present (*N*=100, 200, 300), we can assign the order of around twenty picoseconds. Regarding the bigger nanodroplets, it is more difficult to define a time scale since it depends on when one considers the processes have ended, since recombination happens.

A more quantitative analysis can be carried out inspecting different properties and analysing how does the size of the droplet effect to the evolution of these properties. In Figure 7.2 it is plotted the evolution of the expectation value of the relative coordinate, i.e. <r> for the different droplet sizes, while the corresponding velocities $\langle v_r \rangle$ are collected in Figure 7.3. These plots ends at the time the wave packet begins to be absorbed. The evolution of positions is really smooth and the main observation that can be done is to perceive the effect of the size in the trajectories, even inducing recombination for the higher sizes (N= 1000).

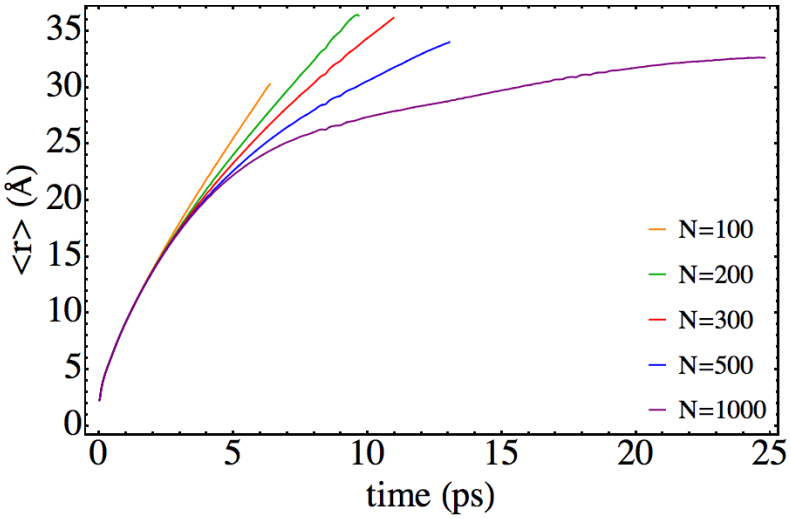

Figure 7.2. Evolution of the mean value of the relative coordinate for Br_2 for different droplet sizes.

Regarding the velocities, stronger dependences on time are obtained that provide additional useful information on the process (Figure 7.3 The evolutions have always oscillatory character, due to the fact that $\langle v_r \rangle$ results from the combination (sum) of the contributions of the bound and non-bound parts of the wave packet. The former is what generates the oscillations since it corresponds to a vibrational wave packet relaxation. This is the only effect of this part of the wave function to the $\langle v_r \rangle$, since the position is steady (i.e. does not change during the evolution). Therefore, the moving part of the wave packet is what generates the main profile that resembles the one obtained in the case of Cl_2, and we address the reader to Chapter 4 for detailed discussion.

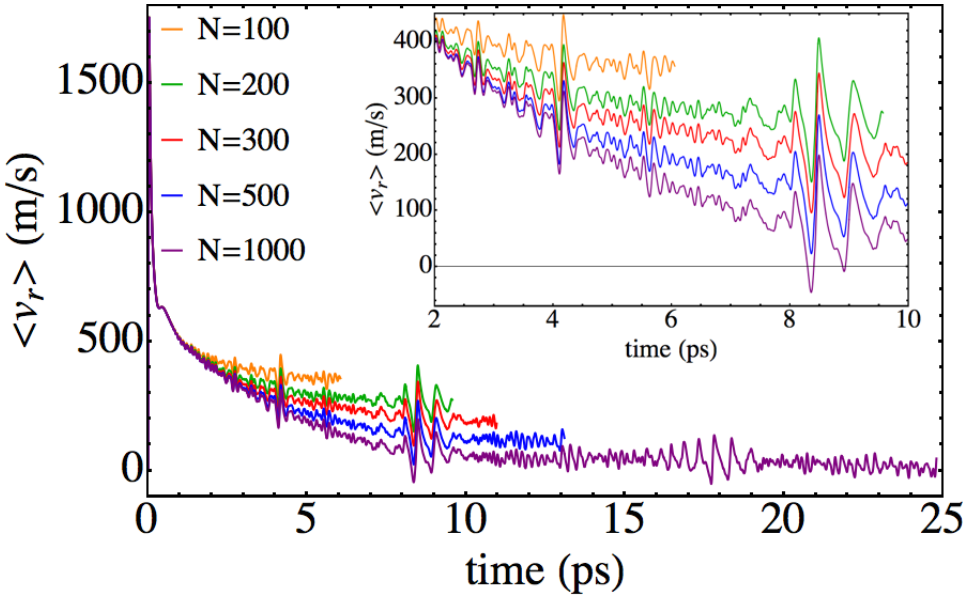

Figure 7.3. Evolution of the mean value of the relative velocity for Br_2 for the different droplet sizes.

Other important features that can be observed in Figure 7.3. consist in the existence of localized increases in the amplitude of the oscillations, which are independent of the droplet size. These take place at a time of around 4 ps, 8 ps and 16 ps, respectively. From the analysis of the movies it comes out that the former is due to the splitting of the wave packet. A detailed view of these situations (Fig.7.3. inner panel) shows that firstly a decrease of the velocity is produced, followed by an increase. This can be interpreted as follows. When the wave packet splits, the fraction of the middle rapidly moves towards the centre of the droplet. Thus, this reduction of the mean velocity is related with the small fraction of the wave packet arriving to the region where the electronic potential plays an important role, decelerating this fraction and so, decreasing the value of the velocity (negative velocity). This is followed by an increase of the velocity when this fraction of the wave packet rebounds from the potential walls. Therefore, this is the fingerprint of a vibrational relaxation process, but corresponding with a small fraction of the wave packet.

We now focus on the energies involved in the process. The Br_2 total energy, which is defined as the sum of the kinetic and the electronic (B state) potential, at initial time is about 2133.2 K, which is roughly about one order of magnitude less than in the case of Cl_2 (11094 K). Thus, this fact and the higher mass of bromine compared to chlorine lead to much lower velocities implied in the present photodissociation. In Figure 7.4 the temporal evolution of this quantity is represented. The general profile resembles the one obtained for chlorine and only

few differences are present. Notice that in the present study negative energies can be achieved, since a part of the wave packet is placed in the electronic well (bonded).

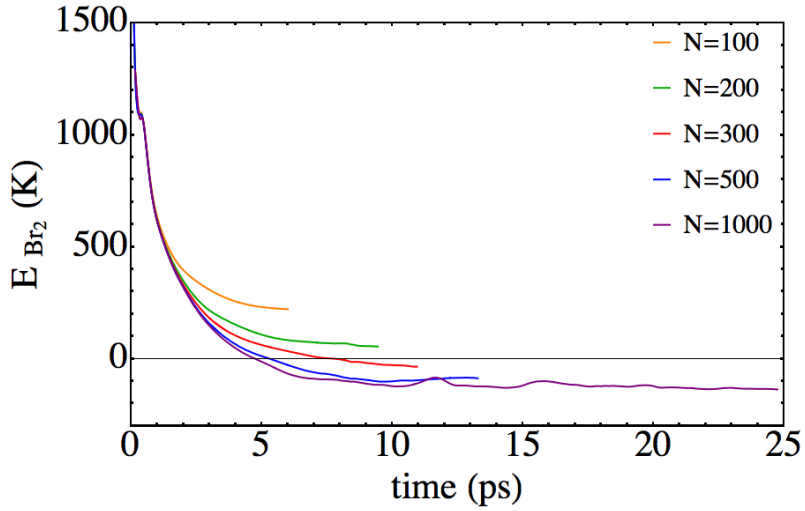

Figure 7.4. Time evolution of the total energy of Br_2, defined as the sum of the Br-Br electronic plus the relative kinetic energy.

To conclude this part, is important to focus on the velocity distributions of the photofragments, keeping in mind that the complete wave function does not leave the nanodroplet and, hence, these distributions correspond only to the leaving fraction. The different behavior obtained for the case of Br_2 (and also for I_2) does not allow us to proceed following the same procedure used in the Cl_2 case (when determining the velocity distribution by means of the asymptotic wave packet in momentum representation). Here, the wave packet in momentum representation has a contribution coming from the bound part (around 17%, for the two smallest nanodroplets), and so this does not exactly correspond to the velocity (or momentum) of the Br atoms leaving the droplet. Thus, we adopted a different treatment, carrying out a flux analysis of the wave packet in position representation at the edge of the relative coordinate grid, just before the NIP begins to absorb it. A brief explanation of this procedure is exposed in the Appendix.

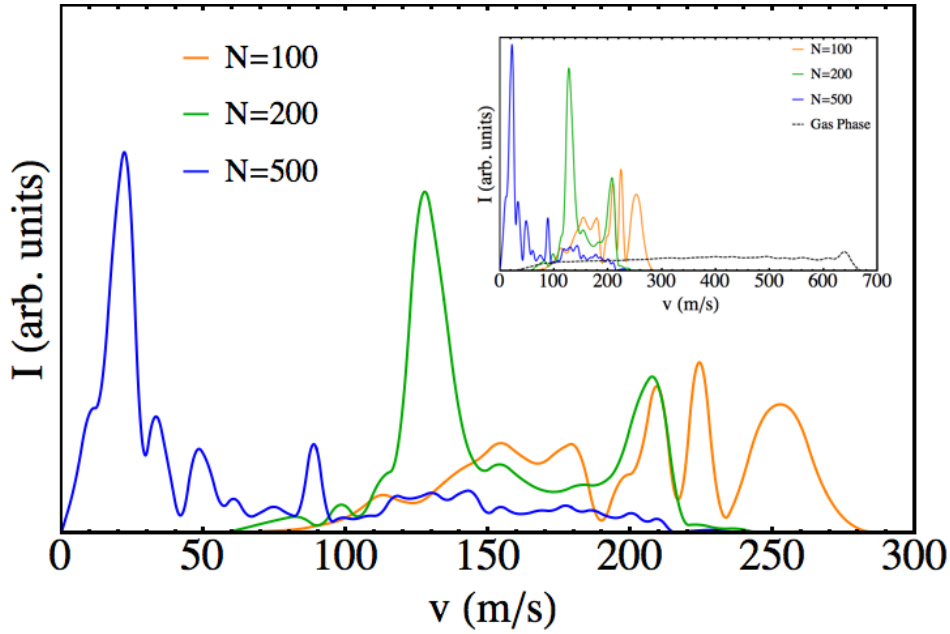

Figure 7.5. Velocity distribution of the Br atomic fragments for different nanodroplet sizes. The gas phase results within the same theoretical approach are also shown for the sake of completeness.

The velocity distributions obtained are plotted in Figure 7.5, together with the corresponding one obtained for the same process in gas phase using the same approximations. As in the case of Cl_2, an oscillating pattern is found (probably arising from quantum resonances). The velocities are much smaller than those observed for Cl_2. For the case of N=500, it is even reached the limit in which there is a probability of Br leaving at almost zero velocity (limit of the bound state). The effect of the droplet is clear: the cage effect highly reduces the mean velocities of the leaving fragments and induces the oscillating structures in the velocity distribution. The average velocities of the fragments are collected in Table 7.1.

Now, let us pay attention to the photodissociation of I_2. We have only examined for a nanodroplet of 100 ^{4}He atoms. The main feature observed is a strong dependence of the results on the potential energy surface (PES). The PES selected is the one in Reference 6, where the energy is described in terms of a sum of 2-body and 3-body terms. We have observed that presence of the 3-body term leads to a different dynamics. Concretely, total recombination of iodine atoms is found when using the full PES, while some probability for the atoms of leaving the nanodroplet is obtained when neglecting this term. Thus, considering that for this molecule important non-adiabatic couplings are expected to be presented we have decided not to go further into this study.

7.4 Mass Effects (X_2 "isotope" like of Cl_2)

The aim of this section is to shed some light on the influence of the atomic masses in the photodissociation dynamics. Thus, five different values of masses have been selected in order to cover enough a wide range of them and to make the investigation computationally affordable. These correspond to m = 0.25, 0.50, 0.75, 1.0 and 1.5 (written in terms of the chlorine mass units m_{Cl}). Furthermore, in order to ensure that the differences in the dynamical behaviour come only, exclusively from the mass effects, we have kept frozen the rest of the inputs. This framework includes using the same initial relative coordinate wave packet that corresponds to the ground state for the chlorine molecule.

Notice that the election of maintaining the initial vibrational ground state wave packet of Cl_2, i.e. $\varphi_{X_2}(v = 0)$, produces slight differences in the initial kinetic energy (ZPE) due to the different masses considered. Since this energy is related to the uncertainty principle rather than a purely translational kinetic energy, we do not expect this to influence the mechanism of the process in a significant way. If we had decided to calculate the corresponding ground state for each mass would have produced a wide variety of initial potential energies for the dynamics, when the Franck-Condon principle is applied. The energies of the model molecules at the initial time of the dynamics are collected in the Table 7.2.

Table 7.2. Initial (t=0) energies for the different masses. The corresponding zero point (kinetic) energies are also present and the relatives differences between the cases.

m_X (m_{Cl} units)	$\langle E \rangle_{kin}$ (t=0) (ZPM) (K)	$\langle E \rangle_{tot}$ (K)	% dif. $\langle E \rangle_{tot}$
0.25	797.8	11891.9	0.0
0.5	398.7	11492.8	3.4
0.75	265.8	11359.9	4.5
1	199.2	11293.3	5.0
1.5	132.8	11226.5	5.6

Some movies (Appendix) have also been prepared for the present investigation for the sake of clarity. As expected, the mechanism is very close to the one observed for chlorine and this will not be repeated here. However, the large energy exchange produced for the lowest masses can even induce the recombination of the X_2. For $m=0.50m_{Cl}$ the dissociation probability is only about ~14%, and for $m=0.25m_{Cl}$ full recombination of the wave packet is produced. In the former case, the wave packet remains for a long time close to the droplet

surface until the (large) Cl_2-helium attractive interaction induce the re-solvation (at the surface) of a fraction of the Cl_2 wave packet and it is split in two parts. The solvated part suffers recombination and the remaining one leaves the droplet and dissociate. The photodissociation process for the $m=0.25m_{Cl}$ "isotope" has a rather different mechanism, since the energy exchange is very efficient and the wave packet comes back to the centrum before reaching the nanodroplet surface. However, this process of recombination does not happen directly and there is present a "rebound" effect, due to the high excitation of the droplet (density waves) (cf. Figure 7.7). In Figure 7.6 some snapshots corresponding to the case $m=0.25m_{Cl}$ are shown in order to visualize its mechanism.

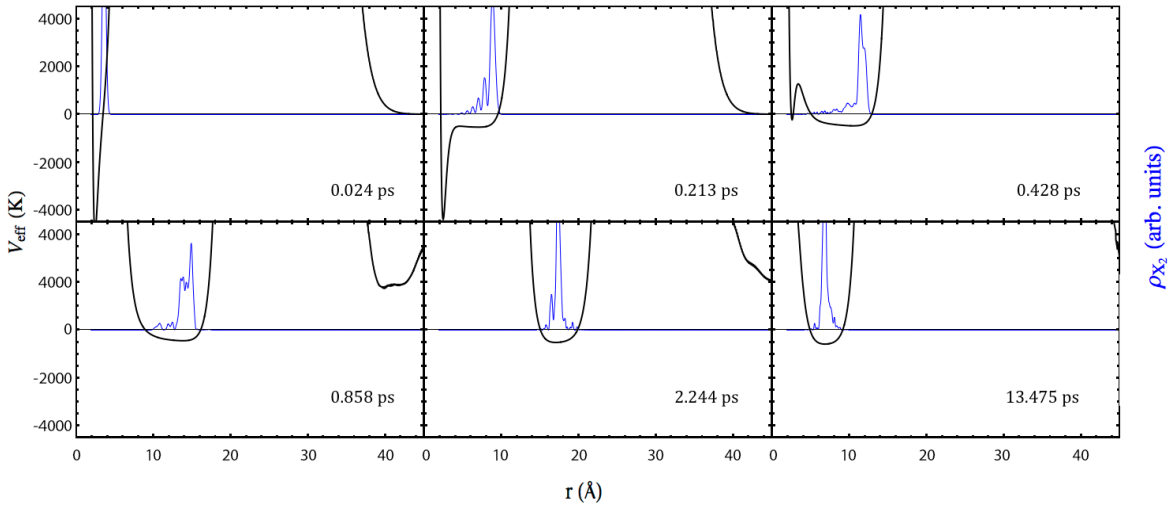

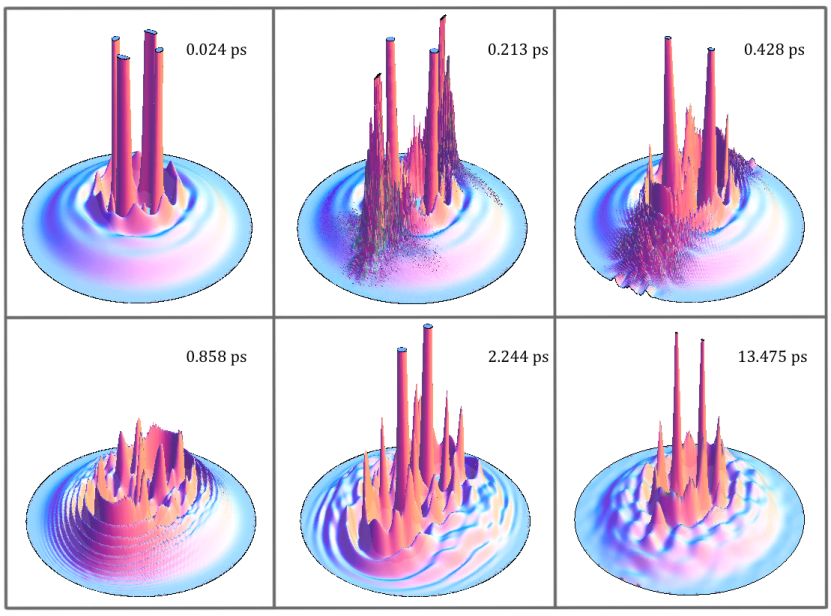

Figure 7.6. (up) Snapshots of the $X_2(m=0.25m_{Cl})$ wave packet (blue) and the effective potential (black). (down) The corresponding snapshots for the helium density in the xz-plane.

In Figures 7.7 and 7.8 it is shown the temporal evolution of the mean values of the relative coordinate and its corresponding velocity, respectively. These plots also end when the NIP begins to absorb the wave packet. The general behaviour is the already observed for the case of Cl_2, but for the lower masses the energy exchange is so effective that the atomic fragments can even stop and lead to the recombination process, i.e., negative relative velocity (see inner panel of Fig. 7.7). It can also be observed the "rebound" effect taking place during recombination of the $m=0.25m_{Cl}$ case.

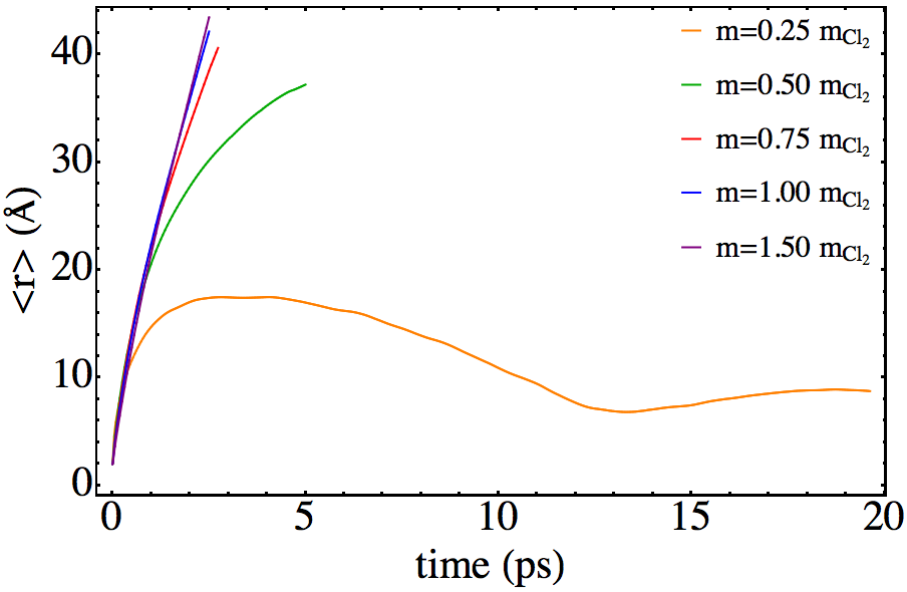

Figure 7.7. Time evolution of the mean value of the relative coordinate for the different cases studied.

The most important feature observed is the strong relationship between the mass and the energy exchange: the lower the mass, the higher the energy exchange, and this may lead to the recombination of the fragments. For the lowest mass considered ($m = 0.25\ m_{Cl}$) the whole wave packet recombines, while for $m = 0.50\ m_{Cl}$ a small fraction leaves the droplet and the remaining part of the wave packet recombines. These calculations are still running at the present date, and so we cannot provide more information about this up to now. In Table 7.2 there are given the values of the (kinetic) energy of the atomic fragments and the percentage of energy released to the droplet.

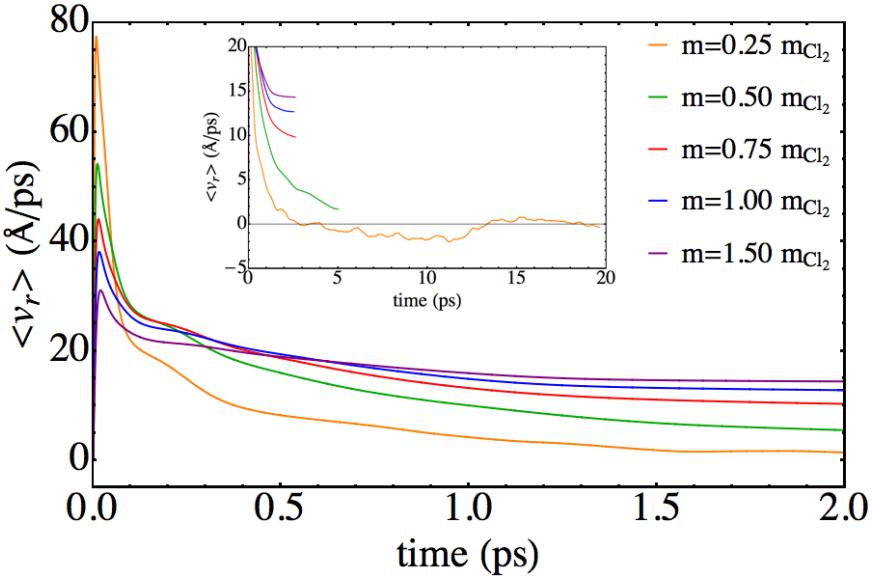

Figure 7.8. Time evolution of the mean value of the relative velocity for the different masses.

In order to deepen into the mechanism of the energy exchange, in Figure 7.9 the evolution of the energy of the molecule (kinetic and electronic potential) has been drawn. Two markedly regimes are present: the very initial time, form 0 to around 0.1 ps, and the rest, from around 0.1 ps to the end. It is clear that the fastest energy exchange is produced during the first regime. This corresponds to the collision of the atoms with the walls of the helium cavity (from 0 to ~0.01 ps the potential energy of X_2 is transformed in kinetic energy due to the electronic potential). The second regime correlates with the atoms travelling through the nanodroplet at velocities higher than Landau's velocity, so this is a viscous flow (cf. Chapter 4).

Table 7.2. Values of the X_2 energies (kinetic plus electronic potential) at the end of the process and velocity distributions of the X atomic fragments.

m_X (m_{Cl} units)	E final (K)	% Energy of initial E	<v_X> final (m/s)
0.25	-	-	-
0.5	-	-	242[a]
0.75	790.8	7.0	493
1	1736.5	15.4	628
1.5	3294.2	29.3	716

[a]This corresponds only to the leaving fraction of the wave function.

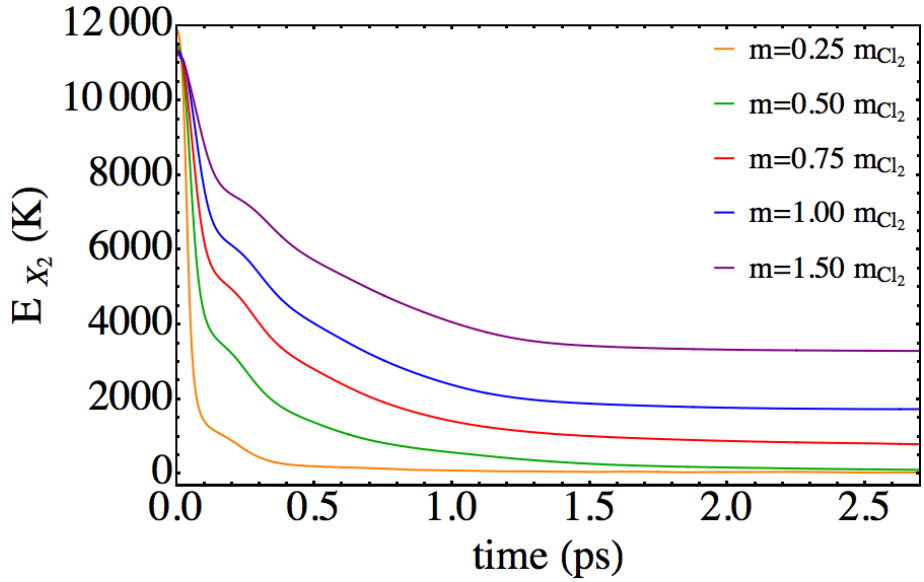

Figure 7.9. Time evolution of the energy of X_2 (kinetic + electronic potential) for the different masses.

The evolution of the X_2-helium interaction energy is shown in Figure 7.10. The profiles resemble very much to the ones of Cl_2. It can be observed that initial peak, which corresponds to the initial collision between the X atoms and the walls of the cavity, increases when the mass of X decreases. This suggests that for the lighter masses the walls of the helium cavity and the X atoms get closer than fro the larger, probably due to the higher velocities reached by these cases (given certain amount of energy, the larger the mass the lower the velocity). A more detailed analysis regarding the energy exchange mechanism will be considered in the future.

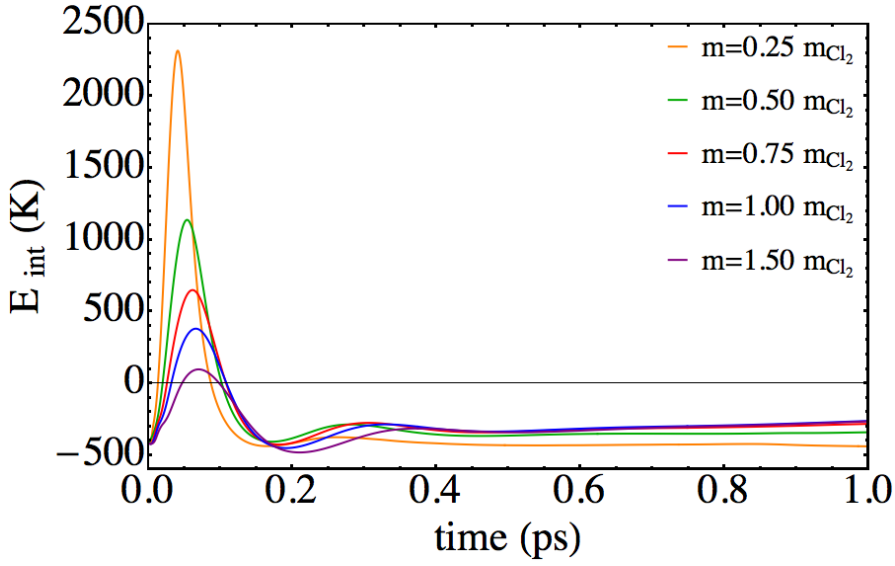

Figure 7.10. Time evolution of the X_2-helium interaction energy for the different masses considered.

To conclude this section, we focus into the velocity distribution of the leaving X atoms (cf. Figure 7.11). As for the case of Cl_2 (m=1.00 m_{Cl}) quantum resonances are also present. Another relevant feature is that for the m=0.50 m_{Cl} the velocity distribution presents its lower contribution slightly further away from the zero value, which means that the dissociative part of the wave packet resulting from the splitting process by the helium environment is "completely" free in energy terms (important kinetic energy). It is worth noting that this mechanism of recombination is not the same that was observed for the larger droplets regarding the photodissociation of the Br_2 molecule (for the N=500 there is some probability to detect leaving fragments at very small velocity (quasi bound))

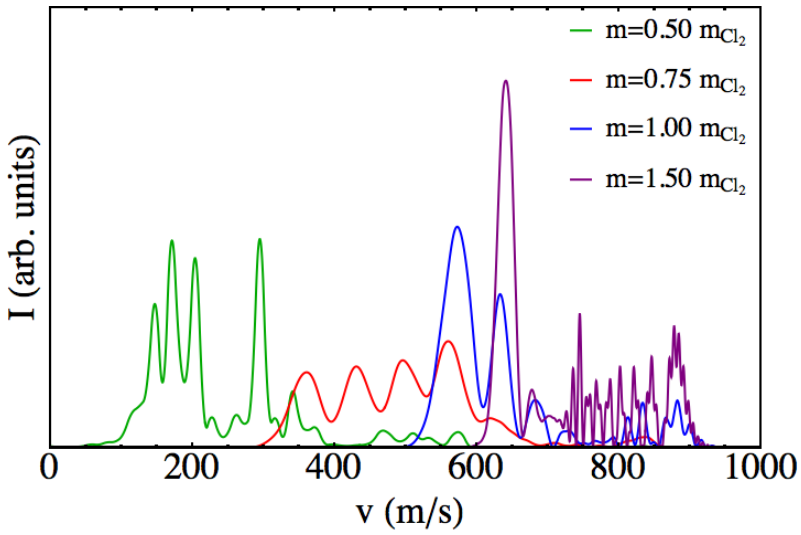

Figure 7.10. Velocity distributions of the X(m) photofragments.

7.5 Summary and conclusions

In the present chapter additional relevant aspects regarding the photodissociation dynamics of homonuclear diatomic molecules inside helium nanodroplets have been explored. In the first investigation regarding Br_2 and I_2, it has been pointed out the existence of larger time-scales for the process compared with the Cl_2 molecule. Also, it has been seen the possibility of nanodroplet-induced recombination process for the larger nanodroplets.

This study is just a first stage in the investigation of the photodissociation of Br_2 and I_2 in helium nanodroplets, since non-adiabatic couplings are not included in the theoretical framework. This approximation is not as good as it was for Cl_2 and non-adiabatic effects should be included in the calculations of Br_2 and I_2 to have more accurate results. In this

context, it is worth noting that this could increase the probability of the dissociative process, since potential energy curves crossings could generate repulsive forces.

Regarding the mass effects, we have pointed out the key role played by the mass in the exchange energy mechanisms. In this study, a fully recombination process has been observed for the lower mass considered.

To conclude, it is interesting to add a final remark on the physical interpretation of the results obtained related with the specificities of the theoretical method used. In these calculations we obtained situations in which the nanodroplet is doped with only a fraction of chemical specie, and the physical interpretation of these situations is not fully clear.

The theoretical framework used corresponds to a mean field approximation, which means that the different particles (nanodroplet and chemical specie) "see" each other as a mean field, i.e., as a spatial distribution. This underestimates the real correlation existing between the particles. In the case of the He-He correlations, although the DFT description is a mean field these correlations are somehow accounted for by the phenomenological energy density functional. However, the possible impurity-liquid helium correlations have only been included at a mean field level of description. Hence, this kind of process leading to such special situations suggest the necessity of including in the theoretical treatment more correlation between the liquid and the impurity in order to describe more accurately the nature of this process. Of course, this is out of the scope of the present thesis and, perhaps, in the future some insight towards this problem will be considered.

7.6 Appendix

Here we briefly show the procedure of obtaining velocity distributions from a flux analysis. The equations are written for a three dimensional (3D) case but the 1D situation is equivalent.

Let ψ be the wave function of the system, then the associated flux in quantum mechanics is given by the following expression:

$$\boldsymbol{j} = -\frac{i\hbar}{2m}\{\psi^*(\boldsymbol{\nabla}\psi) - \psi(\boldsymbol{\nabla}\psi^*)\} \tag{A7.1}$$

This quantity is defined in order to follow a continuity equation (the same as the hydrodynamic equation, Eq. A7.2) in which the (probability) density is given by the usual quantum mechanics formula ($\rho = \psi\psi^*$).

$$\frac{\partial\rho(\boldsymbol{r},t)}{\partial t} + \boldsymbol{\nabla}\boldsymbol{j}(\boldsymbol{r},t) = 0 \tag{A7.2}$$

This equation provides to the flux the usual meaning of the number of particles (or probability) flowing per unit time and unit area. This interpretation, in turn, allows to define the velocity through the relationship:

$$\boldsymbol{j}(\boldsymbol{r},t) = \boldsymbol{v}(\boldsymbol{r},t)\rho(\boldsymbol{r},t) \tag{A7.3}$$

Then, to compute the velocity distribution corresponding to the flow of particle density at a particular point ($\boldsymbol{r}_{analysis}$) we have to add the velocity corresponding to some density that crosses the analysis region, but weighted with the density in order to account for the contribution of the corresponding velocity. Therefore, the flux must be time integrated:

$$\int dt\rho\left(\boldsymbol{r}_{analysis},t\right)\boldsymbol{v}\left(\boldsymbol{r}_{analysis},t\right) = \int dt\boldsymbol{j}\left(\boldsymbol{r}_{analysis},t\right) \tag{A7.4}$$

Thus, the quantity we are looking for consists to the time integral of the flux at the corresponding regions. In practice, this integral is calculated as a sum and the time spacing is given by the time step of the dynamical simulation. At the end, the velocity space must be discretized into bins in order to build the histogram corresponding to the distribution. Therefore, there is some arbitrarity in doing so, that might condition the resulting shape of the distribution. Different binning's have been checked for each distribution obtained until

convergence is reached. To illustrate this effect, in Figure A7.1 are shown different profiles coming from different binning (n indicates the number of intervals used) but sharing the same input data (*N*=200 case).

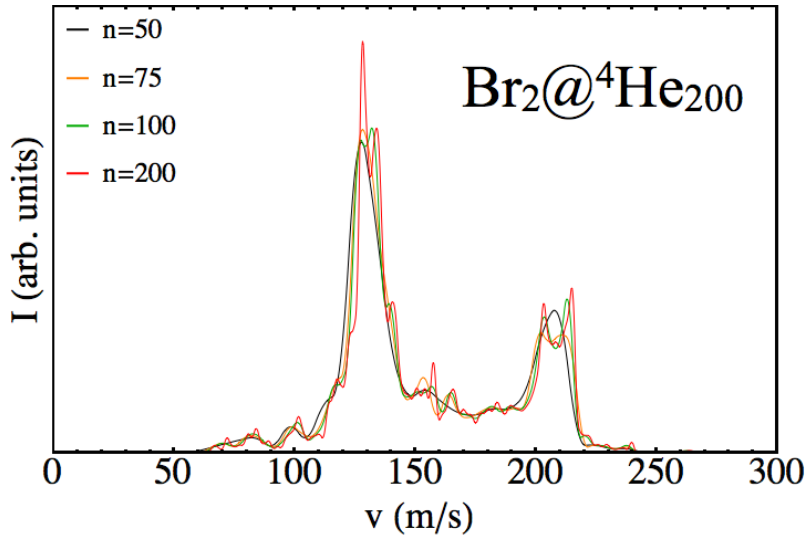

Figure A7.1. Velocity distributions of Br arising from different binings.

Furthermore, this working scheme to compute the velocity distributions is equivalent to the one using the wave packet in momentum representation, provided the region of analysis is enough asymptotic (i.e., essentially zero interaction potential between the atoms and the nanodroplet).

The method used in order to estimate the quality in the flux evaluation and the temporal integration by means the continuity equation is explained below. Integrating Eq. A7.2 in the whole space leads to:

$$\int d\boldsymbol{r}\frac{\partial\rho(\boldsymbol{r},t)}{\partial t} = -\int d\boldsymbol{r}\,\boldsymbol{\nabla j}(\boldsymbol{r},t) \tag{A7.5}$$

$$\frac{\partial}{\partial t}\int d\boldsymbol{r}\rho(\boldsymbol{r},t) = -\oint d\boldsymbol{S}\cdot\boldsymbol{j}(\boldsymbol{r},t) \tag{A7.6}$$

where the Stoke's theorem (right-hand side of the equation) and Leibniz derivation rule under integral sign have been used from eq.A7.5 to eq.A7.6. Then, integrating over time leads to:

$$\int d\boldsymbol{r}\rho(\boldsymbol{r},t) - \int d\boldsymbol{r}\rho(\boldsymbol{r},t=0) = -\int dt\oint d\boldsymbol{S}\cdot\boldsymbol{j}(\boldsymbol{r},t) \tag{A7.7}$$

$$\int d\boldsymbol{r}\rho(\boldsymbol{r},t) + \int dt \oint d\boldsymbol{S} \cdot \boldsymbol{j}(\boldsymbol{r},t) = 1 \qquad \text{(A7.8)}$$

Thus, the remaining norm of the wave function added to the temporal integration of the flux crossing the closed limiting surface before the region where the NIP works must be constant and have a unit value. We have calculated this quantity for all the calculations obtaining values differing from 1 of the order of 10^{-3}. Therefore, we expect that accurate enough results are obtained in both the flux calculation and the temporal integration.

Movie 7.1. Time evolution of the Br_2 relative coordinate wave packet (red) and the effective potential (black) (up left) and in momentum (in $Å^{-1}$, down left) representations. Time evolution of the helium density in the xz plane as 2D (up right) and 3D (down right) plots. The droplet is formed by N=100 ^{4}He atoms.

Movie 7.2. As movie 7.1 but for N=200 ^{4}He atoms.

Movie 7.3. As movie 7.1 but for N=300 ^{4}He atoms.

Movie 7.4. As movie 7.1 but for N=500 ^{4}He atoms.

Movie 7.5. As movie 7.1 but for N=1000 ^{4}He atoms.

Movie 7.6. Time evolution of the X_2 (m=0.25m_{Cl}) relative coordinate wave packet (red) and the effective potential (black) (up left) and in momentum (in $Å^{-1}$, down left) representations. Time evolution of the helium density in the xz plane as 2D (up right) and 3D (down right) plots. The droplet is formed by N=300 ^{4}He atoms.

Movie 7.7. As movie 7.6 but for m=0.50m_{Cl}.

Movie 7.8. As movie 7.6 but for m=0.75m_{Cl}.

Movie 7.9. As movie 7.6 but for m=1.50m_{Cl}.

7.7 References

[1] Braun, A.; Drabbels, M. *J. Chem. Phys.* **2007**, *127*, 114303.

[2] Vilà, A; González, M.; Mayol, R. *J. Chem. Theory Comput.* **2015**, *11*, 899.

[3] Valdés, A.; Prosmiti, R.; Villarreal, P.; Delgado-Barrio, G. *Mol. Phys.*, **2004**, 102, 2277.

[4] Delgado-Tellez, L.; Valdés, A.; Prosmiti, R.; Villarreal, P.; Delgado-Barrio, G. *Int. J. Quant. Chem*., **2012**, 112, 2971.

[5] Dalfovo, F.; Lastri, A.; Pricaupenko, L.; Stringari, S.; Treiner, J. *Phys. Rev. B*, **1995**, *52*, 1193.

[6] García-Vela, A. *J. Phys. Chem. A*, **2005**, 109, 5545.

[7] García-Vela, A. *J. Chem. Phys*, **2005**, 123, 124311.

[8] da Silva Gomes, J.; Gargano, R.; Martins, J. B. L.; Guilherme, L.; de Macedo, M. *J. Phys. Chem. A*, **2014**, 118, 5818.

[9] Assano, Y.; Yabushita, S. *Bull. Korean Chem. Soc*., **2003**, 24, 703.

[10] Barrow, R. F.; Clark, T. C.; Coxon, J. A.; Yee, K. K. *J. Mol. Spect*., **1974**, 428.

[11] Tellinghuisen, J. *J. Chem. Phys.*, **2011**, 115, 10417.

[12] Tashiro, M.; Ehara, M.; Kuma, S.; Miyamoto, Y.; Sasao, N.; Uetake, S.; Yoshimura, M. *Prog. Theor. Exp. Phys.*, **2014**, 013B02.

[13] Vala, J.; Kosloff, R.; Harvey, J. *J. Chem. Phys*., **2001**, 114, 7413.

8. Quantum dynamics of the pick up process of atoms by superfluid helium nanodroplets. The Ne+(^{4}He)$_{1000}$ system

8.1 Introduction

The investigation of the structure, energy and dynamics of superfluid helium nanodroplets ((^{4}He)$_N$; T=0.37 K) is a well-established research area in physics.[1,2] From a fundamental point of view these nanodroplets have a large interest because of their intermediate size, which essentially ranges from clusters to the bulk liquid, which allows to obtain a deep insight into the properties of quantum fluids and on the manner their properties evolve as the system size does. Moreover, helium nanodroplets can be used as low temperature matrices for high resolution spectroscopic studies, due to chemically inert character of He and the superfluid behavior of liquid ^{4}He below T=2.17 K. [3,4,5]

On the other hand, even though the contributions reported so far on the chemical reactivity in helium nanodroplets have been important (see, e.g., Refs. 6, 7, 8 and 9, and the references cited therein), the strength of these efforts is not comparable to those performed in the context of the physical studies. Lately, however, it seems that the chemical interest on this quantum fluid has increased significantly; and this probably results from the new possibilities offered by helium nanodroplets in the synthesis of new chemical species. Thus, they allow obtaining species that would not be stable in gas phase as, e.g., some metallic nanoclusters[10] and nanowires.[11]

Furthermore, little effort has been addressed up to date to explore the chemical reaction dynamics in the (^{4}He)$_N$ quantum fluid, both experimental (photodissociation of alkyl iodides in (^{4}He)$_N$)[12,13,14] and theoretically (photodissociation of Cl_2(B) in superfluid[9] and non-superfluid[15] helium nanodroplets). Although the main interest of our group in this context focuses on the theoretical study of the reaction dynamics inside helium nanodroplets, before

studying these processes we consider it is very interesting to characterize the pick up (or capture) process of chemical species by superfluid (^{4}He)$_N$, which corresponds to the previous stage needed for studying reactions inside nanodroplets. The dopant species in addition to be involved as a reactant, of course, can also be used as a probe in order to extract information about the nanodroplets.

Helium nanodroplets can capture a very wide range of atomic and molecular species, e.g., Ar_n,[16] Kr_n,[17] transition metal atoms (Cr_n,[18] Cu_n,[19]..), radical species from organic molecules (ethyl radical),[20] aromatic organic molecules and related species (anthracene, pyrromethene, porphyrin derivatives),[21] fullerene and small molecules ($C_{60}(H_2O)n$, $C_{60}(NH_3)n$ and $C_{60}(CO_2)n$).[22] etc. Nevertheless and rather surprisingly, very little is known about the dynamics of the capture process, which has been the object of very little attention at the theoretical level.[23]

Therefore, the ability of nanodroplets to capture almost any chemical species is of crucial importance and has been the main motivation of this work. Thus, we have theoretically investigated the quantum dynamics of the pick up process of a Ne atom by a superfluid helium nanodroplet of 1000 helium atoms (N=1000), Ne + (^{4}He)$_N$ → Ne@(^{4}He)$_{N'}$, exploring a rather wide range of velocities (90-1300 m/s), which are representative of those typical in a pick up experimental chamber. To the best of our knowledge this is the first quantum dynamics study carried out on the pick up process.

The superfluid helium nanodroplet was described by the time dependent density functional theory (TDDFT) and the Ne atom was described quantum-mechanically using a wave packet, i.e., following the same hybrid approach proposed by us recently.[9] Due to the high computational effort needed for a quantum description of the capture problem, we have restricted the study to the case of zero total angular momentum (head-on collisions).

The Ne + (^{4}He)$_N$ system was chosen primarily by the fact that, among all the analogous systems in which we can consider the capture of a noble gas atom, i.e., Rg + (^{4}He)$_N$ → Rg@(^{4}He)$_{N'}$ (Rg: He, Ne, Ar, Kr, Xe, Rn), and regardless of helium, it is the one that, due to the small mass of neon, is more likely to present a quantum behavior. Moreover and as a curiosity, it should be noted that it was in molecular beams experiments involving Ne and clusters of He where it was clearly shown for the first time that helium was able to capture atomic species.[24]

This chapter has the following structure: the theoretical methods employed are concisely explained in section 8.2; the description and analysis of the most important results achieved is given in section 8.3; and to finish the summary and conclusions are reported in section 8.4. Supplementary useful information has been included in the Appendix.

8.2 Theoretical methods

The study of the dynamics of the pick up process has been carried using a quantum treatment of the system, i.e., the impinging Ne atom and the helium nanodroplet, following an analogous theoretical approach as that proposed by us recently to describe the photodissociation of diatomic molecules in helium nanodroplets.[9] Thus, we have combined one of the main theoretical procedures employed to describe rather large systems of bosonic liquid helium (TDDFT; from hundred to thousands of atoms) and a usual method in gas phase time dependent quantum reaction dynamics (quantum wave packets (WP)), to account for the evolution of the helium nanodroplet and the neon atom, respectively. This strategy allows us to investigate relatively big nanodroplets, in this way making possible the (highly desirable) interaction with the experiments.

For the TDDFT description of the superfluid liquid helium, we have used the so-called Orsay-Trento phenomenological functional,[25] neglecting the backflow term and the non-local contribution to the helium correlation energy for computational reasons.[9,23] This functional is characterized via the $\mathcal{E}_c[\rho_{He}]$ term in equation 1b, which corresponds to the potential and correlation energy density of superfluid helium.

Since in this first study we only consider the situation of zero angular momentum, only a one-dimensional (z-axis) standard quantum wave packet dynamics is needed to describe the evolution of the (dopant) Ne atom. This is equivalent to treat the x and y neon degrees of freedom classically, and so they are represented in the total spatial wave function of Ne as a Dirac delta distribution, i.e., $\Psi_{Ne}(\boldsymbol{r}_{Ne}) \cong \phi_{Ne}(z_{Ne})\delta(x_{Ne})\delta(y_{Ne})$. Consequently, we have not paid attention neither on the effects of the natural spreading of the wave packet during the approach of the Ne atom to the nanodroplet, nor on the natural zero point motion inside the droplet in the (x, y) perpendicular directions. These effects would merely produce small perturbations to the physics of the pick-up process, [26] in which we are really interested, but largely increasing the computational cost of the calculations.

A detailed description of the TDDFT+WP method for doped (X_2 diatomic molecules) superfluid helium can be found in our previous work,[9] and here we will report the main equations and particularities of the present study. For the modeling of the Ne + (^{4}He)$_N$ system, the quantum action in terms of the effective complex wave function of (^{4}He)$_N$, $\Psi_{He}(\boldsymbol{R}_{He}, t) \equiv \sqrt{\rho_{He}(\boldsymbol{R}_{He}, t)}$, and the z-axis wave packet of Ne, $\phi_{Ne}(z_{Ne}, t)$, read as:

$$\mathcal{A}[\Psi_{He}, \phi_{Ne}] = \int dt \Big\{ E[\Psi_{He}, \phi_{Ne}] - i\hbar \int d\boldsymbol{R}_{He}\, \Psi^*_{\boldsymbol{He}}(\boldsymbol{R}_{He}) \frac{\partial}{\partial t} \Psi_{He}(\boldsymbol{R}_{He}) + -i\,\hbar \int dz_{Ne}\, \phi^*_{Ne}(z_{Ne}) \frac{\partial}{\partial t} \phi_{Ne}(z_{Ne}) \Big\} \tag{8.1a}$$

where E is the total energy of the system that is given by the following expression:

$$\begin{aligned} E[\Psi_{He}, \phi_{Ne}] = {} & \frac{\hbar^2}{2m_{He}} \int d\boldsymbol{R}_{He}\, |\boldsymbol{\nabla}\Psi_{He}|^2 + \int d\boldsymbol{R}_{He}\; \mathcal{E}_c[\rho_{He}] \\ & + \int d\boldsymbol{R}_{He} \int dz_{Ne}\, V_{He-Ne}(z_{Ne}, \boldsymbol{R}_{He})\, \rho_{He}(\boldsymbol{R}_{He}) |\phi_{Ne}(z_{Ne})|^2 \\ & - \frac{\hbar^2}{2m_{Ne}} \int dz_{Ne}\, \phi^*_{Ne}(z_{Ne}) \frac{\partial^2}{\partial {z_{Ne}}^2} \phi_{Ne}(z_{Ne}) \end{aligned} \tag{8.1b}$$

To obtain the equations of motion governing the time evolution of helium and the Ne atom, the quantum action (Eq. 8.1a) has to be minimized by performing variations of the wave functions Ψ_{He} and ϕ_{Ne}. This leads to a pair of coupled non-linear Schrödinger-like equations:

$$i\hbar \frac{\partial}{\partial t} \Psi_{He}(\boldsymbol{R}_{He}) = \left[-\frac{\hbar^2}{2m_{He}} \boldsymbol{\nabla}^2 + \int dz_{Ne}\, V_{He-Ne}(z_{Ne}, \boldsymbol{R}_{He})\, |\phi_{Ne}(z_{Ne})|^2 + + \frac{\delta \mathcal{E}_c[\rho_{He}]}{\delta \rho_{He}} \right] \Psi_{He}(\boldsymbol{R}_{He}) \tag{8.2a}$$

$$i\hbar \frac{\partial}{\partial t} \phi_{Ne}(z_{Ne}) = \left[-\frac{\hbar^2}{2m_{Ne}} \frac{\partial^2}{\partial {z_{Ne}}^2} + \int d\boldsymbol{R}_{He} V_{He-Ne}(z_{Ne}, \boldsymbol{R}_{He}) \rho_{He}(\boldsymbol{R}_{He}) \right] \phi_{Ne}(z_{Ne}) \tag{8.2b}$$

Equations 8.2a and 8.2b have been discretized using Cartesian grids. We have employed different grids (depending of the initial velocity of the Ne atom) to properly account for the physics of each case; since the spacing in the coordinate grid is proportional to the maximum value of the (conjugated) momentum grid. The characteristics of the different grids used are given in Tables A8.1 and A8.2.

The time propagation has been performed using the Adams predictor-corrector-modifier method,[27] initiated by a fourth order Runge-Kutta method[28] (the time step used varied from 3.0 10^{-4} to 8.0 10^{-5} ps from 90 to 1300 m/s, respectively). The derivatives for the kinetic energy terms have been calculated in momentum space by means of a Fourier transform using the FFTW package of Ref. 29.

In order to absorb the helium density evaporated from the nanodroplet and to avoid non-physical reflections of the helium effective wave function, a quartic negative imaginary potential (NIP) has been introduced in the edges of the grid.[30] We also applied a NIP to the edges of the Ne grid so as to account for the possibility of rebound of a fraction of the wave packet due to the collision with the nanodroplet. The NIPs have the following expression:

$$V_{\mathrm{NIP}} = -i\,A\frac{5}{2}\left(\frac{d-d_{\mathrm{NIP}}}{L}\right)^4 \tag{8.3}$$

for $d > d_{\mathrm{NIP}}$, where the absorption strength (A) is equal to 331.5 and 3315.0 K Å^{-4} for the Ne atom and helium, respectively, the length (L) is equal to 1 Å, and the location (d_{NIP}) of the NIPs are indicated below. The atomic NIP is placed in the z axis at 12.1 Å (<v_0>=90-500 m/s) and 8.8 Å (<v_0>=800-1300 m/s) with respect to the (^{4}He)$_N$ surface (nanodroplet radius=25 Å). The NIPs for (^{4}He)$_N$ are located in the z axis at 13.1 Å (<v_0>=90-500 m/s) and 9.8 Å (<v_0>=800-1300 m/s) with respect to the nanodroplet surface, while for the x and y axis they are at 12.6 Å (<v_0>=90-500 m/s) and 10.6 Å (<v_0>=800-1300 m/s).

Concerning the initial conditions for the dynamics, we have considered a pure helium nanodroplet of 1000 ^{4}He atoms and a minimum uncertainty Gaussian wave packet describing the Ne atom (Eq. 8.4). The wave packet has been centered in the z-axis at μ = -35 Å, which is far enough from the nanodroplet to consider the situation as asymptotic (Ne-helium interaction energy = -0.065 K). For the width of the wave packet we selected the value σ=0.8 Å^{-1} since this leads to a description of the WP with almost the same number of points in the position and momentum grids.

$$\phi_{Ne}(z_{Ne}, t=0) = \frac{1}{(2\pi\sigma^2)^{1/4}} e^{-\frac{(z_{Ne}-\mu)^2}{4\sigma^2}} e^{i\frac{p_0}{\hbar}(z_{Ne}-\frac{\mu}{2})} \tag{8.4}$$

The initial values of the energies involved can be seen in Table 8.1. The numerical parameters defining the Cartesian grids of the Ne atom and helium are given in Tables A8.1

(including the propagation time steps) and A8.2, while the final simulated times are reported in Table A8.3.

Table 8.1. Initial values of the energies (in K) involved in the process.[a]

N	$E_{\text{Interac.}}$Ne-helium	E_{Kin} helium	$E_{\text{Pot+Corr}}$ helium
1000	-0.065	124.51	-5520.0

[a]E_{Kin} Ne (K) = 9.74, 17.31, 53.02, 108.2, 300.6, 769.4, 1731.2 and 2031.7 for $\langle v_0 \rangle$ (m/s) = 90, 120, 210, 300, 500, 800, 1200 and 1300, respectively.

8.3 Results and discussion

The process of the capture of neon atoms by helium nanodroplets with zero impact parameter (i.e., angular momenta equal to zero) has been studied at several initial velocities of Ne ($\langle v_0 \rangle$ = 90, 120, 210, 300, 500, 800, 1200 and 1300 m/s). These velocities have been selected in order to account for representative velocities of a Maxwell velocity distribution of Ne atoms at T = 300 K (Figure 8.1), i.e., for rather typical experimental conditions in the pick up chamber.

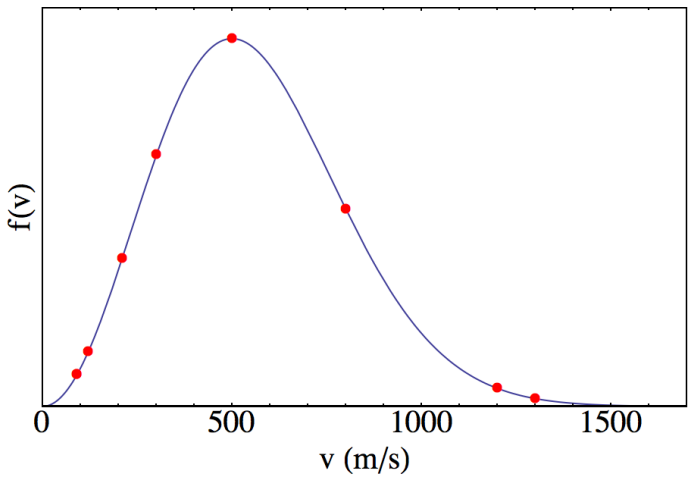

Figure 8.1. Maxwell velocity distribution of Ne at a temperature of 300 K. The red points indicate the velocities considered in this work.

The simulated times are not the same for all cases (Table A8.3). With the exception of the two higher velocities we have stopped the calculations at a time around 150-200 ps. This choice is mainly based on physical arguments, which will be clear hereafter, and also due to the high computational cost of these calculations.

To visualize the dynamical mechanism of the picking up of a Ne atom by a helium nanodroplet, some movies have been prepared, which include the probability density of the Ne atom wave packet in coordinate ($|\phi_{Ne}(z_{Ne})|^2$) and momentum ($|\tilde{\phi}_{Ne}(p_{z_{Ne}})|^2$) representations and the helium density in the z-axis and in the xz plane (cf. movies 8.1-8.3 in the Appendix for $\langle v_0 \rangle$=210, 500 and 800 m/s, respectively). Moreover, Figure 8.2 shows snapshots of the temporal evolutions of $|\phi_{Ne}(z_{Ne})|^2$ and helium density at selected times for $\langle v_0 \rangle$=500 m/s (maximum of the Ne velocity distribution; cf. Fig. 8.1), and Figure A8.1 shows the analogous representation for $|\tilde{\phi}_{Ne}(p_{z_{Ne}})|^2$.

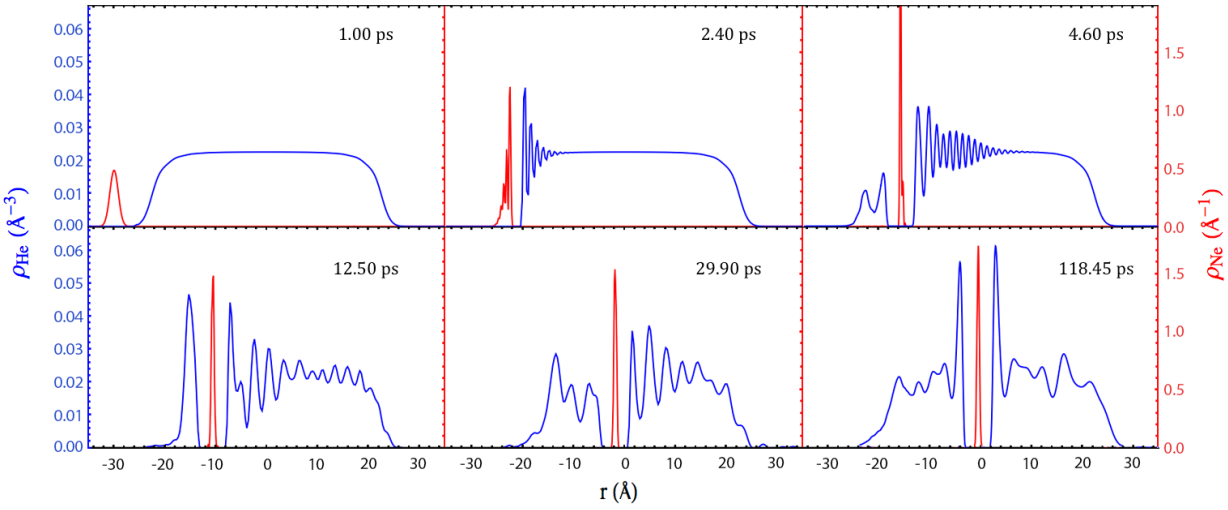

Figure 8.2. Snapshots showing the temporal evolution of the probability density of the Neon wave packet, $\rho_{Ne} \equiv |\phi_{Ne}(z_{Ne})|^2$, and helium density, ρ_{He}, along the z-axis for $\langle v_0 \rangle$=500 m/s. The system is moving from left to the right with the exception of the last snapshot where the reverse occurs.

Leaving out the Ne atom approach to the nanodroplet, three different steps can be identified in the pick up process. The first one corresponds to the penetration of the atom through the nanodroplet surface, which acts as a dynamical potential barrier. Once the Ne atom is inside the nanodroplet its velocity decreases due to the interaction with the helium environment. Then, when the atom velocity reaches a limiting value below the Landau's critical velocity (≈58 m/s (0.58 Å/ps) in superfluid (bulk) helium[31,32] and also recently observed in nanodroplets with $N \geq 1000$ [33]), it remains stable until the atom approaches to the nanodroplet inner surface and bounces back. It should be noted here that, due to the (reasonable) simplifications made in the helium functional to make possible the present calculations, the critical velocity is about 90 m/s.[33] At this stage of the process the only mechanism of exchanging energy from the moving Ne atom to the nanodroplet is based on

the activation of the surface excitation modes. This is a very slow relaxation mechanism that occurs each time the atom reaches the nanodroplet inner surface and because of this we stopped the simulations for computational reasons.

Focusing on the first step of the process, a wide range of different behaviors is found, depending on the initial velocity. For the softer impacts ($<v_0>$ = 90 and 120 m/s) some fraction of the wave packet is reflected during the collision with the nanodroplet. Thus, for the 90 m/s case the 88.0% of the WP is captured while for 120 m/s a value of 98.5% is obtained. The remaining cases have a penetration coefficient of 100%, i.e., all the WP is captured by the nanodroplet. Although a detailed characterization of the dependence of the penetration probability with the initial velocity and the analysis of possible quantum effects as tunnelling or resonances (quasi bound states) has a significant interest, it is out of the scope of the present study and we expect to investigate them in a future work.

When the Ne atom collides with the nanodroplet surface, an oscillatory pattern, which increases with the initial velocity, can be observed in both the Ne wave packet probability density and the helium density (cf. Figure 8.2 and movies 8.1-8.3). The dynamical behaviour is essentially the same for the full penetration cases, with only small differences. The wavelength of the helium density oscillations decreases with the initial velocity (collision energy), indicating that the nanodroplets become progressively more excited as $<v_0>$ increases. The formation of a stable solvation shell around the Ne atom is only produced when the nanodroplet is not highly excited, because in the former situation the helium density waves destroy the solvation structures which are permanently being formed and destroyed. Besides, from the evolution of the helium density in the xz plane it can be seen the very small distortion suffered by the geometry of the nanodroplet. This has been found in other dynamical processes occurring in helium nanodroplets, such as the photodissociation of Cl_2[9] and the ionization of heavy atoms,[34] where higher energies were involved.

From Figure A8.1 ($<v_0>$=500 m/s) and movies 8.1-8.3 ($<v_0>$=210, 500 and 800 m/s, respectively) it can be seen that the Ne wave packet probability density in momentum space moves towards lower momentum values, when the collision with the nanodroplet surface takes place. In all cases, at a certain time, the square modulus of WP(p) adopts a Gaussian-type shape centered at a particular value of momentum; and this happens when the (mean) velocity of Ne is below the Landau's critical velocity.

This means that the square modulus of WP(r) has also a Gaussian profile (the Fourier transform of a Gaussian function is a function of the same type). Therefore, keeping in mind that these wave functions are eigenfunctions (solutions) of an harmonic oscillator problem and in virtue of the Galilean transformation, we infer that WP(r) is placed in a harmonic-like potential moving at constant velocity. This is consistent with the fact that the wave function is placed around the minimum of a moving potential, and so it is locally quadratic, which is also reasonable from a classical point of view, since the force must be zero in the minimum of a potential. Therefore, an almost isotropic distribution of helium must surround the impurity in order to produce such a essentially symmetric, potential, as can be confirmed by movies 8.1-8.3. Finally, when the Ne atom reaches the nanodroplet inner surface, the momentum wave packet moves passing through the zero value and the sign of the momentum changes.

The mean values are useful in this context and the time evolution of the mean value of the Ne atom position, i.e., $\langle z_{Ne} \rangle$, is plotted in Figure 8.3. In this and the following figures, the temporal evolution of magnitudes associated to $\langle v_0 \rangle$=90 and 120 m/s cases finishes at t = 31.1 and 19.4 ps, respectively, because at these times the NIP begins to absorb and then the wave packets are not longer normalized.

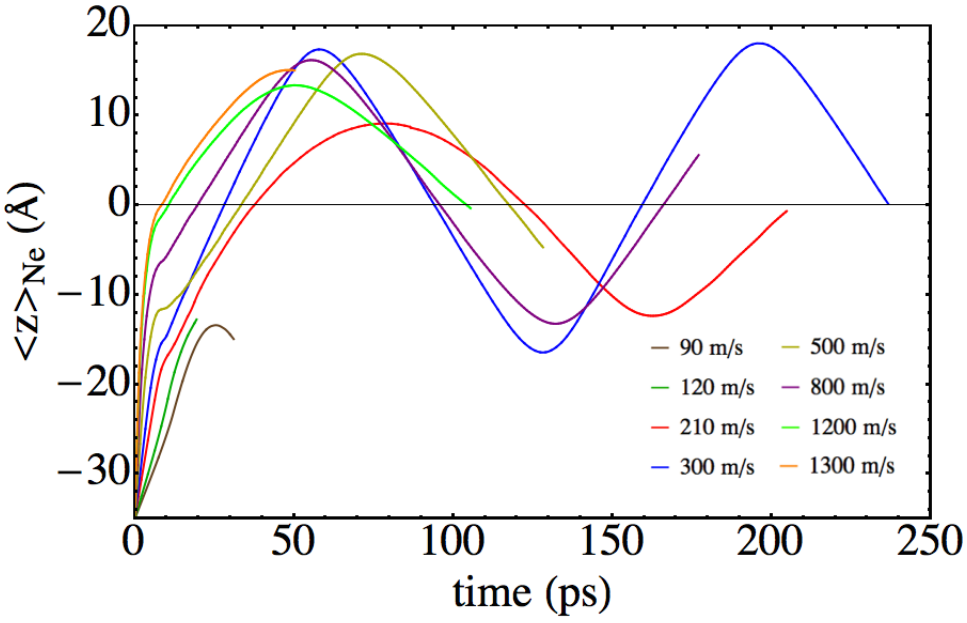

Figure 8.3. Temporal evolution of the mean value of the Ne atom position, as a function of $\langle v_0 \rangle$. Smaller simulated time intervals are considered for the lower velocities (90 and 120 m/s) due to the absorption of a fraction of the neon wave packet by the NIP.

For $\langle v_0 \rangle$=300 m/s the calculations show up to three rebounds of WP(r) with the nanodroplet surface. The amplitude of the oscillations does correlate in a simple way with the

initial velocity value, and the $\langle v_0 \rangle$=210 m/s case has lower turning points than the other velocities. It can also be seen that the turning points are not symmetric. Both facts point out how the helium density waves, whose magnitude depends on the initial collision energy, influence the dynamics. This is probably due to the rather comparable value of the Ne and He masses ($m_{Ne}/m_{He} \approx 5$). For heavier dopants a different behavior would be expected.

The temporal evolution of the mean values of the Ne velocity, focusing on the collision and the atomic motion inside the nanodroplet, is presented in Figure 8.4. For the higher velocities ($\langle v_0 \rangle$=1300, 1200, 800 and 500 m/s) the deceleration follows, on the overall, almost the same curve and at around t=8-9 ps $\langle v_{Ne} \rangle$ reaches a minimum. This minimum is due to a push of the helium density waves that happens when a relatively stable helium solvation shell is formed (cf. movies 8.1-8.3). So that, during the process of changing from a slightly asymmetric to a symmetric potential well (quadratic), a small kick to the Ne atom is produced.

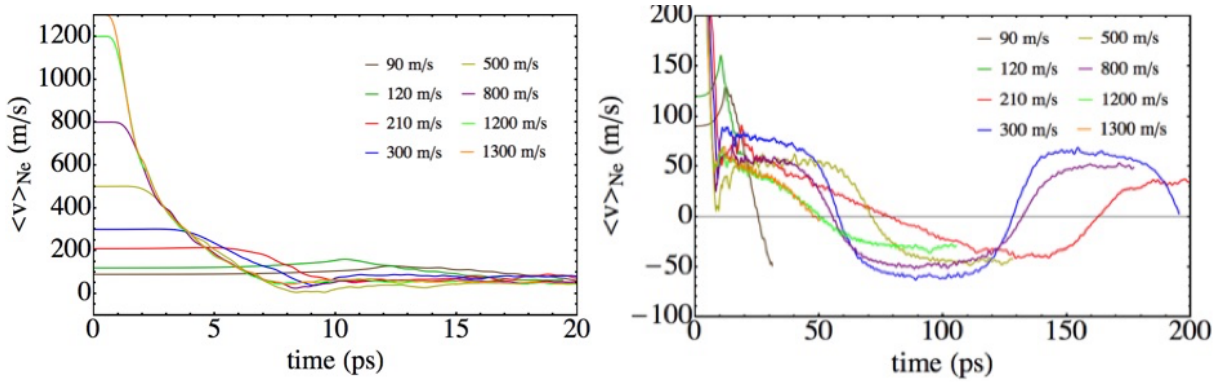

Figure 8.4. Temporal evolution of the mean value of the velocity as a function of $\langle v_0 \rangle$, focusing in the initial part of the collision (up) and during the travelling of the Ne atom through the nanodroplet (down).

This means that the momentum transfer is not unidirectional, as there is also a small momentum transfer from the helium to the Ne atom. This also occurs for $\langle v_0 \rangle$=300 and 210 m/s but it is less evident, since the excitation of the helium nanodroplet is smaller. For the softer collision conditions ($\langle v_0 \rangle$=90 and 120 m/s) there is a remarkable acceleration before the penetration of the nanodroplet surface, due to the attractive interaction between the Ne atom and the nanodroplet. This is not observed in the other cases since their velocities are high enough, so that the approaching process is similar to a solid collision.

The evolution of the velocities once the Ne atom is inside the nanodroplet is also shown in Figure 8.4. For most cases the velocity remains constant during the atom travel

through the bulk-like part of the nanodroplet. This is consistent with the existence of a Landau's critical velocity in helium nanodroplets recently reported experimental and theoretically.[33] Within the TDDFT level of theory, using the Orsay-Trento functional and neglecting the backflow and correlation alpha terms a value of 90 m/s has been determined. Here we have obtained an analogous result, but with a quantum (particle) probe (Ne atom) rather than a classical one as in the theoretical study of Ref. 33.

This phenomenon is clearly evident after the first collision with the nanodroplet inner surface. Each pick up case examined has a different limiting velocity and this arises from the different initial collision conditions (the reason of this behaviour will be explained in the next paragraphs). Once the Ne atom is moving below the Landau's critical velocity, the only possible mechanism to release energy to the nanodroplet results from the excitation of the surface modes (ripplons), and this occurs every time the atom collides with the nanodroplet inner surface. Because of this we decided to finish the calculations, since an oscillating pattern in the $\langle v_{Ne} \rangle$ vs. time dependence is expected to be present for a very long period of time. Hence, the continuation of the simulations is not expected to give new insights into the physics of the process.

The analysis of the evolution of $\langle v_{Ne} \rangle$ versus $\langle z_{Ne} \rangle$ allows us to obtain some more light on the mechanism of the pick up process (Figure 8.5), paying attention to the different limiting velocities found. This plot corresponds to the representation of the average trajectories in phase space, excepting that the mass of the Ne atom is not multiplying the mean velocity along the z axis. The dashed line in Figure 8.5 shows the z value for the pure nanodroplet surface (radius of 25 Å), and from around this point the Ne velocity begins to change (increasing or decreasing).

Two markedly different regions are present, corresponding to the two regimes of the pick up dynamics. The first region presents two straight lines in the $\langle v_{Ne} \rangle$ versus $\langle z_{Ne} \rangle$ plot: a horizontal line (constant velocity) that is followed by a oblique line (deceleration). The second line indicates the presence of a friction force of the type $F_f = -b\langle v_{Ne} \rangle$, resulting from the interaction of Ne with the helium nanodroplet. That is to say, the helium behaves as a conventional fluid as it has also been recently reported by us in a Cl_2 photodissociation quantum study.[9] So that, during the first dynamic regime, there is an important energy release

from the Ne atom to the helium nanodroplet (which is particularly important for $\langle v_0 \rangle$ above 120 m/s), with the subsequent rapid decrease of the Ne velocity.

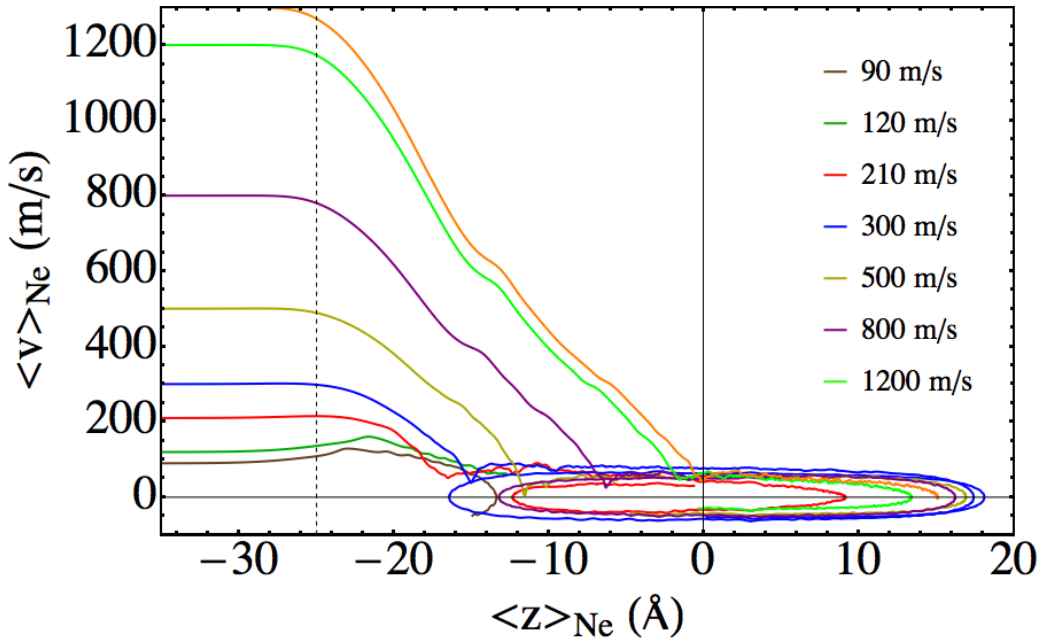

Figure 8.5. Trajectories of the mean values of the Ne atom velocity and position as a function of $\langle v_0 \rangle$. The dashed line shows the z value for the pure nanodroplet surface.

The second $\langle v_{Ne} \rangle$ vs. $\langle z_{Ne} \rangle$ region follows after the first region and presents average trajectories with an ellipsoidal-like shape that corresponds to the oscillations of the Ne atom inside the nanodroplet (from the right to left and so on). These phase-orbits are almost closed and each studied case has its own "ellipse". Excepting the case of $\langle v_0 \rangle$=210 m/s, whose phase trajectory is slightly different, the others follow a similar pattern. From Figure 8.5 we can also see that each $\langle v_0 \rangle$ value results in a different $\langle z_{Ne} \rangle$ value, once the trajectory of the mean values gets into its own ellipsoidal-like motion in phase space and, of course, also results in a different excitation of the nanodroplet (Table 8.2).

Table 8.2. Final excitation energy per He atom of the nanodroplet

$\langle v_0 \rangle$ (m/s)	210	300	500	800	1200	1300
D*e* (K)	0.09	0.15	0.28	0.33	0.39	0.42

In the $\langle z_{Ne} \rangle$ points near the nanodroplet surface there is a net force pointing towards the center due to the non-symmetric solvation of the dopant. Observing the quasi-ellipses, we see that the curvature of the phase-trajectories takes place from a distance of around 10 Å off the nanodroplet center, independently of the case considered. Therefore, for the Ne atom

impurity there is a part of the $^4He_{1000}$ nanodroplet that shows bulk-like character and has a length of about 20 Å. This would be a sort of measure of the completeness (effective symmetry) of the Ne atom solvation and, of course, we expect that this value will depend on both the helium and the impurity (dopant) considered. In this region, once the atom velocity becomes smaller than the Landau's critical velocity, it would remain essentially constant if the nanodroplet is not so excited.

From these considerations we can understand better the origin of the different "ellipses" found in the calculations. Disregarding the effects produced by the density waves in liquid helium (excitation), the phase trajectory would begin to become similar to an ellipse when the atom reaches the Landau's critical velocity, unless this velocity is reached in a "non-bulk" zone of the nanodroplet. This together with the remaining excitation of the nanodroplet will determine the shape of the "ellipse" in each case.

We estimated the excitation energy per helium atom of the nanodroplet at the time when the phase trajectory becomes an "ellipse" by $\Delta e = e - e_{Ne@\,^4He_{1000}}$, where $e \equiv E/N$ is the energy of the nanodroplet divided by the number of helium atoms, and $e_{Ne@\,^4He_{1000}}$ is the corresponding equilibrium energy (these energies only correspond to helium, i.e., neither the Ne-helium interaction energy nor the Ne kinetic energy are included; Table 8.2). Hence, when the Ne atom moves at a constant velocity the excitation of the nanodroplet is not the same for all the cases examined. This would also explain the fact that for the higher initial velocities the "turning points" are closer to the center of the nanodroplet, because there are energetic helium density waves reflecting at the nanodroplet surface and pushing the Ne atom back towards the centre.

To complete the analysis of the pick up process we focused our attention into the evolution of *E*/*N* on time. During the collision of neon with the nanodroplet surface there is important energy exchange from the atom to the nanodroplet (Figure 8.6). Besides, for all the $\langle v_0 \rangle$ values the *E*/*N* vs. time dependence shows the same behaviour. At the beginning *E*/*N* increases (first monotonically and then non-monotonically ("oscillations")), then reaches a maximum and, finally, decreases with time, due to the evaporation of helium atoms (Figure 8.7), and tends to a constant value. Structures ("oscillations") are also evident in Figure 8.4, when showing the mean value of the Ne velocity vs. time, which is directly related to its kinetic energy.

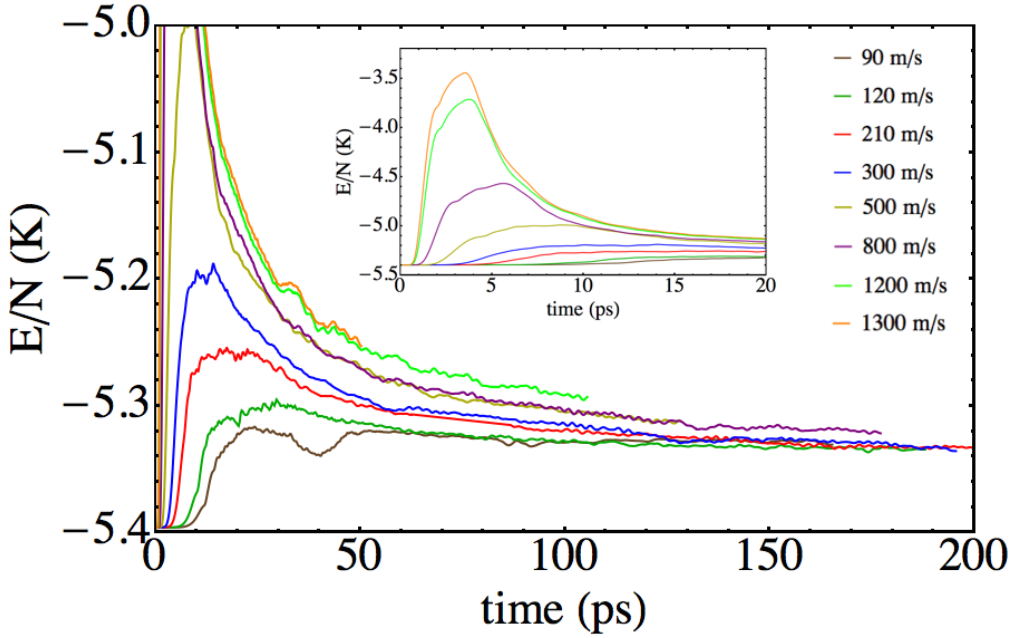

Figure 8.6. Time evolution of the energy per helium atom of the nanodroplet as a function of $<v_0>$. The inner panel focus on the initial part of the collision.

The asymptotic behaviour of the *E*/*N* vs. *t* curves suggests that at around 150-200 ps all the doped nanodroplets are almost relaxed (Figure 8.6). This time scale is shorter but comparable with that found in the case of the relaxation of nanodroplets of different sizes (*N*=50-500) after the photodissociation of a Cl_2(B) embedded molecule (several hundred picoseconds).

The *E*/*N* value obtained in the asymptote is somewhat greater than that for the nanodroplet at *t*=0 (Figure 8.6). To clarify this result we have carried out a static calculation of the Ne@^{4}He$_{1000}$ nanodroplet, obtaining a *E*/*N* value of -5.35 K, which compares very well with the ≈-5.33 K value determined for the asymptotic value (there is a little difference (≈1.3%) in the number of He atoms of both nanodroplets; cf. Figure 8.7). Therefore, the *E*/*N* change observed in the asymptote is only due to the differences in the initial and final situations (non-doped vs. doped nanodroplets, respectively).

To conclude, we have compared the kinetic energy corresponding to the zero point motion of the Ne atom doping the static nanodroplet with the asymptotic values of the present dynamics study. The asymptotic values of the Ne atom kinetic energy ranges from around 7.0 K up to 10.5 K, for the case in which the impurity is moving faster ($<v_0>$ = 1300 m/s). From a 3D wave packet static calculation of a Ne atom doped nanodroplet of 1000 ^{4}He atoms, we obtained a Ne atom kinetic energy of 17.3 K. Now, taking into account that within the present

approximation only one dimension is considered for the Ne motion, we estimate a value of 17.3/3=5.8 K corresponding to each coordinate. So that, we infer that when the atomic impurity reaches its limit velocity, there is more kinetic energy corresponding with the zero point energy motion (5.8 K) than purely translational (from 1.2 to 4.7 K).

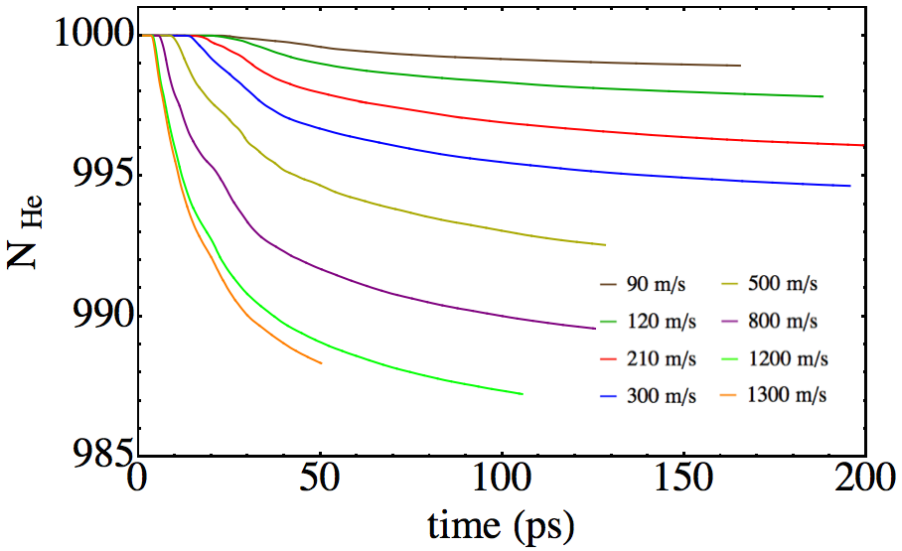

Figure 8.7. Time evolution of the number of helium atom of the nanodroplet as a function of $<v_0>$.

8.4 Summary and conclusions

The quantum dynamics of the process of capturing a Ne atom by a superfluid helium nanodroplet formed by 1000 ^{4}He atoms, T=0.37 K, with a zero impact parameter (zero angular momentum) has been studied within a TDDFT (helium) + WP (Ne) theoretical framework. Thus, the influence of a rather wide range of neon mean velocities (90-1300 m/s) on the dynamics has been explored. To the best of our knowledge this is the first quantum dynamics study of the pick up process by helium nanodroplets reported so far.

The velocities were selected according to the velocity distribution of the neon dopant atom at room temperature (T=300 K), which corresponds to a common situation in the pick up chamber employed in the experiments. For the Ne atom mean velocities equal to 210 m/s and above the atom is always captured by the helium nanodroplet. However, for lower velocities the probability of capture is below the unity (for 90 and 120 m/s is equal to 0.880 and 0.985, respectively) and diminishes as the impinging Ne atom velocity decreases.

The main energy exchange is produced during the collision of the atom with the nanodroplet surface. The resulting excess of energy placed in the doped nanodroplet is

progressively released by evaporation of some ^{4}He atoms. The importance of vaporization increases with the mean velocity of neon, but only a small percentage of ^{4}He atoms is evaporated (a maximum value of around 1.5% is found for the higher mean velocity analyzed (1300 m/s)).

The mean value of the Ne atom position inside the nanodroplet follows an oscillatory trajectory, as a result of multiple sequential collisions with the inner surface of the nanodroplet. It has also been observed that, when the Ne atom mean velocity is below the Landau's critical velocity, there is no a net force acting on the atom and due to this its mean velocity remains constant. This is probably the common behavior for nanodroplets which include a bulk-like zone if moderate collision energies are involved.

In this situation the only energy exchange that occurs has minor character and takes place when the atom collides with the inner surface and leads to some excitation of the surface modes (ripplons) of the nanodroplet. Moreover, it is interesting to note that the (initially Gaussian) Ne wave packet evolves in momentum space until it turns out to be again a Gaussian wavepacket centered at a given mean velocity.

In the future we hope to be able to investigate the influence of angular momentum on the dynamics of the pick up process using the quantum dynamics theoretical method employed here.

8.5 Appendix

Table A8.1. Cartesian grids for the Ne atom and helium and propagation time steps.

$\langle v_0 \rangle$ (m/s)	z_{Ne} min (Å)	z_{Ne} max (Å)	z max (Å)	x max (Å) [a]	Δt (ps)
90	-40.0	35.0	38.1	37.6	$3.0\ 10^{-4}$
120	-40.0	40.0	38.1	37.6	$2.5\ 10^{-4}$
210	-40.0	40.0	38.1	37.6	$2.5\ 10^{-4}$
300	-40.0	40.0	38.1	37.6	$2.0\ 10^{-4}$
500	-40.0	40.0	38.1	37.6	$1.0\ 10^{-4}$
800	-40.0	45.0	34.8	35.6	$9.0\ 10^{-5}$
1200	-40.0	40.0	34.8	35.6	$9.0\ 10^{-5}$
1300	-40.0	40.0	34.8	35.6	$8.0\ 10^{-5}$

[a] y max = x max.

Table A8.2. Spatial separation (h) of the Cartesian grids for the Ne atom and helium.

$\langle v_0 \rangle$ (m/s)	h_{zNe} (Å)	h_z (Å)	h_x=h_y (Å)
90	0.115	0.3	0.4
120	0.114	0.3	0.4
210	0.114	0.3	0.4
300	0.114	0.3	0.4
500	0.114	0.3	0.4
800	0.089	0.2	0.4
1200	0.067	0.2	0.4
1300	0.062	0.2	0.4

Table A8.3. Final propagation times.

$\langle v_0 \rangle$ (m/s)	t_{final} (ps)
90	165.4
120	188.2
210	204.7
300	195.5
500	128.2
800	177.1
1200	105.5
1300	50.2

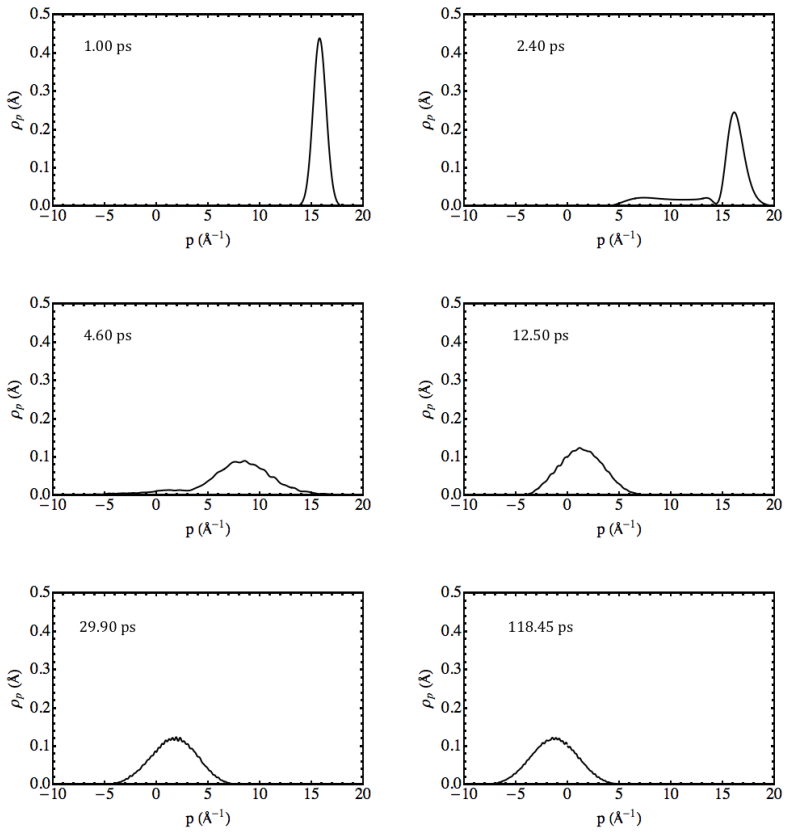

Figure A8.1. Snapshots showing the temporal evolution of the probability density of the Neon atom wave packet in momentum representation, $\left|\tilde{\phi}_{Ne}(p_{z_{Ne}})\right|^2$, for $\langle v_0 \rangle$=500 m/s and the same times considered in Figure 8.2.

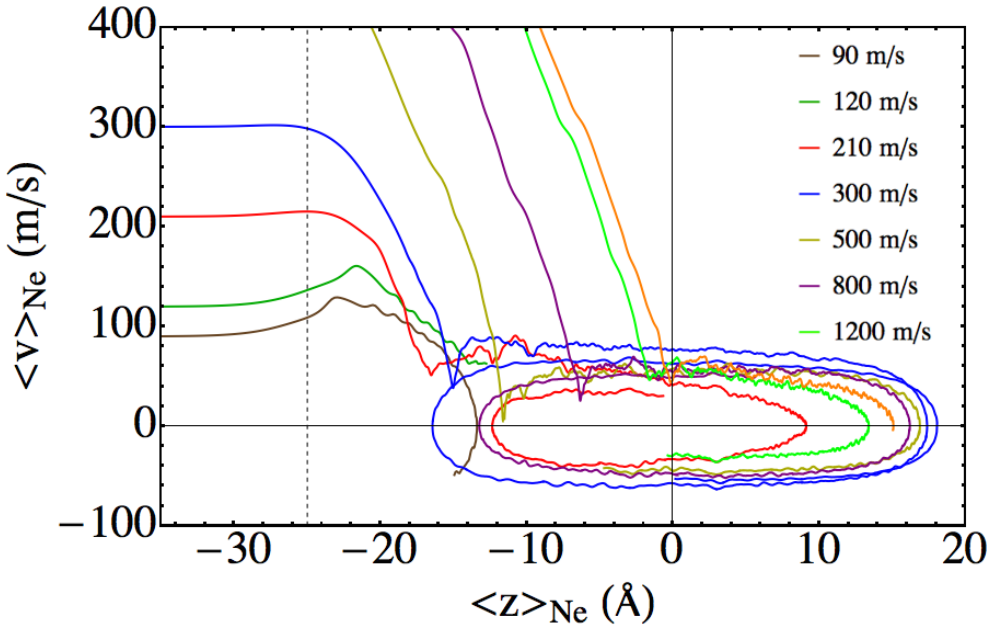

Figure A8.2. Trajectories of the mean values of the Ne atom velocity and position as a function of $\langle v_0 \rangle$. The dashed line shows the z value for the pure nanodroplet surface. This is a more detailed version of Figure 8.5 emphasizing the "ellipses" regions.

Movie 8.1. Time evolution of the Ne atom z-axis wave packet (squared modulus) in coordinate (in Å; up left) and momentum (in Å^{-1}, down left) representations. Time evolution of the helium density along the z-axis (up left) and in the xz plane as 2D (up right) and 3D (down right) plots. This is for $\langle v_0 \rangle$=210 m/s and the simulated time is 205 ps.

Movie 8.2. As movie 8.1 but for $\langle v_0 \rangle$=500 m/s and the simulated time is 128 ps.

Movie 8.3. As movie 8.1 but for $\langle v_0 \rangle$=800 m/s and the simulated time is 177 ps.

8.6 References

[1] Toennies, J. P.; Vilesov, A. *Angew. Chem. Int. Ed*., **2004**, 43, 2622.

[2] Barranco, M.; Guardiola, R.; Hernández, S.; Mayol, R.; Navarro, J.; Pi, M. Helium Nanodroplets: An Overview. *J. Low Temp. Phys.*, **2006**, 142, 1.

[3] Goyal, S; Schutt, D. L; Scoles, G. *Phys. Rev. Lett.* **1992**, 69, 933.

[4] Hartmann, M; Miller, R. E; Toennies, J. P; Vilesov, A. *Science*. **1996**, *272*, 1631.

[5] Vilà, A; González, M.; Mayol, R.; Paniagua, M. *RSC Adv.* **2014**, 4, 44972.

[6] Douberly, G. E.; Miller, R. E. *J. Phys. Chem. B*, **2003**, 107, 4500.

[7] Krasnokutski, S. A.; Huisken, F. *J. Phys. Chem. A*., **2011**, 115, 7120.

[8] Yang, S.; Ellis, A. M. *Chem. Soc. Rev.* **2013**, 42, 472.

[9] Vilà, A; González, M.; Mayol, R. *J. Chem. Theory Comput.*, **2015**, 11, 899.

[10] Yang, S.; Ellis, A. M.; Spence, D.; Feng, C.; Boatwright, A.; Latimer, E.; Binns, C. *Nanoscale*. **2013**, *5*, 11545.

[11] Latimer, E.; Spence, D.; Feng, C.; Boatwright, A.; Ellis, A. M.; Yang, S. *Nano Lett.* **2014**, 14, 2902.

[12] Braun, A.; Drabbels, M. *J. Chem. Phys., **2007,*** 127, 114303.

[13] Braun, A.; Drabbels, M. *J. Chem. Phys., **2007,*** 127, 114304.

[14] Braun, A.; Drabbels, M. *J. Chem. Phys., **2007,*** 127, 114305.

[15] Takayanagi, T.; Shiga, M. *Chem. Phys. Lett.* **2003**, 372, 90.

[16] da Silva, F. F.; Bartl, P.; Denifl, S.; Echt, O.; Märk, T. D., Scheier, P. *Phys. Chem. Chem. Phys.* **2009**, 11, 9791.

[17] Schoebel, H.; Bartl, P.; Leidlmair, C.; Denifl, S.; Echt, O.; Maerk, T. D.; and Scheier, P. *Eur. Phys. J. D* **2011**, 63, 209.

[18] Ratschek, M.; Koch, M.; Ernst, W. E. *J Chem. Phys.* **2012**, 136, 104201.

[19] Lindebner, F.; Kautsch, A.; Koch, M.; Ernst, W. E. *Int. J. Mass Spectrom*. **2014**, 365-366, 255.

[20] Raston, P. L.; Agarwal, J.; Turney, J. M.; Schaefer III, H. F.; Douberly, G. E. *J. Chem. Phys.* **2013**, 138, 194303.

[21] Premke, T.; Wirths, E.-M.; Pentlehner, D.; Riechers, R.; Lehnig, R.; Vdovin, A.; Slenczka, A. *Front. Chem.* **2014**, 2, 51.

[22] Schöbel, H.; Leidlmair, C.; Bartl, P.; Denifl, S.; Märk, T. D.; Echt, O.; Scheier, P. *J. Phys.: Conf. Ser.* **2012**, 388, 012044.

[23] Leal, A.; Mateo, D.; Hernando, A.; Pi, M.; Barranco, M. *Phys. Chem. Chem. Phys.*, **2014**, 16, 23206.

[24] Scheidemann, A.; Toennies, J. P.; Northby, J. A. *Phys. Rev. Lett.* **1990**, 64, 1899.

[25] Dalfovo, F.; Lastri, A.; Pricaupenko, L.; Stringari, S.; Treiner, J. *Phys. Rev. B*, **1995**, 52, 1193.

[26] Some static calculations have been done in order to obtain the width of the wave packet of the Ne atom inside the helium nanodroplet, obtaining a rather small value. This suggests that our approach is realistic enough.

[27] Ralston, A.; Numerical Integration Methods for the Solution of Ordinary Differential Equations. In *Mathematical Methods for Digital Computers*; John Wiley & Sons, **1960**.

[28] Thompson, R. J. *Commun. ACM*. **1970**, 13, 739.

[29] Frigo, M.; Johnson, S. G. IEE Proceedings **2005**, 93, 216.

[30] Vibók A.; Balint-Kurti G. G. *J. Phys. Chem.* **1992**, 96, 8712.

[31] Tilley, D. R.; Tilley, *Condensates and Excitations. Superfluidity and Superconductivity*, Institut of Physics Publishing, **1990**.

[32] Annet, J. F., *Superfluid Helium-4. Superconductivity, Superfluids and Condensates*, Oxford University Press, **2004**.

[33] Brauer, N. B.; Smolarek, S.; Loginov, E.; Mateo, D.; Hernando, A.; Pi, M.; Barranco, M.; Buma, W. J.; Drabbels, M. *Phys. Rev. Lett*., **2013**, 111, 153002.

[34] Mateo, D.; Leal, A.; Hernando, A.; Barranco, M.; Pi, M.; Cargnoni, F.; Mella, M.; Zhang, X.; Drabbels, M. *J. Chem. Phys.*, **2014**, 140, 131101.

9. Synthesis reaction of homonuclear van der Waals dimer inside helium nanodroplets: The case of Ne_2

9.1 Introduction

The capture and solvation of impurities by superfluid ^{4}He nanodroplets has attracted the interest of many investigators by several reasons. From a reaction dynamics viewpoint, these systems constitute genuine nanoreactors, offering the possibility of having a single reactive collision inside one droplet. Furthermore, the excess excitation coming from the kinetic energy of the reactants is easily released from the droplet by evaporation of some helium atoms.

Apart from these properties mainly related with the pickup of the impurities, there are other remarkable features important for the chemical reactivity inside these nanodroplets. The solvation shells formed around the impurities, which can be bubbles (low interacting dopants) or snowballs (strongly interacting dopants), are able to stabilize the metastable chemical species that would not be formed in gas phase. Moreover, the inert chemical character of helium together with its superfluid behaviour make the high resolution spectroscopic analysis of products feasible. Thus, this allows a good characterization of the reaction mechanism.

On the other hand, the study of reaction dynamics inside helium nanodroplets is also useful to deepen into the complicated behaviour and properties of superfluid liquid helium, considering the widely kinds of motions provided by a chemical reaction, e.g. translational, vibrational and rotational. In this sense, in addition to of the interest of chemical rections, the chemical species produced can also be regarded as probes for investigating the helium properties. For some reviews or studies on this topic see, e.g., the papers in Refs. 1,2,3,4.

Recently, we proposed a hybrid scheme (TDDFT + wave packet dynamics) for the theoretical study the photodissociation of Cl_2 inside helium nanodroplets[5]. This is the first

theoretical attempt to this topic considering superfluid nanodroplets. Here, we extend the study of reaction dynamics inside helium nanodroplets into a more complex situation, involving the synthesis of a van der Waals dimer, concretely the Ne_2. Few years ago, Eloranta studied at a DFT level of theory this dimer as a first stage for investigating the formation of quantum gels[6,7] by doping liquid helium with many Ne atoms. He determined an effective adiabatic potential energy surface for the Ne_2, considering an instantaneous relaxation of the liquid for each relative distance of the neon atoms. A potential energy barrier of about a few kelvins was obtained, depending on the potential energy curves used. Our approach to this van der Waals reaction is completely different, since we have carried out a real-time dynamics study of the reactive process.

Recently, we performed a study of the pick up of a Ne atom by helium nanodroplets (see Chapter 8). This investigation can be considered as a first stage for the present study, since some aspects needed for the present work were examined there. Following the same idea we used to study the capture, we focus first our work on this problem into the quantum mechanical description of the process, at angular momentum equal to zero. Therefore, in this initial work we study the prototypical reaction of the synthesis of a homonuclear diatomic molecule inside helium droplets restricting to the simplest case, where no angular momentum is present. Moreover, the computational method developed to perform the present investigation is promising, since it will be useful for the study of other interesting situations, such as, the photodissociation of heteronuclear molecules (center of mass effects, isotopic effects, etc.).

9.2 Theoretical methods

In the present study we consider the ground electronic state of the species because of the large energy separation with respect to the first excited state which is a characteristics of the noble gases systems. Thus, this work has been performed assuming an electronic adiabatic approach. So that, within the mentioned approximation adopted the schematic representation of the process would be like:

$$Ne(^1S) + Ne(^1S)@^4He_N \rightarrow Ne_2(^1\Sigma^+_g, v=0, j=0)@\,^4He_{N'} + (N\text{-}N')\,^4He$$

As previously mentioned, the methodology used in this work is an extension of the one developed for the study of photodissociation of homonuclear diatomic molecules inside helium nanodroplets[5]. Thanks to the zero angular momentum situation, the present problem has five degrees of freedom: three corresponding to the coordinates of the helium effective complex wave function and two to the dimer (relative coordinate and the center of mass).

We use the same quantum description for the helium and the relative Ne-Ne coordinate degrees of freedom, and the center of mass coordinate follows a classical mechanics approach. This theoretical treatment highly reduces the computational cost comparing with treating all degrees of freedom in a quantum fashion, and is based on the mass of the effective particles corresponding to each degree of freedom. The effective mass evolving in the relative coordinate for the present case is $\mu_{Ne_2} = m_{Ne}/2$; while the total mass, moving in the center of mass coordinate, is $M_{Ne_2} = 2m_{Ne}$.

There are two features involved in this approach that are mixed together: the coordinates used and the physical (quantum vs. classical) description. A brief discussion of this is important to justify the suitability of our choice. Excepting the mean field approximation coming from the DFT description of helium, a full quantum mechanical description of the dimer would imply its global wave function. This wave function could be written both in two coordinate systems, i.e., positions of the two Ne atoms, or in the relative coordinate and center of mass framework. Apart from possible difficulties in the interpretation of the results, the election of the coordinate system has, of course, no effect in the description of the system, and the two options would be completely equivalent.

However, for computational reasons some reasonable approximations are necessary in order to reduce the complexity of the problem. Within a quantum description of the system, a simplification can be done by a factorization of the global wave function into two independent functions, corresponding to each degree of freedom. This corresponds to a mean field description and has the consequence of loosing some part of the correlation between the two atoms forming the dimer. For the purposes of the present work it is more convenient to work with relative coordinates rather than the position ones.

Focusing in the molecule, ignoring if forming (synthesis) or destroying (dissociation), the natural way to describe it is by means of the relative coordinate, since the separation of the two atoms is what is really important, no matter where they are placed. This argument is

reinforced when focusing on the vibration, which cannot be satisfactorily described using a quantum mean field description. However, using a relative coordinate wave packet gives some correlation between the motions of the two atoms. Furthermore, if we had used position coordinates, although we had treated each Ne atom with a quantum description, i.e., including the zero point motion, it would be difficult to get an accurate definition for the formation of the molecule.

Within the mentioned approximations, a quantum action is proposed in which the energy density of the liquid helium is given by the so-called Orsay-Trento phenomenological functional[8]. For computational reasons, the backflow and the non-local contribution to the correlation energies have been neglected. This action (Eq. 9.1) is written in terms of the dynamical objects of the study, i.e., the effective complex wave function for the helium, defined by $\Psi_{He}(t, \boldsymbol{R}_{He}) \equiv \sqrt{\rho_{He}(t, \boldsymbol{R}_{He})}$, the relative coordinate wave packet $\varphi_{rel}(r)$ and the center of mass coordinate R_{CM}.

$$\begin{aligned}\mathcal{A}[\Psi_{He}, \varphi_{rel}, R_{CM}] \\ &= \int dt \Big\{ E[\Psi_{He}, \varphi_{rel}, R_{CM}] - i\hbar \int d\boldsymbol{R}_{He}\, \Psi^*_{\boldsymbol{He}}(\boldsymbol{R}_{He}) \frac{\partial}{\partial t} \Psi_{He}(\boldsymbol{R}_{He}) \\ &- i\hbar \int dr\, \varphi^*_{rel}(r) \frac{\partial}{\partial t} \varphi_{rel}(r) - M_{Ne_2} {v_{CM}}^2 \Big\}\end{aligned} \tag{9.1}$$

,where the energy is given by

$$\begin{aligned}E[\Psi_{He}, \varphi_{rel}, R_{CM}] \\ &= \frac{\hbar^2}{2m_{He}} \int d\boldsymbol{R}_{He}\, |\boldsymbol{\nabla}\Psi_{He}|^2 \\ &+ \int d\boldsymbol{R}_{He}\; \mathcal{E}_c[\rho_{He}] \\ &+ \int d\boldsymbol{R}_{He} \int dr\, V_{He-Ne_2}(r, \boldsymbol{R}_{He}, R_{CM})\, \rho_{He}(\boldsymbol{R}_{He}) |\varphi_{rel}(r)|^2 \\ &- \frac{\hbar^2}{2\mu_{Ne_2}} \int dr\, \varphi^*_{rel}(r) \frac{\partial^2}{\partial r^2} \varphi_{rel}(r) + \int dr\, V_{Ne_2}(r)\, |\varphi_{rel}(r)|^2 + \frac{1}{2} M_{Ne_2} {v_{CM}}^2\end{aligned} \tag{9.2}$$

Regarding the interaction potentials we have followed the common pairwise strategy expressing the three-body potential V_{He-Ne_2} by a sum of two corresponding two-body V_{He-Ne} terms. Both the V_{Ne_2} and V_{He-Ne} interaction energy potentials are obtained from Reference 9. In order to obtain the set of coupled equations of motion governing the evolution of each

degree of freedom, a minimization of the action by varying each dynamical object has to be made. Then, we arrive at the following expressions (Equations 9.3a, 9.3b and 9.3c, respectively):

$$i\hbar\frac{\partial}{\partial t}\Psi_{He}(\boldsymbol{R}_{He}) = \left[-\frac{\hbar^2}{2m_{He}}\boldsymbol{\nabla}^2 + \int dr\, V_{\mathrm{He}-Ne_2}(r,\boldsymbol{R}_{He},R_{CM})\,|\varphi_{rel}(r)|^2 + \frac{\delta\mathcal{E}_c[\rho_{He}]}{\delta\rho_{He}}\right]\Psi_{He}(\boldsymbol{R}_{He})$$

$$i\hbar\frac{\partial}{\partial t}\varphi_{rel}(r) = \left[-\frac{\hbar^2}{2\mu_{Ne_2}}\frac{\partial^2}{\partial r^2} + V_{Ne_2}(r) + \int d\boldsymbol{R}_{He}V_{He-Ne_2}(r,\boldsymbol{R}_{He},R_{CM})\rho_{He}(\boldsymbol{R}_{He})\right]\varphi_{rel}(r)$$

$$M_{Ne_2}\frac{d^2R_{CM}}{dt^2} = -\frac{d}{dR_{CM}}\int d\boldsymbol{R}_{He}\int dr\, V_{He-Ne_2}(r,\boldsymbol{R}_{He},R_{CM})\,\rho_{He}(\boldsymbol{R}_{He})|\varphi_{rel}(r)|^2$$

For solving equations 9.3a and 9.3b a discretisation of the space in a grid of points has been done (Table 9.1). The derivatives in Eq. 9.3c have been calculated by means of the chain rule taking advantage of the analytical fitting of V_{He-Ne_2} the potential. The temporal integration have been done using Adams predictor-corrector-modificator method[10], initiated by a forth order Runge-Kutta[11]. Moreover, a quartic negative imaginary potential (NIP) has been defined at the edges of the helium Cartesian grid in order to absorb some density evaporated from the droplet.

Table 9.1. Parameters defining the helium and neon grids for the different velocities.

v_0 (m/s)	hz_{Ne} (Å)	hz (Å)	hx=hy (Å)
90	0.115	0.3	0.4
120	0.114	0.3	0.4
210	0.114	0.3	0.4
300	0.114	0.3	0.4
500	0.114	0.3	0.4
800	0.089	0.2	0.4
1200	0.067	0.2	0.4
1300	0.062	0.2	0.4

To finish the description of the methodology used we now focus on the initial conditions for the dynamics. They consist in a doped nanodroplet $Ne@^4He_N$ (N=200, 500 and

1000) together with an impinging Ne atom, located far away from the droplet (where, essentially, no interaction is present). The approximation restricts the problem to a single dimension, and hence the initial time static (ground state) calculation must be consistent with it. Thus, in the initial static nanodroplets the Ne impurity has been treated quantum mechanically in the z-axis motion, with its wave function and the corresponding zero point motion, and classically in the a x and y axis, which can be considered just as an external potential. Of course, this introduces a small anisotropy in the droplet density (see Figure 9.1). However, if the static droplet were computed considering the full Ne wave function, the droplet would start its motion without the external boost; just because of the different treatments of the impurity considered in the statical and to the dynamical. The numerically obtained z-axis wave packet is then fitted to a Gaussian function.

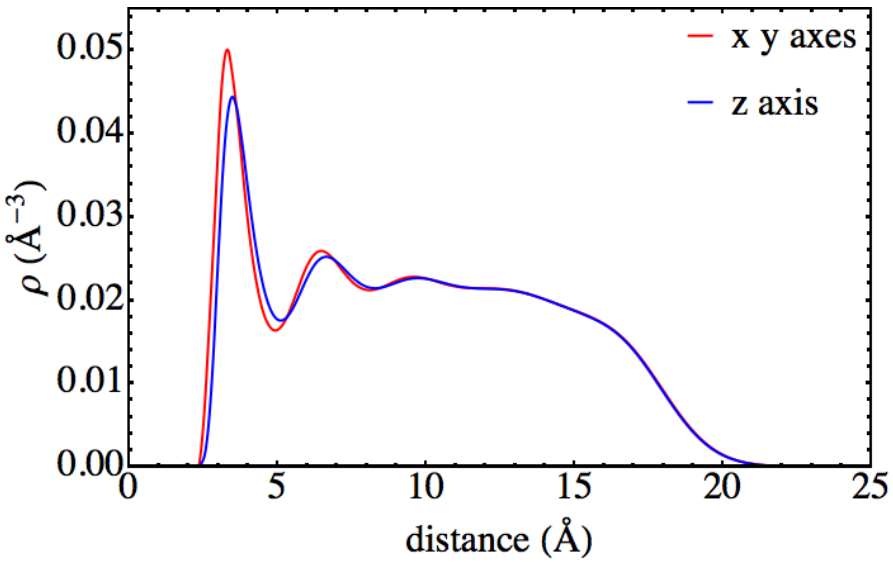

Figure 9.1. Helium density profiles in z and x y axes for the initial time of the calculation.

On the other side, when changing from the static to the dynamic calculation, the input wave packet describing the relative coordinate must be consistent with the corresponding "translational" wave function of the inner Ne. To do so, we made use of the probability density meaning of quantum wave functions. Having defined the mean value of the initial position of both Ne atoms, we infer $R_{CM,t=0}$ and $\langle r \rangle_{t=0}$. Thus, scanning the different possible values of the relative coordinate (grid values) gives the corresponding values of the position of the inner Ne atom (Eq. 9.4a). Then, we associate a probability to this configuration by means of the "translational" wave function $\phi_{Ne\ inner}(z)$ coming from the ground state calculation (Eq 9.4b):

$$z(r_i) = R_{CM,t=0} + \frac{1}{2} r_i \qquad \forall r_i \in grid[r_{min}, r_{max}] \tag{9.4a}$$

$$|\varphi_{rel}(r_i)|^2 = \left|\phi_{Ne\ inner}(z(r_i))\right|^2 \tag{9.4b}$$

This is the way we have defined the initial relative wave packet density. Finally, a boost operator is applied to this motionless wave function to give it the corresponding initial relative velocity, which is easily obtained from the change of coordinates.

$$\varphi_{rel}(r_i) = \sqrt{|\varphi_{rel}(r_i)|^2}\, Exp\left\{ i \frac{\mu_{Ne_2} v_{rel,t=0}}{\hbar} (r_i - \langle r \rangle_{t=0}/2) \right\} \tag{9.5}$$

9.3 Results and discussion

The formation of the van der Waals diatomics Ne_2 inside helium nanodroplets has been studied for Ne + Ne@(^{4}He)$_N$ considering different initial velocities (collision energies) of the impinging Ne atom. These have been selected in order to sample the Maxwell velocity distribution of Ne at room temperature (typical experimental conditions). The six cases studied correspond to the initial velocities <v_0>= 120, 300, 500, 750, 800 and 1000 m/s (Figure 9.2) and the nanodroplet of 500 ^{4}He atoms. The effect of the nanodroplet size on the reaction mechanism has been also investigated. Thus, some representative initial velocities have been chosen (<v_0>= 120, 300 and 800 m/s) for nanodroplets of 200 and 1000 helium atoms.

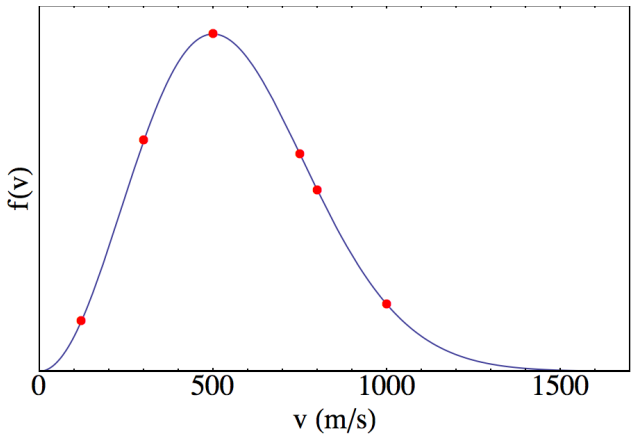

Figure 9.2. Maxwell velocity distribution for Ne at a temperature of 300 K. Red points representing the selected velocities in the present work.

In order to understand the mechanism of this reaction in the Appendix some movies corresponding to several collision energies (cf. movies 9.1, 9.2 and 9.3) can be seen (and Figure 9.3 shows the mechanism for the v=300 m/s) . The first step for the reaction of formation of the van der Waals dimer consists in the pickup the impinging neon atom by the neon-doped helium nanodroplet, where in this first investigation we have considered the total angular momentum equal zero. This process resembles the one studied before (see Chapter 8) but with some peculiarities owing to the presence of the Ne atom dopant inside the droplet

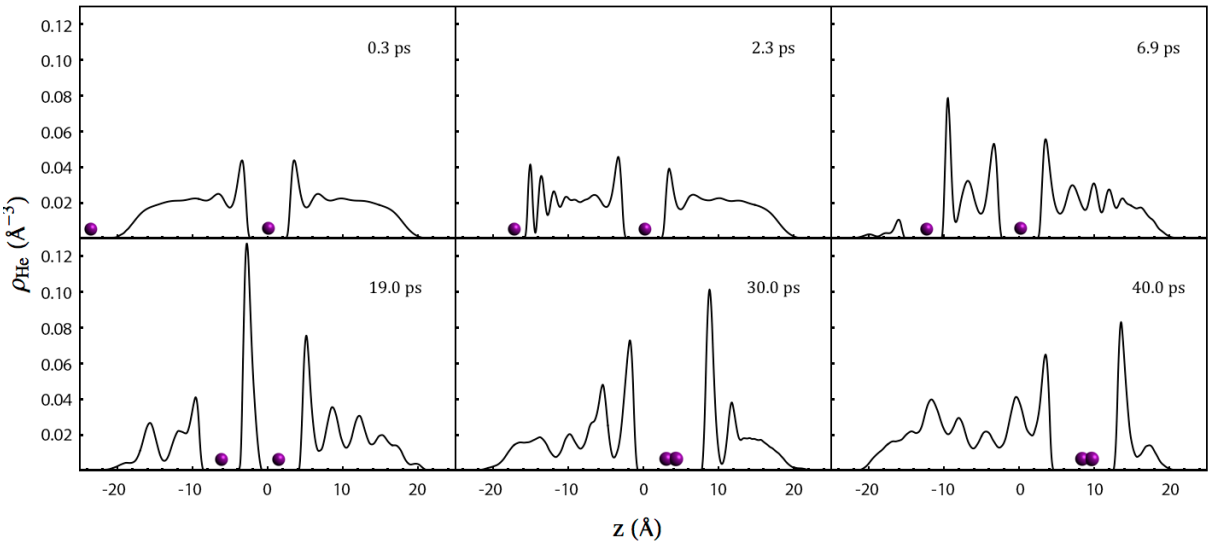

Figure 9.2. Snapshots corresponding to the time evolution of the helium density in the molecular axis (z). The position of the Ne atoms is schematically represented by the purple balls. The impinging velocity is 300 m/s and the droplet is formed by 500 ^{4}He atoms.

Firstly, it is worth noting that in the theoretical approach adopted here the possibility to account for the partial penetration into the droplet, due to a partial reflection with the surface, cannot be described. This phenomenon is purely quantum, and so it is related to the wave nature of the particles. The wave function present in our investigation corresponds to the relative distance motion involving the Ne atoms degree of freedom. So that, this makes the wave packet always confined by the potential, because there is always one Ne atom placed inside the droplet. Therefore, keeping the center of mass constant at a certain value, when varying the value of the relative coordinate, the inner atom approaches to the walls of the helium bubble and, hence, the potential becomes repulsive.

Nevertheless, this reasoning supports the idea that our theoretical model is satisfactory for the description of the process we are interested in, instead of considering two translational wave functions (one for each Ne atom). This later approach would lead to situations to

happen whose physical meaning would not be so clear. For low collision velocities is possible that only a part of the full wave function of the impinging atom penetrates the nanodroplet, and so there is the possibility of forming a molecule consisting less than two neon atoms that may lead to interpretation problems.

Furthermore, the inspection of the animations shows the existence of another difference when comparing with the capture occurring in a pure nanodroplet. The high reduction of the impinging Ne atom velocity due to the presence of the inner Ne atom. For some special cases (<v_0>=300, 500 and 800) this can even produce the rebound of the former Ne atom (negative velocities). To clarify this effect we have estimated the expected position of each neon atom (A and B) by:

$$z_{Ne\binom{A}{B}} = R_{CM} \pm \frac{1}{2}\langle r \rangle \tag{9.6}$$

The time evolution of these values and the corresponding velocities are plotted in Figure 9.3. The solid and dashed lines correspond to the estimated positions of the impinging and the inner Ne atoms, respectively. This effect is present for all the collision energies studied, excepting for the softer one (<v_0> = 120 m/s). A detailed visualization of the animations points out that this effect can be caused by different reasons, which depends on the case. For low velocities this is probably manly due to the reflection of the helium shock waves initially generated by the impurity, while for high velocities this results from the huge compression of helium density between the two atoms.

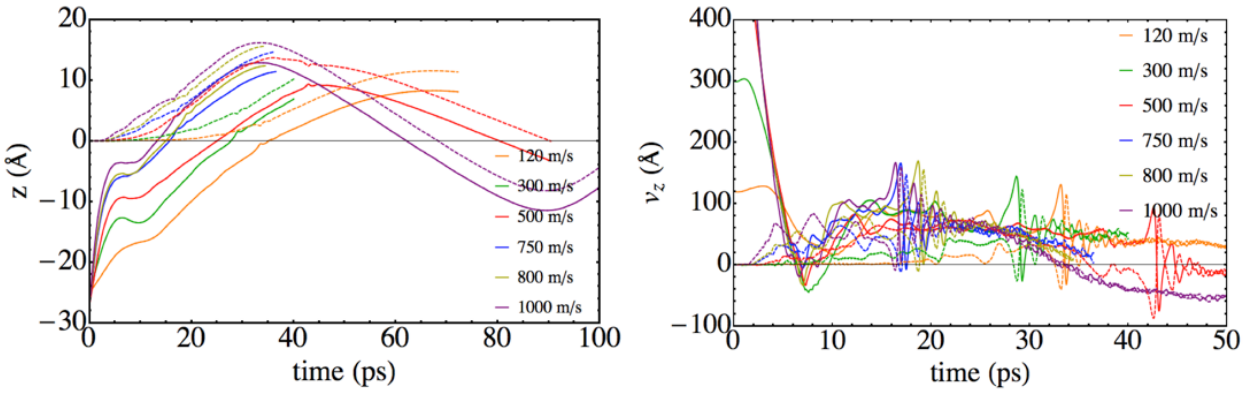

Figure 9.3. Time evolution of the position (left) and velocity (right) of the colliding (solid line) and inner (dashed line) Ne atoms.

Regarding the formation of the van der Waals molecule, which is characterized by the relative coordinate wave packet. It can be inferred that the mechanism of this process is not

unique, but depends on the situation. For the nanodroplets with N=500 ^{4}He atoms we found that in all the cases considered the Ne_2 dimer is obtained close to the center of the droplet, excepting for $\langle v_0 \rangle$ = 500 m/s. In this case, the Ne atoms move through the nanodroplet at a fairly constant distance between them until they get close to the surface, where the complex is formed. This is a rather complex process involving many degrees of freedom and it is not clear the reason why one or another mechanism occur. We consider reasonable, however, that small changes in the initial conditions produce strongly different mechanisms since, at the end, this consist in a wave phenomenon.

The temporal evolution of the relative coordinate expected value $\langle r \rangle$, for different velocities and the nanodroplet with N=500 is represented in Figure 9.4. At the initial times, $\langle r \rangle$ mainly corresponds to the motion of the impinging Ne atom, since the inner Ne atom is almost at rest until it begins to experience the perturbations in the helium density generated by the former. Excepting for the lowest velocity case, the atoms relative motion presents a time interval at which they are separating from each other. Afterwards, they gradually get closer until reaching an asymptotic value of <r>, which is the same in all cases.

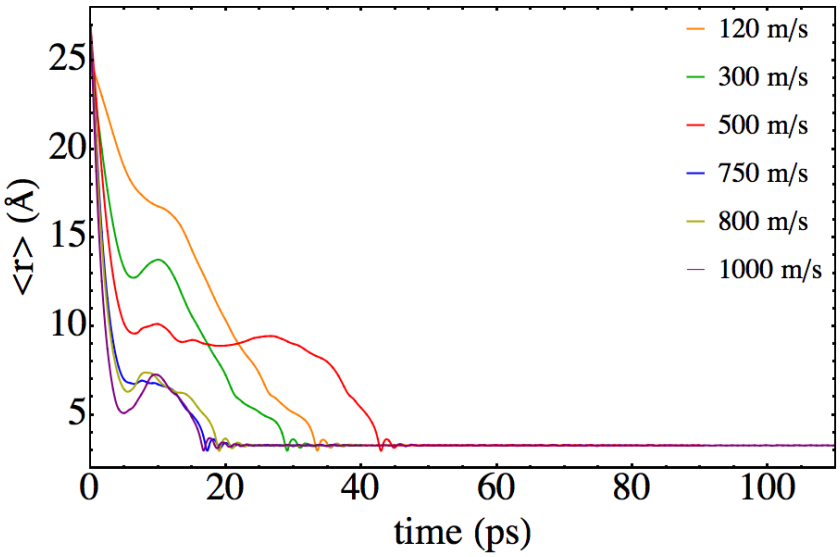

Figure 9.4. Time evolution of the expected value of the relative coordinate for the different colliding velocities considered.

Different definitions can be adopted for the formation of the Ne_2 dimer. From a structural point of view the formation of the complex could be described by the time when the value of <r> crosses for the first time the asymptotic value. After that, the complex is just relaxing (releasing its excess energy). On the other side, from an energetic perspective the van

der Waals molecule can be considered synthetized when the two atoms are in a bound state, i.e. when the total relative energy defined by $\langle E_{total,\ rel}\rangle \equiv \langle E_{pot\ Ne-Ne,\ rel}\rangle + \langle E_{kin,\ rel}\rangle$ is negative. The time evolution of the total relative energy is plotted in Figure 9.5. It is inferred that two possible definitions given above almost lead to the same result, since the dashed lines correspond to the times adopting the former definition. Having defined the formation of the van der Waals dimer by means of the "geometrical" definition, we estimate a time scale of about 20-40 ps, depending on the collision energy and the mechanism for the formation. We expect this process to last some longer times when angular momentum is present, because orbital motion will also occur. Regarding the last restriction, a brief exploration will be considered afterwards.

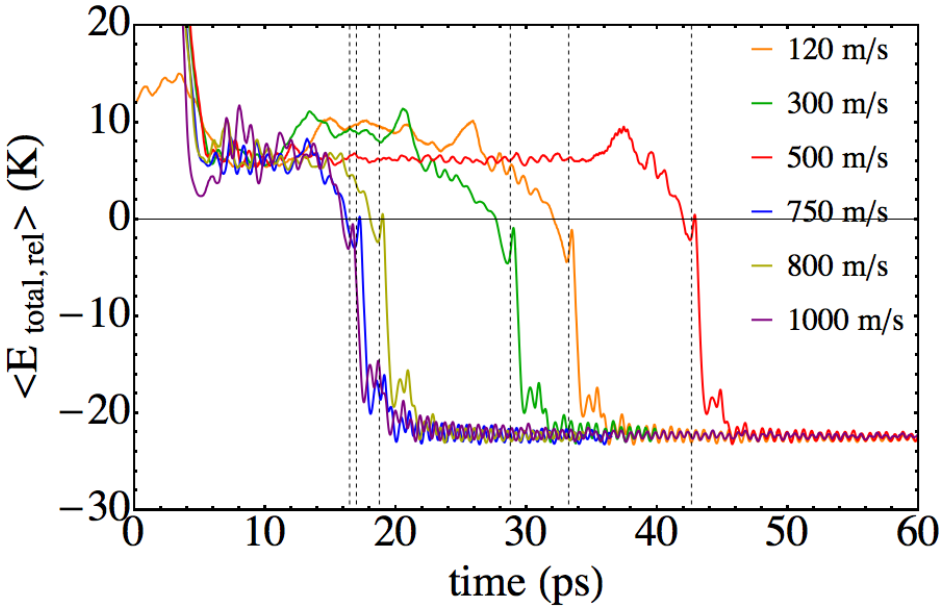

Figure 9.5. Time evolution of the total relative energy (kinetic + Ne-Ne potential).

Furthermore, once the van der Waals diatomics is formed, a vibrational relaxation process takes place. This process lasts until the relative coordinate wave packet corresponds to the ground state vibrational wave function (v=0). This process correlates with the oscillations observed in the <r> value around its asymptotic value (Figure 9.4) which has a time-scale of 5 ps. The pattern of the vibrational relaxation of the complex mediated by the helium droplet is really similar for all the cases, indicating that this process is not really influenced by the slight differences in the excitation of the droplet. In Table 9.2 are compiled the values of the energy per helium atom (E/N) for each case at the moment of the (structural) formation of the molecule.

The energy flux between the molecule and the droplet is not monotonic but the energy is being exchanged back and forth between them (cf. Figure 9.5). The main amount of energy release is produced at the beginning, and by a careful visualization of the animations it is inferred that this is clearly mediated by the emission of a helium density wave of high amplitude. This corresponds to the first re-increase in the <*r*> value. After the emission of this wave, the relaxation continues but more slowly, with some energy exchanges in the two directions. At the end, very small oscillations in the <*r*> value are present, reflecting the slightly changes in the effective potential governing the evolution of this degree of freedom. It is worth noting that, within the studied conditions, once the van der Waals molecule is formed it is never broken again.

Table 9.2. Ne_2 formation time and energy per ^4He atom for the helium nanodroplet with N=500 and several initial velocities of the impinging Ne atom.

v_0 (m/s)	Ne_2 formation time (ps)	E/N (K)
120	33.2	-4.59
300	28.8	-4.55
500	42.6	-4.57
750	17.0	-4.41
800	18.7	-4.42
1000	16.5	-4.35

It is worth to focus our attention in the nature of the synthetized van der Waals complex, as well as its affectation by the helium droplet. We expect the same process but involving pure chemical bonds (high energies implied) would not modify the formed molecule. Nevertheless, in the present case, the dimer Ne-Ne (well depth 41.15 K) van der Waals interaction is of the same order of magnitude as the interaction with the solvent Ne-He (well depth 21.02 K). This fact, together with the large number of helium atoms forming the droplet make that this environment strongly influences the formation of the complex.

We have inferred a limit value <r> around 3.27 Å. This is relatively close to the minimum of the Ne-Ne potential energy curve (3.1 Å) but there is around a 5% of difference. Furthermore, the <r> value corresponding with the vibrational ground state (v=0) in gas phase is 3.34 Å (see Ref.9). To visualize the effect of the solvent into the Ne_2 van der Waals complex in Figure 9.6 it is plotted the different potentials that influence the relative coordinate degree of freedom, and there is superimposed the asymptotic wave packet (black) and the corresponding one for the gas phase (v=0, red). The helium generates a deeper

potential but much more width and smooth around the minimum of Ne-Ne potential. Therefore, the position of the global minimum is not highly modified by the droplet and just produces the slight reduction of the Ne-Ne van der Waals bond distance. Thus, we infer that the presence of the helium environment slightly compresses the Ne_2 dimer (cf. Fig. 9.6). This probably results from a rather complex energy balance involving: Ne_2-helium, Ne-Ne interaction and surface tension corresponding to the walls of the cavity. The overlap between the droplet and gas phase Ne_2 vibrational wave packets is 83%.

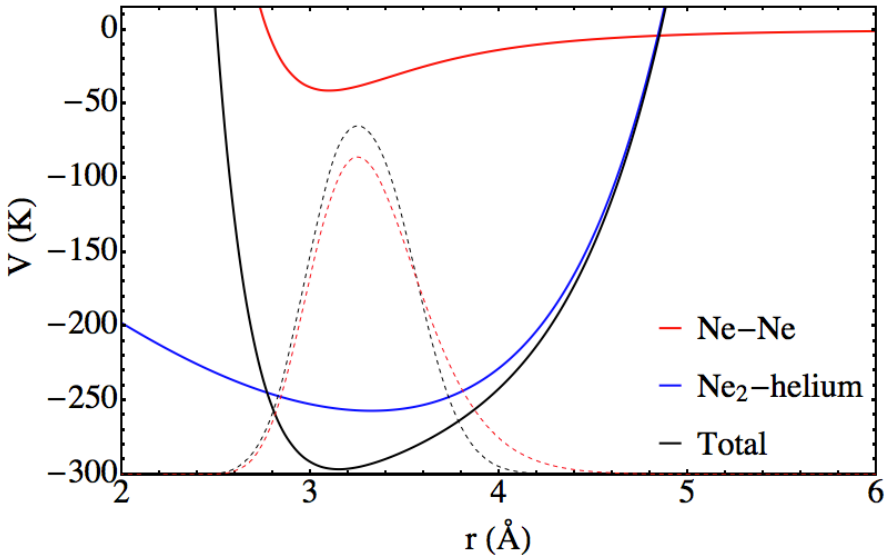

Figure 9.6. Interaction potentials (Ne-Ne and Ne_2-helium) that influence the Ne-Ne relative coordinate degree of freedom and the asymptotic relative coordinate wave packet (dashed, black). The v=0 gas phase relative coordinate wave packet is shown in red dashed lines.

The energy analysis (see Table 9.3) shows that the droplet wave packet has around 1 K more of total relative energy (kinetic + Ne-Ne potential). Of course, this difference is completely compensated by the Ne_2-helium (attractive) interaction, which takes a value of around -250 K. The compression of the dimer induced by the droplet results in a lower Ne-Ne potential energy (~1 K), but a higher kinetic energy (~2 K).

Table 9.3. Energy characterization of the ground state relative coordinate (vibrational) wave packets corresponding to the gas phase and in the $^4He_{500}$ nanodroplet.

Phase	$E_{Kin\ relative}$ (K)	$E_{pot\ Ne\text{-}Ne}$ (K)	E_{Total} (K)
Gas	7.46	-30.93	-23.47
$^4He_{500}$	9.47	-32.00	-22.54

To conclude this section let us mention an introductory exploration on the effect of the droplet size on the process studied in the present chapter. We have simulated this reaction for the impinging velocities of 120 and 800 m/s also in nanodroplets of 200 and 1000 ^{4}He atoms. For the *N*=200 the van der Waals dimer is always formed by a "direct" mechanism, i.e., the two Ne atoms are always getting closer until Ne_2 is synthetized. The small size of this droplet does no let other possibilities. For the *N*=1000 and v=120 m/s Ne_2 is formed near the center of the droplet (cf. Movies 9.4 and 9.5), while for v=800 the mechanism is more complex, since the high helium density oscillations produced by during the impact motives the motion of the inner Ne and the dimer is not formed until this one collides with the droplet surface (see Movies 9.6 and 9.7). These results reinforce the idea of the complexity of the mechanism with no monotonic tendencies. Moreover, noting that for *N*=200 the droplet suffers high shape deformations which does not happen for the N=1000 ^{4}He atoms nanodroplets.

9.4 Summary and conclusions

The process of capturing a neon atom by a helium nanodroplet (formed by one thousand atoms) with a null impact parameter (zero angular momentum) has been studied within a TDDFT theoretical framework. Different collision velocities have been explored according to the velocity

The capture of the impinging Ne atom is not very modified respect to the pure droplets by the presence of the inner Ne atom, and just produced a higher reduction of the velocity of the former one respect to the pure droplet case.

The mechanism of the formation of the Ne_2 dimer does not vary in a precise manner. Depending on the impinging velocity and the droplet size the Ne atoms follow different paths until the van der Waals dimer is formed. This suggests that this is a very complex phenomenon that is related with the nature of the helium density wave produced during the collision (related with the initial velocity) and their reflection with the droplet surface (related with the nanodroplet size).

Regarding the structure of the Ne_2 van der Waals dimer, it has been pointed out that this does not depend on the collision velocity of the outer Ne nor in the droplet size. It is

slightly compressed by the presence of the helium and its vibrational wave packet is only modified in a 17%.

Further studies implying purely chemical (chemical bonds) molecules will be considered, paying more attention into deepen into the vibrational relaxation process of a chemical molecule inside helium nanodroplets. We expect this process will take longer time than for the Ne_2 case (or other van der Waals dimer). Moreover, the computational method (code) developed in the present study will be applied to the study of the photodissociation dynamics of heteronuclear diatomic molecules inside helium nanodroplets (Chapters 4, 5 and 6). Thus, further investigations on this topic will be carried out.

9.5 Appendix

Movie 9.1. Time evolution of the relative coordinate wave packet (squared modulus) in position (up) and momentum (down) representations. The effective potential is shown tighter in the panel corresponding to wp(r). Time evolution of the helium density in the xz plane as 2D (up right) and 3D (down right) plots. This is for $<v_0>$=120 m/s and N=500, and the simulated time is 72 ps.

Movie 9.2. As movie 9.1 but for $<v_0>$=500 m/s and the simulated time is 90.1 ps.

Movie 9.3. As movie 9.1 but for $<v_0>$=1000 m/s and the simulated time is 115.1 ps.

Movie 9.4. As movie 9.1 but for $<v_0>$=120 m/s and N=200, and the simulated time is 112.2 ps.

Movie 9.5. As movie 9.1 but for $<v_0>$=800 m/s and N=200, and the simulated time is 51.1 ps.

Movie 9.6. As movie 9.1 but for $<v_0>$=120 m/s and N=1000, and the simulated time is 66.1 ps.

Movie 9.7. As movie 9.1 but for $<v_0>$=800 m/s and N=1000, and the simulated time is 70.1 ps.

9.6 References

[1] Toennies, J. P.; Vilesov, A. *Angew. Chem. Int. Ed*., **2004**, 43, 2622.

[2] Yang, S.; Ellis, A. M. *Chem. Soc. Rev.* **2013**, *42*, 472.

[3] Krasnokutski, S. A.; Huisken, F. *J. Phys. Chem. A*., **2011**, 115, 7120.

[4] Yang, S.; Ellis, A. M. *Chem. Soc. Rev.* **2013**, 42, 472.

[5] Vilà, A; González, M.; Mayol, R.. *J. Chem. Theory Comput.*, **2015**, 11, 899.

[6] Eloranta, J. *Phys. Rev. B.* **2008**, 77, 134301.

[7] Eloranta, J. *J. Low Temp. Phys.*, **2011**, 162, 718.

[8] Dalfovo, F.; Lastri, A.; Pricaupenko, L.; Stringari, S.; Treiner, J. *Phys. Rev. B*, **1995**, *52*, 1193.

[9] Cybulski, S. M.; Toczylowski, R. R. *J. Chem. Phys*., **1999**, 111, 10520.

[10] Ralston, A.; Wilf, H. S. (Eds.). *Mathematical Methods for Digital Computers (vol I)*; John Wiley & Sons, **1960**.

[11] Thompson R. J. *Comunications of the ACM*. **1970**, *13*, 739.

10. Conclusions

This thesis consists in a compendium of theoretical studies of physico-chemical processes involving superfluid helium nanodroplets where most of them have been investigated for the first time. It begins with a *static-type* study regarding the structure, energetic and spectroscopy of the oxygen-doped helium nanodroplets, while the remaining and most important part of the thesis correspond to real-time simulations of the processes of interest. To do this, a quantum mechanical description has been employed, in which the superfluid liquid helium is described through a phenomenological density functional theory and the atomic or molecular impurities are described by standard quantum mechanics.

In addition to the conclusions coming from the different studies carried out here on superfluid helium nanodroplets, it is worth mentioning that a very important part performed in the present thesis corresponds to the development of the computational codes needed. This part of the effort includes the programming strategies, which are mainly based on physical concepts. Without them most of the calculations of the present thesis would not be affordable and for this reason it is important to mention this here, although they do not correspond to conclusions in a natural sense.

The main conclusions obtained from the results of the studies performed in this thesis are the following:

1) No large differences are found in the structure and energy of oxygen-doped helium nanodroplets when changing the electronic state of O(^{3}P, ^{1}D and ^{1}S). The similar polarizabilities of oxygen in these states and the van der Waals character of the O-He interaction support this fact. The main variations occur in the anisotropy of the helium density induced by the open-shell singlet diradical states, i.e., ^{1}D and ^{1}S.

2) The spectroscopic results obtained for the ^{1}D$\leftarrow{}^1$S electronic transition are consistent with the highly desirable behaviour of the helium nanodroplets (acting as a matrix

where to perform high-resolution spectroscopy studies), because only a very small shift was found respect to the gas phase value.

3) The photodissociation dynamics of Cl_2 induced by the B←X electronic transition inside helium nanodroplets takes place in the picoseconds time-scale, for nanodroplet sizes ranging from 50 (0.85 ps) up to 500 ^{4}He atoms (2.57 ps).

4) A very efficient energy exchange have been found for the photodissociation process, releasing from 57% to 91% of the Cl_2 energy for the smallest and biggest nanodroplets considered, respectively. Also, it has been shown that its mechanism does not depend on the droplet size.

5) Linear relationships were found between the average Cl velocity and the ^{4}He atom evaporated respect to the radius of the nanodroplet for the photodissociation process.

6) The nanodroplet relaxation after the photodissociation of Cl_2 inside helium nanodroplets has been also investigated. The mechanism of this process does not vary very much with the droplet size and a time-scale of about five hundred picoseconds has been obtained for the relaxation time.

7) For the nanodroplet relaxation process a simple (inverse law) dependence of the excitation energy per atom and time has been found, with two regimes corresponding to high and low excitation energies.

8) The results of the droplet relaxation process can be rationalized by means of two simple models. The first one consists in a phenomenological approach considering the excitation energy per atom as the driven force of the process. The second corresponds to the well-know RRK statistical kinetic model for unimolecular reactions.

9) The photodissociation of Cl_2 inside the helium nanodroplets whose size ranges form 50 to 500 ^{4}He atoms leads to the formation of (confinement) quantum resonances in the velocity distribution of the chlorine fragments (reaction observable). The quantum interferences are produced at the early times of the photodissociation process due to the interaction between the molecule and the helium environment.

10) Within the theoretical approach considered (electronic adiabaticity and rotational degrees of freedom neglected) it has been determined that the dissociation probability of Br_2 induced by the B←X electronic transition is not complete. This is valid for this

reaction in both gas phase and inside helium nanodroplets. The dissociation probability decreases when increasing the droplet size. For the N=1000 ^{4}He atoms nanodroplet a full recombination of Br_2 has been found.

11) The results of the photodissociation of I_2 (B←X transition) inside helium nanodroplets strongly depend on the inclusion or not of the three-body term in the I_2-He potential interaction. Namely, when this term is considered a full recombination is obtained even for the nanodroplet with 100 ^{4}He atoms.

12) For the photodissociation dynamics of homonuclear "isotopic" variants of Cl_2, the lower the mass of the atoms the larger energy exchange between the dissociating molecule and the helium nanodroplet. In some cases this fact even motivates the complete recombination of the molecule.

13) The peak of the interaction energy between the homonuclear "isotopic" variants of Cl_2 and the helium arising from the initial collision of the atoms with the solvation cavity increases when the mass of the atoms decreases, i.e., for the lower masses the atoms and the liquid get closer at this moment of the process.

14) Regarding the capture process of Ne atoms by helium nanodroplets with zero angular momentum (J=0), it has been determined that the pickup probability is complete for velocities equal and above 210 m/s. In contrast, for the lower velocities considered (90 and 120 m/s) the probability of capture is no longer one, with fragment of the wave packet bounces back when the collision with the nanodroplet is produced.

15) The main energy exchange involved in the pickup process takes place during the collision with the nanodroplet surface, i.e. during the entrance into the droplet. The excess energy deposited in the droplet is released by the evaporation of some atoms.

16) A Gaussian shape is reached for the Ne wave packet in momentum representation, when the mean value of its velocity is lower than Landau's critical velocity for liquid helium, due to the lack of friction forces.

17) In the synthesis reaction of formation of the van der Waals dimer Ne_2 inside a nanodroplet of 500 ^{4}He atoms, it has been observed that for all the Ne impinging velocities considered the dimer is formed close to the center of the droplet, excepting in

the case of v=500 m/s that leads to the formation of the dimer close to the nanodroplet surface.

18) The conclusion 17) and additional calculations considering different droplet sizes suggest that the synthesis reaction mechanism is rather complex and a variety of places for the Ne_2 formation are found.

19) The vibrational relaxation of the Ne_2 dimer does not depend neither on the nanodroplet size nor on the impinging velocity of the Ne and it is mainly mediated by the emission of a helium density wave.

20) The structure of the Ne_2 dimer is highly influenced by the presence of the nanodroplet. After the vibrational relaxation of the dimer, the overlap of the corresponding vibrational wave packet with the corresponding one for v=0 in the gas phase is 83.4%.

11. Resum en català

11.1 Introducció

L'estudi de les nanogotes d'heli superfluid ha esdevingut una important àrea de recerca en les últimes dècades. Aquesta agrupa esforços provinents de les comunitats química i física, representant un camp de recerca fronterer entre ambdues disciplines. El seu atractiu resideix en una gran diversitat de motius, des de perspectives més fonamentals fins a d'altres més aplicades. Aquesta introducció s'inicia amb una breu immersió en les propietats de l'heli líquid, seguit d'una descripció de les nanogotes d'heli i el seu interès des de diferents perspectives, fins a arribar al marc en el qual s'ubica la present tesi doctoral.

L'heli és el segon element més lleuger de la taula periòdica (nombre atòmic 2). La seva estructura electrònica de capa tancada ($1s^2$), juntament amb el reduït nombre d'electrons, que li confereix una polaritzabilitat molt baixa, provoquen que aquest element gaudeixi d'una gran estabilitat química. Un tret diferencial molt important de l'heli és que és l'únic element que es manté en estat líquid a una temperatura de (gairebé) zero Kelvin. Es tracta d'un fenomen purament quàntic directament relacionat amb el principi d'incertesa de Heisenberg, tenint en compte les peculiaritats d'aquest element: massa molt lleugera i molt baixa interacció interatòmica ja que és de tipus van der Waals (interacció dipol induït-dipol induït). Això obre la possibilitat de tenir matrius en fase líquida a temperatures extremadament baixes (0.37 K pel cas de les nanogotes de ^{4}He).

Hi ha només dos isòtops estables d'heli presents en la natura: ^{4}He i ^{3}He, essent el primer molt més abundant $n_{^3He}/n_{^4He}$=1.38·10^{-6}. L'heli-4 conté dos neutrons al nucli mentre que l'heli-3 només un, fet que es tradueix en el caràcter bosònic i fermiònic, respectivament. En ambdós isòtops existeixen dues fases líquides, una de les quals (la corresponent a més baixa temperatura) és superfluida, mentre que l'altra és un fluid normal. L'origen físic de la fase superfluida és diferent per a cada isòtop, que fa que la temperatura de transició entre la fase normal i la fase superfluida tingui lloc a temperatures diferents (2.17 K el ^{4}He i 10^{-3} K el

^{3}He). A partir d'aquí quan es parli d'heli líquid farà referència a l'isòtop bosònic ^{4}He, ja que en els estudis d'aquesta tesi tracten solament amb aquest. Hom pot trobar diverses maneres de definir superfluïdesa, segons el procediment experimental emprat per al seu estudi. Una de les definicions més acceptades de superfluïdesa és l'habilitat d'un líquid per fluir sense viscositat a través d'un capil·lar, o sigui, sense pèrdues d'energia ni moment.

Les nanogotes d'heli superfluid són agregats d'àtoms d'heli que poden variar des d'unes poques desenes fins a l'ordre de 10^7 àtoms d'heli, en funció de les condicions experimentals escollides per generar-les. La manera més habitual de formar-les és per mitjà d'una expansió adiabàtica a alta pressió d'heli líquid o gas a través d'un petit orifici d'uns pocs micròmetres. Aquesta expansió provoca l'agregació dels àtoms fins a formar les gotes estables, que es troben a una temperatura de 0.37 K. Una de les característiques més remarcables de les nanogotes d'heli és la seva habilitat per capturar gairebé qualsevol espècie química, ja sigui atòmica o bé molecular, de gran diversitat de mides.

Degut a les peculiars propietats de les nanogotes d'heli, s'han anat desenvolupant una gran diversitat d'investigacions relacionades, enfocades des de diferents perspectives. L'inici del seu estudi, des d'una vessant més fonamental, va ser dut a terme per la comunitat física i estava relacionada amb la superfluïdesa i els fluids quàntics. La superfluïdesa és una propietat intrínsecament macroscòpica, degut a que l'existència de fase líquida com a tal implica una gran quantitat d'àtoms. D'altra banda, està directament relacionada amb el fet que moltes de les partícules del sistema estiguin en un mateix estat quàntic (mono-particular). És per això que les nanogotes ofereixen l'oportunitat de veure com emergeix i evoluciona aquesta propietat a l'incrementar la mida del sistema, des d'un clúster de pocs àtoms fins a una gota formada per milers d'àtoms. Això permet aprofundir en la seva comprensió des d'una perspectiva microscòpica.

El dopatge de les gotes d'heli permet extreure'n una gran quantitat d'informació, fent servir les impureses com a sondes. Per mitjà de mètodes espectroscòpics es pot determinar com és la solvatació de les espècies químiques dins d'aquestes nanogotes, i d'aquí inferir-ne les seves propietats. Gràcies a estudis com aquest es va poder comprovar experimentalment que les molècules poden rotar i fluir (per sota d'una certa velocitat crítica) dins les nanogotes, cosa que posa de manifest la superfluïdesa experimentada a nivell microscòpic.

L'ús de nanogotes d'heli com a matriu ha tingut un creixement molt considerable en els darrers anys. En aquest tipus d'investigacions, juguen un paper secundari ja que l'objectiu no consisteix en l'estudi de les seves propietats sinó en les de les especies químiques dopants. Aquest tipus d'aplicació és la que ha despertat més interès a comunitat química degut a la gran diversitat de possibilitats que ofereix.

La molt baixa temperatura de les gotes d'heli (0.37 K) desperta l'interès en l'ús com a matriu ja que accentua la manifestació de les propietats quàntiques de les especies solvatades en el seu interior. A més, a l'haver-hi menys estats quàntics poblats significativament, facilita l'anàlisi dels seus espectres. La poca activitat química de l'heli fa que les especies dopants no es vegin massa pertorbades per l'heli i, per tant, com si estiguessin quasi en fase gasosa. Controlant el procediment experimental de dopatge es poden aconseguir amb relativa facilitat que les gotes continguin tant sols una espècie química. D'aquesta manera s'eliminen els efectes de les possibles col·lisions (interaccions) entre les diferents molècules presents en els experiments en fase gas (efectes de pressió), encara que sigui a molt baixa pressió. Finalment, la superfluïdesa d'aquestes gotes fa que les molècules immerses en les nanogotes d'heli puguin moure's i rotar lliurement, com si estiguessin al buit, sempre i quan les velocitats siguin suficientment baixes. En aquest context, en el qual les nanogotes d'heli juguen un rol més aplicat, es realitzen estudis que van des de síntesi de molècules metastables, nanoclusters metàl·lics o nanofilaments fins a l'espectroscòpia d'alta resolució.

Una altra variant de la investigació relacionada amb les nanogotes d'heli dopades, però amb una perspectiva menys aplicada és l'estudi de la dinàmica de reaccions en medi condensat (fase líquida). Aquesta àrea de recerca està esdevenint molt activa els darrers anys degut a que té molt interès discernir el rol del solvent en el mecanisme d'una reacció en fase líquida. Les nanogotes d'heli són un solvent pràcticament inert químicament, però és el líquid quàntic per excel·lència, així que és esperable el descobriment de fenomenologies noves molt interessants per a la dinàmica de reaccions. A dia d'avui, s'han realitzat molt pocs estudis en aquest context, tant a nivell experimental com teòric. És per això, que l'objectiu principal de la present tesi doctoral consisteix en una primera immersió a nivell teòric en aquest emergent camp d'investigació.

Existeix una gran diversitat de metodologies teòriques per a l'estudi de l'heli líquid. El mètode teòric emprat en la present tesi doctoral per descriure aquest líquid quàntic és el *Density Functional Theory* (DFT) i la seva extensió a situacions que consideren l'evolució

temporal *Time Dependent DFT* (TDDFT). En aquest marc teòric l'energia s'escriu com un funcional de la densitat, i per tant, la caracterització del sistema (heli líquid) recau en la forma que pren aquest funcional. En aquest cas, es tracta d'un funcional fenomenològic, el qual depèn de diversos paràmetres que s'ajusten per tal de reproduir-ne els valors experimentals de les propietats més importants. Aquesta és pràcticament l'única aproximació teòrica capaç de descriure l'heli líquid superfluid que permet realitzar simulacions temporals de processos en temps raonables, així com també de descriure gotes suficientment grans, comparables a les experimentals.

Aquesta tesi està estructurada en deu capítols. Els dos primers consisteixen en una introducció més profunda de la presentada aquí de l'heli líquid superfluid i les nanogotes i la descripció general dels mètodes teòrics emprats en l'estudi d'aquests sistemes. Seguidament es presenta l'únic estudi de la tesi que no està relacionat amb la simulació temporal de processos dinàmics, sinó que és de tipus estàtic (no involucra el temps). En ell s'investiga l'estructura, energètica i espectroscòpia electrònica de nanogotes d'heli dopades amb oxigen atòmic en els seu estats electrònics de menor energia.

A partir del capítol 4 comencen els estudis relacionats amb simulacions d'evolucions dinàmiques de processos fisico-químics que involucren les nanogotes d'heli. Primerament, en els capítols 4, 5, 6 i 7 es presenten estudis vinculats al procés de fotodissociació de molècules diatòmiques homonuclears dins d'aquestes matrius.

Concretament, el capítol 4 presenta l'estudi d'aquesta reacció pel cas de la molècula de Cl_2. A continuació, en el capítol 5 s'investiga el procés de relaxació de la gota subseqüent al procés estudiat anteriorment. En el capítol 6 s'aprofundeix en l'estudi de les ressonàncies quàntiques observades en les distribucions de velocitats dels fragments resultats de la reacció (àtoms de clor). Per a concloure l'estudi de la fotodissociació de molècules diatòmiques homonuclears en gotes d'heli, el capítol 7 es presenta el mateix l'estudi per a dos halògens diferents: el Br_2 i el I_2, així com també s'aprofundeix en discernir l'efecte de la massa dels àtoms sobre aquest tipus de reaccions en nanogotes d'heli superfluid.

Els capítol 8 i 9 estan força relacionats. En el primer s'investiga, a nivell quàntic, el procés de captura d'un àtom de neó per part de gotes d'heli, mentre que en el segon l'entrada d'un segon àtom permet investigar la formació del dímer de van der Waals Ne_2.

Finalment, la tesi finalitza amb les conclusions finals, les quals es troben recopilades en el capítol 10.

11.2 Estructura, energètica i espectroscòpia electrònica de $O@(^4He)_N$

Aquest estudi té com a objectiu central estudiar l'estructura i energètica de nanogotes d'heli dopades amb àtoms d'oxigen en diferents estats electrònics, fent èmfasi en l'efecte del canvi d'estat electrònic. S'han considerat els tres estats electrònics de l'oxigen atòmic de menor energia: el fonamental ^3P, i els dos primers excitats ^1D i ^1S. No obstant, també s'han calculat les corbes d'energia potencial de més baixa energia per aquest sistema, donat que aquestes no es trobaven a la literatura científica.

Les corbes de potencial han estat calculades a nivell quàntic per mitjà d'un mètode *ab initio*, concretament el icMRCI, incloent-hi a més la correcció de superposició de base (BSSE). S'ha utilitzat una base consistent amb la correlació, amb funcions de polarització quíntuple zeta amb funcions centrades en l'enllaç de van der Waals (aug-cc-pV5Z+b basis set). Finalment, els punts calculats han sigut ajustats a funcions analítiques de tipus Aguado-Paniagua.

L'estat electrònic fonamental de l'heli és (^1S) i, per tant, el seu núvol electrònic consisteix en una distribució isòtropa i sense moment angular, ni orbital ni d'espín. Aquest no és el cas de l'estat fonamental de l'oxigen, que pren valors no nuls del moment angular orbital (L=1) i d'espín (S=1). Ometent els graus de llibertat d'espín, la existència de moment angular no nul provoca l'aparició de dues corbes d'energia potencial (Σ i Π) corresponents al dímer He-O, correlacionant ambdues amb els àtoms en els seus estats fonamentals.

En aquest estudi s'ha considerat una interacció a parelles entre l'oxigen en un estat electrònic donat i els diversos àtoms d'heli configurant la gota[i] . Això fa que pels casos amb L diferent de zero, s'hagi de determinar el potencial anisòtrop He-O a partir dels potencials els dímers, per tal de tenir en compte que la interacció de l'oxigen no pot ser de tipus sigma, pi o delta amb cadascun dels àtoms d'heli que l'envolten.

[i] De fet, en el present estudi treballem amb la densitat i no amb àtoms ubicats en posicions determinades

Els potencials anisòtrops han sigut estimats per mitjà d'un tractament pertorbatiu. Aquest es basa en considerar com a sistema l'àtom d'oxigen (incloent-hi els graus de llibertat electrònics) i, com a pertorbació l'efecte generat per un àtom d'heli situat a una certa distància i orientació. Aquest és un procediment raonable tenint en compte la feble interacció (de tipus van der Waals) que hi ha entre aquests dos àtoms.

En base a la determinació del potencial anisòtrop $O(^3P)$-$He(^1S)$, s'ha calculat l'estructura de les gotes dopades amb oxigen en el seu estat electrònic fonamental, considerant gotes formades per diferents nombre d'àtoms. Com és raonable esperar, tot i tractar-se d'una impuresa atòmica, la solvatació de l'heli esdevé no isòtropa, tal i com es pot observar en la Figura 11.1.

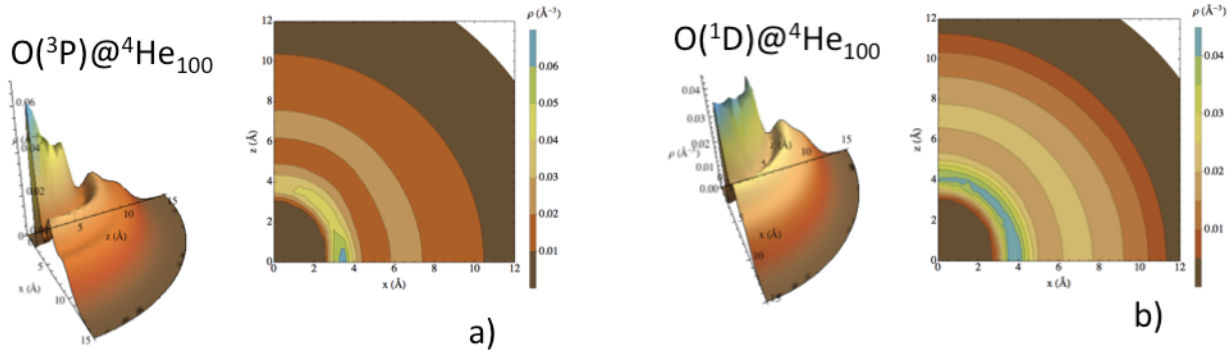

Fig. 11.1. Representacions tridimensional (esquerra) i bidimensional (dreta) de la densitat de l'heli en el pla xz, per una gota amb N=100 i els estats electrònics de l'oxigen: $O(^3P)@^4He_{100}$; (b) $O(^1D)@^4He_{100}$.

També s'ha estudiat l'espectroscòpia electrònica d'emissió corresponent a la transició $^1D \leftarrow ^1S$, que és rellevant degut a la metastabilitat de l'estat ^1S. En aquest estudi s'ha fet ús del principi de Frack-Condon semiclàssic per a l'espectroscòpia en fase condensada. Per tant, la geometria (configuració) de la gota s'ha considerat congelada durant la transició electrònica, i és la corresponent a la gota $O(^1S)@^4(He)_N$. S'han obtingut els espectres per a gotes de diferent número d'àtoms i s'han interpretat aquests resultats d'una anàlisi basada en termes de grups de simetria puntual (veure figura 11.2). L'eixamplament degut a la diferents geometries (disposicions dels àtoms de He) per una densitat s'ha tingut en compte per mètodes estocàstics.

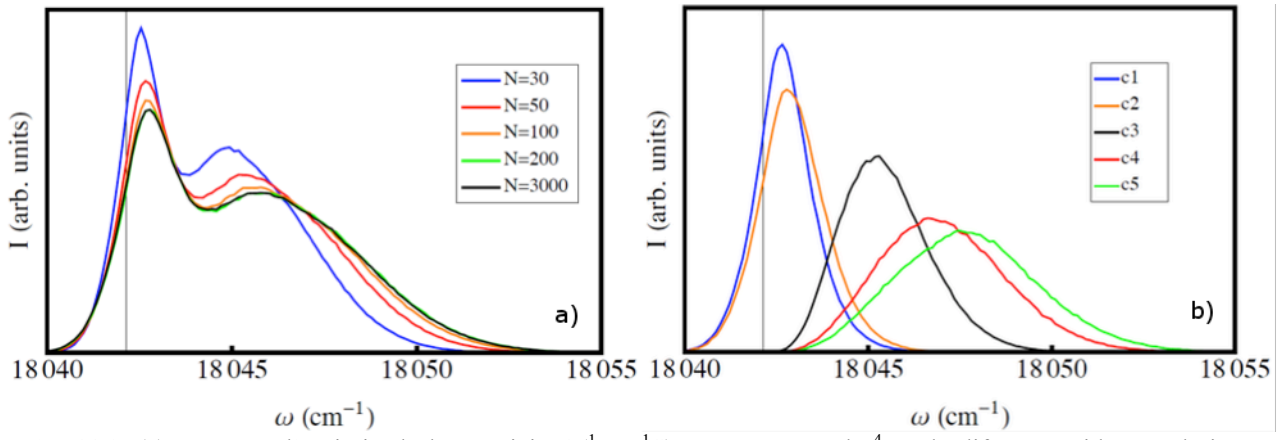

Fig. 11.2. (a) Espectre d'emissió de la transició $O(^1D \leftarrow ^1S)$ en nanogotes de ^4He de diferents mides. La línia vertical el nombre d'ones de la transició en fase gasosa. (b) Les cinc components que contribueixen a l'espectre d'emissió de la transició $O(^1D \leftarrow ^1S)$ en nanogotes de $^4He_{100}$.

Com es pot observar, la presència de la gota provoca, principalment, un lleuger eixamplament del senyal i desplaçament de la transició respecte a la fase gasosa (línia recta gris). Això posa de manifest la gran qualitat de les nanogotes d'heli com a matriu per realitzar-ho espectroscòpia d'alta resolució.

11.3 Dinàmica de la fotodissociació de molècules diatòmiques homonuclears en nanogotes d'heli. El cas del $Cl_2@(^4He)_N$

Aquest estudi presenta una metodologia teòrica per tal d'investigar la dinàmica de la fotodissociació de molècules diatòmiques homonuclears immerses en nanogotes d'heli, basada en una descripció quàntica tant de l'heli com de la impuresa X_2. Com a cas concret d'aplicació d'aquest mètode, s'estudia la fotodissociació del Cl_2 induïda per la transició electrònica $X \rightarrow B$.

El model es basa en un mètode híbrid en el qual s'utilitza *Time Dependent Density Functional Theory* (TDDFT) per a descriure l'heli líquid i dinàmica quàntica per la descripció de la molècula. En aquest estudi s'han hagut d'assumit diverses aproximacions (justificables) per tal de fer-lo viable a nivell computacional. En primer lloc, els graus de llibertat rotacionals de la molècula no s'han considerat. Això està justificat tant per la baixa temperatura de la gota (0.37 K), que fa que només el nivell j=0 estigui inicialment (significativament) poblat, així com per la rapidesa del procés (pocs picosegons) comparada amb l'escala de temps corresponent a la rotació del Cl_2 (període rotacional). També s'ha assumit que la dinàmica

transcórre adiabàticament a nivell electrònic, és a dir, que no hi ha canvis d'estat electrònic durant el procés degut a acoblaments no adiabàtics induïts pel líquid. Tenint en compte les corbes de potencial i els acoblaments, aquesta aproximació és ben plausible. Finalment, s'ha fet ús del principi de Frank-Condon i, per tant, tant la geometria de la molècula (funció d'ona vibracional) com la de la gota s'han considerat congelades durant la transició electrònica, doncs els electrons es mouen molt més ràpidament que no pas els nuclis atòmics. Aquestes aproximacions, juntament amb la simetria del problema, permeten descriure la molècula per mitjà d'un sol gran de llibertat, corresponent a la distancia relativa entre els seus dos àtoms.

La situació inicial (t=0) de la dinàmica consisteix en la gota en el seu estat fonamental, és a dir, $Cl_2(X,v=0,j=0)@(^4He)_N$. En la figura 11.3 es troben representats la densitat de l'heli corresponent a l'estat fonamental, les corbes corresponents als diferents estats electrònics del Cl_2 i la transició estudiada (fletxa vermella). S'ha estudiat aquest procés per a gotes de mida diferent (N=50, 100, 200, 300 i 500), per tal de determinar-ne la influència sobre els observables de la reacció (distribució de velocitats dels àtoms de Cl).

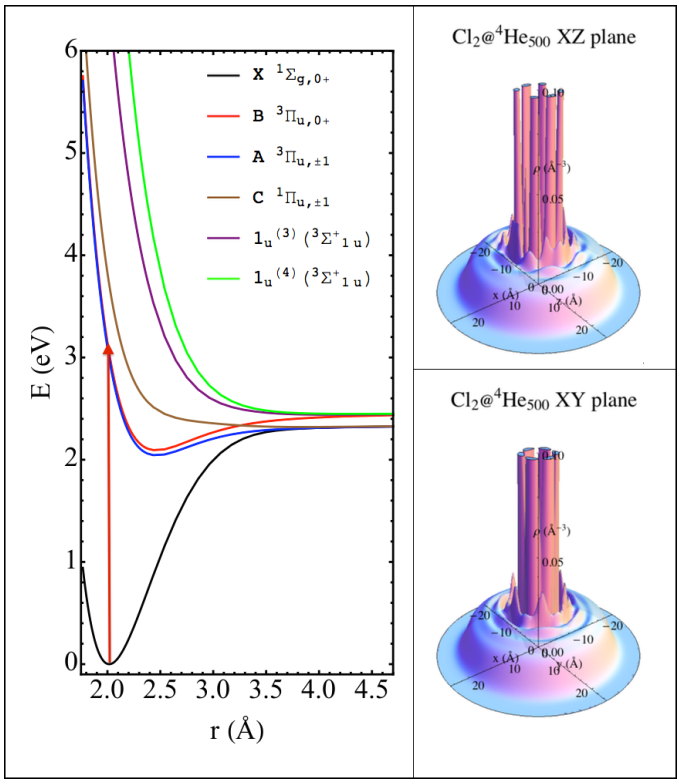

Figura 11.3. Esquerra: estat fonamental (X) i les cinc més baixes excitades (A, B, C, $1_u^{(3)}$ i $1_u^{(4)}$) corbes d'energia potencial del Cl_2, on la fletxa vermella mostra la transició electrònica B ← X. Els límits de dissociació corresponen a $Cl(^2P_{3/2})$ + $Cl(^2P_{3/2})$ (àtoms en l'estat fonamental) i $Cl(^2P_{3/2})$ + $Cl(^2P_{1/2})$ (estat fonamental i excitat, respectivament). Dreta: densitat de l'heli en els plans xz i xy corresponents a $Cl_2(X, v=0)@(^4He)_{500}$. La molècula està orientada segons l'eix z.

A partir de la visualització del material electrònic de l'Apèndix (Chapter 4) o bé de les Figures 11.4 s'obté una imatge acurada del mecanisme de la reacció. Es pot observar com el xoc dels àtoms de Cl contra les parets de la cavitat on està inicialment ubicada la molècula genera unes intenses ones de densitat en la gota. Després l'heli ocupa l'espai romanent entre els dos àtoms de Cl, generant d'aquesta manera una cavitat per cadascun d'ells. Finalment, els àtoms arriben a la superfície i abandonen la gota. S'ha obtingut que l'escala de temps per aquest procés és d'uns pocs picosegons, en funció del nombre d'àtoms de la gota.

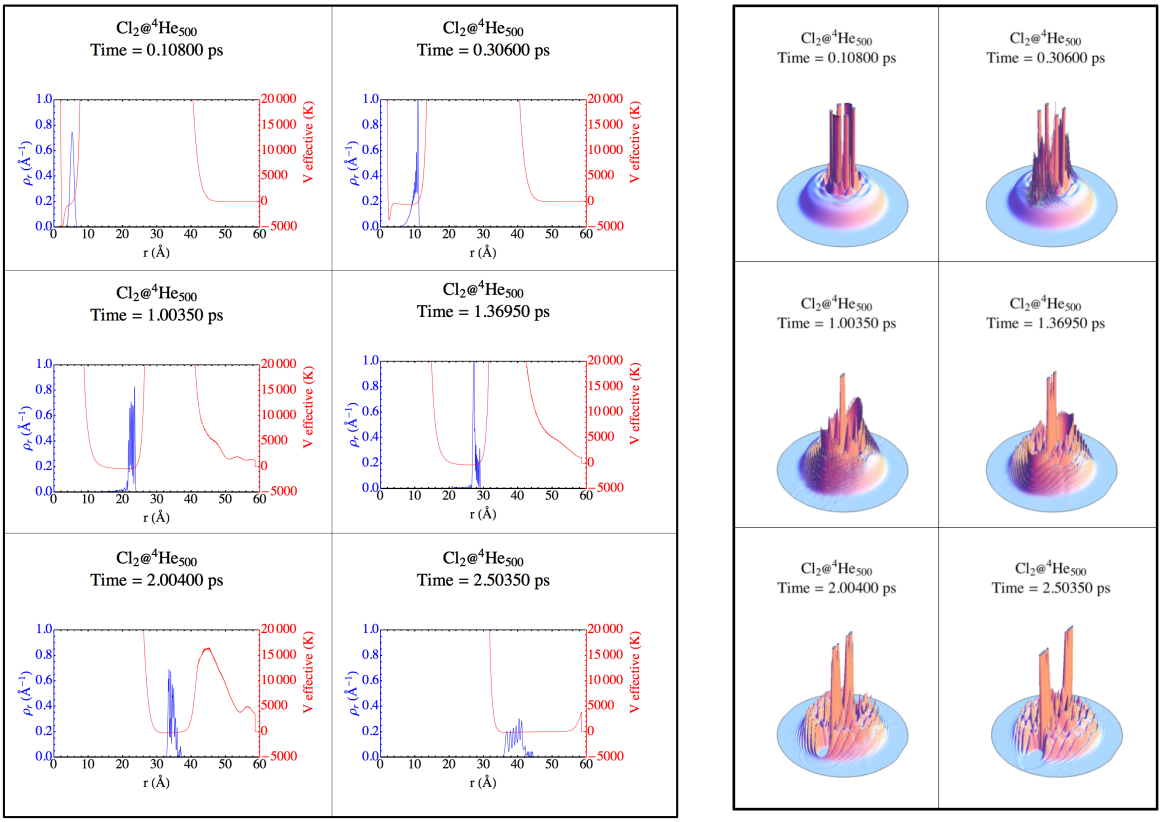

Figura 11.4. Esquerra: evolució del paquet d'ones (blau) de la coordenada relative del Cl_2, juntament amb el potencial efectiu (vermell). Dreta: densitat de l'heli en el pla xz.

S'ha posat de manifest un bescanvi d'energia molt eficient de la molècula vers la gota, la qual es va eliminant per mitjà de l'evaporació d'àtoms d'heli. Durant la col·lisió inicial dels àtoms de Cl contra les parets de la cavitat és quan es produeix l'intercanvi energètic més ràpid, que correspon gairebé al 50% de l'energia inicial. Una vegada s'ha produït el trencament de la molècula i cada àtom està viatjant per l'interior de la gota s'ha pogut determinar que, sota aquestes condicions extremes, l'heli es comporta com un fluid ordinari, el qual exerceix una força de fricció proporcional a la velocitat de l'àtom en moviment. Això es deu al fet que les velocitat implicades són clarament (ordres de magnitud) superiors a la

velocitat crítica de Landau, per sota de la qual les partícules flueixen sense ser frenades (líquid no viscós).

L' observable de reacció consisteix en les distribucions de velocitat dels àtoms de clor sortints. Com s'observa en la Figura 11.5 aquestes tenen una gran estructura oscil·latòria. Aquest fenomen correspon a ressonàncies de confinament, que són estudiades amb profunditat en el capítol 6.

Finalment, s'han trobat algunes dependències lineals relacionant el valor esperat de la velocitat dels àtoms de Cl sortint i el nombre d'àtoms d'heli evaporats respecte al radi de la gota (o $N^{1/3}$, que és equivalent assumint una forma esfèrica per la gota).

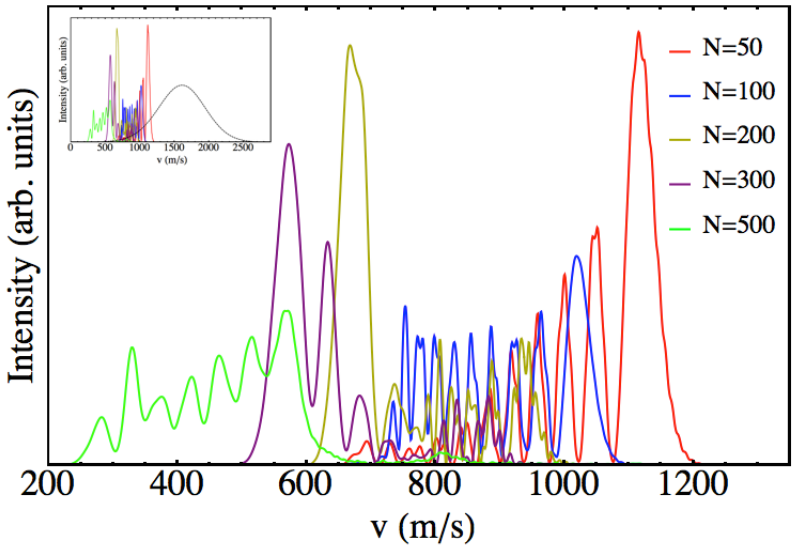

Figura 11.5. Distribucions de velocitat dels àtoms de Cl per a les diferents nanogotes $[Cl_2(B)@(^4He)_N]^*$. També s'inclou el resultat corresponent a la fase gasosa (línia negra de la subfigura).

11.4 Dinàmica de la relaxació de nanogotes d'heli posterior a la fotodissociació de molècules diatòmiques homonuclears. El cas del $Cl_2(^4He)_N$

L'intens bescanvi energètic que té lloc durant la fotodissociació del Cl_2 fa que la gota quedi fortament excitada una vegada els àtoms de clor han sortit del seu interior. Considerant la totalitat del procés com una reacció química, aquesta es pot esquematitzar en tres etapes diferents:

$$Cl_2(X)@(^4He)_N + h\nu \rightarrow [Cl_2(B)@(^4He)_N]^*$$

$$[Cl_2(B)@(^4He)_N]^* \rightarrow Cl + Cl^* + [(^4He)_{N'}]^* + (N\text{-}N')\ ^4He$$

$$[(^4He)_{N'}]^* \rightarrow (^4He)_{N''} + (N'\text{-}N'')\ ^4He$$

El primer pas correspon a l'absorció del fotó que motiva el procés dinàmic. A efectes de la modelització, durant aquest pas s'assumeix que el principi de Frank-Condon és aplicable i, per tant, l'única implicació és un canvi sobtat del potencial d'interacció Cl-Cl, passant de la corba de l'estat fonamental (X) a la de l'estat B. La segona etapa correspon a l'estudi descrit el l'apartat anterior (Chapter 4). Finalment, l'últim pas és el que correspon a la relaxació de la gota per mitjà de l'evaporació d'àtoms d'heli (Chapter 5).

Durant aquest estudi la metodologia teòrica emprada és solament el TDDFT ja que només hi ha evolució de l'heli. S'ha determinat una escala de temps per aquest procés de l'ordre del centenar de picosegons. Durant la relaxació s'observa (veure animacions Apèndix Chapter 5) com l'amplitud de les ones de densitat de la gota va disminuint amb el temps, així com petites fraccions de densitat d'heli sortint de la gota (evaporació). S'ha obtingut una llei de proporcionalitat inversa entre l'energia d'excitació per àtom d'heli i el temps. A fi d'aprofundir en els resultats obtinguts en termes energètics hem proposat dos simples models que ajuden a aprofundir en aquest fenomen.

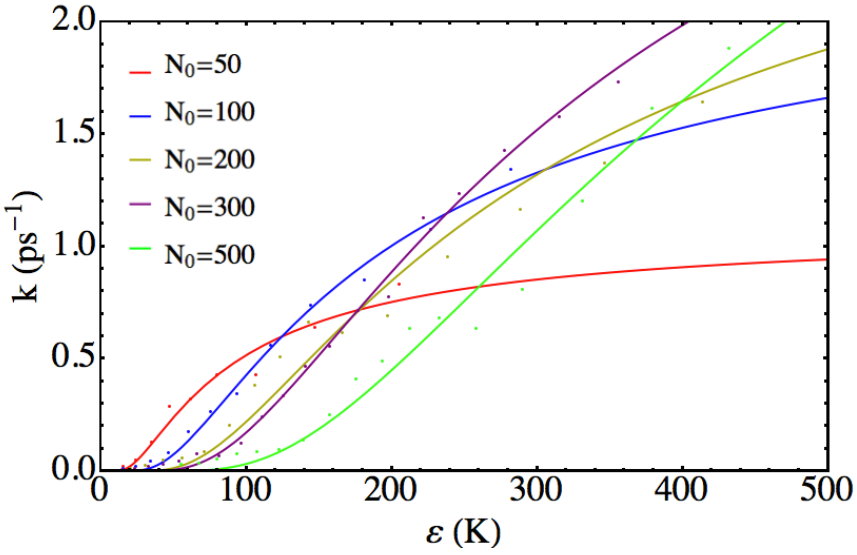

Figura 11.6. Constants de velocitat per a l'evaporació de cada àtom en funció de l'energia d'excitació per a les diferents mides de gota considerades.

El primer correspon a l'aplicació del conegut de la teoria de reaccions unimoleculars model anomenat *Rice Ramsperger Kassel* (RRK), assumint el procés d'evaporació com la

fragmentació d'una supermolècula (gota). Els resultats obtinguts s'ajusten prou bé a aquest model, cosa que posa de manifest la versemblança del tractament RRK, el qual es basa en considerar que l'energia en excés està distribuïda estadísticament en diversos oscil·ladors harmònics. Els resultats de les constants de velocitat obtingudes per les diferent evaporacions i energies d'excitació així com els ajustos segons el model RRK per totes les nanogotes considerades es mostren en la figura 11.6.

L'objectiu principal del segon model consisteix en trobar una llei simple però aplicable per totes les gotes. D'aquesta manera els paràmetres són una representació de la naturalesa comuna de totes elles, o sigui, l'heli líquid. El model proposat assumeix que la reducció de l'energia per àtom deguda a l'evaporació d'un àtom d'heli és proporcional a l'excés d'energia per àtom. A nivell general, els resultats s'ajusten prou raonablement bé a aquest model (figura 11.7).

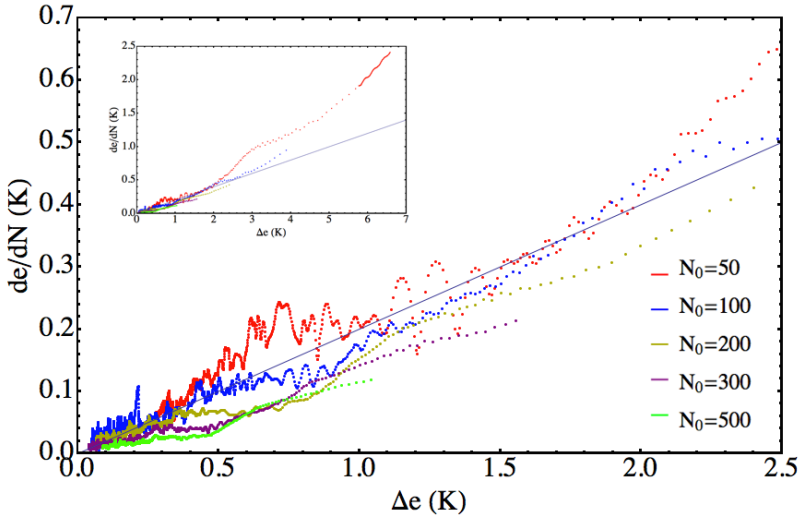

Figura 11.7. Variació de l'energia per àtom d'heli al variar el nombre d'àtoms de la gota (de/dN) respecte l'energia d'excitació per àtom (Δe).

11.5 Ressonàncies quàntiques en la fotodissociació del $Cl_2(B)$ en nanogotes d'heli superfluid

En aquest capítol s'aprofundeix en les ressonàncies observades en les distribucions de velocitat dels àtoms de clor. Per tant, es tracta d'una extensió del capítol 4 focalitzant en la comprensió d'aquest fenomen.

En l'estudi de la fotodissociació, la molècula és descrita per mitjà d'un paquet d'ones corresponent a la distància relativa entre els àtoms. De la representació del paquet d'ones asimptòtic (quan els àtoms ja estan lluny de la gota) en l'espai de moments s'obté la distribució de velocitats. Durant la seva evolució s'ha pogut comprovar que la forma resultant de la ressonàncies prové de tres contribucions diferents.

En primer lloc, i més important, és la generació inicial d'una estructura molt marcada durant la col·lisió dels àtoms amb les partes de la cavitat on resideix inicialment la molècula dins de la gota. Aquesta formació és (gairebé) igual per a totes les mides de gota considerades i la separació entre els pics generats segueix un patró ben definit.

En segon lloc, quan cada àtom de clor està viatjant en la seva pròpia cavitat dins de la gota la funció d'ona en espai de moments va evolucionant de manera suau, sense grans canvis. Aquest procés és equiparable al d'una partícula en una caixa de potencial en moviment (dinàmica).

Finalment, la darrera contribució en la forma final de les distribucions de velocitats té lloc en el moment en què els àtoms de clor arriben a la superfície de la gota. En aquestes regions, l'àtom ja no està isòtropament solvatat, cosa que motiva una modificació final en la distribució de velocitats dirigit cap a velocitats menors. Aquesta situació es correspon a una lleugera desacceleració deguda a la interacció atractiva entre la gota i cada àtoms de clor.

11.6 Fotodissociació: Altres halògens i efecte de la massa

Aquest capítol conclou l'estudi de reaccions de fotodissociació de molècules diatòmiques homonuclears en nanogotes d'heli superfluid. S'investiguen dues casuístiques més, relacionades amb aquests processos: la fotodissociació del dues molècules diatòmiques homonuclears formades pels dos halògens següents augmentant el nombre atòmic: el Br_2 i el I_2 i la influència de la massa dels àtoms en aquest procés. La metodologia teòrica emprada és la mateixa que la descrita en el capítol 4. Algun dels càlculs implicats en aquest capítol no ha finalitzat però, degut a la gran quantitat de resultats ja obtinguts s'ha considerat adient la inclusió d'aquest capítol en la tesi.

S'ha estudiat la dissociació del Br_2 explorant diferents mides de gota (N=100, 200, 300, 500 i 1000), així com el procés en fase gasosa sota les mateixes aproximacions, per tal de detectar l'efecte d'aquesta matriu. Un resultat important que diferencia aquesta recció de l'equivalent pel Cl_2 és que la probabilitat de dissociació no és completa, fins i tot en fase gasosa. És a dir, una fracció de la funció d'ona roman ubicada de manera permanent entorn el pou del potencial electrònic (estat B). Per tant, una part d'aquesta es troba en un estat lligat. Això fa que la fenomenologia de la dinàmica per aquesta reacció sigui diferent, doncs hi ha un procés de fragmentació del paquet d'ones, mediat per l'heli.

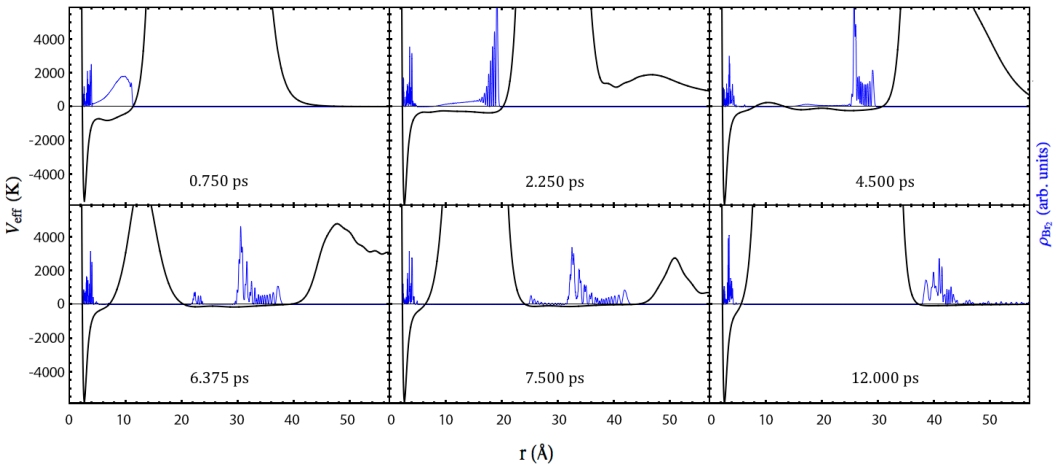

Figura 11.8. Evolució temporal del paquet d'ones de la coordenada relativa (blau), juntament amb el potencial efectiu (negre) que governa la seva dinàmica (suma del potencial electrònic Br-Br més el Br_2-heli).

Una vegada es produeix la fragmentació, la dinàmica ve donada per al contribució de les dues parts (veure animacions Apèndix 7 i Figura 11.8). El fragment "lligat" experimenta un procés de relaxació vibracional mediada per l'heli. Aquest es posa de manifest en el patró oscil·latori de rerafons que es troba en l'evolució de la velocitat (Figura 11.9) . Aquest es un procés és lent (comparat amb la fotodissociació) i no es correspon amb l'objectiu principal de la present investigació. Pel que fa al fragment dissociatiu, aquest presenta una dinàmica similar a la del clor, però molt més suau (velocitats més baixes i masses més grans).

Pels casos de les gotes més grans (N=500 i 1000) s'arriba, fins i tot, a produir un procés de recombinació induït per la nanogota. És a dir, es bescanvia tanta energia cinètica que, quan els àtoms arriben a les proximitats de la superfície, la interacció atractiva de la gota és suficientment gran com per induir la recombinació.

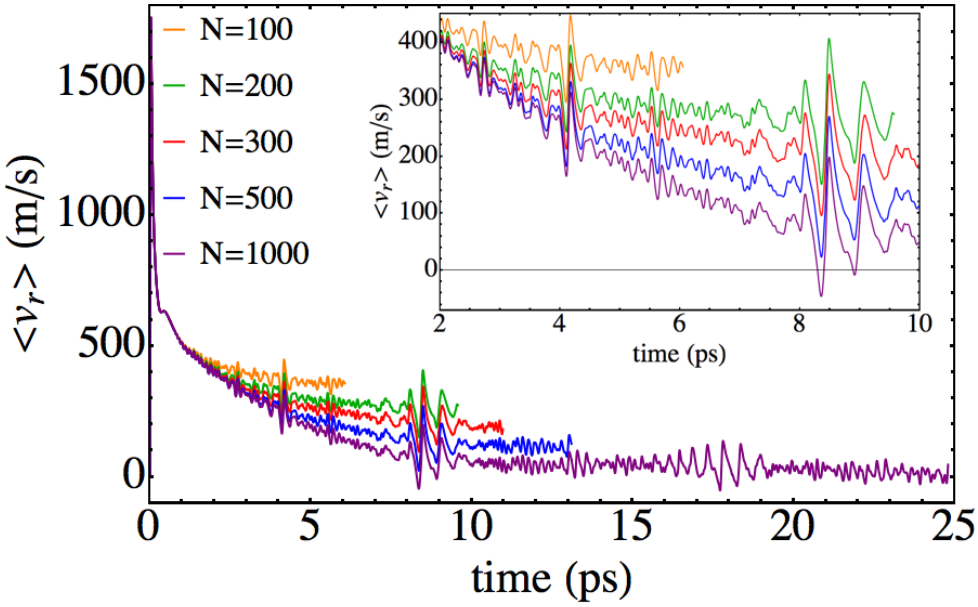

Figura 11.9. Evolució temporal del valor esperat de la velocitat relativa per a les diferents mides de gota estudiades.

Pel que respecte a la dissociació del I_2, només s'ha realitzat una exploració preliminar ja que s'ha comprovat que la tendència a dissociar és molt menor. A més, la fenomenologia d'aquest procés es veu molt afectada pels potencials utilitzats.

Amb l'objectiu la influència de la massa dels àtoms en la fotodissociació s'ha modelitzat aquesta reacció per a unes hipotètiques molècules idèntiques al clor, exceptuant-ne la seva massa. D'aquesta manera es mantenen controlades la resta de variables (potencials i mida de gota fixada N=300 ^{4}He àtoms) per tal de poder assignar inequívocament els diferents comportaments obtinguts a les diferents masses. Per la mateixa finalitat s'ha mantingut constant el paquet d'ones inicial, tot i no ser el corresponent a l'estat fonamental, per tal d'obtenir energies inicials iguals (principalment es tracta d'energia potencial).

En la Figura 11.10 es veu l'evolució de l'energia d'aquestes molècules, definida com la suma de l'energia potencial X-X (electrònica) més la cinètica, per a les diferents masses considerades. S'observen clarament dos règims, els quals es veuen més diferenciats a mesura que disminueix la massa. El primer correspon a la pèrdua d'energia degut a la col·lisió amb les parets de la cavitat de la gota, mentre que el segon al fluir dels àtoms a través d'un fluid viscós.

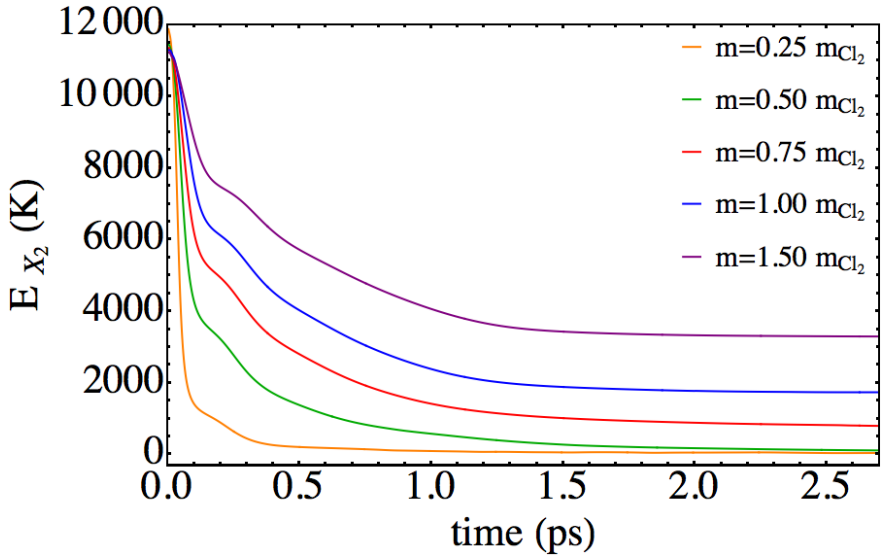

Figura 11.10. Evolució de l'energia de la diatòmica (potencial X-X més cinètica relativa) per a les diferents masses considerades.

En aquest estudi també s'han detectat processos de recombinació pels casos de massa més petita, ja que el bescanvi d'energia és més efectiu i, per tant, els àtoms dissociats es frenen més ràpidament.

11.7 Captura d'àtoms de Ne per part de nanogotes d'heli

L'habilitat de les nanogotes d'heli superfluid per capturar gairebé qualsevol espècie química és una de les seves característiques més remarcables. En aquest capítol es modelitza teòricament aquest procés pel cas d'àtoms de neó.

Degut a la lleugeresa del Ne el seu tractament ha de ser de tipus quàntic ja que té un moviment de punt zero considerable. Per tant, seguint l'esquema emprat en les dissociacions, es proposa un mètode híbrid en el qual s'utilitza TDDFT per a la descripció de l'heli líquid mentre que la partícula està descrita mitjançant la dinàmica quàntica. Durant aquest estudi s'ha plantejat una situació simplificada, considerant només el cas de moment angular nul, és a dir, col·lisions que incideixen en la direcció normal a la superfície de la gota. Això permet descriure la dinàmica del Ne unidimensionalment, d'aquesta manera es redueix considerablement el cost computacional de l'estudi.

Malgrat aquesta restricció, s'han obtingut resultats interessants que permeten observar el comportament de l'heli superfluid des de la perspectiva d'una "sonda" quàntica. D'altra banda, és important tenir en compte que aquest procés pot considerar-se com un primer pas per a la reacció de formació del dímer de van der Waals Ne_2 dins de gotes d'heli (Chapter 9).

S'han seleccionat vuit velocitats incidents diferents per tal de comprovar l'efecte de l'energia de col·lisió sobre el procés de captura. Aquestes han estat escollides per tal de mostrejar adientment la distribució de Maxwell de velocitats a temperatura ambient, cosa que reprodueix les condicions del procés experimental. La mida de gota corresponen escollida correspon a 1000 àtoms d'heli, semblant a les utilitzades experimentalment.

La comprensió del mecanisme del procés es pot inferir a través de la visualització les animacions en què es mostra tant el paquet d'ones del Ne en representació de posicions i moments, com la densitat de l'heli en el pla que conté l'eix d'incidència (Apèndix del Chapter 8) i de la Figura 11.11.

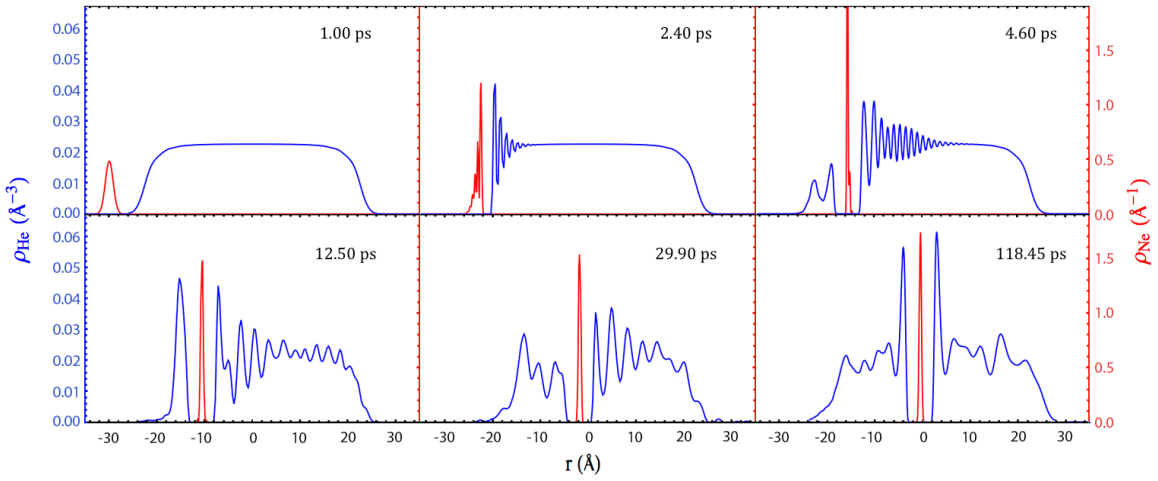

Figura 11.11: Evolució temporal de la densitat de l'heli segons l'eix z (blau) i del paquet d'ones del Ne (vermell) pel cas de $\langle v_0 \rangle$=500 m/s.

La velocitat del Ne es redueix ràpidament a l'entrar a la gota, generant-se unes ones de densitat en la gota, la longitud de les quals disminueix a l'augmentar l'energia de l'impacte. Durant aquest xoc es produeix el bescanvi d'energia més ràpid. Aquest fet es pot fàcilment observar de la Figura 11.12 ja que, al no considerar l'estructura interna, l'energia del Ne és només cinètica (proporcional a v^2)

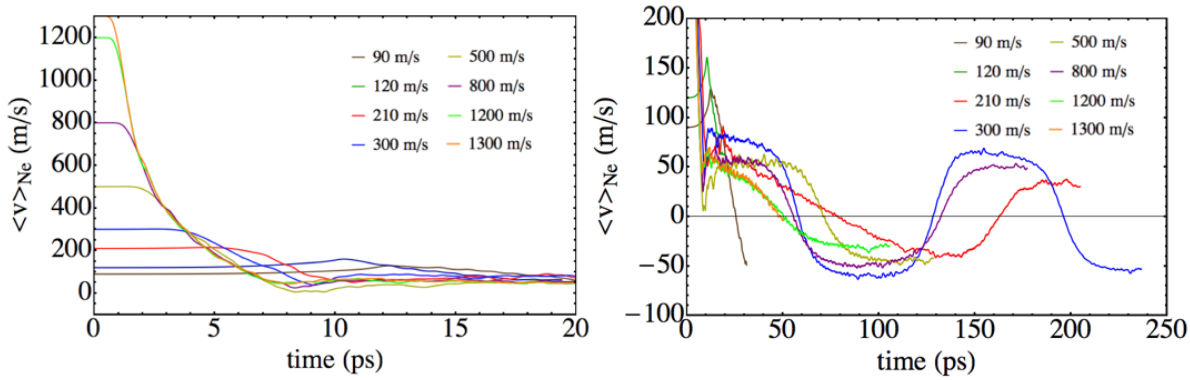

Figura 11.12. Evolució temporal del valor esperat de la velocitat focalitzant a: (a) col·lisió inicial i pèrdua d'energia i (b) trajecte del Ne a través de la gota.

Un fet remarcable que s'ha trobat en aquest estudi és veure com el valor esperat de la velocitat de l'àtom de Ne roman constant a partir d'un cert instant, i tant sols canvia de signe quan el Ne arriba a la superfície de la gota. Aquest fet es tradueix en un paquet d'ones en espai de moments de perfil gaussià, que no varia gaire amb el temps. Això posa de manifest el caràcter superfluid de l'heli líquid sota aquestes condicions.

Una manera interessant de visualitzar el procés que aporta molta informació està recollida en la Figura 11.13. Aquesta vindria a ser l'equivalent a les trajectòries fàsiques de la mecànica clàssica, però en aquest cas en termes de valors esperats (quàntic). Per simplificar el discurs, durant la discussió següent es parlarà de posicions i velocitats fent referència, és clar, als corresponents valors esperats. La línia gris discontínua d'aquests gràfics representa el valor aproximat del radi de la gota. S'observa clarament com la velocitat del Ne disminueix dràsticament en la col·lisió amb la superfície. Un altre fenomen important és que la velocitat roman constant quan es troba en les zones interiors de la gota. Això permet definir una mena de zona en la qual la gota té caràcter de bulk.

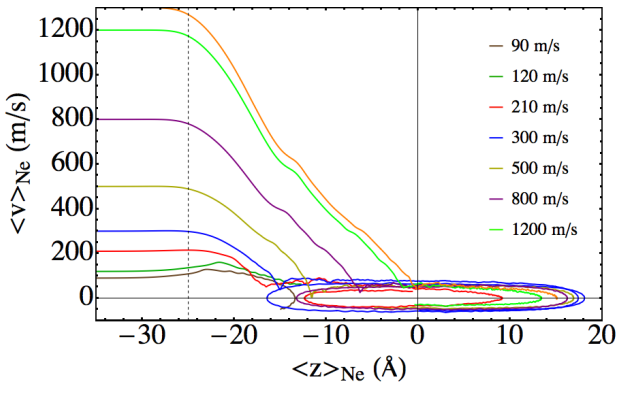

Figura 11.13. "Trajectòries fàsiques" dels valors esperats de la velocitat i posició.

11.8 Reacció de síntesi d'un dímer de van der Waals en nanogotes d'heli: El cas del Ne_2

Aquest darrer estudi consisteix en una extensió de l'anterior ja que el dopatge amb un primer àtom de neó és el pas previ a la posterior captura d'una altre per tal de produir-se la reacció. D'altra banda, també està relacionat amb els capítols inicials, doncs en certa manera, el procés de síntesi és la reacció inversa a la fotodissociació. En aquest cas, però, el dímer format no és un compost amb un enllaç químic (elevada energia), sinó de tipus van der Waals. En aquesta primera investigació, igual que en el cas de la captura del Ne, només s'ha considerat la situació col·lineal, o sigui, sense moment angular per tal de simplificar l'estudi.

Cal esmentar, l'aportació principal d'aquest treball fa referència a la metodologia desenvolupada, doncs permetrà l'estudi d'altres processos com podria ser el de la fotodissociació d'una molècula asimètrica. S'estén el mètode descrit en el Chapter 4, incorporant també la dinàmica del centre de massa (CM) del dímer. La dinàmica d'aquest grau de llibertat s'ha descrit a nivell clàssic, fet justificat pel gran valor (a priori) de la massa efectiva corresponent (suma de la dels dos àtoms). Així doncs, la metodologia combina un tractament quàntic a nivell TDDFT per a l'heli superfluid, dinàmica quàntica per a la coordenada relativa entre les partícules i dinàmica newtoniana per al centre de masses del dímer.

En el present estudi hem escombrat diverses velocitats de l'àtom de Ne incidint en una gota dopada de 500 àtoms d'heli ($Ne@(^4He)_{500}$). Aquestes velocitats han estat seleccionades d'acord amb la distribució e Maxwell a la temperatura ambient. El mecanisme del procés es pot observar en la Figura 11.14 i en les animacions (Apèndix Chapter 9). S'observa que per totes les velocitats estudiades el dímer es forma en les proximitats del centre de la gota, exceptuat el cas de 500 m/s, que es forma a la superfície.

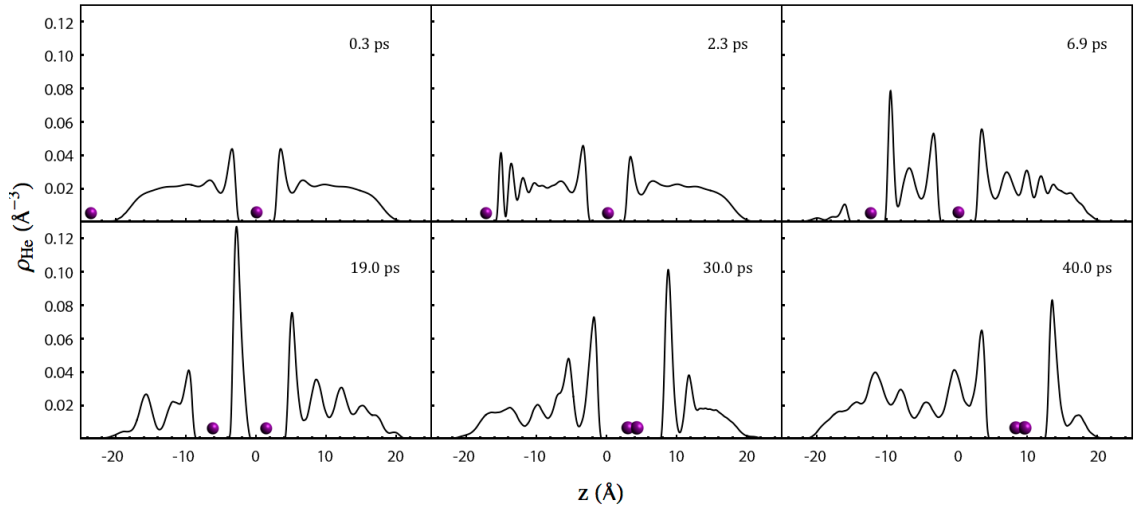

Figura 11.14. Evolució temporal del procés de síntesi del Ne_2, pel cas d'una velocitat del Ne incident de 300 m/s.

En la Figura 11.14 es mostra una estimació de les evolucions temporals de les posicions i velocitats dels dos àtoms de Ne. Es pot observar de la figura de les velocitats l'efecte de tenir la gota prèviament dopada, que provoca que una forta reducció de la velocitat del Ne entrant, arribant fins i tot a parar-se (velocitats negatives), a diferència del que passava en la captura amb la gota pura.

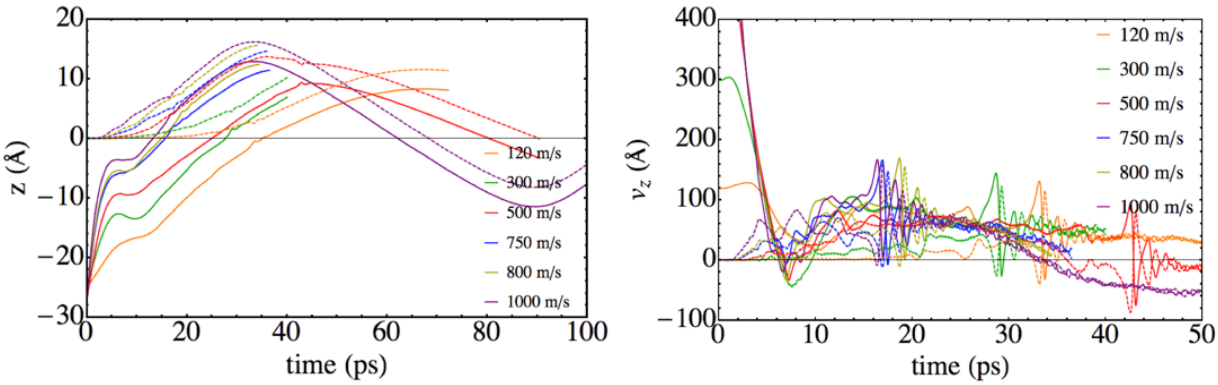

Figura 11.14. Evolució temporal de les posicions i velocitats del Ne entrant (línia contínua) i Ne inicialment al centre de la gota (línia discontinua).

Quan es forma la molècula s'observa una forta oscil·lació en les velocitats dels àtoms deguda a l'efecte de la interacció Ne-Ne. Aquest procés ve a ser una relaxació vibracional d'un dímer de van der Waals. D'aquests gràfics també es pot inferir una escala de temps del per al formació de la molècula (per les condicions estudiades) de l'ordre d'unes desenes de picosegons, dependent del cas.

Finalment, remarcar la considerable modificació del dímer de Ne_2 respecte a la fase gas degut a la presència del líquid (Figura 11.15) ja que la interacció Ne-Ne és molt dèbil i del mateix ordre de magnitud que la Ne-He. Això fa que el potencial efectiu total tingui un pes molt important al generat per l'heli, modificant així les característiques del dímer format. El solapament de la funció d'ona vibracional després de relaxar-se amb la corresponent al v=0 en fase gasosa és d'un 83.4%. No és esperable que s'observi aquest fenomen per dímers amb enllaços químics (molècules pròpiament dites)

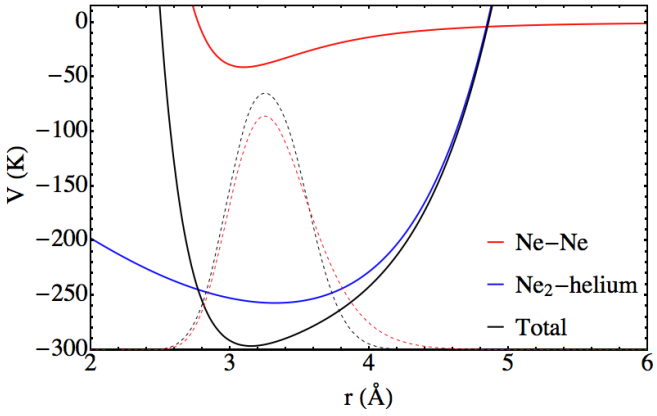

Figura 11.15. Potencial efectiu final (línia negra), juntament amb les seves dues contribucions: el potencial Ne-Ne (vermell) i el Ne_2-heli (blau). En línia discontinua es mostren els paquets d'ona corresponents a: final dins la nanogota (negre) i v=0 en fase gasosa (vermell).

11.9 Conclusions

Les conclusions principals obtingues en els estudies realitzats en la present tesi són les següents:

1) No s'han trobat gran diferències en l'estructura i energètica de les gotes dopades amb oxigen atòmic al variar-ne el seu estat electrònic O(^{3}P, ^{1}D and ^{1}S). Estat resultat es justifica pel la similitud en les polaritzabilitats d'aquests estats juntament amb el caràcter van der Waals de la interacció O-He. Les principal variació és l'anisotropia en la densitat d'heli induïda pels estats singlets dirradicals, o sigui, el ^{1}D i ^{1}S.

2) Els resultats obtinguts en l'espectroscòpia d'emissió electrònica per la transició ^{1}D←^{1}S concorden amb el fet que les gotes d'heli són una matriu ideal on realitzar-hi

estudis d'espectroscòpia d'alta resolució, ja que només s'ha produït un lleuger desplaçament i eixamplament respecte al valor obtingut en la fase gasosa.

3) La dinàmica de la fotodissociació del Cl_2 en nanogotes d'heli superfluid té lloc en l'escala de temps del picosegons; per nanogotes variant des de 50 (0.85 ps) fins a 500 (2.57 ps) àtoms de ^4He.

4) S'ha posat de manifest un bescanvi d'energia molt eficient pel procés de la fotodissociació, a través del qual el Cl_2 arriba perdre des d'un 57% fins un 91% de l'energia per la major i menor gota considerades, respectivament. A més, s'ha verificat que el seu mecanisme no depèn de la mida de la gota.

5) Pel procés de la fotodissociació del Cl_2 en nanogotes d'heli, s'han trobat dues relacions lineals entre la velocitat dels àtoms de Cl sortint i el nombre d'àtoms d'heli evaporats respecte al radi de la gota.

6) El mecanisme de relaxació de la nanogota, una vegada han marxat els àtoms de clor, no depèn massa de la mida de gota. Per aquest procés s'ha obtingut una escala de temps de l'ordre de cinc-cents picosegons.

7) En la relaxació de la gota s'han obtingut unes relacions simples (proporcionalitat inversa) entre l'energia d'excitació per àtom d'heli i el temps, amb dos règims diferents corresponents a una gran i petita excitació de la gota.

8) Els resultats de la relaxació de la gota subseqüent a la fotodissociació del clor han sigut racionalitzats per mitjà de dos models simples. El primer és de caire fenomenològic i consisteix en suposar que la força impulsora de l'evaporació és l'energia d'excitació per àtom. El segon és l'anomenat RRK, un model estadístic extensament emprat en l'estudi de les reaccions unimoleculars.

9) La fotodissociació del Cl_2 en nanogotes d'heli superfluid dóna peu a la formació de ressonàncies quàntiques (de confinament) en les distribucions de velocitat del Cl (observable de reacció). Durant els temps inicials dels procés és quan tenen lloc les interferències quàntiques degudes a la interacció entre la gota i la molècula.

10) Dins del l'aproximació teòrica emprada (electrònicament adiabàtic i omissió de la rotació), s'ha determinat que la probabilitat de dissociació del Br_2 induïda per la transició electrònica $B \leftarrow X$ no és completa. Aquesta probabilitat disminueix a

l'augmentar la mida de la gota. S'ha determinat una probabilitat de recombinació total pel cas d'una gota amb N=1000 àtoms de ^{4}He.

11) Els resultats de la fotodissociació del I_2 (transició B←X) depenen significativament de la inclusió del terme de tres cossos en el potencial d'interacció I_2-He. Quan s'inclou aquest terme s'obté una recombinació total del paquet d'ones pel cas d'una gota de 100 àtoms d'heli.

12) En les fotodissociacions variant les masses dels àtoms de la molècula diatòmica s'obté un bescanvi energètic entre la molècula diatòmica i la gota major com menor és la massa dels àtoms que la conformen. Per alguns casos aquest bescanvi és tant eficient que s'arriba a produir la recombinació.

13) El pic en l'energia d'interacció entre les variants "isotòpiques" del Cl_2 i la gota degut a la col·lisió inicial dels àtoms amb les parets de la cavitat augmenta com menor és la massa. Això posa de manifest que els àtoms i l'heli estan més propers en aquest instant com menor és la massa.

14) S'ha determinat que la probabilitat de captura d'un àtom de Ne amb moment angular nul (J=0) per part d'una nanogota formada per 1000 àtoms d'heli és completa per a velocitats incidents majors a 210 m/s. Per a velocitats menors una part del paquet d'ones és reflectit al produir-se la col·lisió amb la superfície de la gota.

15) El bescanvi més important d'energia de l'àtom de Ne cap a la gota es produeix durant la col·lisió inicial. L'energia transmesa a la gota és alliberada per mitjà de l'evaporació d'àtoms d'heli.

16) Quan el valor esperat de la velocitat de l'àtom de Ne és menor que la velocitat límit de Landau el paquet d'ones en la representació de moments adopta una forma gaussiana, que es deu a l'absència de forces.

17) Per la síntesi del dímer de van der Waals Ne_2 dins nanogotes d'heli superfluid de N=500 àtoms s'ha observat que per a totes les velocitats de col·lisió estudiades aquest es forma en les proximitats del centre de la gota, exceptuant pel cas de v=500 m/s, en què es forma a la seva superfície.

18) La conclusió 17) i d'altres resultats considerant mides de gota més gran posen de manifest que el mecanisme de la reacció de síntesi del Ne_2 dins de nanogotes és força complex i aquest es forma en diferents regions de la gota.

19) La relaxació vibracional del Ne_2 dins la nanogota té lloc de la mateixa manera, independentment de la mida de la gota i la velocitat de col·lisió considerades. L'energia es transfereix principalment per l'emissió d'una ona de densitat d'heli.

20) La estructura del dímer de van der Waals Ne_2 es veu influenciada per al presència de la gota. El solapament entre el paquet d'ones final i el corresponent a la fase gasosa (v=0) és d'un 83%.